



# Structure and dynamics of the interface between interlacing flux tubes observed at the earth's magnetopause by MMS mission

Issaad Kacem

## ► To cite this version:

Issaad Kacem. Structure and dynamics of the interface between interlacing flux tubes observed at the earth's magnetopause by MMS mission. Astrophysics [astro-ph]. Université Toulouse 3 Paul Sabatier (UT3 Paul Sabatier), 2018. English. NNT: . tel-01916537

**HAL Id: tel-01916537**

**<https://theses.hal.science/tel-01916537>**

Submitted on 8 Nov 2018

**HAL** is a multi-disciplinary open access archive for the deposit and dissemination of scientific research documents, whether they are published or not. The documents may come from teaching and research institutions in France or abroad, or from public or private research centers.

L'archive ouverte pluridisciplinaire **HAL**, est destinée au dépôt et à la diffusion de documents scientifiques de niveau recherche, publiés ou non, émanant des établissements d'enseignement et de recherche français ou étrangers, des laboratoires publics ou privés.



# THÈSE

En vue de l'obtention du

**DOCTORAT DE L'UNIVERSITÉ DE TOULOUSE**

Délivré par : *l'Université Toulouse 3 Paul Sabatier (UT3 Paul Sabatier)*

---

---

Présentée et soutenue le 11/10/2018 par :

**ISSAAD KACEM**

**Structure et dynamique de l'interface entre des tubes de flux  
entrelacés observés à la magnétopause terrestre par la mission MMS**

---

---

## JURY

SÉBASTIEN GALTIER  
ROCH SMETS  
GENEVIÈVE SOUCAIL  
KARINE ISSAUTIER  
MATTHIEU  
KRETZSCHMAR  
CHRISTIAN JACQUEY  
VINCENT GÉNOT

Rapporteur  
Rapporteur  
Examineur  
Examineur  
Examineur

Directeur de thèse  
Co-directeur de thèse

---

### École doctorale et spécialité :

*SDU2E : Astrophysique, Sciences de l'Espace, Planétologie*

### Unité de Recherche :

*Institut de Recherche en Astrophysique et Planétologie (UMR 5277)*

### Directeur(s) de Thèse :

*Christian JACQUEY et Vincent GENOT*

### Rapporteurs :

*Sébastien GALTIER et Roch SMETS*



# STRUCTURE AND DYNAMICS OF THE INTERFACE BETWEEN INTERLACING FLUX TUBES OBSERVED AT THE EARTH'S MAGNETOPAUSE BY MMS MISSION

by

**Issaad Kacem**

A thesis submitted to Paul Sabatier University  
for the degree of Doctor of Philosophy

defended on Thursday October 11, 2018 at 14:00 PM.

Supervisor:	Christian JACQUEY	
co-Supervisor:	Vincent GENOT	
Thesis committee:	Sébastien GALTIER,	LPP
	Roch SMETS,	LPP
	Geneviève SOUCAIL,	IRAP
	Karine ISSAUTIER,	LESIA
	Matthieu KRETZSCHMAR,	LPC2E
	Olivier LECONTEL,	LPP

An electronic version of this thesis is available at

<http://thesesups.ups-tlse.fr>.



*"The plain fact is that the planet does not need more successful people. But it does desperately need more peacemakers, healers, restorers, storytellers, and lovers of every kind. It needs people who live well in their places. It needs people of moral courage willing to join the fight to make the world habitable and humane. And these qualities have little to do with success as we have defined it."*

*David W. Orr*

To the most important person in my life.

# CONTENTS

<b>List of Figures</b>	<b>v</b>
<b>List of Tables</b>	<b>xiii</b>
<b>Acknowledgements</b>	<b>xv</b>
<b>Abstract</b>	<b>xix</b>
<b>Résumé</b>	<b>xxi</b>
<b>Introduction Générale</b>	<b>xxiii</b>
<b>1 Introduction</b>	<b>1</b>
1.1 Physics of collisionless plasmas . . . . .	1
1.1.1 Solar and astrophysical plasmas . . . . .	1
1.1.2 Collisionless plasmas properties . . . . .	2
1.1.3 Kinetic and fluid description . . . . .	8
1.1.4 Frozen-in magnetic field condition . . . . .	9
1.2 Magnetic reconnection in collisionless plasmas . . . . .	10
1.2.1 The principle of magnetic reconnection . . . . .	11
1.2.2 Differential ion-electron motion: Hall fields and currents . . . . .	12
1.2.3 Anomalous resistivity model for magnetic reconnection . . . . .	15
1.2.4 Reconnection rate . . . . .	15
1.2.5 Energy conversion rate . . . . .	16
1.2.6 Observational constraints for magnetic reconnection analysis . . . . .	17
1.3 The Earth's magnetosphere . . . . .	18
1.3.1 Large-scale structure of the Earth's magnetosphere . . . . .	18
1.3.2 Solar wind-Magnetosphere coupling: Dungey's cycle . . . . .	23

1.4	Magnetic reconnection at the Earth's magnetopause . . . . .	24
1.4.1	The dayside magnetopause and the boundary layer . . . . .	24
1.4.2	Flux transfer events . . . . .	25
1.4.3	FTEs characteristics . . . . .	26
1.5	Wave-Plasma interactions . . . . .	27
1.5.1	Linear plasma wave theory . . . . .	29
1.6	Overview of the thesis . . . . .	32
<b>2</b>	<b>Instrumentation and analysis techniques</b>	<b>33</b>
2.1	The Magnetospheric Multiscale mission (MMS). . . . .	33
2.2	Mission and measurements requirements . . . . .	33
2.3	Mission operations . . . . .	36
2.4	Instrument descriptions . . . . .	37
2.4.1	Hot Plasma Suite . . . . .	37
2.4.2	Energetic Particles Detector Suite . . . . .	42
2.4.3	Fields Suite . . . . .	43
2.4.4	Electron drift instrument (EDI). . . . .	45
2.4.5	Two Active Spacecraft Potential Control Devices (ASPOC) . . . . .	45
2.5	Data analysis techniques. . . . .	46
2.5.1	Magnetopause model . . . . .	46
2.5.2	Magnetopause transition parameter . . . . .	48
2.5.3	Curlometer technique . . . . .	49
2.5.4	Variance analysis: current density measurements . . . . .	51
2.5.5	Multi-Spacecraft Timing Analysis: structures orientation and motion . . . . .	53
2.5.6	Walén test . . . . .	54
2.6	Spectral analysis . . . . .	57
2.7	Analysis method for Lower Hybrid Drift Waves (LHDWs) . . . . .	58
2.8	WHAMP simulations . . . . .	60
<b>3</b>	<b>Magnetic reconnection at a thin current sheet separating two interlaced flux tubes near the Earth's magnetopause</b>	<b>61</b>
3.1	Introduction . . . . .	61

3.2	Instrumentation and data . . . . .	62
3.3	Spacecraft location and configuration . . . . .	63
3.4	Solar wind observations . . . . .	65
3.4.1	Expected location of the reconnection sites [Trattner et al. (2007)] . . .	69
3.5	Large time-scale observations. . . . .	70
3.5.1	Boundary layer structure . . . . .	70
3.5.2	Magnetopause transition parameter . . . . .	75
3.6	Analysis of the event . . . . .	76
3.6.1	Observations. . . . .	76
3.6.2	Small-scale current sheet . . . . .	83
3.7	Discussion and interpretation . . . . .	89
3.7.1	Phenomenological interpretation . . . . .	89
3.7.2	Possible reconnection at the thin current sheet . . . . .	93
3.8	Summary and conclusion . . . . .	97
<b>4</b>	<b>Plasma waves study for the event of 7 November 2015</b>	<b>99</b>
4.1	Introduction . . . . .	99
4.2	Instrumentation . . . . .	99
4.3	Main features observed around the current sheet . . . . .	100
4.4	Plasma waves. . . . .	100
4.4.1	Whistler waves. . . . .	100
4.4.2	Lower Hybrid Drift Waves (LHDWs) . . . . .	107
4.5	Discussion . . . . .	114
4.6	Summary and conclusions. . . . .	116
<b>5</b>	<b>Summary and conclusions</b>	<b>117</b>
5.1	Summary of results . . . . .	117
5.2	Outlook on possible developments . . . . .	120
5.3	A wider perspective on this work . . . . .	121
<b>A</b>	<b>Résumé et conclusions</b>	<b>123</b>
A.1	Résumé des résultats . . . . .	123

A.2 Perspectives sur les développements possibles . . . . .	125
A.3 Perspectives plus larges . . . . .	127
<b>Bibliography</b>	<b>133</b>

# LIST OF FIGURES

1	Artist concept of the Magnetospheric Multiscale (MMS) mission to study magnetic reconnection. Credits: NASA. . . . .	xxvi
1.1	Examples of plasmas. . . . .	2
1.2	The ranges of temperature and densities of plasmas ( $1\text{eV} \sim 11600\text{K}$ ). Figure from Peratt (1996). . . . .	3
1.3	Electron trajectory in a uniform magnetic field. The magnetic field lines are shown as straight purple arrows. . . . .	6
1.4	The definition of the pitch angle $\alpha$ for a particle gyrating around the magnetic field lines. . . . .	6
1.5	Ions motion in the presence of a density gradient. More ions are moving downwards than upwards giving rise to a drift velocity perpendicular to the magnetic field and to the density gradient. . . . .	7
1.6	A 2-D schematic view of the magnetic reconnection process. (a) Two opposite magnetic field (blue and green) from different plasma regimes, are encountering each other. The field lines are separated by a thin current sheet which is shown in pink, the inflow plasma from both side (purple arrows) stream into the current sheet, (b) The magnetic fields are strongly pushed towards each other, (c) a diffusion region is formed (black box) where the two magnetic fields create an X-line configuration and (d) these fields can cross the current sheet by merging into a pair of kinked lines, which will be carried away as the magnetic tension acts to straighten them. The yellow arrows represent the outflow plasma jets. The big circles represent ions while the small circles represent electrons. . . . .	13

1.7	Two-dimensional reconnection topology. The pink (green) box of $\delta_i$ ( $\delta_e$ ) is the ion (electron) diffusion region. The black lines show the magnetic field lines. The dashed black lines are the separatrices. The blue arrows show the plasma flow outside the diffusion region. Ions are decoupled from the magnetic field in the ion diffusion region, creating the Hall magnetic (yellow and violet quadripolar structure) and electric field patterns (magenta arrows). The ion flow is shown by dashed green arrows. The electrons remain magnetized in the ion diffusion region and they follow the trajectories shown by red arrows. Electrons are demagnetized in the electron diffusion region. . . . .	14
1.8	Zoom around the diffusion region shown in Figure 1.6-(d). The field line diffuses over the half-width of the diffusion layer, $\delta$ , which is much smaller than the system size, $2L$ . . . . .	16
1.9	A schematic view of the spiral Parker structure in the equatorial plane and orbit of the Earth in 1 AU, showing the interplanetary magnetic field (IMF) lines frozen into a radial solar wind with an expansion at speed of $400 \text{ km s}^{-1}$ . As the plasma passes Earth's orbit moving parallel to the Sun-Earth line, the IMF typically creates an angle of $45^\circ$ . (Sun and Earth are not to scale). . . . .	19
1.10	Three-dimensional cutaway view of the Earth Magnetosphere showing currents (white arrows), fields and plasma regions. This figure is from Pollock et al. (2003). . . . .	21
1.11	Observations from MMS 1 on 1 December 2017 between 10:00 and 16:00 UT while the spacecraft were moving from the magnetosphere to the solar wind. (a) the magnetic field components and intensity, (b) the ion density, (c) the ion velocity components, (d) ion spectrogram and (e) electron spectrogram. .	22
1.12	The schematic figure of plasma flow through the magnetosphere driven by magnetic reconnection. The numbered field lines show the evolution of a field line involved in the Dungey cycle. Figure from Kivelson et al. (1995). . . .	23
1.13	Interior structure of magnetic field lines in a flux rope. Figure from Russell and Elphic (1978). . . . .	26
2.1	Instruments onboard each MMS spacecraft. Figure from Burch et al. (2016). .	34

2.2	MMS orbital geometry and science Regions of Interest (ROI). Figure from Tooley et al. (2016). . . . .	35
2.3	Schematic of the MMS formation as a science instrument concept (image credit: NASA). . . . .	35
2.4	Ecliptic-plane sketch of MMS orbit. The region of interest is shown in blue and burst data intervals are shown in red. Figure from Burch et al. (2016). . .	37
2.5	Polar angle FOV configuration of each top hat plasma spectrometer. The spacecraft +Z axis is also indicated. Figure from Pollock et al. (2016). . . . .	39
2.6	DES detection system. Figure from Pollock et al. (2016) . . . . .	39
2.7	(Left) Azimuthal FOV configuration of the eight spectrometers for each species. Each spectrometer, exercising four deflected fields of view, yields 32 azimuth samples for each species. (Right) The azimuth zones for each DES (DIS). Figure from Pollock et al. (2016) . . . . .	40
2.8	Schematic drawing of the HPCA sensor together with characteristic ion and electron trajectories. Figure from Young et al. (2016). . . . .	42
2.9	Magnetopause location and shape on 7 November 2015 using Shue model. .	47
2.10	Boundary coordinate system. $N$ points outward to the local magnetopause, $L$ is the projection of the Earth's magnetic dipole field and the $M$ completes the right-handed set, pointing downward ( $M = N \times L$ ). . . . .	48
2.11	A scatter plot of the perpendicular electron temperature against the electron density. A fourth order polynomial curve was fitted to the points. The $\tau$ parameter for each particular point is obtained by projecting it into the nearest point of the fitting curve as shown by the red line. Then, we evaluate the length of the curve between its beginning and the projected point as illustrated by the green curve. . . . .	50
2.12	Illustration of the average current density estimation using the curlometer technique . . . . .	51
2.13	Sketch of a planar discontinuity moving at a constant velocity $V$ toward four spacecraft flying in a tetrahedral formation. . . . .	54



2.14	(a) deHoffmann Teller analysis: the convection electric field $E_c(= -\mathbf{V} \times \mathbf{B})$ vs. the de-HT frame electric field $E_{HT}(= -\mathbf{V}_{HT} \times \mathbf{B})$ and a linear regression fit, (b) Walen analysis: $V'^{(i)}$ vs. $V_A^i$ of all three components and a linear regression fit. Blue, green, and red dots denote $x$ , $y$ , and $z$ components in the GSE frame. Figure from Phan et al. (2013).	56
3.1	GSE equatorial-plane projection of the MMS orbit on November 7, 2015 and the normal to the magnetopause (green arrow) corresponding to the spacecraft location in the ecliptic plane. The event presented in this study occurred between 14:16:05 and 14:17:20 UT. The red line corresponds to the crossing of a boundary layer. The large blue diamond shows the position at 14:15:00 UT. The probable magnetopause is indicated by green line and shaded boundaries.	64
3.2	MMS orbit on November 7, 2015 in the XZ plane at 14:00:00 UT. The large diamond is the approximate location of the spacecraft. The magnetic field lines are plotted in purple and are calculated using the Tsyganenko model [Tsyganenko and Stern (1996)].	65
3.3	Configuration of the MMS tetrahedron at 09:30:54 UT on November 7, 2015. TQF is the tetrahedron quality factor, which compares the actual tetrahedron to a regular tetrahedron [Fuselier et al. (2016)].	66
3.4	Solar wind conditions from the OMNI 1 minute resolution database from 06 November 2015-00:00 UT through 09 November 2015-12:00 UT. (a) Interplanetary magnetic field components and amplitude in GSE coordinates, (b) plasma temperature, (c) plasma density, (d) plasma $\beta$ parameter, and (e) disturbance storm time (DST) index.	67
3.5	Solar wind conditions from the OMNI 1 minute resolution database from 06 November 2015-00:00 UT through 09 November 2015-12:00 UT. (a) Interplanetary magnetic field components and amplitude in GSE coordinates, (b) Disturbance Storm Time index. Solar wind conditions during 08:00-20:00 UT on 7 November 2015, (c) Interplanetary magnetic field components in GSE coordinates, (d) solar wind dynamic pressure, and (e) Alfvén Mach number.	68

3.6	The magnetopause shear angle seen from the Sun with the predicted reconnection and MMS locations at the magnetopause. Courtesy from <i>K.J. Trattner</i> .	71
3.7	Survey data from MMS1 on 7 November 2015 between 13:00 and 15:00 UT. (a) Magnetic field from FGM, (b) electron and ion densities, (c) ion velocity, (d) electron spectrogram provided by FPI, (e) ion spectrogram provided by FPI, (f) $He^{2+}$ spectrograms from HPCA and (g) $O^+$ spectrogram from HPCA. . . . .	72
3.8	The variations of $B_z$ as a function of $B_y$ during the time of the LLBL crossing with the logarithmic of the ratio of electron density over perpendicular electron temperature is represented by the colors of the dots on November 7, 2015 between 13:00 and 15:00 UT. . . . .	73
3.9	The $X_{GSE}$ component of the spacecraft position on November 7, 2015 between 13:00 and 15:00 UT Earth Radii. The vertical dashed lines delimit the boundary layer. . . . .	74
3.10	Transition parameter calculated for MMS1 calculated from FPI measurements.	76
3.11	An overview of MMS1 observations between 14:15:45 and 14:17:20 UT in GSE coordinates on 7 November 2015. (a) Magnetic field components and total field strength, (b) pressures (red= plasma (ion), green= magnetic, and black= total), (c) current density from curlometer technique, (d) ion velocity components, (e) electron (black) and ion (red) densities. The black vertical dashed lines labelled T0 to T5, correspond to times 14:16:04; 14:16:25; 14:16:40; 14:16:43; 14:16:58 and 14:17:05 UT. . . . .	78
3.12	MMS1 data between 14:15:45 and 14:17:20 UT of (a) $B_y$ and the magnetic field strength in GSE coordinates, (b) electron energy spectrum. Electron pitch angle distribution in the range of (c) 98-127 eV, (d) 451-751 eV, and (e) 3304-11551 eV. . . . .	79
3.13	(a) Magnetic field magnitude, (b)-(d) magnetic field components in the magnetopause LMN frame, (e) angle $\Psi$ between the magnetopause normal and the magnetic field, (f)-(h) ion velocity components in the magnetopause LMN frame, (i) parallel (black) and perpendicular (red) ion velocity in the GSE coordinates system. The black vertical dashed lines labelled $T_0$ to $T_5$ are shown at the same times as in Figure 3.11. . . . .	81

3.14 $B_y$ component of the magnetic field in the GSE coordinates system from the four MMS spacecraft. The horizontal dashed lines represents the several contours of different $B_y$ values that were used to calculate their normal directions and propagation velocities. . . . .	84
3.15 The relative orientation of the PCS frame ( $\mathbf{U}_P$ , $\mathbf{U}_J$ and $\mathbf{U}_V$ ) to the GSE frame. The thick violet arrow shows the direction of the current sheet propagation velocity obtained from multi-spacecraft data analysis. The PCS frame corresponds to a translation of the GSE frame in the direction of the current sheet propagation velocity combined with a rotation about the $Y_{GSE}$ direction. . .	84
3.16 Current density obtained from curlometer technique on 7 November 2015 between 14:16:35 and 14:16:50 UT. (a) in GSE coordinates, (b) in the current principal axis frame. . . . .	85
3.17 Data from MMS1 between 14:16:38 and 14:16:44 UT (a) current density components in the GSE coordinates system, (b) parallel, perpendicular and the total current densities, (c) electrons and ions current densities as well as the current density obtained from the curlometer technique and the current density obtained from $ne(\mathbf{V}_i - \mathbf{V}_e)$ , (d) current density components in the PCS frame (obtained from the curlometer technique), (e) magnetic field components in the PCS frame, (f) ion velocity components in the PCS frame, (g) ion velocity components in the PCS frame between 14:16:05 and 14:17:20 UT. . .	87
3.18 A schematic view of the crossing of the current structure in the PCS frame. The orange, green and magenta arrows show the magnetic field orientation in the $FT_A$ , current structure and $FT_B$ respectively. The black arrows in the $\mathbf{U}_J$ ( $\mathbf{U}_V$ ) direction correspond to the main (bipolar) current density. The two oppositely directed red arrows in the $\mathbf{U}_P$ direction illustrate the compression of the current structure. The red arrows with yellow edges show the ion jet observed in the current structure. The spacecraft trajectory across the structure is represented by the dashed black arrow. . . . .	92
3.19 (a) Ion density,(b) Ion skin depth between and (c) the protons Larmor radius 14:16:05 and 14:17:20 UT. . . . .	94

3.20	Between 14:16:38 and 14:16:44 UT: (a) $\mathbf{B}$ data, (b) FPI currents, (c,d,e) comparison between EDP electric field data (black), $-\mathbf{V}_e \times \mathbf{B}$ (green) and $-\mathbf{V}_i \times \mathbf{B}$ (red). . . . .	95
3.21	Between 14:16:38 and 14:16:44 UT: (a) $\mathbf{B}$ data, (b) current density $qn(\mathbf{V}_i - \mathbf{V}_e)$ obtained from the computed moments of ion and electron distribution functions, (c) ion velocity, (d) to (g) $\mathbf{J} \times \mathbf{E}'$ for MMS1, MMS2, MMS3 and MMS4. . . . .	96
4.1	Between 14:16:38 and 14:16:44 UT: (a) $\mathbf{B}$ data, (b) FPI currents, (c,d,e) comparison between EDP electric field data (black), $-\mathbf{V}_e \times \mathbf{B}$ (green) and $-\mathbf{V}_i \times \mathbf{B}$ (red), (f) ion velocity,(g) parallel and perpendicular electron temperatures and (h) electron density. . . . .	101
4.2	MMS1 observations on 7 November 2015 between 14:16:36 and 14:16:46 UT: (a) magnetic field components and amplitude, (b,c) band-pass filtered between 256 and 512 Hz EDP and SCM waveforms in MFA (d, e) omnidirectional E and B PSD,(f) waveangle and (g) Ellipticity. . . . .	102
4.3	(a) magnetic field components and amplitude in GSE coordinates, (b) to (d) the components of Poynting flux of electromagnetic fields. . . . .	103
4.4	Waveforms of the first Whistler wave packet between 14:16:40.5 and 14:16:40.9 UT in GSE coordinates. (a) the magnetic field components, (b) the magnetic field filtered between 40 and 100 Hz, (c) the electric field components and (d) parallel electric field calculated by using the EDP data and the survey magnetic field and its associated error bars (pink shading). . . . .	104
4.5	Zoom on the first Whistler wave packet between 14:16:40.72 and 14:16:40.76 UT (yellow shaded area in Figure 4.4). Panels are similar to 4.4. . . . .	105
4.6	Waveforms of the first Whistler wave packet between 14:16:41.75 and 14:16:41.90 UT. Same legends as Figure 4.4. . . . .	106
4.7	Electron pitch angle distributions averaged between 14:16:41.226-14:16:41.496 UT. Parallel (0°), perpendicular (90°), and anti-parallel (180°) phase space densities are represented by blue, green, and red traces, respectively. . . . .	107

4.8	Waveforms of the lower hybrid drift waves in MFA. (a) $B_X$ , $B_Y$ and $B_Z$ , (b) the magnetic field filtered between 40 and 100 Hz, (c) electron density from the four spacecraft and (d-g) parallel and perpendicular electric field also filtered between 40 and 100 Hz for MMS1, MMS2, MMS3 and MMS4, respectively. . .	109
4.9	Ion diamagnetic velocity obtained from (a) equation 4.3 and (b) equation 4.2.	111
4.10	Electric drift speed $(\mathbf{E} \times \mathbf{B})/B^2$ . . . . .	111
4.11	(a) Electron and (b) ion perpendicular velocities in GSE coordinates from FPI.	112
4.12	The $y$ component of: electron diamagnetic current density (blue), ion diamagnetic current density obtained as $j_{diaI} = enV_{d_{i1}}$ (green), perpendicular current densities obtained from FPI (red), perpendicular current densities obtained from the curlometer technique (purple) and ion diamagnetic current density obtained from equation $j_{diaI_2} = enV_{d_{i2}}$ (yellow). . . . .	113
4.13	Parallel (a) and perpendicular (b) current densities obtained from the curlometer technique, the particle, the ions ( $enV_{\parallel(\perp,i)}$ ) and the electrons current densities ( $-enV_{\parallel(\perp,e)}$ ). . . . .	114
4.14	Sketch of a reconnection site. At the top, different kinds of wave spectra commonly observed near reconnection sites are sketched. The common places to observe those waves are marked in different gray shadowing. Typical electron distribution functions in the vicinity of the separatrix are indicated as well. Figure from Vaivads et al. (2006). LHD = Lower Hybrid Drift, W = Whistler, ESW = Electrostatic solitary waves and L/UH = Langmuir/upper-hybrid waves.	115

# LIST OF TABLES

2.1	Top level burst-mode parameters. Table from Burch et al. (2016). . . . .	37
2.2	The suggested values of $\tau$ for the magnetosheath, the outer boundary layer, the inner boundary layer and the magnetosphere. . . . .	49
3.1	The instruments that were used for this study along with their corresponding resolution in Survey and Burst modes. . . . .	63
3.2	Average positions of THB, THC, Wind and Ace in $R_E$ between 11h00 and 15h00 UT in GSE coordinates. . . . .	68
3.3	Local magnetopause coordinate system obtained from the minimum variance analysis of the magnetic field. $\lambda_L/\lambda_M = 5.75$ , $\lambda_L/\lambda_N = 18.64$ and $\lambda_M/\lambda_N = 3.23$ . . . . .	77
3.4	Local magnetopause coordinate system obtained from the minimum variance analysis of the magnetic field. $\lambda_L/\lambda_M = 5.75$ , $\lambda_L/\lambda_N = 18.64$ and $\lambda_M/\lambda_N = 3.23$ . . . . .	83
3.5	The normal directions and the velocities of the propagating structure obtained by performing the timing method for multiple values of $B_y$ . Mean value are: $V = 66.88 km/s$ and $N_c = [-0.54, -0.03, 0.84]$ , and the angle of each normal vector relatively to the the $X$ axis. . . . .	85
3.6	Results of the variance analysis of the current density obtained from the curlometer technique. $\lambda_1/\lambda_2 = 2.8$ , $\lambda_1/\lambda_3 = 43.2$ and $\lambda_2/\lambda_3 = 15.43$ . . . . .	86
3.7	The unit vectors defining the PCS (Propagating Current Structure) frame. . . .	86
4.1	Times corresponding to the observations of the LHDW. . . . .	108

4.2	Properties of the LHDWs in GSE coordinates system for MMS1, MMS2, MMS3 and MMS4, respectively. $V_x, V_y, V_z$ give the direction of propagation of the waves, $\ \boldsymbol{v}\ $ gives its amplitude, $f$ is the waves frequency, $f_{LH}$ is the LHDWs frequency, $\lambda_{\perp}$ is the perpendicular wavelength, $k_{\perp}\rho_e$ is the position of the maximum growth rate of the waves, $\delta\phi/T_e$ is the ratio between the electrostatic potential and the electron temperature and $cc$ is the correlation coefficient between the potential obtained from $\delta B_{\parallel}$ and from $\delta E_{\perp}$ . . . . .	109
4.3	Properties of the first packet of LHDWs in GSE coordinates system for MMS1, MMS2, MMS3 and MMS4, respectively. . . . .	110
4.4	Properties of the second packet of LHDWs in GSE coordinates system for MMS1, MMS2, MMS3 and MMS4, respectively. . . . .	110

# ACKNOWLEDGEMENTS

I would like to express my sincere gratitude to everyone who supported me and who's continuing to support me at every step.

First of all, I would like to thank my parents, brothers and sisters for the endless encouragement and the precious support they offered me throughout my life. Thank you for inspiring me to follow my dreams and for teaching me to never give up.

I am deeply indebted to the person that changed my life without even trying. Your existence is what brightens my world. *You mean so much to me.*

I had the great chance to start my PhD only few months after the launch of the (MMS) Magnetospheric Multiscale mission. I would like to thank the MMS operation and instrument teams as well as the science team. I would like to thank the scientists that I had the opportunity to meet during workshops and especially Marit Oieroset, Charlie Farrugia, Tai Phan, Hiroshi Hasegawa, Olivier LeContel, Mitsua Oka, James Drake, Stephan Eriksson, Drew Turner, Eastwood Jonathan, Karlheinz Trattner, Daniel Graham, Stephen Fuselier, Daniel J. Gershman and Barbara Giles. I would like to thank them for the fruitful discussions we had. A special thanks to the mission PI, Jim Burch, for his encouraging and kind words. They mean a lot to me.

I take this opportunity to express my profound gratitude to Christian Jacquey, my principal supervisor, for his exemplary guidance and valuable critiques throughout the course of my PhD. On a personal level, Christian inspired me by his passionate attitude. My grateful thanks are also extended to Vincent Génot, my secondary supervisor, for his valuable advices throughout my research.

Besides my supervisors, I would like to thank the rest of my dissertation committee members: Geneviève Soucail, Karine Issautier, Sébastien Galtier, Roch Smets and Mathieu Kretschmar for their remarks and comments.

I would also like to extend my deepest gratitude to Benoit Lavraud. Thank you for being such an amazing team leader. Thank you for your kindness and benevolence. Thank you



for sharing your knowledge and time.

I wish to thank the PEPS team members, and in particular Aurélie Marchaudon, for engaging in remarkable scientific discussions and Emmanuel Penou who provided the "CL" data analysis and visualization software. Thanks also to Alexis Rouillard, your humor is a breath of fresh air.

I am also grateful to my collaborators. I spent one month at "Laboratoire de Physique des Plasmas" (LPP) where I had the chance to collaborate with fantastic researchers. More specifically, I would like to thank Olivier LeContel and Hugo Breuillard for their continuous support and for providing me the great opportunity to work on plasma waves. I also spent two months at the "Institute of Space and Astronautical Science" (ISAS/JAXA) where I have collaborated with Hiroshi Hasegawa. I would like to thank him for his great mentorship and guidance.

I would also like to thank the Lab director, Philippe Louarn, for his generous support.

I would like to express my very great appreciation to everyone at the IRAP administration, and in particular to Dorine Roma and Josette Garcia.

A special thanks to Mina and Henda for being so attentive and caring. Nobody in the world can make me laugh the way Mina does!

I would like to thank my lab mates for their continued support. Morgane, thank you for always being here for me. Thank you for being such a good friend. Mikel, I think you already know it, I am so thankful for each moment we spent together, for all the shared secrets, wishes, tears, and laughter. Thank you for your friendship. I will always treasure the memories we shared in my heart. I will carry them with me all the days of my life. Yoann, thank you for taking the time to listen to my problems and help me find the solutions. Thank you for showing that you care! This dissertation would not have been possible without your precious "mms tools". Sid, I am thankful to you for your contribution. You were a fantastic officemate. Thank you for providing me with a daily dose of sarcasm and for all the funny "memes" you've made ;) Nathanael, I think that the first thing anyone can think to thank you for is the coffee machine! But for me, you are a trustworthy and caring friend. Kévin, thank you for sharing your experience and all your advice. Mathieu, I am very happy to share MY office with you. Thanks for your time and effort helping me when I needed it. Jérémy, thank you for being the reason I met Marie ;) Thank you for your care and for the

history lessons! Baptiste, I am glad to have met you. You have a great sense of humor. Your smile spreads happiness to those around you. Michael, thank you for your continuous support and encouragement. It's a pleasure to have a friend like you. I would also like to thank Edoardo, Eduardo, Mika, Margaux, Jason, Killian, Kalyani, Min-kyung, Marina, Gaëlle, Amal, Thanasis, Shirley, Rui and Illya.

Thanks to the "petits stagiaires": Ilona, Guillaume <sup>1</sup>, Nicolas, Quentin, Thibaut, Emeline, Charles, Lydia and Vincent for making my experience in IRAP exciting and fun. Pierre, thank you for the fun moments and the discussions we had in coffee breaks.

I am also grateful to Frédérique Said and Jean-François Georgis for their support in my teaching experience.

Thanks are also due to the (CNRS) "Centre National de la Recherche Scientifique", (CNES) "Centre National d'Etudes Spatiales" and "Université Paul Sabatier" for their financial support.

I am also grateful to Théo. Your friendship means a lot to me.

I am grateful to my Lebanese friends who shared with me unforgettable moments and memories during my years in France ( and also in Lebanon for some of them <3 ): Hiba, Imane, Maya, Riham, Sabine, Sarah, Nour, Duaa, Zeina, Amani, Mirna, Nour, Mostafa, Joe, Tarek, Mohanad and Abed. I am very proud of you all. It's very reassuring to have you by my side.

I also wish to thank my childhood friends Dalal, Raeda, Safaa, Khitam and Maria. I love you so much. Spending time with you always puts me in a good mood.

Special thanks to Dominique, Philippe, Damien and Daizy. You are a wonderful family. Thank you for all your support. Thank you for having faith in me. It meant so much and it still does. I also wish to thank Cléo, you cannot imagine how much I am glad I met you. I am looking forward for the trips we planned to do! Thanks also to François-Xavier and Louis-Alexandre. Your help has been invaluable to me.

Many thanks to my friends in Toulouse, Soundous, Kahina, Mehdi, Pierre, Aziz, Imane, Amira, Walid, Leila and Karim. Thank you for the beautiful moments and lovely surprises <sup>2</sup>. Thank you for listening, caring and helping.

Last but not least, I would like to express my deepest gratitude to Céline, Elisa and Nahia.

---

<sup>1</sup>Les angles sont en micro-ampères!

<sup>2</sup>Soun and Kahi: my birthday is not in January!

I hope the best for you. I love spending time with you. Céline, you are one of the strongest woman I have ever met: Don't ever forget that.

# ABSTRACT

Magnetic reconnection is a ubiquitous and fundamental process in space plasma physics. The MMS mission launched on 12 March 2015 was designed to provide in-situ measurements for analyzing the reconnection process at the Earth's magnetosphere. In this aim, four identically instrumented spacecraft measure fields and particles in the reconnection regions with a time resolution which is one hundred times faster than previous missions. MMS allows for the first time to study the microscopic structures associated with magnetic reconnection and, in particular, the thin electron diffusion region. At the Earth's magnetopause, magnetic reconnection governs the transport of energy and momentum from the solar wind plasma into the Earth's magnetosphere through conversion of magnetic energy into kinetic and thermal energies after a rearrangement of magnetic field lines. Flux Transfer Events (FTEs) are considered to be one of the main and most typical products of magnetic reconnection at the Earth's magnetopause. However, more complex 3D magnetic structures with signatures akin to those of FTEs might also occur at the magnetopause like interlaced flux tubes resulting from magnetic reconnection at multiple sites. The first part of the work presented in this thesis consisted of the investigation of one of these events that was observed, under unusual and extreme solar wind conditions, in the vicinity of the Earth's magnetopause by MMS. Despite signatures that, at first glance, appeared consistent with a classic FTE, this event was interpreted to be the result of the interaction of two separate sets of magnetic field lines with different magnetic connectivities. The high time resolution of MMS data allowed to resolve a thin current sheet that was observed at the interface between the two sets of field lines. The current sheet was associated with a large ion jet suggesting that the current sheet was submitted to a compression which drove magnetic reconnection and led to the formation of the ion jet. The direction, velocity and scale of different structures were inferred using multi-spacecraft data analysis techniques. This study was completed with a plasma wave analysis that focused on the reconnecting current sheet.



## RÉSUMÉ

La reconnexion magnétique est un processus omniprésent et fondamental dans la physique des plasmas spatiaux. La "Magnetospheric multiscale mission" (MMS) de la NASA, lancée le 12 mars 2015, a été conçue pour fournir des mesures in-situ permettant d'analyser le processus de reconnexion dans la magnétosphère terrestre. Dans ce but, quatre satellites identiquement instrumentés mesurent les champs électromagnétiques et les particules chargées dans les régions de reconnexion, avec une résolution temporelle cent fois meilleure que celle des missions précédentes. MMS permet, pour la première fois, d'étudier les structures microscopiques associées à la reconnexion magnétique et, en particulier, la région de diffusion électronique. Au niveau de la magnétopause terrestre, la reconnexion magnétique a un rôle chef dans le transport de l'énergie du vent solaire vers la magnétosphère terrestre, en convertissant l'énergie magnétique en énergie cinétique et thermique. Les événements à transfert de flux (FTEs) sont considérés comme l'un des produits principaux et les plus typiques de la reconnexion magnétique à la magnétopause terrestre. Cependant, des structures magnétiques 3D plus complexes, avec des signatures similaires à celles des FTEs, peuvent également exister à la magnétopause. On retrouve, par exemple, des tubes de flux entrelacés qui résultent de reconnexions magnétiques ayant eues lieu à des sites différents. La première partie de cette thèse étudie l'un de ces événements, qui a été observé dans des conditions de vent solaire inhabituelles, au voisinage de la magnétopause terrestre par MMS. Malgré des signatures qui, à première vue, semblaient cohérentes avec un FTE classique, cet événement a été interprété comme étant le résultat de l'interaction de deux tubes de flux avec des connectivités magnétiques différentes. La haute résolution temporelle des données MMS a permis d'étudier en détail une fine couche de courant observée à l'interface entre les deux tubes de flux. La couche de courant était associée à un jet d'ions, suggérant ainsi que la couche de courant était soumise à une compression qui a entraîné une reconnexion magnétique à l'origine du jet d'ions. La direction, la vitesse de propagation et la taille de différentes structures ont été déduites en utilisant

des techniques d'analyse de données de plusieurs satellites. La deuxième partie de la thèse fournit une étude complémentaire à la précédente et s'intéresse aux ondes observées autour de la couche de courant.

# INTRODUCTION GÉNÉRALE

La reconnexion magnétique est l'un des processus les plus importants dans la physique des plasmas spatiaux qui se produit dans la quasi-totalité de l'Univers: dans les plasmas astrophysiques, dans l'environnement terrestre, dans les galaxies, et au niveau du Soleil également. Ce processus fondamental se déclenche lorsque des lignes de champ de directions opposées se rapprochent. Ce réarrangement de polarité de champ magnétique s'accompagne d'une dissipation rapide de l'énergie magnétique qui est transférée aux particules chargées sous forme de chauffage et d'écoulement. Au-delà de la reconnexion magnétique elle-même, l'analyse et la caractérisation de ses produits (structures de courant, fronts d'injection, cordes de flux...) permettront de mieux comprendre ce processus.

La reconnexion magnétique joue un rôle crucial dans les relations Soleil-Terre et dans la dynamique de la magnétosphère. Au niveau de la magnétopause, elle est le principal processus assurant le transport d'énergie du vent solaire vers la magnétosphère. Elle résulte de l'interaction entre les lignes de champ du milieu interplanétaire et celles du champ magnétique terrestre. Elle se produit également dans la couche de plasma de la queue magnétosphérique.

Les événements à transfert de flux (FTEs) sont considérés comme l'un des produits principaux et les plus typiques de la reconnexion magnétique à la magnétopause terrestre. Ils sont caractérisés par un pic d'intensité du champ magnétique et une signature bipolaire sur la composante du champ magnétique normale à la magnétopause. Cependant, des structures magnétiques 3D plus complexes peuvent également exister à la magnétopause. Ce manuscrit reporte l'analyse de l'une d'entre elles observée par la mission MMS (Magnetospheric multiscale).

Les propriétés à grande échelle de la reconnexion magnétique sont assez bien connues grâce aux missions magnétosphériques précédentes (THEMIS, CLUSTER,...), mais l'étude des mécanismes à petite échelle n'a été possible qu'avec la mission Magnetospheric Multiscale (MMS). MMS est une mission de la NASA qui comprend quatre satellites en configu-



ration tétraédrique avec de petites distances inter-satellites (de l'ordre de 10 km à comparer avec 100 à 1000 km pour Cluster). MMS a été lancée le 12 mars 2015 et a été conçue pour fournir des mesures in-situ permettant d'analyser avec la précision nécessaire et inégalée auparavant le processus de reconnexion à la magnétopause terrestre. Les instruments à bord de MMS offrent des mesures des champs électromagnétiques et des particules, avec une résolution temporelle cent fois meilleure que celle des missions précédentes. MMS a permis d'accéder, pour la première fois, à la dynamique des électrons, alors que toutes les missions précédentes ont été limitées à observer la dynamique des ions qui a lieu sur une plus grande échelle.

Parmi les laboratoires impliqués dans la mission MMS, on compte deux laboratoires français: l'Institut de Recherche en Astrophysique et Planétologie (IRAP) à Toulouse et le Laboratoire de Physique des Plasmas (LPP) à Paris.

Ma thèse a été centrée sur l'exploitation des données fournies par MMS. Ce manuscrit se divise en cinq chapitres précédés par la présente introduction générale:

- Dans le **Chapitre 1**, un aperçu des concepts de base de la physique des plasmas en rapport avec la thèse est présenté. Ensuite, une brève description des plasmas du système solaire est donnée, suivie d'une introduction à la reconnexion magnétique à la magnétopause puis aux événements de transfert de flux.
- La première section du **Chapitre 2** fournit une introduction à la mission MMS avec une brève description des principaux instruments utilisés dans cette thèse. La deuxième section présente les techniques d'analyse utilisées.
- Le **Chapitre 3** étudie un événement qui a été observé par MMS au voisinage de la magnétopause terrestre. Une comparaison de cet événement avec les FTEs classiques a été effectuée. Une interprétation phénoménologique a été aussi proposée afin de mieux comprendre les observations. La structure d'une couche de courant observée au centre de l'événement ainsi que sa géométrie spécifique intéressante ont également été décrites. Ensuite, les observations de particules à haute résolution ont été utilisées, ainsi que les données de champ magnétique pour tester l'hypothèse de reconnexion au sein de la couche de courant.

- Le **Chapitre 4** est consacré à l'étude des ondes observées au cours de l'événement discuté dans le chapitre 3 et en particulier autour de la couche de courant.

En conclusion, un sommaire des résultats ainsi que quelques perspectives de recherche sont énoncées et discutées dans le **Chapitre 5**.

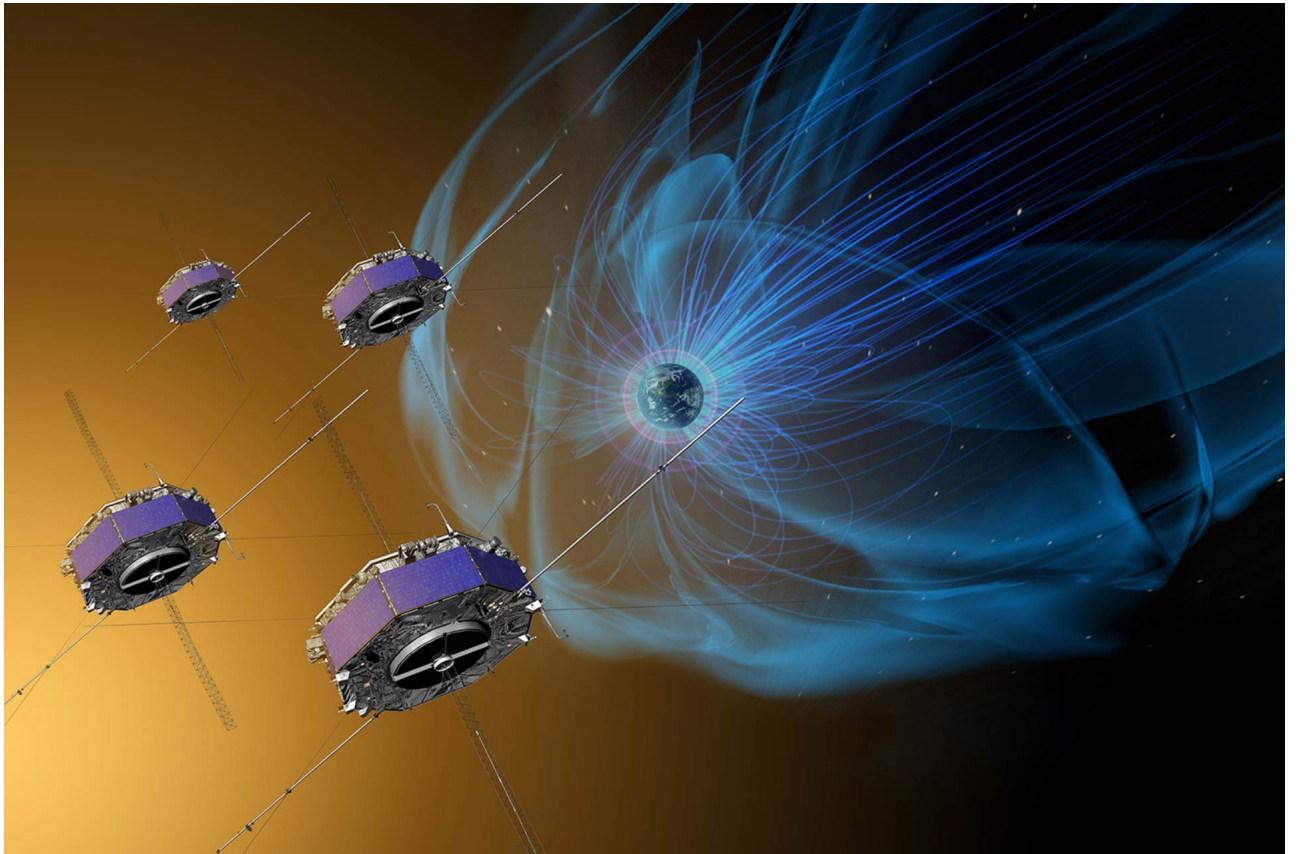


Figure 1 – Artist concept of the Magnetospheric Multiscale (MMS) mission to study magnetic reconnection.  
Credits: NASA.

# 1

## INTRODUCTION

In this chapter, we will present an overview of the basic plasma physics concepts of relevance to the thesis. Then, a brief description of the solar system plasmas will be given, followed by an introduction to magnetic reconnection at the magnetopause then to Flux Transfer Events and to other products of magnetic reconnection.

### 1.1. PHYSICS OF COLLISIONLESS PLASMAS

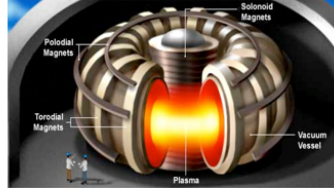
#### 1.1.1. SOLAR AND ASTROPHYSICAL PLASMAS

Most of the ordinary matter in the Universe is known to be made of plasma. A plasma is a globally neutral ionized gas consisting of positively and negatively charged particles that exhibits a collective behavior [Chen (1974)]. Plasmas are found throughout the Solar System and beyond. The Earth's magnetosphere, gaseous nebulae, the solar corona and solar wind, the tails of comets and the Van Allen radiation belts are made of plasmas. Some of the main examples of plasmas can be sorted with respect to their temperature and density as shown in Figure 1.2. As seen, the electron temperature of plasmas may vary over about 7 orders of magnitude and their electron density vary over about 30 orders of magnitude.

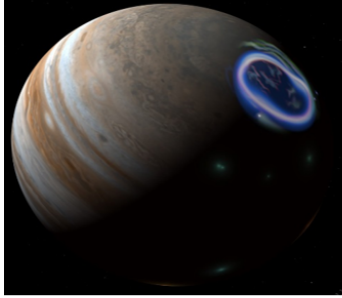
Plasmas may be classified in different ways. We can, for example, distinguish **collisional** from **collisionless** plasmas. In a plasma, two charged particles can interact by collisions



**Solar corona**



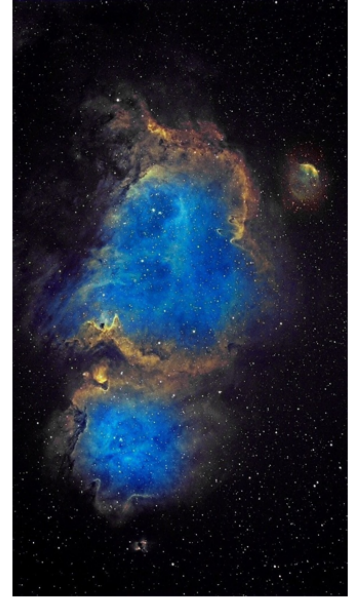
**Tokamak**



**Aurora**



**Astrophysical jet**



**Nebula**

Figure 1.1 – Examples of plasmas.

through the Coulomb force. Collisionless plasmas, as the name says, are plasmas where the collisions between particles do not play a significant role in the dynamics of the plasma. The mean free path, i.e. the mean distance a particle travels between two successive collisions, is larger than the typical macroscopic length scale over which plasma quantities vary. In other words, the collision frequency is much smaller than the characteristic frequencies of the medium. Collisionless conditions are quite frequent in astrophysics when the plasmas are sufficiently diluted like found in the collisionless shocks for supernovae. Also, the solar wind and planetary magnetospheres, which are the main plasmas considered in this thesis, exclusively consist of collisionless plasmas.

### 1.1.2. COLLISIONLESS PLASMAS PROPERTIES

A charged particle generates an electrical Coulomb potential field. The effect of this Coulomb potential is that a particle attracts oppositely charged particles and repels like-charged particles. In a plasma, there is an abundance of negatively and positively charged particles so that a cloud of oppositely charged particles forms around a charged particle. This effect is known as Debye Shielding and maintains the quasi-neutrality of a plasma on large scales.

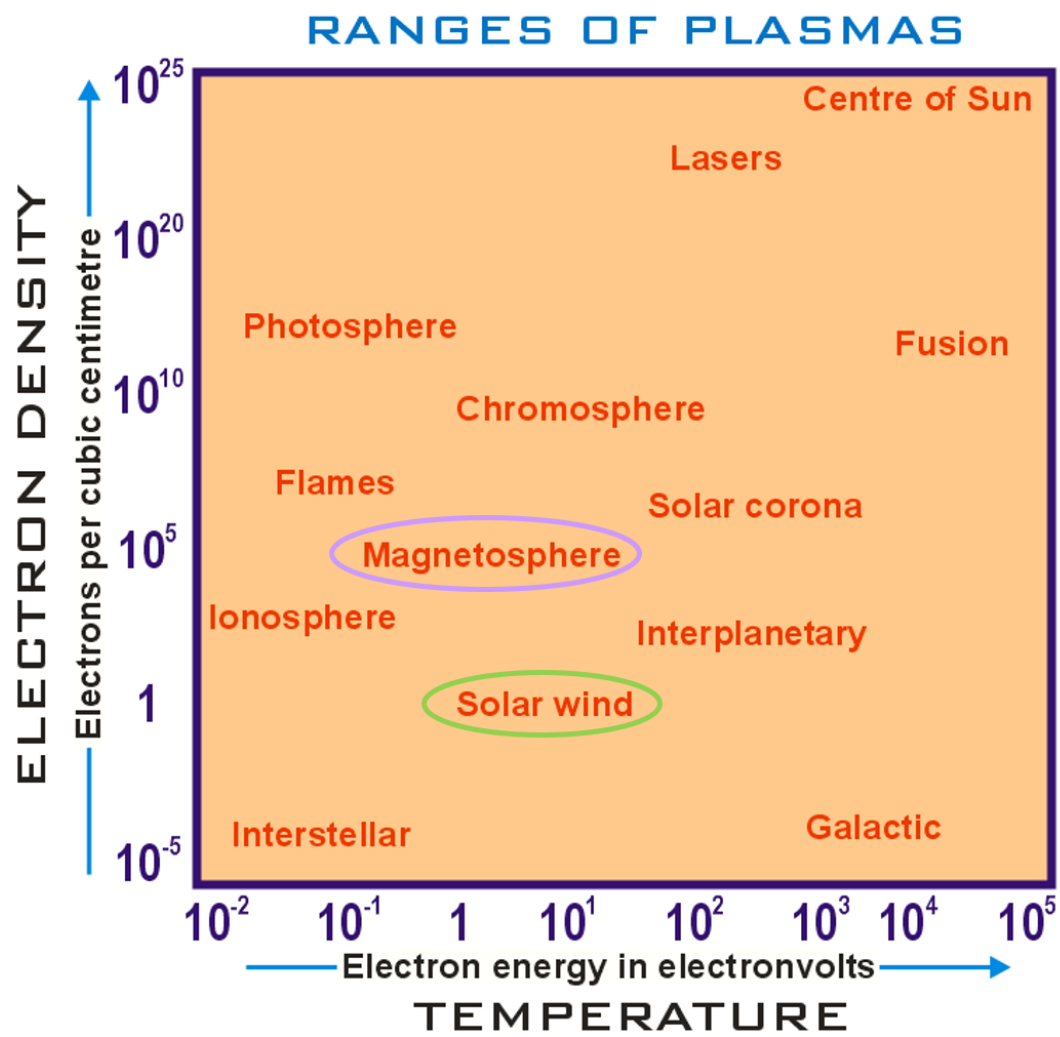


Figure 1.2 – The ranges of temperature and densities of plasmas ( $1\text{eV} \sim 11600\text{K}$ ). Figure from [Peratt \(1996\)](#).

The spatial scale over which the charge neutrality is violated is called the **Debye length**:

$$\lambda_D = \sqrt{\frac{\epsilon_0 k_B T_e}{n e^2}} \quad (1.1)$$

where  $\epsilon_0$  is the permittivity of free space,  $k_B$  is the Boltzmann constant,  $T_e$  is the electron temperature,  $n$  is the plasma density and  $e$  is the elementary charge. The Debye length  $\lambda_D$  is defined as the scale size on which the Debye shielding occurs. In a plasma, the Coulomb force extends to the Debye length. At distances larger than the Debye length ( $d \gg \lambda_D$ ), the potential of a single point charge diminishes exponentially due to Debye Shielding.

The quasi-neutrality of a plasma requires that the scale size of the plasma  $L$  to be much larger than the Debye length  $\lambda_D$ :

$$L \gg \lambda_D \quad (1.2)$$

When the quasi-neutrality of a plasma is disturbed by some external forces, the particles will be accelerated by the resulting electric field. The system then tends to recover the quasi-neutrality. This results in a back and forth movement around the equilibrium position and leads to a collective oscillation of the particles. The typical oscillation frequency is the **plasma frequency** and is given by:

$$\omega_p = \sqrt{\frac{n q^2}{m \epsilon_0}} \quad (1.3)$$

where  $n$ ,  $q$  and  $m$  are the density, charge and mass of the considered particle. The electron plasma frequency  $\omega_{pe}$  is the most fundamental time-scale in fully ionized plasmas.

The plasma frequency  $\omega_p$  yields the expression for the **plasma skin depth** also called the **inertial length**:

$$\delta = \frac{c}{\omega_p} \quad (1.4)$$

where  $c$  is the speed of light.

A particle of charge  $q$  and mass  $m$  moving with a velocity  $\mathbf{v}$ , under the presence of an electric field  $\mathbf{E}$  and a magnetic field  $\mathbf{B}$ , is subject to the Lorentz force:

$$\mathbf{F} = q(\mathbf{E} + \mathbf{v} \times \mathbf{B}) \quad (1.5)$$

The equation of motion of a charged particle in electromagnetic fields is:

$$m \frac{d\mathbf{v}}{dt} = q(\mathbf{E} + \mathbf{v} \times \mathbf{B}) \quad (1.6)$$

In the presence of a uniform magnetic field, without an electric field, the component of velocity parallel to the magnetic field  $v_{\parallel}$  remains at its initial value and the particle is accelerated in a direction perpendicular to  $\mathbf{v}$  and  $\mathbf{B}$ . The particle will have a circular motion around the magnetic field lines, with a **gyrofrequency**, or **cyclotron frequency**  $\omega_c$  and a gyration radius  $\rho_L$ .  $\omega_c$  is given by:

$$\omega_c = \frac{q|B|}{m} \quad (1.7)$$

The radius of the circular motion, centered about the magnetic field lines, is often known as **gyroradius** or **Larmor radius** and is given by:

$$\rho_L = \frac{v_{\perp}}{\omega_c} \quad (1.8)$$

where  $v_{\perp}$  is the perpendicular velocity of the considered particle, respectively. Owing to their opposite electric charge, ions and electrons rotate in opposite directions. In addition to the perpendicular component of the velocity, particles travel with a constant velocity along the magnetic field lines. The particle's path describes a helix as a result of the combination of the parallel and perpendicular velocities (Figure 1.3).

The inertial length and gyroradius are much larger for ions than for electrons since ions are much heavier. The different temporal and length scales in a plasma help to introduce a hierarchy which order the physical processes acting at the respective scales, as will be discussed in Section 1.2 for the magnetic reconnection process. The angle between the particle velocity and the magnetic field is known as the pitch angle  $\alpha$  (Figure 1.4):

$$\alpha = \text{atan}\left(\frac{v_{\perp}}{v_{\parallel}}\right) \quad (1.9)$$

When  $\alpha = 0^\circ$ , this means that the particles are moving purely along the magnetic field lines (also called field-aligned particles). Conversely, particles with  $\alpha = 90^\circ$  move perpendicular to the magnetic field.

Some characteristic velocities in a magnetized plasma are the gyrocenter drifts. For in-



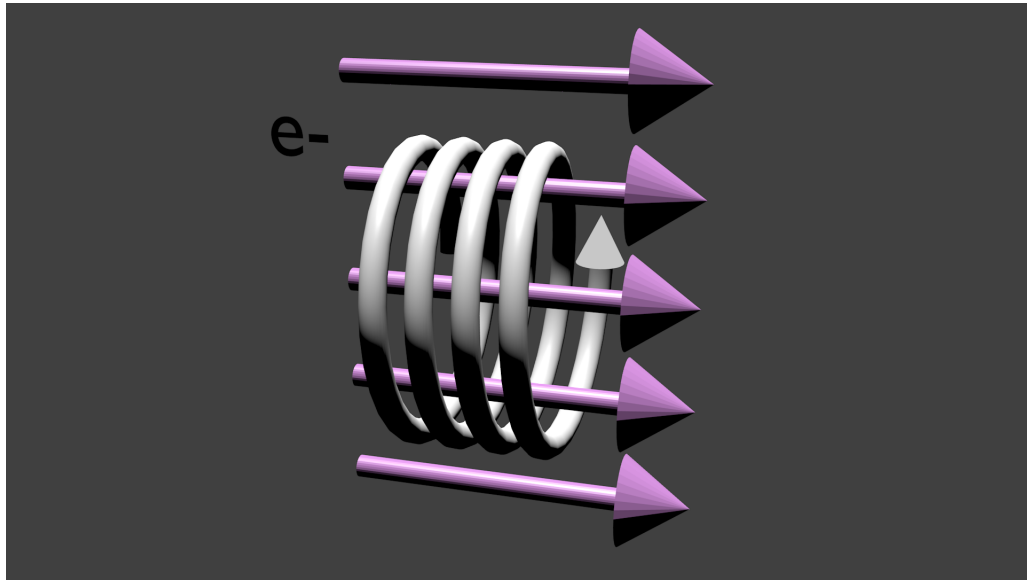


Figure 1.3 – Electron trajectory in a uniform magnetic field. The magnetic field lines are shown as straight purple arrows.

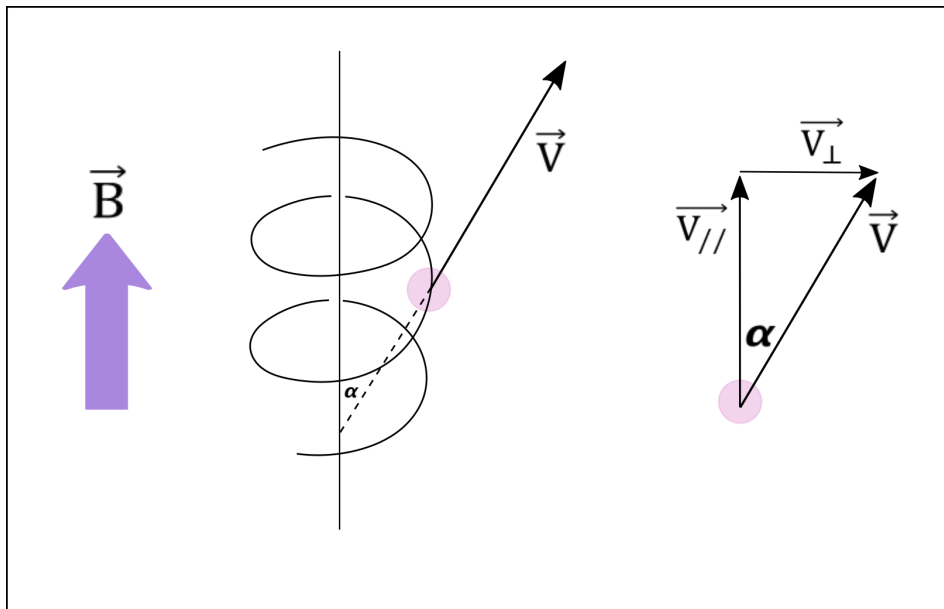


Figure 1.4 – The definition of the pitch angle  $\alpha$  for a particle gyrating around the magnetic field lines.

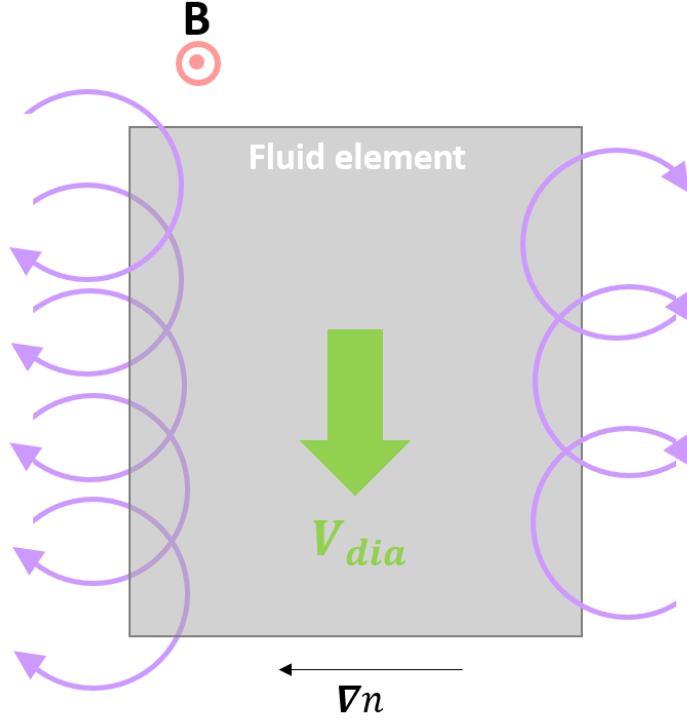


Figure 1.5 – Ions motion in the presence of a density gradient. More ions are moving downwards than upwards giving rise to a drift velocity perpendicular to the magnetic field and to the density gradient.

stance, under the presence of a perpendicular electric field, a drift motion  $V_d$ , relative to the helical orbit of the orbits is added to the particle motion:

$$V_d = \frac{\mathbf{E} \times \mathbf{B}}{B^2} \quad (1.10)$$

This velocity describes the motion of the magnetic field lines and the frozen plasma. The  $\mathbf{E} \times \mathbf{B}$  drift is perpendicular to both the electric and magnetic fields. Both ions and electrons drift in the same direction since  $V_d$  is independent of the sign of the particle charge.

Another gyrocenter drift follows from the presence of a density gradient, when more particles move in the direction of  $\nabla n \times \mathbf{B}$  than in the opposite direction. This effect, illustrated in Figure 1.5, is called diamagnetic drift  $V_{dia}$  which is given by:

$$V_{dia} = \frac{\mathbf{B} \times (\nabla \cdot \mathbf{P})}{nqB^2} \quad (1.11)$$

where  $\mathbf{P} = nT\mathbf{k}_B$ .

An estimate of the relative importance of thermal and magnetic effects is a dimensionless

parameter known as plasma beta. The magnetic field gives rise to a magnetic pressure  $B^2/(2\mu_0)$  which acts perpendicular to the field lines. The ratio of the thermal pressure to the magnetic pressure defines the plasma beta:

$$\beta = \frac{p_{th}}{p_B} = \frac{nk_B T}{B^2/(2\mu_0)} \quad (1.12)$$

where  $T$  is the plasma temperature.  $\beta$  represents the relative importance of the forces exerted on the plasma by the pressure gradients and the magnetic field. In a high-beta or hot plasma, the thermal pressure dominates. Conversely, in a low-beta or cold plasma the magnetic pressure has a larger effect.

### 1.1.3. KINETIC AND FLUID DESCRIPTION

Having discussed how individual particles behave in a plasma, it would be useful to briefly describe another plasma descriptions: the kinetic approach and the fluid approach. The kinetic approach is a statistical description of plasmas that considers the collective behavior and describes the system using the distribution function of the particle populations in phase space instead of solving the equation of motion for each charged particle. Each particle is characterized by its 3D position  $\mathbf{x}_i(t)$  and its 3D velocity  $\mathbf{v}_i(t)$ . The **phase space** is defined by the axes  $(\mathbf{x}, \mathbf{v})$ . The **phase space density**,  $f(\mathbf{x}, \mathbf{v}, t)$ , is the probability density such that  $f(\mathbf{x}, \mathbf{v}, t)d\mathbf{x}d\mathbf{v}$  is the number of particles in phase space volume element  $d\mathbf{x}d\mathbf{v}$  at time  $t$ . The phase space density contains considerable information regarding the physical state of the plasma. This approach is widely used for the calculation of macroscopic plasma parameters, from particle distribution data derived from directional particle count rates observed by spacecraft. The macroscopic plasma parameters (e.g. density, velocity, temperature) are computed as moments of the particle velocity distributions.

The fluid approach is used for describing the macroscopic plasma physics. In this approach, the plasma is considered to be composed of two or more fluids, one for each species. Each fluid can be described by a density, temperature and bulk velocity ( $\mathbf{V}$ ). The magnetohydrodynamic approach (MHD) describes the plasma as a single fluid with macroscopic

variables and neglects the single particle aspects.

#### 1.1.4. FROZEN-IN MAGNETIC FIELD CONDITION

Let us consider now a magnetized and highly conductive (i.e.  $\eta \sim 0$ ) plasma with characteristic scale and time variations which are much larger than those of particle processes. In such situation, particles always perform helical orbits around magnetic field lines (section 1.1.2). The plasma motion then follows the ideal MHD law which can be expressed as:

$$\mathbf{E} = -\mathbf{V} \times \mathbf{B} \quad (1.13)$$

Whenever equation 1.13 holds, the plasma obeys the **frozen-in-flow** condition which states that the magnetic flux is conserved along the plasma flow lines. This can be noticed by combining equation 1.13 with Maxwell-Faraday's Law:

$$\frac{\partial \mathbf{B}}{\partial t} = -\nabla \times \mathbf{E} \quad (1.14)$$

to obtain the magnetic induction equation which governs the magnetic field evolution in time:

$$\frac{\partial \mathbf{B}}{\partial t} = \nabla \times (\mathbf{V} \times \mathbf{B}) \quad (1.15)$$

This equation leads to the frozen-flux theorem, also known as the Alfvén's theorem, which holds that in a perfectly conducting plasma (i.e.  $\eta = 0$ ) the magnetic field lines behave as if they move with the plasma. In other words, the frozen-in theorem states that the magnetic flux passing through any closed surface perpendicular to the magnetic field and moving with the local plasma velocity does not vary in time:

$$\frac{d\phi}{dt} = \iint \left( \frac{\partial \mathbf{B}}{\partial t} - \nabla \times (\mathbf{V} \times \mathbf{B}) \right) d\mathbf{S} = 0 \quad (1.16)$$

where  $\phi$  is the magnetic flux through a variable surface  $S$ . Considering a closed curve  $C$  bounding a surface  $S$ , the magnetic field lines which are enclosed by  $C$  define a magnetic flux tube along which the magnetic flux  $\phi$  is constant.

However, as the spatial scale variation approaches the ion inertial length, the previous

plasma description breaks down and more terms have to be added to the ideal MHD law. Under these conditions, ideal MHD law has to be replaced by the **Ohm's law** [Baumjohann and Treumann (1996)], which in the simplest case, can be expressed as:

$$\mathbf{E} + \mathbf{V}_i \times \mathbf{B} = \eta \mathbf{J} - \frac{1}{n_e e} \nabla \cdot (\mathbf{P}_e) + \frac{1}{ne} \mathbf{J} \times \mathbf{B} - \frac{m_e}{e} \frac{d\mathbf{V}_e}{dt} \quad (1.17)$$

where  $\mathbf{E}$  is the electric field and  $\mathbf{V}_i \times \mathbf{B}$  is the induction electric field associated with the average ion motion perpendicular to the magnetic field direction. The first term on the right-hand side gives the Ohmic resistance term where  $\eta$  is the resistivity. The second term represents the ambipolar electric field created by the electron density gradients in order to maintain the quasineutrality of the plasma when electrons are driven by pressure gradient. The third term expresses the Hall term. The final term expresses the effect of electron inertia. All the term on the right-hand of 1.17 are called non-ideal terms.

An important consequence of the presence these terms is that they may lead to the violation of the frozen-in condition. In other words, whenever the system develops small scale structure, one may expect the frozen-in condition to break down and the plasma dynamics to decouple from the magnetic field.

## 1.2. MAGNETIC RECONNECTION IN COLLISIONLESS PLASMAS

Magnetic reconnection is an ubiquitous energy conversion process in space plasma physics. It is expected to play key role in astrophysical phenomena. In the solar system, the magnetic reconnection allows energy conversion in solar flares, coronal mass ejections or at the earth's magnetopause as result of the interaction between the solar wind and the magnetosphere magnetic field lines. Magnetic reconnection is also found in laboratory experiments, and particularly those about magnetic-confinement fusion. The magnetic reconnection allows the connection between two magnetic field lines previously independent leading to a mixing between the two plasma populations. It also leads to the conversion of magnetic energy into mechanical energy by ejecting heated plasma apart from the reconnection site at the Alfvén speed , which can be expressed as:

$$V_A = c \frac{\omega_c}{\omega_p} = \frac{|B|}{\sqrt{nm\mu_0}} \quad (1.18)$$

where  $\mu_0$  is permeability of free space.

### 1.2.1. THE PRINCIPLE OF MAGNETIC RECONNECTION

Figure 1.6 shows a schematic view of the magnetic reconnection process between two oppositely directed magnetic fields separated by a current sheet (Figure 1.6-(a)). Under the frozen-in condition, magnetic field and plasma from different sources can not mix. The magnetic field lines, initially straight, are pushed towards the current sheet by external forces (Figure 1.6-(b)), until the frozen-in-flow assumption breaks down. The region where the frozen-in condition breaks down (i.e. that the equation 1.13 is not satisfied anymore) is called **diffusion region**. From a kinetic point of view, breaking the frozen-in condition means that particles do not simply gyrate around magnetic field lines but instead perform more complicate orbits. This behavior is possible only where the scale of the system  $L$  is smaller than the dimensions characterizing the particles' motions, i.e. the local gyroradius  $\rho$ . The fluid manifestation of these kinetic effects is the presence of non-ideal terms in the Ohm's law (Equation 1.17). This means that inside the diffusion region, the ideal MHD Ohm's law does not hold anymore (Equation equation 1.13). In the diffusion region, the magnetic field can reconnect taking a X-shape configuration (Figure 1.6-(c)). The point at the center, where the magnetic field strength equals zero, is called **X-point**. Here, the field lines merge and generate two kinked field lines which cross the current sheet. In 3D, the X-point becomes an **X-line** and lies perpendicular to the reconnection plane that drives the reconnection. The presence of an out of plane magnetic field, called guide field, changes the reconnection process. The newly merged field lines are then carried away from the diffusion region (Figure 1.6-(d)). The boundary separating the field lines which have undergone reconnection from those which have not is referred to as the **separatrix** which can be considered as rotational discontinuities.

The magnetic reconnection is also associated with energy conversion. If we consider a rectangular diffusion region with a length of  $2L$  and thickness of  $2\delta$ , the mass conservation law over the contour of the diffusion region can be written as:

$$\oint n\mathbf{V} \cdot d\mathbf{l} = 0 \quad (1.19)$$

In symmetric conditions, where the plasma conditions are identical on both sides of the current sheet, the mass conservation can be expressed as:

$$n_{in}V_{in}L = n_{out}V_{out}\delta \quad (1.20)$$

where  $V_{in}$  and  $n_{in}$  are the plasma velocity and density in the inflow region and  $V_{out}$  and  $n_{out}$  are the plasma velocity and density in the outflow region. Since  $\delta/L \ll 1$ , we can deduce from equation 1.20 that the plasma is accelerated in the diffusion region leading to plasma jets. The magnetic flux conservation can be used to determine the relation between the inflow and outflow magnetic fields and velocities:

$$B_{in}V_{in} = B_{out}V_{out} \quad (1.21)$$

This equation illustrates the conversion of the magnetic energy into kinetic energy since an increasing of velocity between the inflow and outflow regions will be associated with a decreasing of the magnetic field in the corresponding region.

### 1.2.2. DIFFERENTIAL ION-ELECTRON MOTION: HALL FIELDS AND CURRENTS

Magnetic reconnection is a multi-scale process. It occurs basically on three scales:

- The MHD scales:  $L \gg \rho_i$ ,  $T \gg \omega_{pi}^{-1}$ ,
- The ion scales:  $L \sim \rho_i$ ,  $T \sim \omega_{pi}^{-1}$ ,
- The electron scales:  $L \sim \rho_e$ ,  $T \sim \omega_{pe}^{-1}$ .

Figure 1.7 shows more detailed 2-D schematic view of magnetic reconnection where both ions and electrons are considered. Initially, the two anti-parallel magnetic fields in the  $X$  direction are embedded in the plasma which flows with an inflow velocity  $V_{in} = \mathbf{E} \times \mathbf{B}$  or "frozen in" velocity. When the magnetic fields reconnect, magnetic energy will be released in the form of accelerated electrons and ions that rapidly move away from the reconnection region in the  $Y$  direction (horizontal blue arrows). Since ions and electrons have significantly different gyroradii ( $\rho_i \gg \rho_e$ ), the diffusion region develops two-scale structure: the **ion diffusion region** of size of the ion inertial length  $\delta_i = c/\omega_{pi}$  and the **electron diffusion**

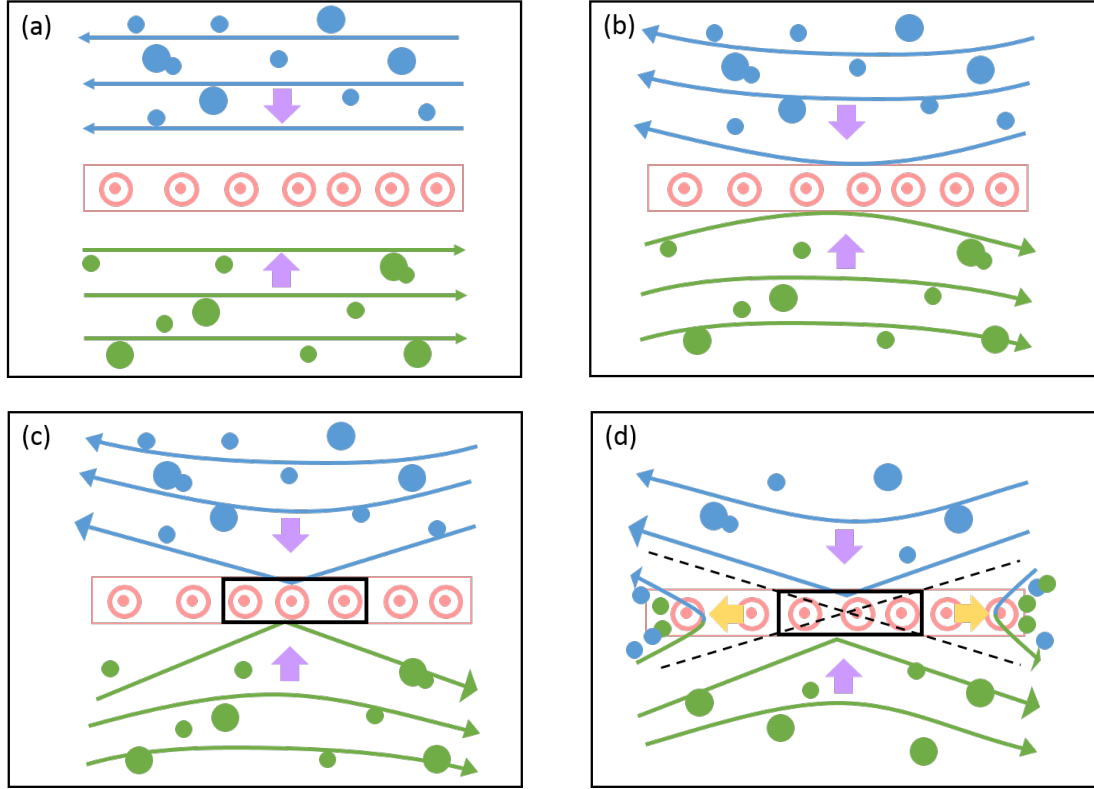


Figure 1.6 – A 2-D schematic view of the magnetic reconnection process. (a) Two opposite magnetic field (blue and green) from different plasma regimes, are encountering each other. The field lines are separated by a thin current sheet which is shown in pink, the inflow plasma from both side (purple arrows) stream into the current sheet, (b) The magnetic fields are strongly pushed towards each other, (c) a diffusion region is formed (black box) where the two magnetic fields create an X-line configuration and (d) these fields can cross the current sheet by merging into a pair of kinked lines, which will be carried away as the magnetic tension acts to straighten them. The yellow arrows represent the outflow plasma jets. The big circles represent ions while the small circles represent electrons.

**region** of size of the electron inertial length  $\delta_e = c/\omega_{pe}$  (pink and green shaded regions in Figure 1.7). In the ion diffusion region, ions do not flow with a  $\mathbf{E} \times \mathbf{B}$  velocity and are demagnetized. The electrons remain frozen in until the electron diffusion region which is a much smaller scale region. Differential motion between unmagnetized ions and magnetized electrons lead to the creation of **Hall currents**  $\mathbf{J} = en(\mathbf{V}_i - \mathbf{V}_e) \sim -en\mathbf{V}_e$  in the reconnection plane. The Hall currents then lead to the creation of out-of-plane magnetic fields in the direction perpendicular to the current density direction. These fields are called the **Hall magnetic fields**. They correspond to a quadrupole pattern of the out-of-plane component of the magnetic field inside the reconnection region on the scale size of the ion diffusion region. They are represented by yellow and violet ovals in Figure 1.7.

When decoupled from the magnetic field in the ion diffusion region, the ions do not obey



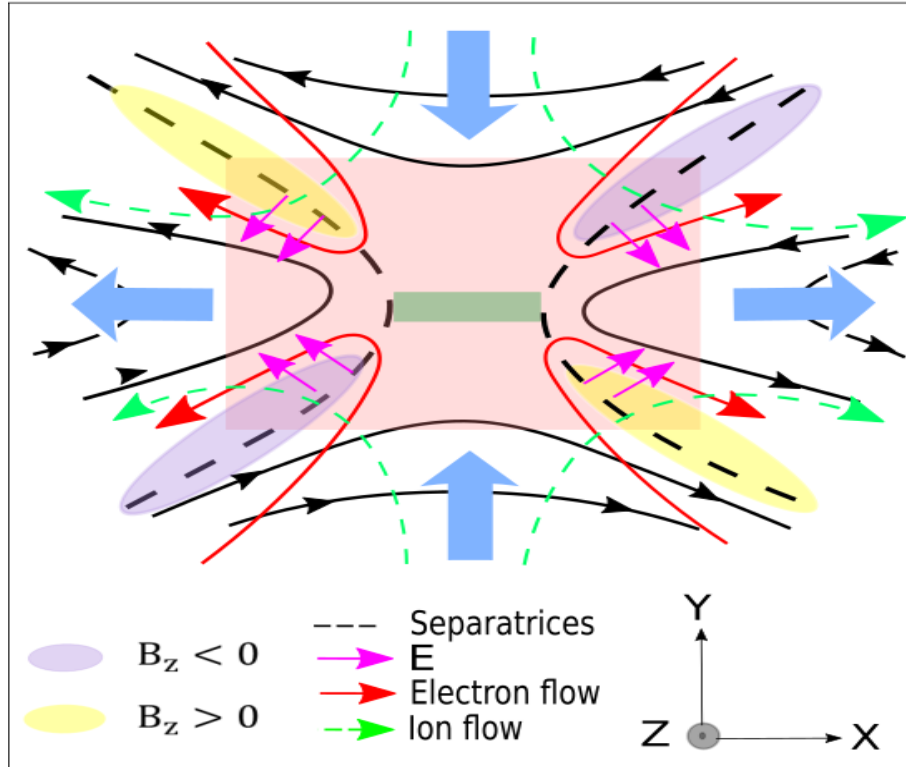


Figure 1.7 – Two-dimensional reconnection topology. The pink (green) box of  $\delta_i$  ( $\delta_e$ ) is the ion (electron) diffusion region. The black lines show the magnetic field lines. The dashed black lines are the separatrixes. The blue arrows show the plasma flow outside the diffusion region. Ions are decoupled from the magnetic field in the ion diffusion region, creating the Hall magnetic (yellow and violet quadrupolar structure) and electric field patterns (magenta arrows). The ion flow is shown by dashed green arrows. The electrons remain magnetized in the ion diffusion region and they follow the trajectories shown by red arrows. Electrons are demagnetized in the electron diffusion region.

the ideal MHD laws ( $\mathbf{E} = -\mathbf{V}_i \times \mathbf{B}$ ) anymore. They now satisfy the **Hall MHD** law:

$$\mathbf{E} = -\mathbf{V}_i \times \mathbf{B} + \frac{\mathbf{J} \times \mathbf{B}}{en} \quad (1.22)$$

The term  $\mathbf{J} \times \mathbf{B}/en$  creates an electric field perpendicular to the magnetic field (magenta arrows). This field is called the **Hall electric field** and points toward the central current sheet at the edge of diffusion region.

In the presence of several types of ions of different masses, multiple ion diffusion regions may exist according to the mass and temperature of each ion population.

### 1.2.3. ANOMALOUS RESISTIVITY MODEL FOR MAGNETIC RECONNECTION

Two major mechanisms may produce resistivity in a plasma. The first possibility results from momentum exchange through electron collisions and corresponds to the **microscopic Ohmic resistivity**. The second possibility does not involve particle-particle interactions but instead consists of a momentum exchange by small-scale wave-particle processes, possibly active also in collisionless plasma regimes. The resistivity resulting from this second mechanism is commonly called **anomalous resistivity** and is substantially larger than the microscopic Ohmic resistivity inside electron diffusion regions, for the plasmas we study throughout this work. Indeed, since strong current density in the dissipation region leads to a large relative streaming between ions and electrons, many plasma instabilities can be excited in this region, notably when the drift velocity of the current-carrying electrons exceeds a certain threshold, such as the electron thermal speed. Waves excited due to instabilities, developing in a naturally turbulent way, provide an efficient mechanism for the scattering of electrons onto ions, ultimately leading to the anomalous resistivity.

### 1.2.4. RECONNECTION RATE

The reconnection rate  $R$  is the amount of magnetic flux reconnecting per unit time per unit length of the reconnection line. The reconnection rate is also defined as the ratio of the plasma flow velocities of the inflow and outflow regions as a first approximation. Considering an elongated magnetic diffusion region (with length  $2L$  and width  $2\delta \ll 2L$  as illustrated in Figure 1.8) which lies between two identical plasmas with oppositely directed magnetic

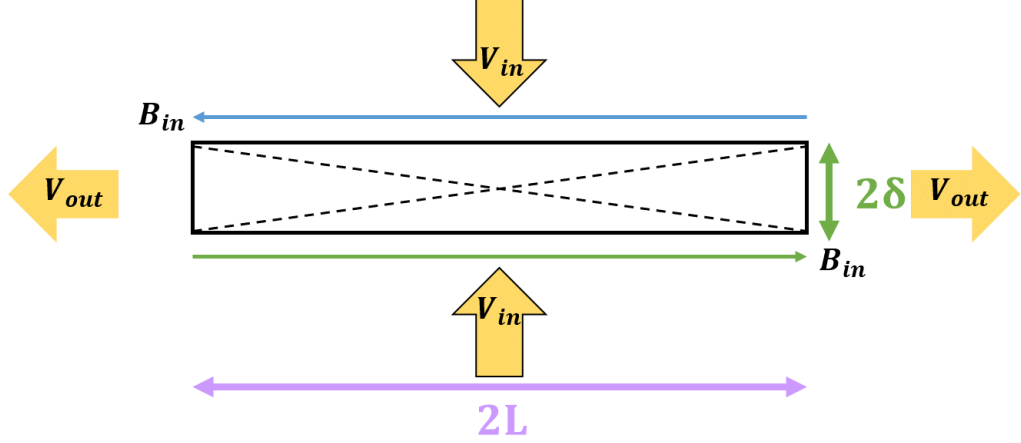


Figure 1.8 – Zoom around the diffusion region shown in Figure 1.6-(d). The field line diffuses over the half-width of the diffusion layer,  $\delta$ , which is much smaller than the system size,  $2L$ .

field lines,  $R$  can be expressed as:

$$R \equiv \frac{V_{in}}{V_{out}} \quad (1.23)$$

The reconnection rate is strongly linked to the geometry of the reconnection and corresponds to the ratio of the angular widths of the outflow to inflow regions ( $\delta/L$ ).

Both observations and models predicted a reconnection rate of 0.1 in normalized units over a wide range of parameters [e.g. [Chen et al. \(2017\)](#); [Liu et al. \(2018\)](#)]. However, despite multiple observational and theoretical works, the physical origin of this value is still unclear [[Cassak et al. \(2017\)](#)]

### 1.2.5. ENERGY CONVERSION RATE

The temporal change of electromagnetic energy density,  $W$ , can be obtained by combining Maxwell's equations:

$$\frac{dW}{dt} = \frac{\partial}{\partial t} \left( \frac{B^2}{2\mu_0} \right) + \nabla \cdot \left( \frac{\mathbf{E} \times \mathbf{B}}{\mu_0} \right) = -\mathbf{J} \cdot \mathbf{E} \quad (1.24)$$

where  $(\mathbf{E} \times \mathbf{B})/\mu_0$  is the Poynting flux. In a steady state, the regions where  $\mathbf{J} \cdot \mathbf{E} > 0$  are sinks of Poynting flux  $S$  and, conversely, regions where  $\mathbf{J} \cdot \mathbf{E} < 0$  are sources of Poynting flux. In the reconnection dissipation region,  $\mathbf{J} \cdot \mathbf{E}$  is supposed to be positive because magnetic reconnection is known to be a dissipative process that converts magnetic energy into heat and kinetic energy.

### 1.2.6. OBSERVATIONAL CONSTRAINTS FOR MAGNETIC RECONNECTION ANALYSIS

Multi-spacecraft studies have proven to be an invaluable tool to better understand the magnetic reconnection process. The Cluster mission [Escoubet et al. (2001)] allowed the study of the magnetic reconnection and its diffusion region at the magnetopause on ion-scales. However, despite numerous studies on this subject, many aspects about magnetic reconnection remain unclear due to the limited resolution of instruments aboard past missions. More recently, the Magnetospheric Multiscale (MMS) mission launched on March 12, 2015 was designed to better understand the magnetic reconnection process. MMS is composed by four identical satellites flying in adjustable tetrahedral formation allowing the observation of the three dimensional structure of magnetic reconnection and the measurements of the spatial gradients of various plasma and field parameters. The MMS mission was designed to answer specific questions about reconnection by providing unprecedented spatial and time resolution measurements. MMS makes the study of microscopic structures and, in particular, of the thin electron diffusion region possible [Burch et al. (2016)]. Previous missions provided observations of relatively large regions of the magnetosphere. They allowed the study of magnetic reconnection at the MHD (e.g. ISEE, AMPTE, Geotail, Wind) and ion (Cluster) scales. The challenge of MMS was thus to extend these understandings to the electron scale. It is at this scale that the magnetic field lines break and reconnect and that the processes leading to the dissipation process that converts magnetic energy into kinetic energy and heat occur. On electronic length scales, the plasma is described by the Ohm's law shown in Equation 1.17. This equation shows the terms that need to be considered when the frozen-in condition is broken: the resistive term, the divergence of the electron pressure tensor and by the electron inertia term. These terms introduce new physics to the system at short scales. In order to take into account these terms, the requirements for MMS were to provide three-dimensional maps of particle distribution functions, electric and magnetic fields, and plasma waves within the electron diffusion region. At the dayside, the densities are high and the scale of the electron diffusion region is of the order of the electron skin depth, i.e. 10 km, or less. The spacecraft separation of MMS is about  $\sim 10$  km while it scans the dayside magnetopause. The time resolution of measurements were

chosen based on the size of the electron and ion diffusion regions and their motions (tens of km/s to 100 km/s) as explained in [Burch et al. \(2016\)](#). For example, an Electron Diffusion Region (EDR) with a width of 5 km and moving at 50 km/s, would contain only one spacecraft for 0.1 s. The time resolution was chosen in such a way that at least three measurements during one crossing of the EDR. Therefore, the full electron distribution functions had to be measured with a time resolution of 30 ms. Applying this to ion diffusion regions, with a dimension of 250 km, the time resolution for ion was set to 150 ms. Therefore, the electrons and ions distribution functions were needed at time resolutions of 30 ms and 150 ms, respectively, compared to 2 s (electrons) and 4 s (ions) on Cluster.

### 1.3. THE EARTH'S MAGNETOSPHERE

#### 1.3.1. LARGE-SCALE STRUCTURE OF THE EARTH'S MAGNETOSPHERE

##### THE SOLAR WIND

The Sun emits a continuous outflow of highly-conducting plasma into the interplanetary medium which is called **Solar Wind**. This term was suggested by [Parker \(1958\)](#) who also predicted that the radial speed of expanding outflow increases with the distance from the Sun, and becomes supersonic before arriving at Mercury's orbit. The plasma of the solar wind consists mainly of protons and electrons, with a small amount of ionized helium and fewer ions of heavier elements.

The observations of solar wind showed that, at the Earth's orbit distance (1 Astronomical Unit), the solar wind parameters are typically:  $\sim 5\text{ cm}^{-3}$  for the electron density,  $\sim 10^5\text{ K}$  for the electron temperature,  $\sim 5 - 10\text{ nT}$  for the magnetic field intensity. The outflow velocities were found to be about  $\sim 300 - 450\text{ km s}^{-1}$  for slow streams and  $\sim 600 - 900\text{ km s}^{-1}$  for fast stream solar wind. The plasma of the solar wind is highly conductive so that the magnetic field of solar origin is frozen in to the plasma, and is carried into interplanetary space with the solar wind outflow, forming the **Interplanetary Magnetic Field** (IMF). The IMF originates in regions on the Sun where the field lines emerging from one region extend virtually indefinitely into space, which are called "open field lines". The feet of the field lines remain frozen into the solar plasma. Therefore, the rotation of the sun combined with the radial propagation of the solar wind leads to the formation of a spiral configuration known as the

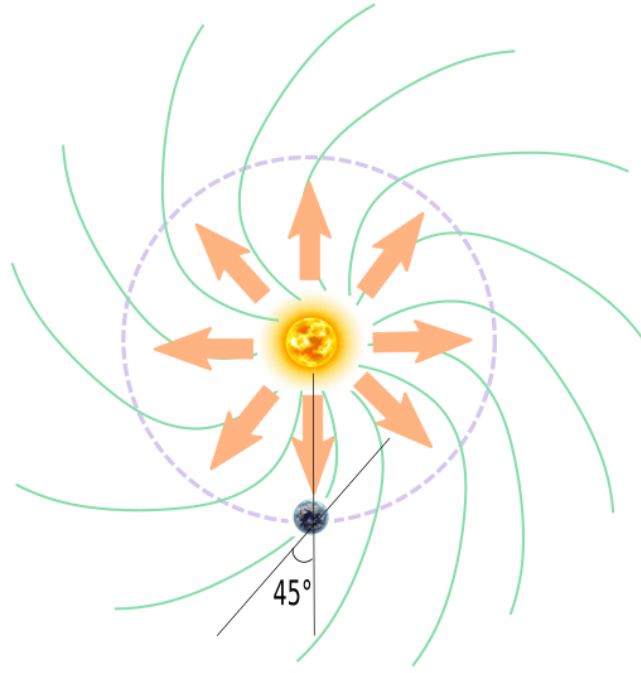


Figure 1.9 – A schematic view of the spiral Parker structure in the equatorial plane and orbit of the Earth in 1 AU, showing the interplanetary magnetic field (IMF) lines frozen into a radial solar wind with an expansion at speed of  $400 \text{ km s}^{-1}$ . As the plasma passes Earth's orbit moving parallel to the Sun-Earth line, the IMF typically creates an angle of  $45^\circ$ . (Sun and Earth are not to scale).

**Parker spiral** (see Figure 1.9). Observed near Earth, the interplanetary magnetic field tends to make  $\sim 45^\circ$  or  $\sim 225^\circ$  angle with Sun-Earth direction.

### THE EARTH'S MAGNETOSPHERE

The plasma of the interplanetary medium is governed by interplanetary magnetic field. But closer to the Earth, the terrestrial magnetic field dominates and creates a cavity in the solar wind [Chapman and Ferraro (1930)], which is called the **magnetosphere**. Figure 1.10 displays a sketch of the structure of the Earth's magnetosphere and large scale current systems. The terrestrial magnetic field provides an obstacle to the solar wind so that the solar wind cannot simply penetrate into the geomagnetic domain. When the supersonic solar wind encounters the Earth's dipolar magnetic field, a shock region is generated upstream the Earth, which is called the **bow shock**. On the Sun-Earth line, the bow shock is located at  $10 - 15 R_E$  (Earth radius) from the Earth, increasing to  $15 - 20 R_E$  towards the dawn and dusk flanks [e.g. Formisano (1979)]. The thickness of the bow shock is of the order of the ion gyroradius ( $\sim 1000 \text{ km}$ ). At the bow shock, the plasma slows down to subsonic speeds, and is compressed to higher densities and temperatures. Through this process, much of

the solar wind kinetic energy is converted into thermal energy, resulting in a temperature increase in the region of shocked plasma called the **magnetosheath** which is formed between the bow shock and the Earth's magnetosphere. The plasma in this region is denser and hotter than solar wind plasma and the magnetic field strength has higher values in this region.

The magnetosheath plasma flows around the magnetosphere. During this encounter, the solar wind is mainly deflected around the magnetosphere, and the kinetic pressure of the solar wind distorts the dipolar field of the Earth such that it is compressed on the dayside and stretched out on the night side [e.g. [Kobel and Fluckiger \(1994\)](#)]. The extension in the night side is known as the **magnetotail**. The boundary between the magnetosheath and magnetosphere is called the **magnetopause**. The magnetopause and the magnetotail are regions within the Earth's magnetosphere where current sheets separate regions of distinct magnetic fields. It is inside these thin boundaries that processes such as magnetic reconnection occur, at the magnetopause in the dayside and in the cross-tail current sheet in the night side. The magnetosphere is the only place in space where plasma micro-processes can be studied since it is the only place accessible in situ by appropriate observatories. The locations of the the bow shock and of the magnetopause mainly depend on the solar wind pressure.

### **Magnetosheath properties**

The plasma and the magnetic field in the magnetosheath are compressed. The main properties of the magnetosheath are:

- Amounts of  $He^{++}$  ions and trace amounts of heavier ions of solar wind origin,
- Typical plasma densities are between 10 and 30  $cm^{-3}$  [e.g. [Phan et al. \(1994\)](#)].
- Thermal particle energies are of order  $\sim 100$  eV for electrons and 1 keV for ions [e.g. [Phan et al. \(1994\)](#)].
- The magnetic field magnitude is enhanced compared with the IMF.

### **Magnetosphere properties**

The plasma properties in the magnetosphere are quite different from those in the magne-

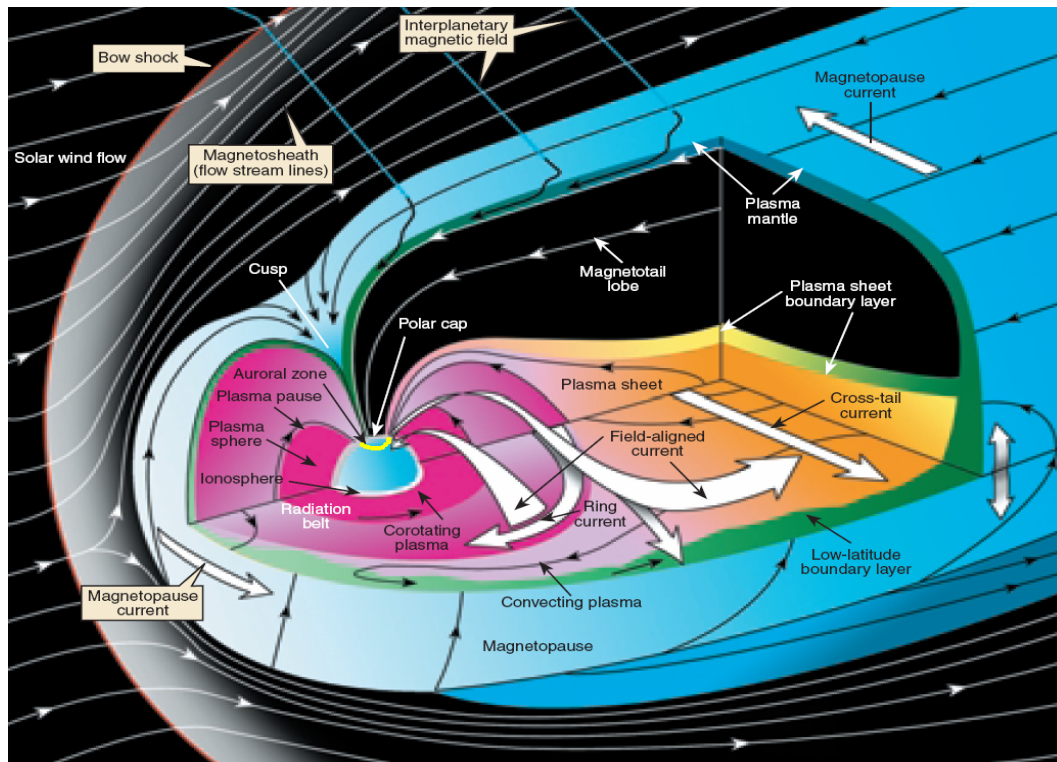


Figure 1.10 – Three-dimensional cutaway view of the Earth Magnetosphere showing currents (white arrows), fields and plasma regions. This figure is from [Pollock et al. \(2003\)](#).

tosheath. The dayside magnetosphere is characterized by:

- Abundance of  $O^+$  ions originated from the ionosphere,
- Lower density and ion velocity than the magnetosheath plasma,
- Northward  $B$ ,
- Electron fluxes at high energies ( $\sim 1$  keV),
- High energy ions (above 4 keV).

Figure 1.11 shows an example of what a spacecraft can observe in the magnetosphere, the magnetosheath and the solar wind. These observations were provided by MMS spacecraft on 1 December 2017 between 10 : 00 and 16 : 00 UT. The spacecraft were initially in the magnetosphere. The main component of the magnetic field was the  $Z$  component. The density was low and there was no plasma flow. The particles energy spectrograms reveal the presence of high-energy ions ( $\sim 10$  keV) and electrons ( $\sim 2$  keV). At  $\sim 11 : 30$ , the spacecraft crossed the magnetopause. Between  $\sim 11 : 30$  and  $\sim 14 : 00$  UT, the spacecraft moved



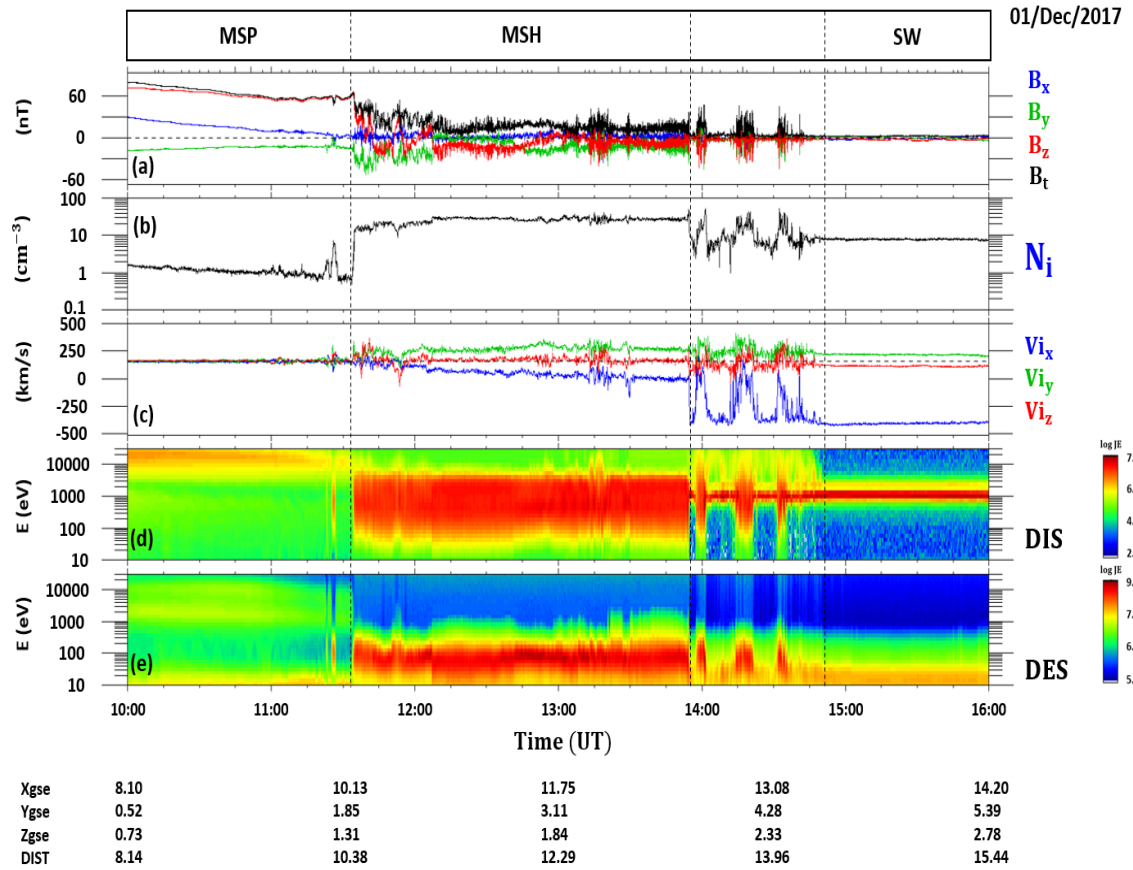


Figure 1.11 – Observations from MMS 1 on 1 December 2017 between 10:00 and 16:00 UT while the spacecraft were moving from the magnetosphere to the solar wind. (a) the magnetic field components and intensity, (b) the ion density, (c) the ion velocity components, (d) ion spectrogram and (e) electron spectrogram.

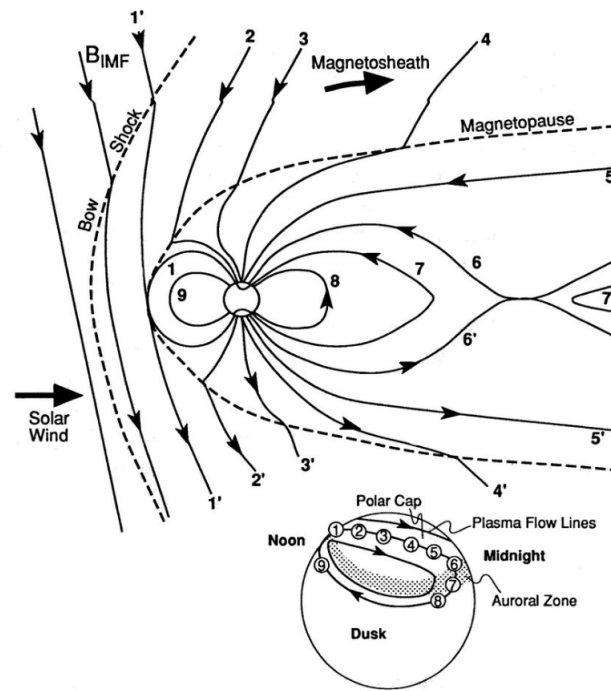


Figure 1.12 – The schematic figure of plasma flow through the magnetosphere driven by magnetic reconnection. The numbered field lines show the evolution of a field line involved in the Dungey cycle. Figure from Kivelson et al. (1995).

to the magnetosheath where the densities were high ( $\sim 20 \text{ cm}^{-3}$ ) and the plasma velocity increased. The particles spectrograms show that ions had energies up to  $\sim 1000 \text{ eV}$  and electrons had energies up to  $\sim 100 \text{ eV}$ . Around  $\sim 14:50 \text{ UT}$ , the spacecraft exited into the solar wind. The magnetic field intensity was low compared to that in the magnetosheath and the magnetosphere. The density remained relatively high ( $\sim 10 \text{ cm}^{-3}$ ) and there was an important flow mainly in the  $-X$  direction. The electron energy was in the order of few tens of eV. While moving from the magnetosheath to the solar wind, between  $13:50$  and  $14:50 \text{ UT}$ , there were multiple incursions into the solar wind and the magnetosheath indicative of several bow shock crossings.

### 1.3.2. SOLAR WIND-MAGNETOSPHERE COUPLING: DUNGEY'S CYCLE

Dungey's cycle is a schematic model for the interaction between the Earth's magnetic field and the interplanetary medium. The stages involved by the Dungey's cycle describe the evolution of magnetic field lines path driven by a typical dayside reconnection during southward IMF orientation and are shown in Figure 1.12. The numbered field lines show the step by step evolution of a field line. When the IMF in the magnetosheath is directed southward,

reconnection occur at the magnetopause near the subsolar point. Newly opened field lines are then carried tailward by the solar wind flow. The motion of the convecting magnetic field lines and the plasma which is frozen in gives rise to a convection electric field. This convection electric field is directed from dawn to dusk. In the magnetotail, the two open field lines reconnect at the current sheet separating the Earthward field in the northern lobe from the anti-Sunward field in the southern lobe. The nightside reconnection site generates an open field line and a closed magnetospheric field line. The newly closed field line then moves Earthward. The convection cycle is completed as the closed field line moves around the flank to replace dayside field lines which have been reconnected.

The Dungey's cycle provides a qualitative description of the solar wind-magnetosphere coupling under quasi-stationary conditions. However, this process is far more complex in reality. Indeed, it is now well known that the magnetospheric dynamics is non-stationary and non-linear.

## 1.4. MAGNETIC RECONNECTION AT THE EARTH'S MAGNETOPAUSE

### 1.4.1. THE DAYSIDE MAGNETOPAUSE AND THE BOUNDARY LAYER

The magnetopause is the boundary between the magnetosphere and the magnetosheath. The magnetopause consists of a current sheet, surrounded by more or less a disturbed boundary layer. The boundary layer basically separates the interplanetary magnetic field from the Earth's magnetic field and is the place where the reconnection occurs leading to mass, energy and momentum transfer from the magnetosheath into the magnetosphere. The magnetopause is associated with a sharp change in the magnetic field. The magnetopause thickness is typically around 80 km but can vary up to 2000 km and it moves quite rapidly with speeds of several 10 km/s in and outward.

From an MHD point of view, the magnetopause can be described either as a tangential discontinuity or a rotational discontinuity [e.g. Hudson (1970)]. For the tangential discontinuity type, there is no magnetic field component normal to the magnetopause. Under this condition, there would be no mixing of the plasma from the two sides of the tangential discontinuity magnetopause. However, when magnetic reconnection occurs between the magnetic fields from the two sides of the magnetopause, there is a non-zero normal

magnetic field component. In this case, the magnetopause is locally and intermittently a rotational discontinuity [e.g. [Sonnerup et al. \(1981\)](#)]. Under this condition, the particles from both side of the magnetopause mix up along the reconnected field lines.

At large scale, boundary layers are formed by the repetitive occurrence of magnetic reconnection at the magnetopause. One boundary layer is created in the magnetosheath outside of the magnetopause and is known as the **magnetosheath boundary layer (MSBL)**. Another boundary layer is formed inside the magnetopause and is usually called **Low Latitude Boundary Layer (LLBL)**. These boundary layers contain a mixture of particles of magnetospheric and interplanetary origins [e.g. [Eastman and Hones \(1979\)](#); [Hall et al. \(1991\)](#)]. During periods of active reconnection, both the ion composition and the electron distribution in the boundary layers are seen to change locally as a result of mixing of magnetospheric and magnetosheath populations.

Generally, the inner boundary layer shows a complex structure with the existence of inner and outer distinct parts of the LLBL [[Le et al. \(1996\)](#); [Fuselier et al. \(1997\)](#); [Onsager et al. \(2001\)](#)]. The solar wind-magnetosheath interaction can be more complicated under unusual conditions of low solar wind Mach number and dynamic pressure. Under such disturbed conditions, the LLBL may consist of two regions: a sheath-like and dense outer part that can be distinguished from a dilute and mixing inner region [[Fujimoto et al. \(1998\)](#)]. The plasma in the outer boundary layer is dominated by solar wind particles while in the inner boundary layer a mixture of particles of solar wind and magnetospheric origins are present with comparable proportions [[Bauer et al. \(2001\)](#)].

#### 1.4.2. FLUX TRANSFER EVENTS

Complex magnetic structures form at the magnetopause as a result of magnetic reconnection. Bursty magnetic reconnection (i.e. short X-line length and short time duration) lead to the formation of flux transfer events (FTEs) on the dayside magnetopause [[Russell and Elphic \(1978, 1979\)](#)] which are embedded in the exhaust. The two prime signatures of FTEs observed in situ are an enhancement in the magnetic field magnitude and a bipolar signature in the component of the magnetic field normal to the magnetopause.

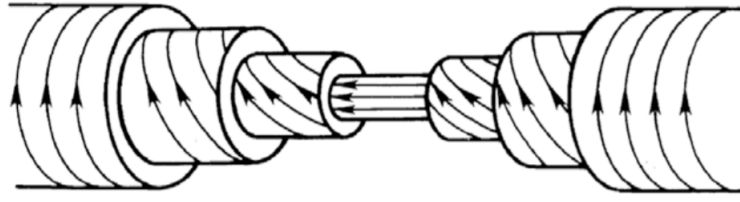


Figure 1.13 – Interior structure of magnetic field lines in a flux rope. Figure from [Russell and Elphic \(1978\)](#).

### 1.4.3. FTEs CHARACTERISTICS

[Russell and Elphic \(1978\)](#) reported observations of FTEs using the initial results of ISEE 1 and 2 magnetometers. During two magnetopause crossings, interplanetary magnetic field were strongly southward and they observed a clear evidence for reconnection. Magnetic field data were projected in a local reference frame system (LMN system) which is discussed in Section 2.5.1. The observations revealed a signature consisting of a bipolar variation in  $B_N$ , with simultaneous variations of the components in  $B_L$  and  $B_M$  which were not consistent with ordinary crossings of the magnetopause. The signatures were observed on both sides of the magnetopause.

[Paschmann et al. \(1982\)](#) reported the most important characteristics of FTEs:

- An enhancement in magnetic field strength  $|B|$  when compared to the ambient field,
- A bipolar variation in  $B_N$ ,
- High energy particles from magnetosphere and low energy particle from magnetosheath are observed within FTEs,
- Anti-correlation of density and temperature inside the structures.

Flux transfer events are interpreted as helical **flux ropes** which are structures of twisted field lines along an axis (Figure 1.13). Near the central axis, the magnetic field is strong and parallel to the axis. For increasing distance from the central axis, the axial magnetic field becomes much weaker while the azimuthal magnetic field increases. In order to sustain this magnetic structure, the current density must be directed along the axis parallel or anti-parallel to the sense of the magnetic field lines in the flux rope. FTEs have been studied using simulations [[Fedder et al. \(2002\)](#); [Raeder \(2006\)](#); [Daum et al. \(2008\)](#)], laboratory experiments [e.g. [Stenzel and Gekelman \(1979\)](#); [Egedal et al. \(2007\)](#); [Fox et al. \(2017\)](#)], ground

measurements [Wild et al. (2001); Lockwood et al. (2001)], and multi-spacecraft missions as Cluster [e.g. Fear et al. (2005); Hasegawa et al. (2006); Roux et al. (2015)], THEMIS [Fear et al. (2009); Silveira et al. (2012)] and now MMS [Farrugia et al. (2016); Hwang et al. (2016)]. The scale size of an FTE in its direction of motion along the magnetopause can be determined from a single-spacecraft observation by multiplying the duration of the signature with an assumed or measured FTE propagation speed. Early measurements estimated it to be of order  $2 - 4R_E$  [Russell and Elphic (1978)]. More recently, Owen et al. (2001) estimated it to be of order  $0.8R_E$ . The scale size of an FTE normal to the magnetopause was estimated to be the order of  $1R_E$  [e.g. Saunders et al. (1984)]. Solar wind and interplanetary magnetic field conditions have important influences on FTEs [Wang Y. L. et al. (2006)].

Multi-spacecraft missions have advanced the understanding of FTEs shape, motion, and extent [e.g. Fear et al. (2009); Trenchi et al. (2016)]. However, despite the abundance of FTE observations, their formation mechanism is not clearly understood yet. More studies are still needed to better understand the detailed structure of FTEs and to link the observed properties to plasma characteristics at the formation site. The magnetic field topology within FTEs and their 3D magnetic structure have also not been completely elucidated.

## 1.5. WAVE-PLASMA INTERACTIONS

Waves are disturbances traveling through matter or space, accompanied by a transfer of energy without any transport of mass. A wave is characterized by its **angular frequency**  $\omega = 2\pi f$  (rad/s) and its **wave vector**  $\mathbf{k}(m^{-1})$ . The vector  $\mathbf{k}$  gives both the direction of propagation of the wave and the wavelength ( $\lambda$ ) such as:  $|\mathbf{k}| = 2\pi/\lambda$ . There is a relation between  $\omega$  and  $\mathbf{k}$  that can be determined by the physical properties of the system. The function  $\omega(\mathbf{k})$  is called the **dispersion relation** for the wave.

The velocity of wave propagation, called the **phase velocity**, is defined as:

$$\mathbf{V}_{ph} = \frac{\omega}{\mathbf{k}} \quad (1.25)$$

The velocity of energy flow, i.e. **group velocity**, is given by:

$$\mathbf{V}_g = \frac{\partial \omega}{\partial \mathbf{k}} \quad (1.26)$$

Plasmas are very rich and complex mediums where a large variety of waves can exist. The types, or modes, of waves depend on the properties of the plasma itself. Plasma waves can be categorized in several ways, we can separate:

- **Electromagnetic** from **electrostatic** waves depending on the existence of magnetic field fluctuations.
- **Longitudinal** from **transverse** waves depending on their angle of propagation. In the longitudinal waves, the wave electric field is in the same direction of the wavenumber ( $\mathbf{E} \parallel \mathbf{k}$  or  $\nabla \times \mathbf{k} = 0$ ), whereas in the transverse waves the wave electric field is perpendicular to the wavenumber ( $\mathbf{E} \perp \mathbf{k}$  or  $\nabla \cdot \mathbf{E} = 0$ ).
- **Parallel** from **perpendicular** waves according to the direction of the wavenumber with respect to the magnetic field. Parallel waves propagate along the magnetic field vector  $\mathbf{B}$  while perpendicular waves propagate at  $90^\circ$ .
- **Left-handed** from **right-handed** waves which depends on the wave polarization. If the wave electric field rotates in the same sense as electrons do around a magnetic field line, the wave is right-handed. In contrast, if the wave electric field rotates in the opposite sense as electrons do around a magnetic field line, the wave is left-handed.

Space plasmas are rich with waves phenomena. The study of plasma waves is complex even in the simplest case of linear waves in homogeneous plasma. The angular frequency  $\omega$  in such conditions is a function of the wavenumber  $\mathbf{k}$  as discussed earlier in this section. The plasma behaves very differently in the directions parallel and perpendicular to the electric field. Indeed, charged particles easily move along the magnetic field lines but the gyration of particles around the magnetic fields leads to a motion in the perpendicular direction. The different behavior of the plasma in these two directions is reflected by dependence of the propagation properties of waves in plasmas on the angle between the direction of propagation of waves and the external magnetic field. Collisionless plasma waves-particle

interactions are considered to be a possible mechanism of acceleration of particles. Waves associated with magnetic reconnection at the magnetopause have been the subject of many studies [e.g. [Labelle and Treumann \(1988\)](#); [Farrell et al. \(2002\)](#); [Khotyaintsev et al. \(2006\)](#)]. Several wave modes are found near the reconnection sites: whistlers, solitary wave structures, lower hybrid drift waves, electron cyclotron waves and Langmuir/upper hybrid waves. More particularly, plasma waves were commonly observed around the reconnection sites covering a broad band of frequencies ( $\omega < \omega_{ci}$  to  $\omega > \omega_{pe}$ ) and in the separatrix region. In the next sections, we will describe the main wave-modes associated with magnetic reconnection after a brief introduction of the linear plasma wave theory.

### 1.5.1. LINEAR PLASMA WAVE THEORY

In this section we will derive the general wave equation using the Maxwell's equations and the Ohm's law. We will then show the general dispersion relation for waves in plasmas. The solutions for the dispersion relation correspond to different plasma wave modes.

The general wave equation can be derived using the Faraday's and Ampère's equations and then taking the curl of the first and the time derivative of the second, and combine, using  $\nabla \times (\nabla \times \mathbf{E}) = \nabla(\nabla \cdot \mathbf{E}) - \nabla^2 \mathbf{E}$ . The general wave equation can thus be expressed as:

$$\nabla^2 \mathbf{E}_1 - \nabla(\nabla \cdot \mathbf{E}_1) = \mu_0 \frac{\partial \mathbf{J}_1}{\partial t} + \mu_0 \epsilon_0 \frac{\partial^2 \mathbf{E}_1}{\partial t^2} \quad (1.27)$$

The usual notation comes from the linearization and is to label the equilibrium quantities with a subscript 0; i.e.  $X_0$ ; and the perturbed quantities with a subscript 1, i.e.  $X_1$ . A variable can thus be expressed as  $X = X_0 + X_1$ . Then the assumption of small perturbations is  $|X_1/X_0| \ll 1$ . For the electric field and the current density, the zeroth-order term is equal to zero. Taking into account the following approximations and transformations:

- The electric field may be approximated as a plane wave:  $\mathbf{E}_1 = E_1^0 e^{i(\mathbf{k} \cdot \mathbf{r} - \omega t)}$ .
- $\nabla \equiv i\mathbf{k}$  and  $\frac{\partial}{\partial t} \equiv -i\omega$ .
- Using Ohm's law, the current can be replaced as  $\mathbf{J} = \bar{\sigma} \cdot \mathbf{E}$  where  $\bar{\sigma}$  is the conductivity tensor.



The equation 1.27 turns into:

$$\left( \left( \mathbf{k}^2 - \frac{\omega^2}{c^2} \right) \bar{\mathbf{I}} - \mathbf{k}\mathbf{k} - i\omega\mu_0\bar{\sigma} \right) \cdot \mathbf{E}_1 = 0 \quad (1.28)$$

The solutions of equation 1.28 can be found by setting the determinant equal to zero:

$$\det \left( \left( \mathbf{k}^2 - \frac{\omega^2}{c^2} \right) \bar{\mathbf{I}} - \mathbf{k}\mathbf{k} - i\omega\mu_0\bar{\sigma} \right) = 0 \quad (1.29)$$

We can define the dielectric tensor as:

$$\bar{\epsilon} = \bar{\mathbf{I}} + \frac{i\bar{\sigma}}{\omega\epsilon_0} \quad (1.30)$$

and re-write the general dispersion relation of a wave in a plasma as:

$$\det \left( \frac{k^2 c^2}{\omega^2} \left( \frac{\mathbf{k}\mathbf{k}}{k^2} - \bar{\mathbf{I}} \right) + \bar{\epsilon} \right) = 0 \quad (1.31)$$

Now, once the expression of  $\bar{\epsilon}$  is known, the solutions of equation 1.31 give the different wave modes in the plasma.

## COLD PLASMA APPROXIMATION

In the cold plasma approximation, the plasma is considered to be consisted of cold electrons. The ions consist of a merely stationary background that ensures the quasi-neutrality of the plasma. The frequencies of waves that can form under such conditions are above the plasma frequencies and the ion cyclotron. In the following sections, we will describe the properties of some of the waves of relevance to the thesis that were found to be observed in the reconnection regions.

### Lower hybrid drift waves (LHDW)

Lower hybrid drift waves are strong plasma waves supported by density gradients. They operate at a frequency range where both electron and ion dynamics are important. That is, LHDWs oscillate at a frequency which is above the ion gyrofrequency but below the electron gyrofrequency:

$$\omega_{ci} \ll \omega_{LH} \ll \omega_{ce} \quad (1.32)$$

The LHDW angular frequency  $\omega_{LH}$  is given by:

$$\omega_{LH} = \frac{\omega_{pi}}{\sqrt{1 + \omega_{pe}^2 / \omega_{ce}^2}} \quad (1.33)$$

where  $\omega_{pe}$  and  $\omega_{pi}$  are the plasma frequencies for electrons and ions.

The LHDWs propagate perpendicularly to the ambient magnetic field and are characterized by short wavelengths (i.e.  $k_{\perp} \rho_e \sim 1$ ). Simulations suggest that the highest-amplitude Lower Hybrid Drift waves are usually located in the regions of sharp density gradient [Vaivads et al. (2006)]. The driving force for the LHDWs, in a simplified picture, is a density gradient with relative flow between ions and electrons due to their different diamagnetic drift. LHDWs are usually associated with strong electric fields on scales smaller than the ion gyroradius. It has also been shown that these waves can be generated by the electron beams generally present at the density gradients [Vaivads et al. (2004)]. The question of whether the LHDW can be responsible for magnetic reconnection or, take part in the dynamic leading to magnetic reconnection is still an open question.

### Whistler waves

The whistler waves can be observed at frequencies below the lower-hybrid frequency  $\omega_{LH}$  (Equation 1.33), but above  $\omega_{ci}$ :

$$\omega_{LH} \ll \omega \ll \omega_{ce} \quad (1.34)$$

At frequencies well below the electron cyclotron frequency, we can approximate the whistler waves frequency to:

$$\omega = \frac{\omega_{ce}}{1 + \frac{\omega_{pe}^2}{k^2 c^2}} \quad (1.35)$$

Whistler waves are right-hand circularly polarized electromagnetic waves that are also transverse. They may be excited by electron temperature anisotropy when  $T_{e\perp} / T_{e\parallel} > 1$  where the subscripts denote perpendicular and parallel directions to the magnetic field [kennel and petscheck, 1966]. In addition to the temperature anisotropy, whistlers can be excited as a consequence of electron beams [Gary and Wang (1996)].

Apart from linear waves, nonlinear modes may also develop in a plasma. Electrostatic solitary waves, for example, are generated out of nonlinear processes. They are characterized by localized bipolar electric fields parallel to the magnetic field [Matsumoto et al. (1994)] which can be observed in the electric field waveform data.

## 1.6. OVERVIEW OF THE THESIS

Chapter 2 provides an introduction to the instrumentation and analysis techniques used in this thesis. This is followed in Chapter 3 by a case study of magnetic reconnection occurring at a thin current sheet separating two interlaced flux tubes near the Earth's magnetopause. Chapter 4 presents the results of the study of plasma waves associated with the event that was discussed in Chapter 3. The work presented in this Chapter has been done at the Laboratory of Plasma Physics (LPP), Paris, under the supervision of Olivier LeContel and Hugo Breuillard. Finally, a summary of the thesis is presented along with some conclusions and potential further research in Chapter 5.

# 2

## INSTRUMENTATION AND ANALYSIS TECHNIQUES

The first section of this chapter provides an introduction to the MMS mission with a brief description of the main instruments that were used in this thesis. The second section covers the analysis techniques used.

### 2.1. THE MAGNETOSPHERIC MULTISCALE MISSION (MMS)

### 2.2. MISSION AND MEASUREMENTS REQUIREMENTS

The MMS mission is a NASA Solar Terrestrial Probe involving a number of institutions in the United States, as well as numerous international partners in Austria, Sweden, France (CNES, IRAP, LPP) and Japan. MMS consists of four identical satellites flying in adjustable tetrahedral formation. The spacecraft were launched on 12 March 2015 from the Cape Canaveral Air Force Station in Florida on an Atlas V launch vehicle into an elliptical  $28^\circ$  inclination orbit with perigee at 1.2 Earth radii ( $R_E$ ) and apogee at  $12 R_E$  for a two-year initial mission phase.

Previous multispacecraft magnetospheric missions (THEMIS and Cluster) allowed the study of magnetic reconnection at the MHD and ion scales. For example, the Cluster spacecraft

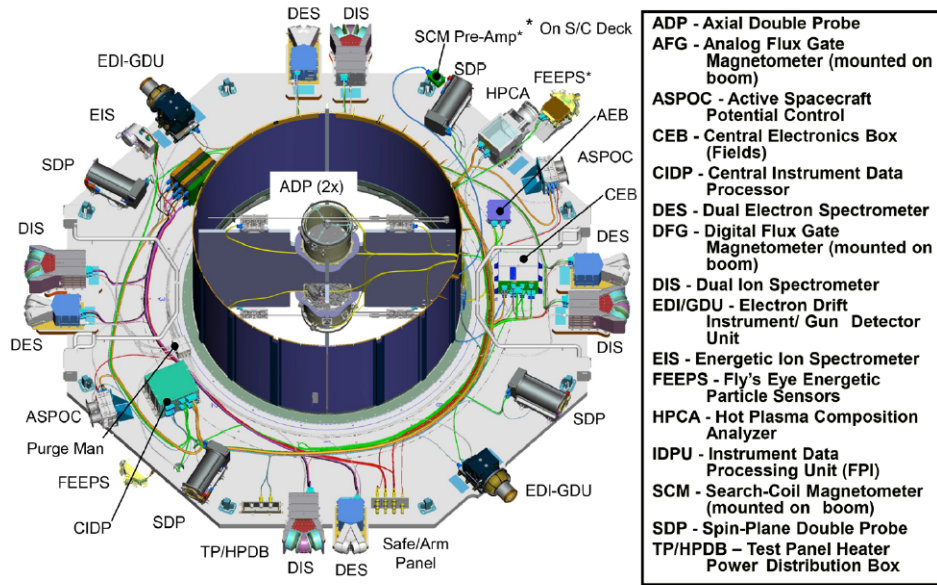


Figure 2.1 – Instruments onboard each MMS spacecraft. Figure from [Burch et al. \(2016\)](#).

orbits were designed to fly through the high-latitude magnetospheric cusps to investigate plasma transfer into the Earth's magnetosphere. The Cluster mission explored more particularly the detailed role of Hall MHD in controlling the reconnection rate and the ion flow through the ion diffusion region. The challenge of MMS was therefore to extend these understandings to the electron scale. For this reason, MMS was designed to provide three-dimensional maps of particle distribution functions, electric and magnetic fields, electric currents and plasma waves within the electron diffusion region with significantly higher time resolution and on closer spacecraft spacing than all the previous missions. Figure 2.1 shows the way the instruments were arranged on each spacecraft. In order to achieve this objective, MMS had to probe the reconnection sites in the tail and at the dayside. The orbit apogees were placed near the expected reconnection sites at  $12 R_E$  on the day side and  $25 R_E$  on the night side. In order to satisfy these requirements, two different orbits were needed for Phases 1 and 2 (Figure 2.2). The first scan of the dayside magnetopause has been done during Phase 1a which started on September 2015. The optimum separation of spacecraft were determined during this phase by adjusting the separation distance between 10 and 160 km. A second scan of the dayside magnetopause was then in Phase 1b with a spacecraft separation fixed at 10 km, which corresponds to the optimum separation found during Phase 1a. After the second scan of the dayside magnetopause, the apogee was

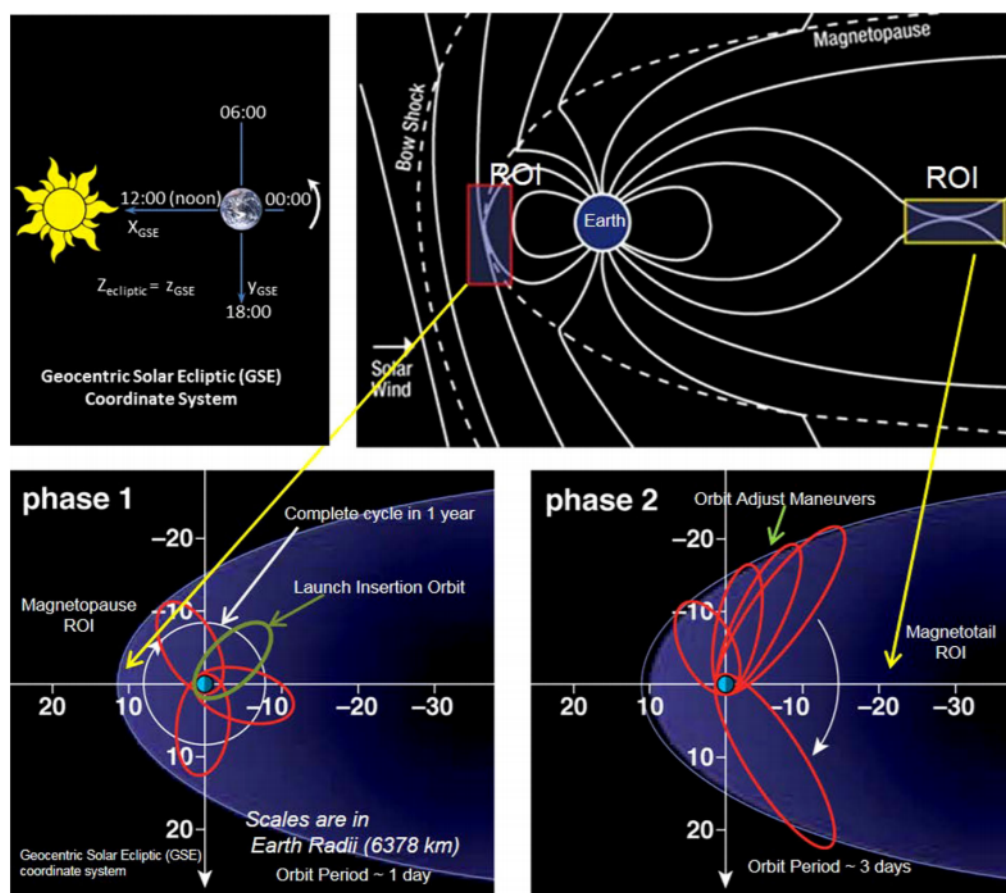


Figure 2.2 – MMS orbital geometry and science Regions of Interest (ROI). Figure from [Tooley et al. \(2016\)](#).

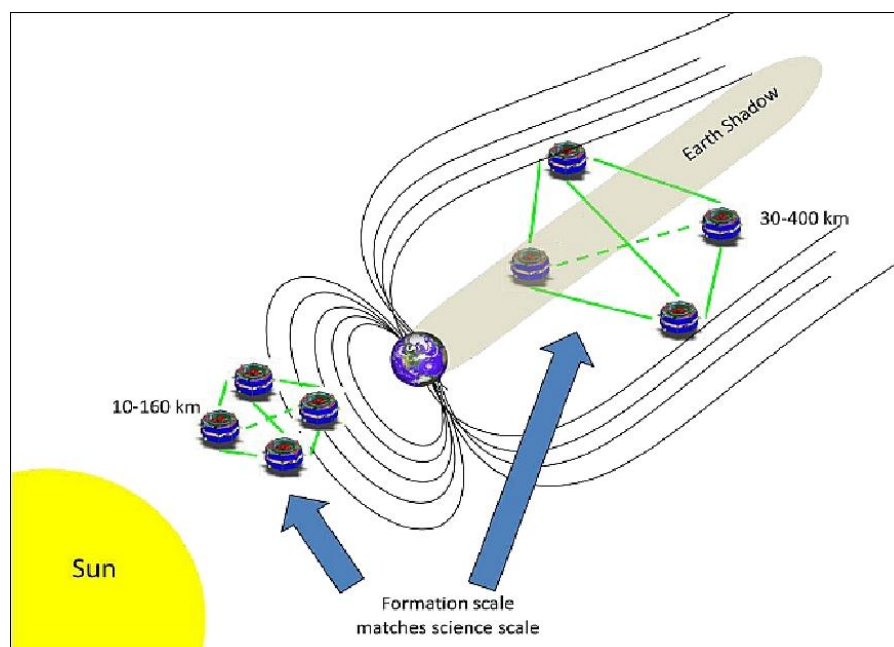


Figure 2.3 – Schematic of the MMS formation as a science instrument concept (image credit: NASA).

raised to  $25 R_E$ . That provides measurements at increasing distances along the dawnside flank of the magnetopause and performs a scan through the magnetotail in Phase 2. During this phase, the spacecraft separation varied between 30 and 400 km in order to obtain the optimum value.

At the dayside, the densities are high and the scale of the electron diffusion region is of the order of the electron skin depth, i.e. 10 km, or less. The spacecraft separation distances had to be as small as 10 km in order to probe this small and moving region. On the night-side, the densities are lower and the spatial dimension of the electron diffusion region is about ten times larger. Therefore, the initial and final spacecraft separations were smaller in Phase 1a than in Phase 2b (Figure 2.3). The tetrahedral configuration of the spacecraft allows the observation of the three dimensional structure of magnetic reconnection and the measurements of three spatial gradient components of various plasma and field parameters. A high-quality tetrahedron is defined as the ratio of the volume of the actual tetrahedron by the theoretical volume of a regular tetrahedron having the same size of at least 0.8. Throughout the regions of interest (ROI), high-quality tetrahedrons are maintained [Fuselier et al. (2016)].

## 2.3. MISSION OPERATIONS

The instruments on-board MMS have two operational modes: slow survey and fast-survey. In the regions of interest, where  $R > 9R_E$  on the day side and  $R > 15R_E$  on the night side, the instruments operate at their maximum speed and the burst data are collected. The regions of interest are orbital segments along which the spacecraft have a significant chance of traversing the predicted reconnection sites (Figure 2.4).

Figure 2.4 shows the segmentation among slow-survey, fast-survey and burst-mode. Only 20 minutes of burst-data can be downloaded per day. Two ways are employed in order to choose the best burst data with the highest science value for transmission. The first way consists of an automatic selection. When the spacecraft are in the regions of interest, each instrument assigns a quality factor to each 10 s segment of its data which help identifying regions with large changes in plasma density and reversals of the magnetic field. Table 2.1 summarizes the top-level burst mode signatures and the associated trigger parameters. On each spacecraft, the quality factors of all the instruments are combined on board generat-

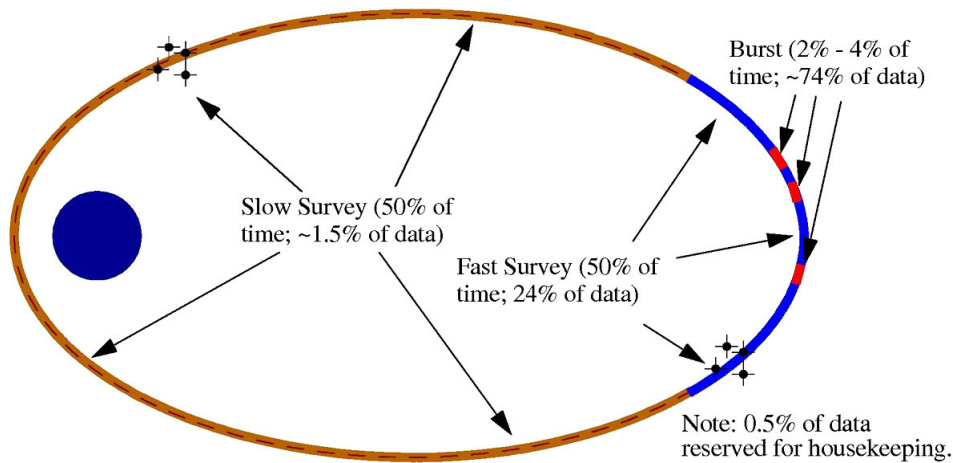


Figure 2.4 – Ecliptic-plane sketch of MMS orbit. The region of interest is shown in blue and burst data intervals are shown in red. Figure from [Burch et al. \(2016\)](#).

Physical signature	Trigger parameter
Reconnection jets	Ion flow reversals
Magnetopause and neutral sheet detection	Large $B$ variations
Large flows surrounding reconnection sites	Large $E$
Magnetopause and neutral sheet detection	large electron currents
Particle acceleration produced by reconnection	Electron and ion beams
Electron diffusion region	$E$ parallel to $B$

Table 2.1 – Top level burst-mode parameters. Table from [Burch et al. \(2016\)](#).

ing a spacecraft data quality index which is transmitted along with the survey data. Then, the quality indices for the four spacecraft give a mission quality index.

The second way is manual and is known as the Scientist-in-the-Loop (SITL). A scientist (the SITL) makes the selection of the burst data based on viewing the survey data and data quality values. The SITL scientists check that the chosen burst-mode intervals are the best and they can change the burst data downlink priorities if needed. Data selection is operated by numerous scientists around the world who take part in the mission, including several researchers at IRAP.

## 2.4. INSTRUMENT DESCRIPTIONS

### 2.4.1. HOT PLASMA SUITE

The hot plasma suite of instruments includes: the Fast Plasma Investigation (FPI) comprised of Dual Ion Spectrometer (DIS) and Dual Electron Spectrometer (DES) and the Hot



Plasma Composition Analyzer (HPCA).

#### FAST PLASMA INVESTIGATION (FPI)

The Fast Plasma Investigation observes the fast-moving plasma. It is dedicated to ensure 3D measurements of the phase space distributions of **electrons** and positively charged **ions** at **30 and 150 ms**, respectively. For this purpose, several high speed sensors were distributed around the spacecraft parameter so that full azimuthal sampling need does not depend on the spacecraft spin as has been common in previous magnetospheric missions.

#### Dual Ion Sensors (DIS) and Dual Electron Sensors (DES)

The high resolution is accomplished by the use of eight top hat spectrometers for each species (electrons and ions), packaged in pairs as "dual spectrometer" on each spacecraft. The four dual spectrometers of each species are placed at 90° angles around the perimeter of the spacecraft. Each group of four dual spectrometers includes four high voltage power supplies for energy and angle selection. DES and DIS cover an energy range of **10 eV to 30 keV**.

The dual ion spectrometers were built by Meisei Electric in Gunma, Japan, under the direction of the Institute of Space and Aeronautical Sciences which is a part of the Japanese Aerospace Exploration Agency. The DIS MicroChannel Plates (MCPs) were procured and tested by the Institut de Recherche en Astrophysique et Planetologie (IRAP) before being delivered to Meisei for integration into the DIS sensors. The angles in the context of the spacecraft geometry are defined as:

- The polar angle  $\theta$ : ranges between 0 and 180° and opens from the spacecraft spin axis (+Z).
- The azimuth angle  $\phi$ : ranges between 0 and 360° and opens from the +X axis with a positive right hand rotation about the spacecraft axis.

The DES and DIS are similar in design. Each sensor consists of two deflectors, an electrostatic analyzer and a Multi-channel plate detector with an anode ring underneath. The deflectors change the path of particles based on their energy before they reach the electrostatic analyzer. Energy/charge sampling is provided by electrostatic energy/charge sweeping over a selection in the range 10 eV/q to 30000 eV/q.

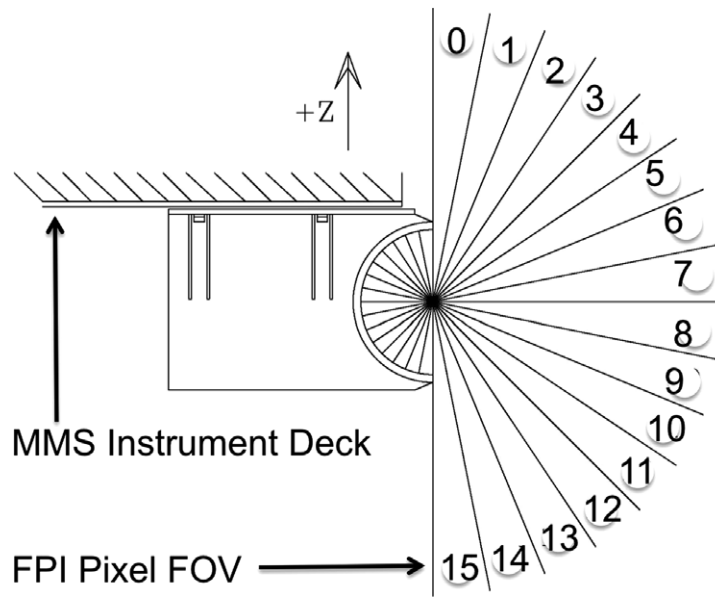


Figure 2.5 – Polar angle FOV configuration of each top hat plasma spectrometer. The spacecraft +Z axis is also indicated. Figure from [Pollock et al. \(2016\)](#).

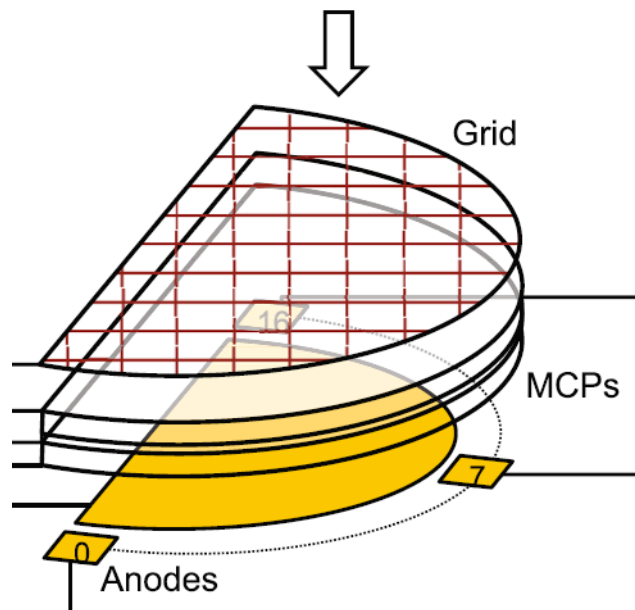


Figure 2.6 – DES detection system. Figure from [Pollock et al. \(2016\)](#)

Each sensor is mounted so that the 16 pixels of its 180° Field Of View (FOV), each nominally 11.25° wide, spans from spacecraft spin axis to anti-spin axis. The pole-to-pole pixel array and the distribution of eight spectrometers around the spacecraft azimuth provide simultaneous sampling in these (polar and azimuthal) orthogonal angular dimensions (Figure 2.5). Together, the eight spectrometers for each species provide eight Fields of view (FOVs)

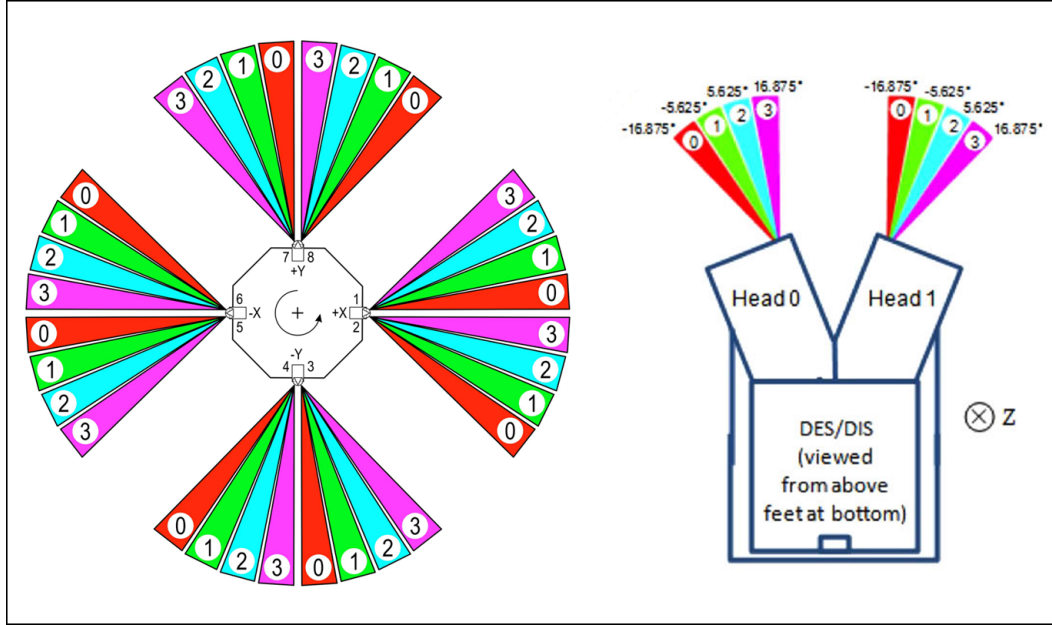


Figure 2.7 – (Left) Azimuthal FOV configuration of the eight spectrometers for each species. Each spectrometer, exercising four deflected fields of view, yields 32 azimuth samples for each species. (Right) The azimuth zones for each DES (DIS). Figure from Pollock et al. (2016)

around the space azimuth, i.e. in the spin plane, providing  $45^\circ$  sampling of the plasma velocity phase space. Coverage of the full sky is accomplished by stepping the field of view of each of the eight sensors through four deflection look directions as illustrated in Figure 2.7. The field of view deflection is incorporated so that the center of each spectrometer may be deflected in spacecraft azimuth by up to  $\pm 16.875^\circ$  (Figure 2.7). This is accomplished by applying positive voltage to curved electrodes located just inside of the sensor entrance apertures. The deflection electrodes steer incoming particles from selected azimuth directions toward the top hat aperture.

To meet temporal requirements, each of the eight ion and electron spectrometers samples four azimuths, providing a total of 32 azimuthal samples separated by  $11.25^\circ$  for each species (Figure 2.7). Nominally identical fields of view are provided for electrons and for ions.

Each of the two sensors in a DES or a DIS has its own detector system, comprised of entrance shield grids, the MCP stack assembly, and 16 discrete anodes, each serviced by a charge sensitive pre-amplifier-discriminator (Figure 2.6). Detector system components are mounted on an anode board. Plasma particles passed by the ESA enter the detector assembly through the grid above the MCP stack. The incoming particles with certain speeds and

directions are allowed to pass through a filter to a sensor plate. Few millions of electrons come out from the exit side of the sensor each time the sensor is hit by an incoming particle and the instrument detects the event. FPI separately measures electrons and ions and can count the number of each kind of particles entering the instrument from a range of directions at different energies during any given time span.

### HOT PLASMA COMPOSITION ANALYZER (HPCA)

Since the physical processes in the ion diffusion region depend on ion mass, a Hot Plasma Composition Analyser (HPCA) is included on-board MMS spacecraft [Young et al. (2016)]. HPCA help observing what ions are present during any given event and therefore helps scientists to determine which kind of plasma was involved, and assess the effects of particles of different charge and mass. HPCA identifies ions that are part of the solar wind such as helium ( $He^{++}$ ) from those that are present in the terrestrial plasma including Helium ( $He^+$ ) and oxygen ( $O^+$ ) and provides measurements of ion fluxes between  $\sim 1$  eV and 40 keV. The instrument relies on the spin of the spacecraft to view a sweep of the sky, gathering a set of observations every **10 seconds**, the equivalent of half of the spacecraft's spin.

HPCA couples a toroidal electrostatic energy analyzer with a carbon-foil based time-of-flight analyzer (Figure 2.8). Incoming ions enter the two concentric toroids with the inner toroid having an adjustable voltage applied to match the energy of the entering ion. A particular voltage determines the energy and arrival angles of incoming ions. When entering the Time of Flight section of the instrument, ions are accelerated. Secondary electrons are generated when an ion passes through an ultra-thin carbon foil. These electrons are accelerated to a specific energy in an applied electric field and are detected in a dedicated position on the Multichannel plate detector. When the electrons are detected, a start signal is transmitted and when the ion hits a stop detector, a stop pulse is generated to determine Time of Flight of the individual ions. This results in measured times of flight which, together with the energy measurement, can be used to determine the mass and with that to identify the ion through  $E = 0.5mv^2$ . Ion flux is determined by counting the numbers of particular ions arriving per second.

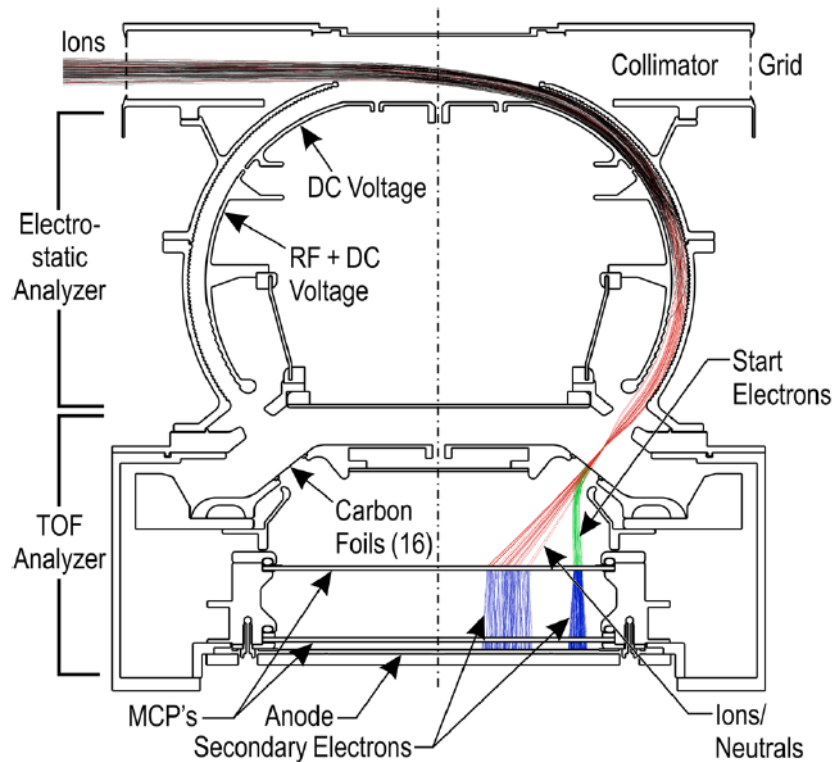


Figure 2.8 – Schematic drawing of the HPCA sensor together with characteristic ion and electron trajectories. Figure from [Young et al. \(2016\)](#).

#### 2.4.2. ENERGETIC PARTICLES DETECTOR SUITE

The EPD [[Mauk et al. \(2016\)](#)] suite detects electrons and ions with energies far exceeding those detectable by FPI and HPCA. Together, the three sets of instruments are necessary to observe the full range of charged particles associated with magnetic reconnection. EPD also remotely senses the structure of the larger space environment surrounding reconnection sites by observing particles coming in from far away. EPD also observes very fast electrons. These high-speed particles are observed through two instruments: the Fly's Eye Energetic Particle Sensor (two per spacecraft) and the Energetic Ion Spectrometer (one per MMS spacecraft).

With two FEEPS and one EIS Instrument, a complete sky coverage is achieved every seven seconds.

#### FLY'S EYE ENERGETIC PARTICLE SENSOR (FEEPS)

FEEPS [[Blake et al. \(2016\)](#)] provides nearly instantaneous all-sky measurements of differential flux of electrons from different streaming directions. FEEPS uses silicon detectors that

absorb the energy of incoming particles which creates a current pulse which can be measured to determine the energy of the particle. With two FEEPS instruments mounted on two opposite sides of the instrument deck of the MMS spacecraft, the instrument achieves a nearly complete view of the sky. FEEPS includes two sets of sensors, one for electrons and one for ions and delivers images of high-energy electrons from **25 keV to over 0.5 MeV** in addition to total ion energy distribution from **45 keV to 0.5 MeV**. In burst mode, the distributions are measured with a time resolution of a time per sector of **0.3125 seconds** in burst mode.

### ENERGETIC ION SPECTROMETER (EIS)

The Energetic Ion Spectrometer [Mauk et al. (2016)] gathers all-sky measurements of the energetic ions, gathering information about their energy, their arrival direction and their mass. EIS determine the mass of ions by measuring their velocity and total energy. The mass information helps determine the fluxes of protons, helium and oxygen ions are present at energies above those reachable by HPCA.

EIS measures the energy of energetic ions from **20 keV for ions and 45 keV for protons up to over 0.5 MeV for oxygen ions** with a resolution of **0.5 s** in burst mode.

### 2.4.3. FIELDS SUITE

The FIELDS suite were designed to determine boundary orientation and motion and detect plasma waves. The field instrument suite provides measurements of the full vector magnetic and electric fields. It consists of six sensors on each spacecraft. The field magnetic sensors consist of two independently designed triaxial fluxgate magnetometers (AFG and DFG), a search coil magnetometer (SCM), and an Electron Drift Instrument (EDI) that measures the in-situ electric and magnetic fields. The fields three-axis electric measurements are provided by two sets of double-probe sensors (SDP and ADP). The calibration and cross-calibration procedures result in errors less than 0.1 nT in **B** and 0.5 mV/m in **E**. Fields suite can gather information more than 1000 times per second.

## ANALOG FLUXGATE MAGNETOMETER (AFG) AND DIGITAL FLUXGATE MAGNETOMETER (DFG)

The use of two independently designed magnetometers aims to avoid single point failures given the high priority of obtaining measurements of the magnetic field vector and field intensities [Russell et al. (2016)]. The overall principle of the two fluxgate sensors is identical. They carry a permeable material that changes properties in response to the presence of magnetic fields. Measuring how they change can be correlated to strength of the field. The ferromagnetic material is surrounded by two coils of wire. One coil runs an alternating electrical current which drives the core through an alternating cycle of magnetic saturation. This changing field induces a current in the second coil which can be measured by a detector. AFG and DFG provide two sets of similar measurements over the frequency range from **DC to 64 Hz**.

## SEARCH COIL MAGNETOMETER (SCM)

The Search Coil Magnetometer SCM [Le Contel et al. (2016)] was designed and built at the Laboratory of Plasma Physics (LPP). SCM measures the three components of the magnetic fluctuations from **1Hz to 6kHz** which includes kinetic Alfvén waves, whistler mode waves and solitary waves.

The SCM instrument consists of three sensors that are mounted in a triaxial configuration to be able to measure magnetic field properties along all three axes. The sensors are precisely aligned with respect to the satellite axis. Each magnetic search coil consists of a fine copper wire wrapped over ten thousand times around a ferrite-metal ferromagnetic core. The copper winding collects the voltage ( $e$ ) induced by the time variation in the ambient magnetic flux:

$$e = -Nd\phi/dt \quad (2.1)$$

where  $\phi$  is the magnetic flux throughout one coil and  $N$  is the number of coils. This voltage can then be used to measure the magnetic field changes.

## SPIN-PLANE DOUBLE PROBE (SDP) AND AXIAL DOUBLE PROBE (ADP)

Two sets of double-probe instruments are implemented on each MMS spacecraft. They determine the electric field by measuring the voltage between two electrodes. The SDP [Lindqvist et al. (2016a)] consists of four wire booms with spherical sensors at the end. SDP measures the electric field in the spin plane by sensing the potential difference between the

four spherical ball electrodes mounted at a spacing of 90°.

The ADP [Ergun et al. (2016)] is aligned through the center of each spacecraft, along its spin axis. It is made of two antennas providing accurate measurements while each spacecraft spins around. The cross-calibrated vector electric field measurements are produced from **DC to 100 kHz**, well beyond the upper hybrid frequencies.

#### 2.4.4. ELECTRON DRIFT INSTRUMENT (EDI)

The electron drift instrument [Torbert et al. (2016)] provides high time resolution ( $\sim 1$  ms) electron flux measurements at few energies near 1 keV. EDI also measures the electric and magnetic fields quite differently from the sensors above. These measurements are provided using the drift of two weak electron beams in nearly opposite directions. In the presence of a homogeneous magnetic field, charged particles perform a circular motion with gyroperiod, superimposed with a constant drift velocity  $V_d$  as discussed in Chapter 1. Each of the emitted beams drifts in the  $\mathbf{E} \times \mathbf{B}$  direction. Electrons are then focused into the detector after one or more gyroperiods.

#### 2.4.5. TWO ACTIVE SPACECRAFT POTENTIAL CONTROL DEVICES (ASPOC)

In sunlight, the spacecraft continuously emit photoelectrons. These photoelectrons positively charge the spacecraft up to several tens of volts. This voltage interferes with the electric field measurements and with the low-energy plasma measurements as well. In order to neutralize the photoelectron current, MMS uses an Active Spacecraft Potential Control device which emits indium ions. As result, the positive spacecraft potential does not exceed **4 volts** [Torkar et al. (2016)]. The ion generators are liquid metal ion sources that consist of a needle covered with indium and heated above the melting point of the metal. Indium atoms are ionized and accelerated outward by an electric field created by applying a sufficiently high electric potential between two electrodes. Two ASPOC devices are installed on each MMS spacecraft.



## 2.5. DATA ANALYSIS TECHNIQUES

### 2.5.1. MAGNETOPAUSE MODEL

It is often useful to be able to anticipate or to have an idea of the magnetopause location and local geometry. In this aim, several empirical models have been developed based on statistical analyses of the magnetopause crossings recorded by the past missions. One of the most used models to describe the magnetopause location and shape is the model proposed by Shue et al. (1997). In this model, the magnetopause is described as a paraboloid parametrized by the  $B_z$  component of the interplanetary magnetic field and the solar wind dynamic pressure  $D_p$ . The functional form of Shue model is given by:

$$r = r_0 \left( \frac{1}{1 + \cos\theta} \right)^\alpha \quad (2.2)$$

$r_0$  is the standoff distance, i.e. the distance at which balance is achieved between the solar wind dynamic pressure and Earth's dipole magnetic field pressure at the subsolar point.  $r$  is the radial distance,  $\theta$  is the solar zenith angle between the Sun-Earth line and the direction carrying  $r$  and  $\alpha$  is the flaring level of the magnetopause. The functional form proposed by Shue et al. (1997) has two parameters  $r_0$  and  $\alpha$  that depend on the IMF  $B_z$  and the solar wind dynamic pressure  $D_p$  as follow:

$$r_0 = \begin{cases} (11.4 + 0.013B_z)(D_p)^{-\frac{1}{6.6}} & , \text{ for } B_z \geq 0 \\ (11.4 + 0.14B_z)(D_p)^{-\frac{1}{6.6}} & , \text{ for } B_z < 0 \end{cases}$$
$$\alpha = (0.58 - 0.01B_z)(1 + 0.01D_p) \quad (2.3)$$

This model is valid for:

- $-18 < B_z < 15 nT$
- $0.5 < D_p < 8.5 nPa$

This model is a simple model which is roughly accurate for most ranges of  $B_z$  and  $D_p$ . It can also be used to calculate the distance from a spacecraft to the magnetopause and the normal direction to the magnetopause. However, when both  $B_z$  and  $D_p$  are extremely large, the Shue et al. (1998) model can be used instead of the Shue et al. (1997) model which is

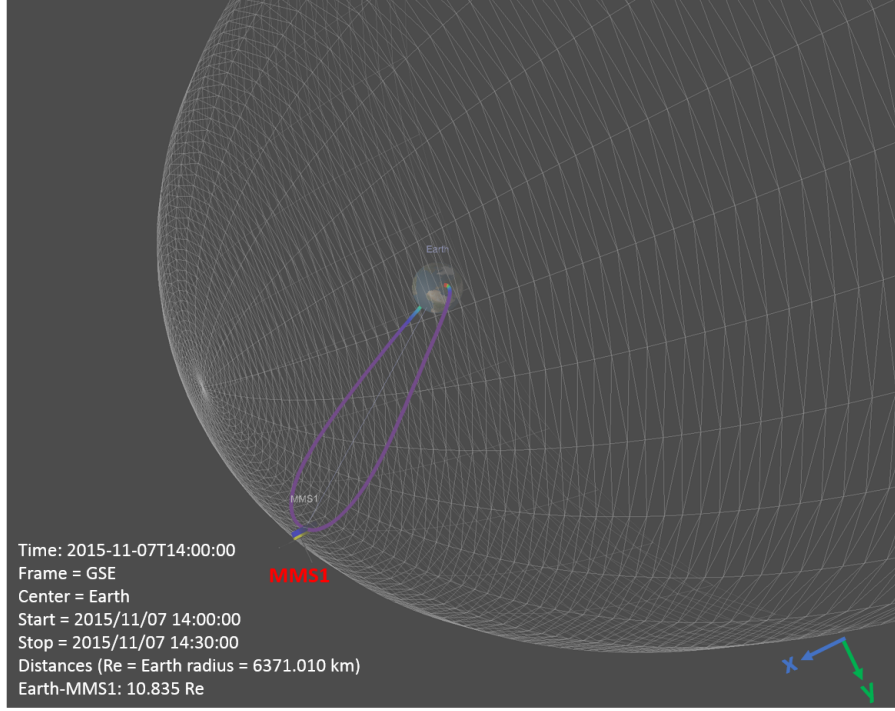


Figure 2.9 – Magnetopause location and shape on 7 November 2015 using Shue model.

inaccurate in such cases. Figure 2.9 shows the location and shape of the magnetopause on 7 November 2015 using Shue model. The values of  $B_z$  and  $D_p$  were obtained from OMNI data. The figure has been generated using 3DView application [Génot et al. (2018)] available on <http://3dview.cdpp.eu>.

### Boundary normal coordinates

To analyze magnetopause dynamics it is convenient to use a coordinate system (LMN) related to the local geometry of the magnetopause as illustrated in Figure 2.10.

A common method to infer the coordinate system is the variance analysis as will be discussed later in this Chapter. The magnetic field in the normal direction is supposed to be constant and gives the direction of the vectors of the LMN coordinates. Another method to predict the LMN vectors is to calculate the magnetopause normal in GSM coordinates using Shue model [e.g. Shue et al. (1997)] as also discussed in the next chapter. When the direction of  $\mathbf{N}$  is determined, we can then, conventionally, determine the direction of  $\mathbf{M}$  as:

$$\mathbf{M} = \frac{\mathbf{N} \times \mathbf{Z}_{GSM}}{|\mathbf{N} \times \mathbf{Z}_{GSM}|} \quad (2.4)$$

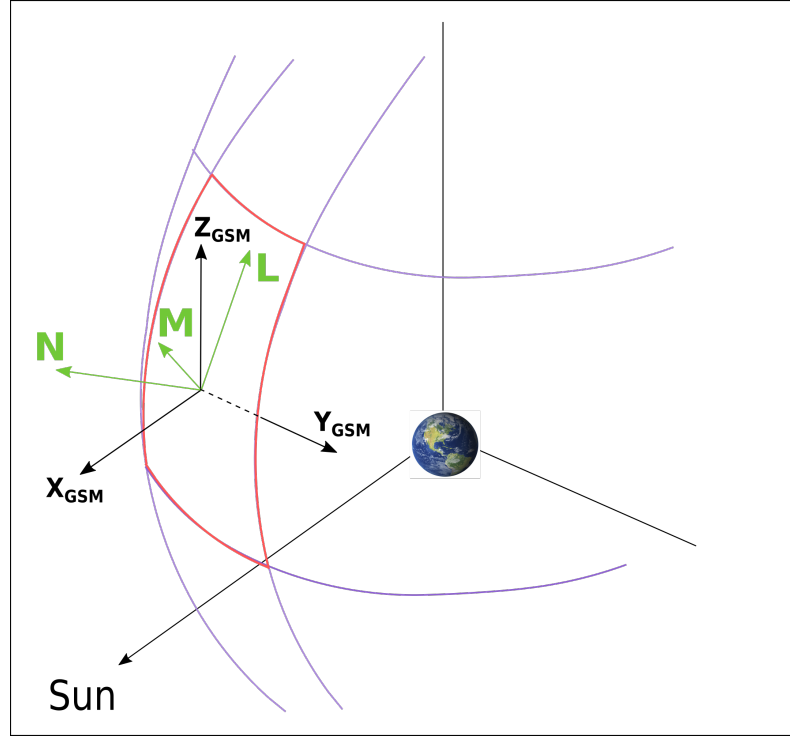


Figure 2.10 – Boundary coordinate system.  $N$  points outward to the local magnetopause,  $L$  is the projection of the Earth's magnetic dipole field and the  $M$  completes the right-handed set, pointing dawnward ( $M = N \times L$ ).

where  $Z_{GSM}$  is the north-south component in the GSM system.

Finally,  $L$ , can be defined as:

$$L = M \times N \quad (2.5)$$

### 2.5.2. MAGNETOPAUSE TRANSITION PARAMETER

Spacecraft observations at the magnetopause are usually complicated because of the boundary motions that add ambiguity to the observations. The magnetopause transition parameter, used for the observation of magnetopause boundary layer, helps reordering the time series data from magnetosheath to magnetosphere by providing information of the effect of boundary motions and of the location of the spacecraft relative to the boundary layer. This parameter was defined by [Hapgood and Bryant \(1990\)](#) based on the observations of [Bryant and Riggs \(1989\)](#) who reported that the electrons in the low latitude boundary layer exhibit an anti-correlated relationship between their density and mean energy.

The magnetopause transition parameter,  $\tau$ , can be calculated by fitting in logarithmic scales the distribution of the electron density against perpendicular electron temperature [[Lockwood and Hapgood \(1997\)](#)]. The curve is empirical, generally represented by a polynomial

$\tau$	Region
$\tau < 20$	Magnetosheath
$95 < \tau < 100$	Magnetosphere

Table 2.2 – The suggested values of  $\tau$  for the magnetosheath, the outer boundary layer, the inner boundary layer and the magnetosphere.

or exponential law.  $\tau$  is calculated by projecting each data point onto the nearest point of the best-fit curve and measuring the length along the curve to each projection. These values are then normalized to extreme values on the curve:

1. 0 equating to the coolest/densest part of the magnetosheath
2. 100 the hottest/rarest point observed in the magnetosphere

The transition parameter can be calculated as:

$$\tau = 100 \frac{x - x_{min}}{x_{max} - x_{min}} \quad (2.6)$$

where  $x_{min}$  is the projected point from an arbitrary point beyond the magnetosheath end of the curve and  $x_{max}$  from the magnetospheric end.

Figure 2.11 demonstrates the calculation of  $\tau$  by fitting a curve over a scatter plot of electron density versus perpendicular temperature in logarithmic scales. After choosing the best fit, which is a fourth order polynomial curve in this case, we can then calculate  $\tau$  as described above and as illustrated in 2.11. Table 2.2 summarizes the suggested values of  $\tau$  for the magnetosheath and the magnetosphere as they have been reported by previous studies [e.g. Lockwood and Hapgood (1997); Bogdanova et al. (2008)]. In the boundary layer,  $\tau$  has values which are greater than 20 but less than 95.

### 2.5.3. CURLOMETER TECHNIQUE

The curlometer technique is a multipoint technique that consists of direct estimation of the current density using spatial gradients of the magnetic field [Dunlop et al. (1988, 2002)]. It has been developed in the context of multi-spacecraft missions and for Cluster initially. The method is based on Ampere's law, which assuming stationarity in the studied medium,

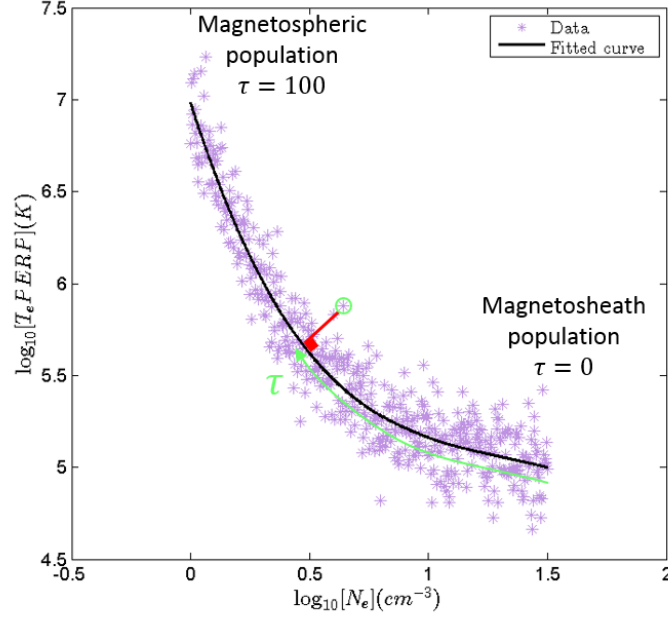


Figure 2.11 – A scatter plot of the perpendicular electron temperature against the electron density. A fourth order polynomial curve was fitted to the points. The  $\tau$  parameter for each particular point is obtained by projecting it into the nearest point of the fitting curve as shown by the red line. Then, we evaluate the length of the curve between its beginning and the projected point as illustrated by the green curve.

can be written as:  $\mu_0 \mathbf{J} = \nabla \times \mathbf{B}$ . The Ampere's law is evaluated at the barycenter of a perfect tetrahedron formed by four spacecraft. The current density is estimated in the direction perpendicular to each face of the tetrahedron as illustrated in Figure 2.12. Assuming the current density is a constant in the whole surface and that the magnetic field changes very slowly, the current density  $\mathbf{J}_{ijk}$  normal to the face delimited by spacecraft  $i, j, k$ , can be estimated via the integral form of Ampère's law as [Dunlop et al. (1988)]:

$$\mu_0 \mathbf{J}_{ijk} \cdot (\Delta \mathbf{r}_{ik} \times \Delta \mathbf{r}_{jk}) = \Delta \mathbf{B}_{ik} \cdot \Delta \mathbf{r}_{jk} - \Delta \mathbf{B}_{jk} \cdot \Delta \mathbf{r}_{ik} \quad (2.7)$$

where the magnetic field data and position data are in cartesian coordinates and where  $i, j, k$  are indices running over the satellites.  $\Delta \mathbf{B}_{ik} = \mathbf{B}_i - \mathbf{B}_k$  and  $\Delta \mathbf{r}_{ik} = \mathbf{r}_i - \mathbf{r}_k$  are the magnetic field and position difference between spacecraft  $i$  and  $k$ , respectively.

Using equation 2.7, we can calculate  $\mathbf{J}_{123}$ ,  $\mathbf{J}_{124}$ ,  $\mathbf{J}_{134}$  and  $\mathbf{J}_{234}$  through each face of the tetrahedron. The total average current density in the tetrahedron,  $\mathbf{J}_{curl}$ , can be derived by projecting each current vector normal to three faces into Cartesian coordinates.

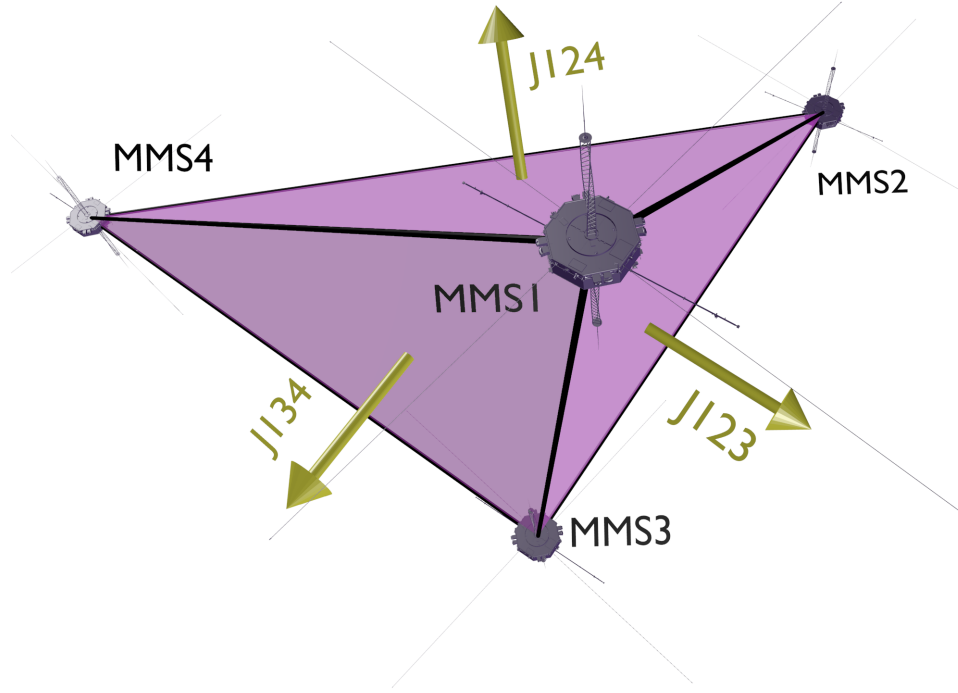


Figure 2.12 – Illustration of the average current density estimation using the curlometer technique

The curlometer technique permits a good estimation of the current density when the spatial-scale variations of the magnetic field are much larger than the spacecraft separation. MMS provided for the first time an estimation of the current density using particle data. The current density can be calculated as  $en(\mathbf{V}_i - \mathbf{V}_e)$  where  $n$  is the density,  $\mathbf{V}_i$  and  $\mathbf{V}_e$  are the ion and electron velocities.

#### 2.5.4. VARIANCE ANALYSIS: CURRENT DENSITY MEASUREMENTS

In order to investigate one dimensional plasma structures such as current sheets or two dimensional structures such as magnetic islands, it is often useful to transform them into a proper reference frame related to their geometry. Often, it is also necessary to establish the orientation of the structures. Variance analysis have proven to be very robust and useful for this purpose. For example, the variance analysis (VA) technique is frequently used to determine the normal direction of the magnetopause: it is applied to the magnetic field data recorded during a magnetopause crossing, and provides the direction along which the magnetic field variation is minimum [Kawano and Higuchi (1996)]. When applied to the magnetic field data during the magnetopause crossings, the VA method assumes the

magnetopause to be thin (one-dimensional:  $\partial/\partial x = 0$  and  $\partial/\partial y = 0$ ) and unchanging in time, i.e.  $\partial \mathbf{B}/\partial t = 0$ , so that only one of the three terms remains in the cartesian expression for the divergence of B. Then, from Maxwell's Law for the magnetic field, we can write:

$$\nabla \cdot \mathbf{B} = \partial B_z / \partial z = 0 \quad (2.8)$$

$(x, y, z)$  is a local cartesian coordinate system with  $z$  axis is pointing along the normal  $\mathbf{n}$  to the magnetopause. Equation 2.8 means that the magnetic field component normal to the magnetopause,  $\mathbf{B}_n$ , is required to be constant across the magnetopause. Therefore, the direction with an approximately constant magnetic field corresponds to the direction normal to the magnetopause.

The variance analysis consists of the diagonalization of the co-variance matrix defined in terms of the measured data and the Cartesian coordinate system in which the measured data are represented [Dunlop et al. (1995)], and then finding the three eigenvalues  $\lambda_i$ , and corresponding eigenvectors  $\mathbf{x}_i$  of the matrix. For example, considering now a serie of  $N$  magnetic field vector measurements,  $\mathbf{B}^{(i)}$  ( $i = 1, 2, 3 \dots N$ ), the magnetic field variance matrix is given by:

$$M_{\mu\nu}^B \equiv \frac{1}{N} \sum_{i=1}^N B_{\mu}^{(i)} B_{\nu}^{(i)} - \left[ \frac{1}{N} \sum_{i=1}^N B_{\mu}^{(i)} \right] \left[ \frac{1}{N} \sum_{i=1}^N B_{\nu}^{(i)} \right] \quad (2.9)$$

or, in a more impact form, it is given by:

$$M_{\mu\nu}^B \equiv \langle \mathbf{B}_{\mu} \mathbf{B}_{\nu} \rangle - \langle \mathbf{B}_{\mu} \rangle \langle \mathbf{B}_{\nu} \rangle \quad (2.10)$$

where  $\mu, \nu = 1, 2, 3$  denote the Cartesian components along the  $(x, y, z)$  system and  $\langle \rangle$  indicates the time average of the respective quantity. Since  $M_{\mu\nu}^B$  is symmetric, the eigenvalues are all real and the corresponding eigenvectors are orthogonal. Provided the variance matrix is not near degeneracy, the eigenvectors ( $\mathbf{x}_1$ ,  $\mathbf{x}_2$  and  $\mathbf{x}_3$ ) correspond to the directions of minimum, intermediate and maximum variance of the time series of vector measurements. The minimum (maximum) variance direction is given by the eigenvector with minimum (maximum) eigenvalue. Obviously, the results of the variance analysis when applied to time series depend on the considered time interval. A matrix is said to be degenerated when it has two eigenvalues that are equal or close to each other (a ratio of less then  $\sim 3$  or

4).

The variance analysis has been widely used on magnetic field data. However, the variance analysis was also performed on time series of the current density  $J$  by e.g. [Xiao et al. \(2004\)](#); [Haaland et al. \(2004\)](#) based on Cluster measurements. The current variance analysis is useful for the estimation of the orientation of a twisted flux tube and was proven to highly enhance the accuracy of the axial orientation [[Zhou et al. \(2006\)](#)]. The current density measurements calculated by the curlometer technique and from particle data are both provided with high resolution by MMS instruments which yield promising results on the variance analysis results when applied to the current density.

### 2.5.5. MULTI-SPACECRAFT TIMING ANALYSIS: STRUCTURES ORIENTATION AND MOTION

In this section we will discuss the multi-spacecraft timing analysis method that attempts to determine the motion of a discontinuity. This method is also called triangulation method or the time-delay method [[Russell et al. \(1983\)](#); [Harvey \(1998a\)](#)]. We will consider the simplest case where four spacecraft (SC) are flying through a planar discontinuity with constant velocity  $V$  as illustrated in Figure 2.13. The four spacecraft perform delayed detection of the same structure at different locations. The timing method exploits the measured time differences between the passage of the discontinuity over satellites, along with the relative positions between the crossing locations, to infer the normal unit vector  $N$  and the normal velocity  $V$ .

First, the discontinuity passage times  $t_\alpha$  have to be determined. Then, if we take the spacecraft 1 as reference, we can write:

$$\mathbf{R}_{\alpha 1} \cdot \mathbf{N} = V(t_\alpha - t_1) \quad (2.11)$$

where  $2 \leq \alpha \leq 4$ ,  $\mathbf{N} = \mathbf{V}/V$  and  $\mathbf{R}_{\alpha 1}$  is the relative position between the crossing locations of the discontinuity observed by  $SC_\alpha$  and  $SC_1$ . The time delays can be estimated by visually picking up the times at which the boundary crosses each spacecraft. In order to get rid of random errors that may occur when applying the timing method, we can consider several contours of the structure, determine the corresponding normal direction and velocity and



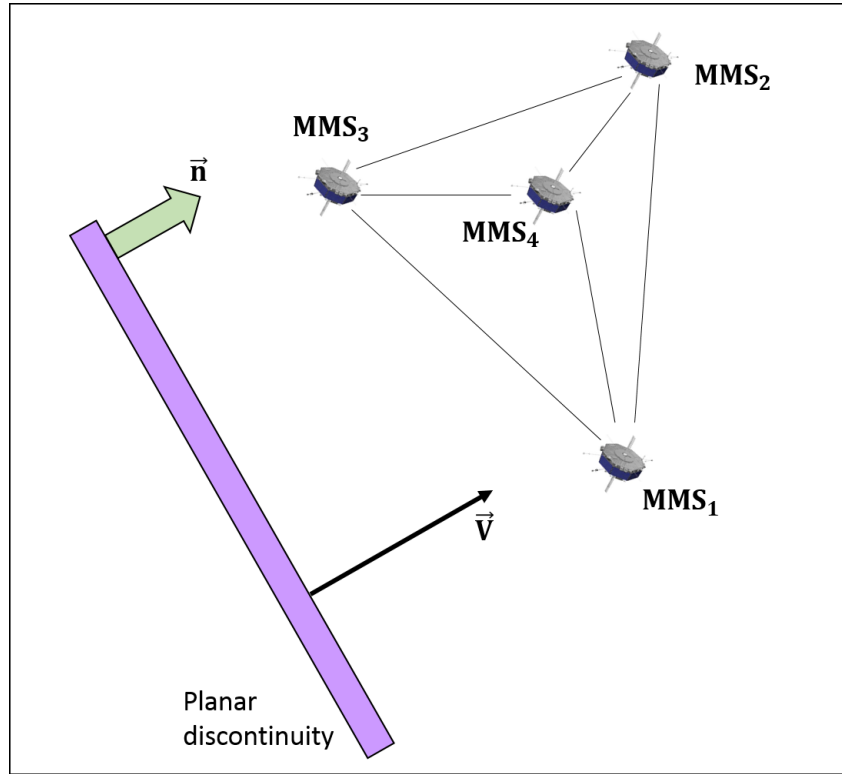


Figure 2.13 – Sketch of a planar discontinuity moving at a constant velocity  $\mathbf{V}$  toward four spacecraft flying in a tetrahedral formation.

then calculate the average normal direction and velocity. These time delays can also be obtained by maximizing the cross-correlation functions between the data streams from different spacecraft [e.g. [Song and Russell \(1999\)](#)]. The measured data of one spacecraft is taken as reference. Then we calculate the cross-correlation between each spacecraft data and the signal of reference. The time delays are determined when the cross-correlation is maximum.

#### 2.5.6. WALÉN TEST

It is usually desirable to study structures such as current sheets, flux ropes or 3-D structures in their co-moving frame. We will now briefly describe the method for finding the so-called de-Hoffmann Teller (HT) frame. We will also present the Walén test which can be used for the purpose of identifying Alfvénic structures from single spacecraft data in the context of magnetic reconnection and interplanetary discontinuities.

The de-Hoffmann Teller frame (HT) is a rest frame in which the convective electric field  $\mathbf{E} = -\mathbf{u} \times \mathbf{B}$  is negligibly small. The velocity of the HT frame can be obtained from exper-

imental data as has been discussed in [Khrabrov and Sonnerup \(1998\)](#). For a time interval with  $N$  measurements of plasma bulk velocity  $\mathbf{u}$  and magnetic field  $\mathbf{B}$ , the electric field for individual measurement  $i$  in the HT frame, where the electric field is as small as possible for the set of measurements, is:

$$\mathbf{E}^{(i)} = -\mathbf{u}^{(i)} \times \mathbf{B}^{(i)} = 0 \quad (2.12)$$

We consider now a frame that moves with a velocity  $\mathbf{V}$ , supposed to be constant, relative to the spacecraft. In this frame, the electric field becomes:

$$\mathbf{E}'^{(i)} = \mathbf{E}^{(i)} + \mathbf{V} \times \mathbf{B}^{(i)} = -(\mathbf{u}^{(i)} - \mathbf{V}) \times \mathbf{B}^{(i)} = 0 \quad (2.13)$$

In order to determine the transformation velocity  $\mathbf{V}$ , the mean square of the electric field,  $D(\mathbf{V})$ , has to be as small as possible for a given set of  $N$  measurements. Therefore,  $D(\mathbf{V})$  has to be minimized:

$$D(\mathbf{V}) = \frac{1}{N} \sum_{i=1}^N \left| \mathbf{E}'^{(i)} \right|^2 = \left| (\mathbf{u}^{(i)} - \mathbf{V}) \times \mathbf{B}^{(i)} \right|^2 \quad (2.14)$$

The minimization of this quantity is obtained by  $\nabla_{\mathbf{V}} D(\mathbf{V}) = 0$  and leads to the determination of the HT velocity  $\mathbf{V}_{HT}$ .

Quality of the HT frame can be assessed by the correlation coefficient  $cc$  between the components of the convection electric field  $\mathbf{E} = -\mathbf{u} \times \mathbf{B}$  and the corresponding values of HT electric field  $\mathbf{E}_{HT} = -\mathbf{V}_{HT} \times \mathbf{B}$  where  $\mathbf{u}$  and  $\mathbf{B}$  are the plasma flow velocity and magnetic field measured in-situ, respectively, and  $\mathbf{V}_{HT}$  is the velocity of the de-HT frame. When the correlation coefficient is  $\sim 1$ , all electric fields are eliminated in the HT frame indicating that the very simple assumptions of the model (constant velocity and planar structure) are fulfilled. The optimal HT speed can be estimated as the one that provides the highest value of the correlation coefficient. An example where a HT frame is well defined with a correlation coefficient of 0.96 is shown in Figure 2.14-(a) indicating a good correlation between the two fields.

After the determination of the HT frame, Walen test can be applied to the observations of fast flows to determine if the flows are Alfvénic. For a rotational discontinuity, the velocity

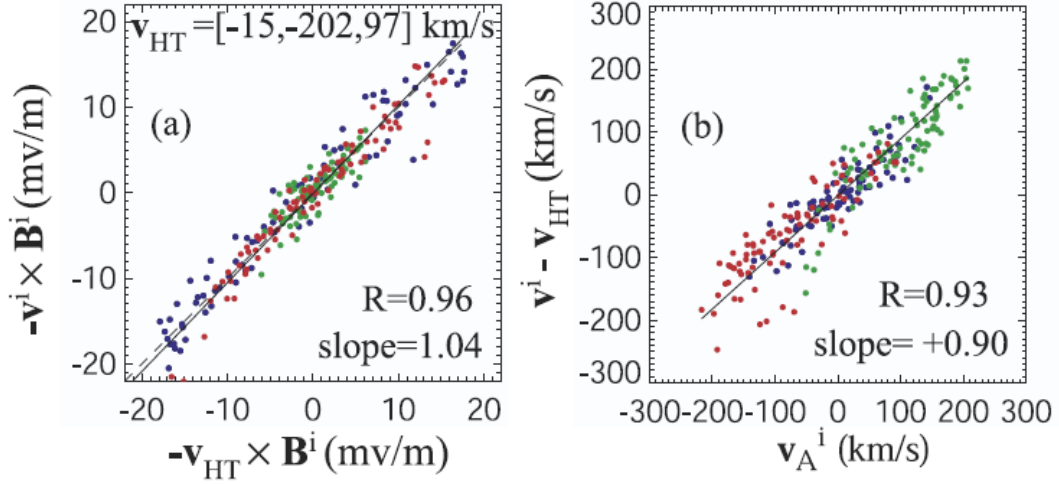


Figure 2.14 – (a) deHoffmann Teller analysis: the convection electric field  $E_c (= -\mathbf{V} \times \mathbf{B})$  vs. the de-HT frame electric field  $E_{HT} (= -\mathbf{V}_{HT} \times \mathbf{B})$  and a linear regression fit, (b) Walén analysis:  $\mathbf{V}'^{(i)}$  vs.  $\mathbf{V}_A^i$  of all three components and a linear regression fit. Blue, green, and red dots denote  $x$ ,  $y$ , and  $z$  components in the GSE frame. Figure from [Phan et al. \(2013\)](#).

changes can be expressed as:

$$\mathbf{u} = \pm \mathbf{V}_A = \pm \frac{\mathbf{B}}{\sqrt{\mu_0 \rho}} \quad (2.15)$$

which is called the Walén relation [[Hudson \(1971\)](#)].  $\mathbf{V}_A^{(i)} = \mathbf{B}^{(i)} (\mu_0 \rho^{(i)})^{-1/2}$  is the local measured Alfvén velocities and  $\rho^{(i)}$  is the measured mass density in the HT frame. The detection of accelerated plasma flows that meet the Walén relation are considered as an evidence for the occurrence of magnetic reconnection at Earth's magnetopause. This is due to the rotational discontinuities generated by magnetic reconnection and bounding the reconnection exhaust. Since across a rotational discontinuity there is a finite mass and magnetic flux flow and the normal components of magnetic field  $B_n$  and velocity  $u_n$  are different from zero and constant across the boundary, the Rankine-Hugoniot (RH) jump conditions predict that the tangential components of the magnetic field  $B_t$  and of the plasma velocity  $u_t$  change across the boundary according to the Walén relation [[Lee et al. \(1996\)](#)]. In this picture, the outflows generated by magnetic reconnection should match the local Alfvén velocity. In the HT frame, the Walén relation can be written as:

$$\mathbf{u}^{(i)} - \mathbf{V}_{HT} = \pm \mathbf{V}_A^{(i)} = \pm \frac{\mathbf{B}^{(i)}}{\sqrt{\mu_0 \rho^{(i)}}} \quad (2.16)$$

for each data point ( $i$ ). The ratio between plasma and Alfvén velocities is a good parameter to qualify the Walén relation. The better the Walén relation is satisfied, the more purely Alfvénic the flows are. The Walén relation is well satisfied when there are well-correlated changes in magnetic field  $\mathbf{B}$  and plasma velocity  $\mathbf{u}$ . When the coefficient of proportionality is close to unity, the Walén test predicts a rotational discontinuity and likely magnetic reconnection. In this case, a scatter plot of the Alfvén velocity versus plasma velocity in HT frame shows a good correlation with a linear regression slope near  $\pm 1$ . Conversely, when the coefficient of proportionality is close to zero, the Walén test predicts that the discontinuity is tangential. Figure 2.14-(b) shows a Walén analysis of the magnetopause. It consists of a component by component scatter plot of the plasma velocities in the HT frame and the local measured Alfvén velocities. The Figure shows that the flow velocity in this frame is 90% of the Alfvén velocity which is in good agreement with the flows being accelerated by magnetic reconnection.

## 2.6. SPECTRAL ANALYSIS

Plasma waves are detected by instruments on-board MMS. To study waves, it is useful to look to the variations of the electric and magnetic fields in the shape of their waveforms. Then, a Fourier analysis allows to get information of which frequencies are dominant in a signal by seeing how much the power is in different frequencies. The Fourier analysis states that a signal can be described as the sum of its components. To calculate the spectrum, we can use the **fast Fourier transform** (FFT). The signal must then be divided into smaller parts and the spectrum for each part has to be calculated. Then, all the individual spectra must be combined to form the spectrogram which allows to see both temporal and spectral information. The spectrogram is a 2-D image with the time on the  $X$  axis and the frequency on  $Y$  Axis. The amplitude of the signal is usually presented in colors. However, a spectral content of a signal does not give all the information about the waves. When we have measurements in more than one dimension, we can look at the polarization of the wave. We can distinguish between electrostatic and electromagnetic waves by using magnetic wave data. We can also calculate the **Poynting flux**, which is the flux of energy in an

electromagnetic wave, as:

$$\mathbf{P} = \frac{\delta \mathbf{E} \times \delta \mathbf{B}}{\mu_0} \quad (2.17)$$

where  $\delta \mathbf{E}$  and  $\delta \mathbf{B}$  are the electric and magnetic fields, respectively. The pointing flux and the group velocity of the wave point in the same direction.

Another polarization parameter is the **Ellipticity** ( $\epsilon$ ) which is defined as the ratio of the minor semi-axis to the major semi-axis of an elliptically rotating field:

$$\epsilon = \frac{B_{minor}}{iB_{major}} \quad (2.18)$$

The value of ellipticity varies between  $-1$  for left-hand circular polarization and  $+1$  for right-hand one. Another simple method for inferring the wave polarization consists of plotting a hodogram of the electric field in the plane transverse to the magnetic field. If the curves rotate right (left) handed around a reference axis, which is typically the ambient magnetic field, the waves are right (left) handed polarized and this corresponds to a positive (negative) ellipticity.

## 2.7. ANALYSIS METHOD FOR LOWER HYBRID DRIFT WAVES (LHDWs)

Lower hybrid drifts waves [Krall and Liewer (1971), Huba et al. (1977)] are commonly observed in space and laboratory at plasma boundaries. The LHDWs are electron scale waves. They are generally associated with electron acceleration [Cairns and McMillan (2005)], strong electric fields and may lead to anomalous diffusion and resistivity [Davidson and Gladd (1975), Silin et al. (2005)]. Lower hybrid drift waves develop at frequencies between the ion and electron gyrofrequencies. Their wavelengths are between the electron and ion thermal gyroradii. Hence, electrons remain magnetized while ions demagnetize from the magnetic field. Norgren et al. (2012) showed that the electrostatic potential of LHDWs and the magnetic field fluctuations are correlated indicating a linear relation between them. The LHDWs are excited through the lower hybrid drift instability (LHDI) [Krall and Liewer (1971)] which is a cross field current driven instability that occurs due to plasma density and magnetic field inhomogeneties. They can be excited when the density gradient scale becomes of the order of the ion gyroradius.

The LHDW properties can be determined using simple spacecraft data. In the next section we will describe the method proposed by [Norgren et al. \(2012\)](#) and [Divin et al. \(2015\)](#) to study LHDW properties. The method allows to analyze plasma waves with frequencies  $f_{ci} \ll f \sim f_{LH} \ll f_{ce}$  where  $2\pi f_{LH} = \omega_{pi} / \sqrt{1 + \omega_{pe}^2 / \omega_{ce}^2}$ . In this method, electrons are assumed to remain magnetized ( $f < f_{ce}$ ) while ions are supposed to be demagnetized ( $f > f_{ci}$ ) from the magnetic field.

In their study they showed a strong correlation between the electrostatic potential associated with the wave and the parallel magnetic field fluctuations. Indeed, that is due to the fact that ions are demagnetized while electrons remain magnetized. Electrons will then carry a current through the electron electric drift  $\delta \mathbf{E} \times \mathbf{B}_0$ . Assuming that ions are stationary, the wave perpendicular current can be written as:

$$\delta \mathbf{j}_\perp = -en_e \frac{\delta \mathbf{E} \times \mathbf{B}_0}{B_0^2} \quad (2.19)$$

Assuming a quasi-electrostatic field, the electrostatic field can be expressed as:

$$\delta \mathbf{E}_\perp = i \mathbf{k}_\perp \delta \phi \quad (2.20)$$

Combining equations 2.19, 2.20 with the Ampère's law  $\nabla \times \mathbf{B} = \mu_0 \delta \mathbf{j}$ , a linear relation between the expected electrostatic potential  $\phi_{\delta B_{||}}$  and the parallel magnetic fluctuations  $\delta B_{||}$  can be derived:

$$\delta \phi_{B_{||}} = \frac{B_0}{n_e e \mu_0} \delta B_{||} \quad (2.21)$$

Moreover, the electrostatic potential associated with the wave can be obtained by integrating the perpendicular electric field, which is the main component of the electric field, along the direction of propagation:

$$\delta \phi_E = \int \delta \mathbf{E}_\perp \cdot \mathbf{v}_{\perp, ph} dt \quad (2.22)$$

where  $\mathbf{v}_{\perp, ph}$  is the perpendicular phase speed.

The propagation direction is determined by cross correlations between the two estimates of the electrostatic potential  $\phi_{\delta B_{||}}$  and  $\phi_{\delta E}$  for different angles of propagation. The amplitude of the propagation velocity is found by fitting the amplitude of the two potentials.

The shape of the potential depends on the propagation direction while its amplitude depends on the propagation velocity. The direction of propagation is determined through cross correlations between the two estimated electrostatic potentials for different angles of propagation in the plane perpendicular to the magnetic field. Then, the amplitude of the velocity is found by fitting the amplitudes of the two estimated electrostatic potentials. The two nearest extremas of the correlation coefficient are used to determine the average frequency of the fluctuations.

## 2.8. WHAMP SIMULATIONS

The dispersion relations of waves in magnetized plasmas can be solved numerically using the WHAMP code: Waves in Hot, Anisotropic, Magnetized Plasmas. The general wave dispersion equation in plasmas is:

$$\mathbf{D}(w, \mathbf{k}) \cdot \mathbf{E}(w, \mathbf{k}) = 0 \quad (2.23)$$

where  $\mathbf{D}(w, \mathbf{k})$  is the dispersion tensor and  $\mathbf{E}(w, \mathbf{k})$  is the wave electric field. As discussed in Chapter 1, the solutions can be found by equating the determinant of the dispersion tensor to zero  $|\mathbf{D}(w, \mathbf{k})| = 0$ . WHAMP solves this equation with a linearized form. WHAMP can include several populations with differing number density, mass, temperature, loss cone, anisotropy and drift parameters for anisotropic Maxwellian distributions [Roennmark (1982)]. The WHAMP interface takes in the plasma parameters and then allows to query the solution point by point in the  $(\mathbf{k}-\omega)$  space. Given an initial  $(k_{\perp}, k_{\parallel})$  point WHAMP tries to find a wave mode close-by and returns the frequency, wave vector and growth rate of the mode among other quantities.

# 3

## MAGNETIC RECONNECTION AT A THIN CURRENT SHEET SEPARATING TWO INTERLACED FLUX TUBES NEAR THE EARTH'S MAGNETOPAUSE

### 3.1. INTRODUCTION

On 7 November 2015 between 13:00 and 15:00 UT, the four MMS spacecraft were moving from the magnetosheath into the magnetosphere through the boundary layer. Around 14:16 UT, the four spacecraft observed a structure that, at first glance, looks consistent with a classic Flux Transfer Event (FTE) in the vicinity of the Earth magnetopause. The four spacecraft were operating in burst mode and were in good tetrahedral configuration, allowing us to use multi spacecraft data analysis methods. Their maximum separation was about 10 *km*.

The event was characterized by a strong peak in the magnetic field and magnetic pressure amplitudes and a bipolar signature on the  $Y_{GSE}$  component of the magnetic field. At the center of the B peak, a strong, thin and localized current structure was observed as



well as an intense ion jet. Solar wind observations showed that the event occurred under low Mach number conditions during the passing of an interplanetary magnetic cloud. In addition, the interplanetary magnetic field components were significantly negative for several hours before the event. Therefore, solar wind conditions were rather unusual. In this Chapter, a comparison of this event and FTEs was performed in the aim of presenting evidences whether the event can be considered as a FTE or not. The analysis showed, based on detailed geometrical considerations as well as on connectivity informations revealed by suprathermal electron properties, that this event is not consistent with a single, homogeneous helicoidal structure as expected for classical FTEs. A phenomenological interpretation was proposed in order to better understand the observations. The substructure of the current sheet and its specific geometry were also described. Then, the high-time-resolution observations of particles were used, along with the high-time-resolution magnetic field data to test for signatures of reconnection at the current sheet. We then discussed if magnetic reconnection could be the process at the origin of the ion jet.

The observations presented in this chapter are mainly from the work published by [Kacem I. et al. \(2018\)](#).

### 3.2. INSTRUMENTATION AND DATA

The magnetopause observations analyzed in this study have been obtained by the MMS spacecraft [[Burch et al. \(2016\)](#)]. We used magnetic field measurements from the fluxgate magnetometers [[Russell et al. \(2016\)](#); [Torbert et al. \(2016\)](#)]. We analyzed ion and electron measurements from the Fast Plasma Instruments [[Pollock et al. \(2016\)](#)]. We also studied current density measurements derived from the curlometer method [[Robert et al. \(1998\)](#); [Dunlop et al. \(2002\)](#)] using magnetic data and by particle measurements as well. At large scale, the event was studied using fast survey mode measurements. The resolutions of the data that were used in this study are shown in Table 3.1. We primarily show data obtained by the MMS1 spacecraft, except when using multi-spacecraft data analysis methods as stated in the text. The  $X$ ,  $Y$  and  $Z$  components of the vectorial quantities in the GSE frame are represented, respectively, in blue, green and red. MMS data visualization and analysis was mainly performed with the CL software.

One minute resolution solar wind conditions are obtained from the OMNI data base [[King](#)

Mode	Instrument	Time resolution
Survey	FGM	62.5 ms
	HPCA	10 s
	FPI	4.5 s
Burst	FGM	128 Hz
	FPI	150 ms for ions and 30 ms for electrons

Table 3.1 – The instruments that were used for this study along with their corresponding resolution in Survey and Burst modes.

and Papitashvili (2005)] which includes solar wind magnetic field and plasma data time-shifted to the Earth’s bow shock nose.

### 3.3. SPACECRAFT LOCATION AND CONFIGURATION

On November 7, 2015, the MMS spacecraft were located in the dusk sector near the magnetopause. The center of mass of the spacecraft tetrahedron was located at  $(8.62, 6.24, -0.89)R_{E_{GSE}}$ . Figures 3.1 and 3.2 show the MMS orbit on November 7, 2015 in the  $XY$  and  $XZ$  planes, respectively. In Figure 3.1, the normal to the magnetopause is represented by a green arrow. The green line shows the mean magnetopause location as computed from Shue et al. (1998) model. This model roughly predicts the location of the magnetopause as a function of the  $B_z$  component of the interplanetary magnetic field and dynamic pressure  $D_p$  of the solar wind which are provided by the OMNI one minute resolution data. According to the spacecraft position (i.e. Figure 3.1), the normal to the magnetopause was expected to be mainly in the  $X_{GSE}$  direction as shown by the green arrow.

The magnetic field lines in Figure 3.2 are derived from the Tsyganenko model [Tsyganenko and Stern (1996)]. On November 7, 2015, the MMS spacecraft formed a relatively proper tetrahedron with a tetrahedron quality factor [Fuselier et al. (2016)] of 0.844 as shown in Figure 3.3. The spacecraft maximum separation was about 10 km. The formation of the spacecraft justifies the use of proper multi-spacecraft methods [Dunlop et al. (1988)] to study small structures that will be introduced in the following sections. Indeed, it has been shown that the use of multi-spacecraft techniques is restricted to scales close to those of the spacecraft separations [e.g. Horbury and Osman (2008)].

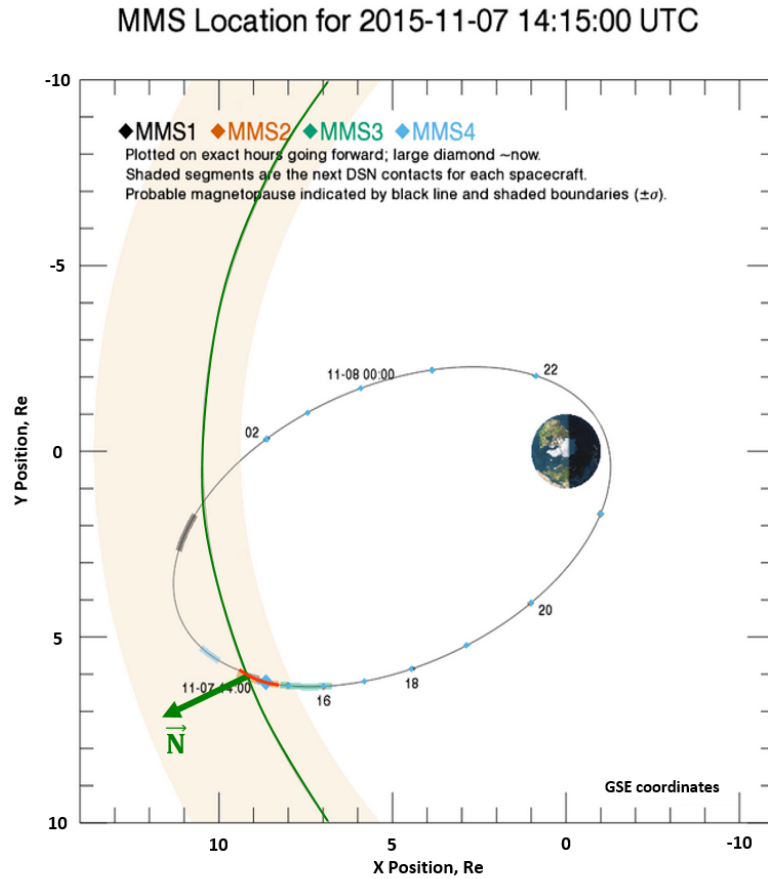


Figure 3.1 – GSE equatorial-plane projection of the MMS orbit on November 7, 2015 and the normal to the magnetopause (green arrow) corresponding to the spacecraft location in the ecliptic plane. The event presented in this study occurred between 14:16:05 and 14:17:20 UT. The red line corresponds to the crossing of a boundary layer. The large blue diamond shows the position at 14:15:00 UT. The probable magnetopause is indicated by green line and shaded boundaries.

### MMS Location for 2015-11-07 14:00:00 UTC

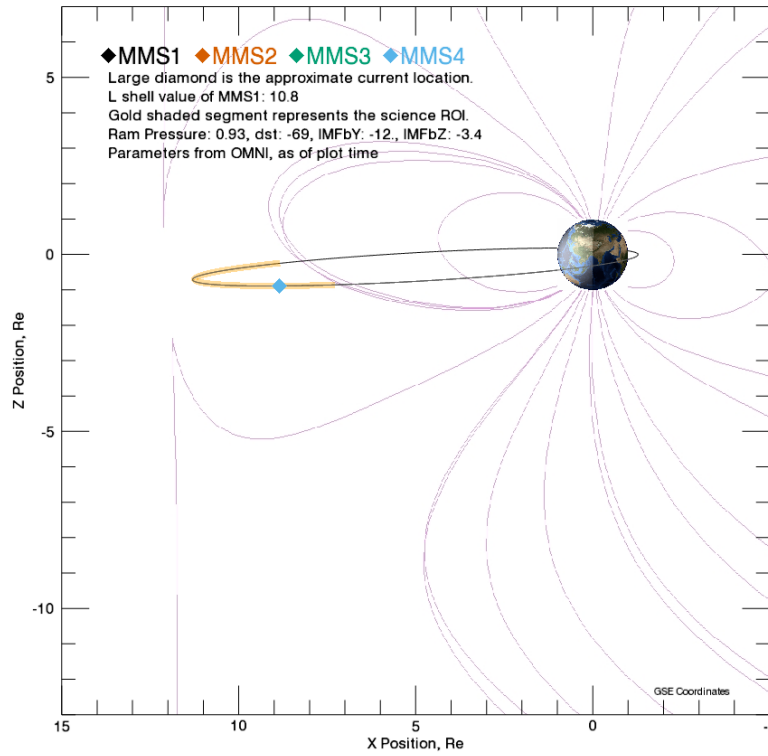


Figure 3.2 – MMS orbit on November 7, 2015 in the XZ plane at 14:00:00 UT. The large diamond is the approximate location of the spacecraft. The magnetic field lines are plotted in purple and are calculated using the Tsyganenko model [Tsyganenko and Stern (1996)].

## 3.4. SOLAR WIND OBSERVATIONS

Figure 3.4 shows 1-min resolution OMNI data over a few days surrounding the event. Panels (a) to (e) show, respectively, the interplanetary magnetic field (IMF), plasma temperature, plasma density, plasma  $\beta$  parameter and disturbance storm time (DST) index. The period of interest, centered around 14:00 UT on 7 November 2015, occurred during the passage of a magnetic cloud at Earth. The magnetic cloud was observed between the afternoon of 6 November 2015 until the afternoon of 8 November 2015 as shown in Figure 3.4. The magnetic cloud was characterized by an enhancement of the field strength with a ratio of  $\sim 3$ , rotation of the magnetic field components, low plasma temperature that varies between 3 and 29 keV and low density that ranged between 1.3 and 5  $cm^{-3}$ , and a low plasma  $\beta$  being between 0.05 and 0.38 which are typical features of magnetic clouds [Burlaga et al.

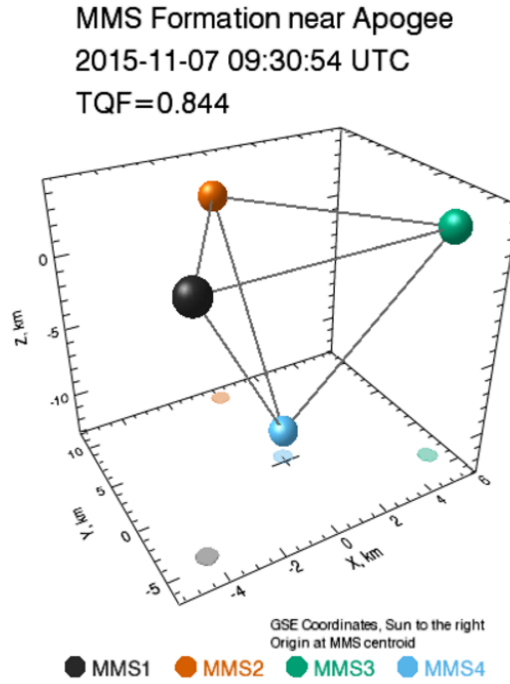


Figure 3.3 – Configuration of the MMS tetrahedron at 09:30:54 UT on November 7, 2015. TQF is the tetrahedron quality factor, which compares the actual tetrahedron to a regular tetrahedron [Fuselier et al. (2016)].

(1981); Lepping et al. (1990)]. Panels (c) to (e) in Figure 3.5 show the magnetic field, dynamic pressure and Alfvén Mach number zoomed in around the time of interest, during the first part of the magnetic cloud when its magnetic field had strong southward and dawnward components. Interplanetary magnetic field components in GSE coordinates are presented in Figure 3.5-a. All IMF components were significantly negative during more than  $\sim 12$  hours, driving a continuously enhanced solar wind-magnetosphere coupling. The solar wind-magnetosphere coupling was thus strongly enhanced during several hours prior to the event. Magnetic reconnection was expected to occur in the southern hemisphere dawn side according to the negative  $B_y$  and  $B_z$  components as suggested by [Trattner et al. (2007)]. Therefore, reconnection sites were expected to be located southward of the spacecraft. For these reasons, we expect the magnetopause to be under extremely disturbed conditions during the event considered in this study. Around 13:22 UT, the dynamic pressure dropped from 2.2 to 0.9 nPa as seen in Figure 3.5-(d). The magnetopause is expected to expand sunward as a response to this variation. The event occurred during a period of both strong driving of the magnetosphere ( $Dst = -69 nT$ ,  $k_p = 4$ ) and low Alfvén Mach number ( $< 3$ ). Under these conditions, solar wind-magnetosphere interaction is expected to

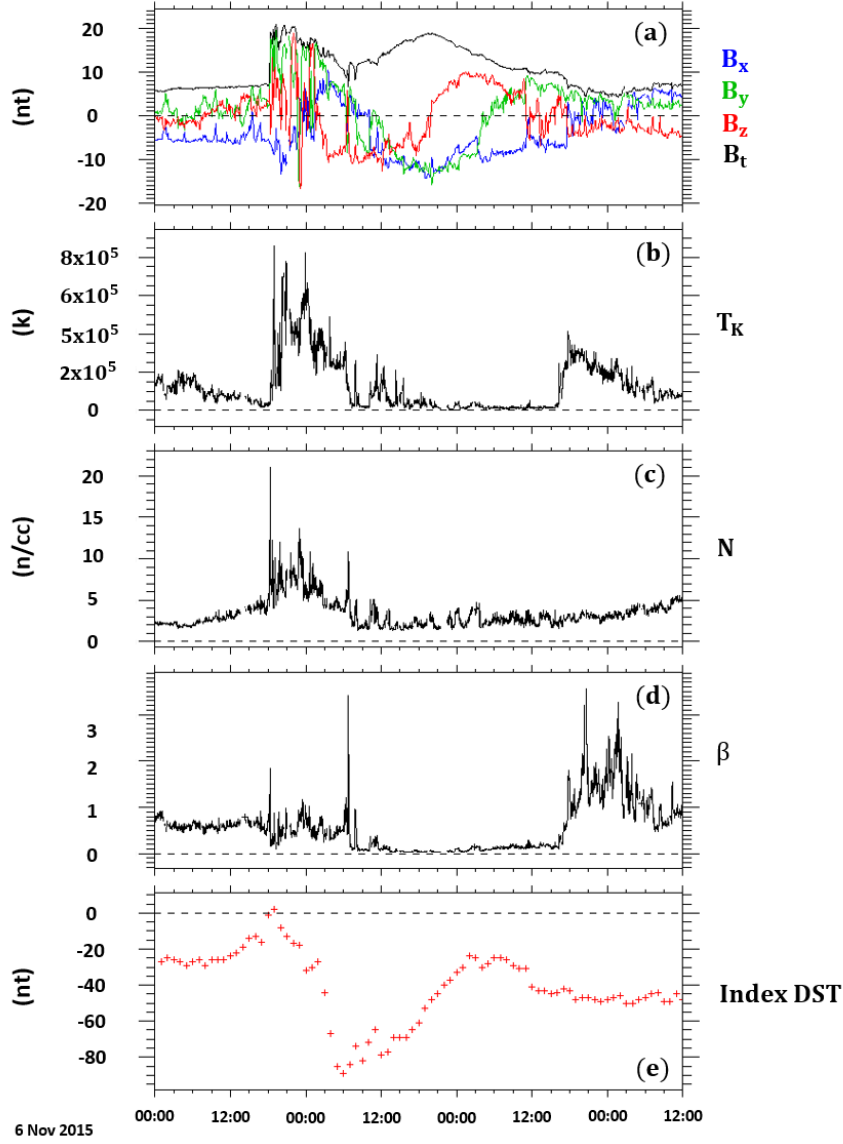


Figure 3.4 – Solar wind conditions from the OMNI 1 minute resolution database from 06 November 2015-00:00 UT through 09 November 2015-12:00 UT. (a) Interplanetary magnetic field components and amplitude in GSE coordinates, (b) plasma temperature, (c) plasma density, (d) plasma  $\beta$  parameter, and (e) disturbance storm time (DST) index.

be altered affecting in particular the flows in the magnetosheath uncommonly enhanced and distributed, the magnetopause shape and magnetic reconnection rate [Lavraud and Borovsky (2008)]. Under low Mach number, the solar wind-magnetosphere interaction become exceptionally different from the typical high Mach number case. Dynamic pressure variations of the solar wind drive large amplitude magnetopause motions, giving rise to a partial compression or relaxation of the magnetosphere [Karlson et al. (1996)].

The features revealed by the OMNI spacecraft were indicative of the large scale conditions

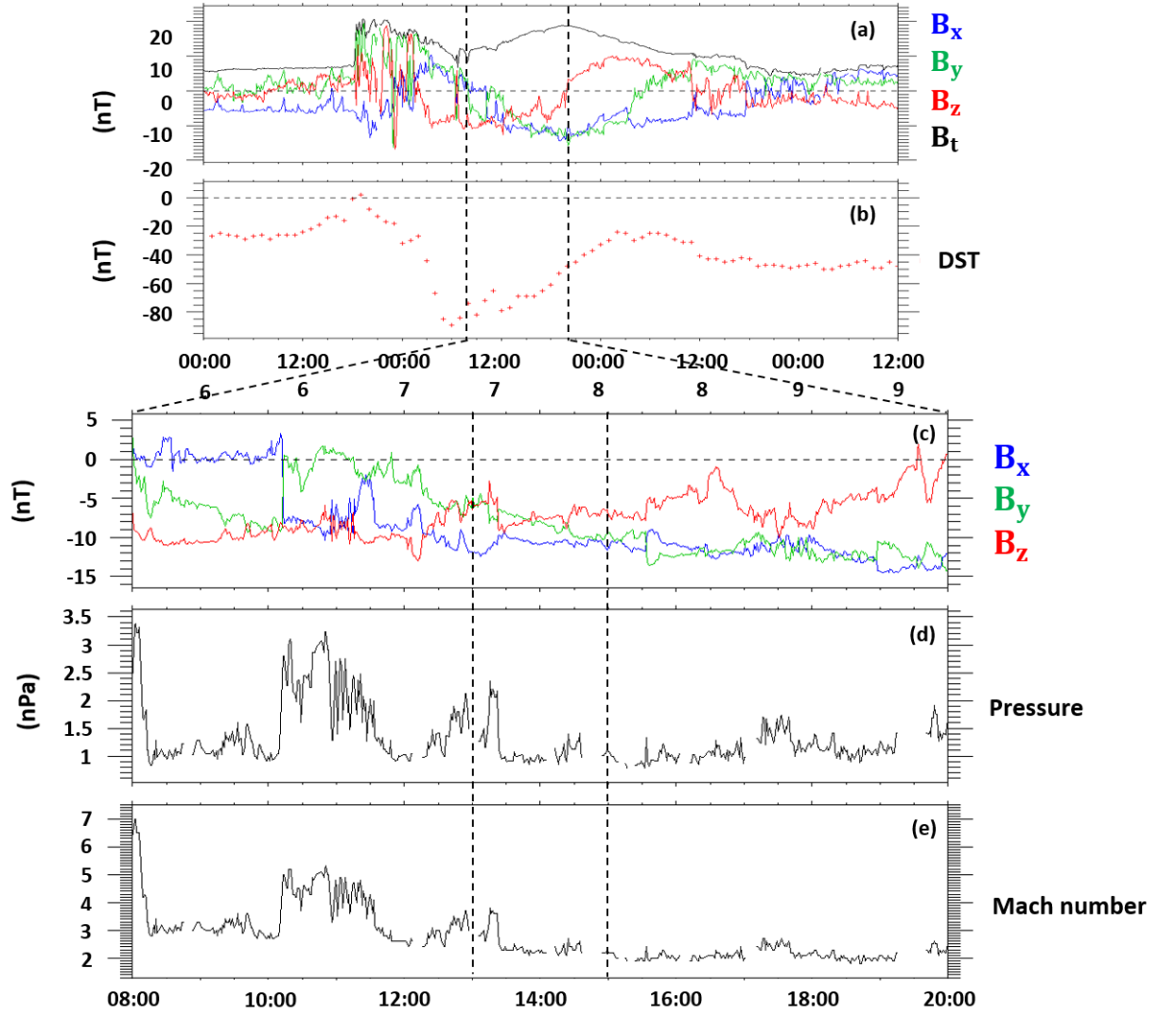


Figure 3.5 – Solar wind conditions from the OMNI 1 minute resolution database from 06 November 2015-00:00 UT through 09 November 2015-12:00 UT. (a) Interplanetary magnetic field components and amplitude in GSE coordinates, (b) Disturbance Storm Time index. Solar wind conditions during 08:00-20:00 UT on 7 November 2015, (c) Interplanetary magnetic field components in GSE coordinates, (d) solar wind dynamic pressure, and (e) Alfvén Mach number.

	$X_{GSE}$	$Y_{GSE}$	$Z_{GSE}$
THB	46.42	-47.04	-0.27
THC	42.72	-46.82	-0.78
WIND	228.58	-97.07	11.05
ACE	234.11	37.49	6.81

Table 3.2 – Average positions of THB, THC, Wind and Ace in  $R_E$  between 11h00 and 15h00 UT in GSE coordinates.

affecting the whole magnetosphere. They were confirmed by the observations of other spacecraft, i.e. Wind, Themis B, Themis C, that were flying in the solar wind during the

time of the event. The average positions of each of these spacecraft between 11h00 and 15h00 UT in GSE coordinates are shown in Table 3.2.

### 3.4.1. EXPECTED LOCATION OF THE RECONNECTION SITES [TRATTNER ET AL. (2007)]

Figure 3.6 shows three shear angle plots that predict X-lines locations at the magnetopause from and around the event at (a) 13:40 UT, (b) 13:51 UT and (c) 14:16 UT. It shows the magnetopause as seen from the sun and color-coded for the magnetopause shear angle between the geomagnetic field and the fully draped IMF (clock Angles (a) 244°, (b) 245° and (c) 259°). Regions of parallel magnetic shear conditions are shown as blue and black areas, while antiparallel magnetic shear at the magnetopause are shown in red ( $> 150^\circ$  shear angle). The black circle depicts the location of the terminator plane that separates the day-side magnetopause (inside the circle) from the nightside magnetopause (outside the circle). The MMS location at the magnetopause is marked by a black symbol. The predicted reconnection location for the solar wind conditions, derived from the Maximum Magnetic Shear model, is shown as a thin white line. At 13:40 UT and 13:45 UT a flow switch is observed and the spacecraft are right next to the predicted line. In that time period, there are several flow switches, but the spacecraft seem to slowly move further away from the predicted line (Figure 3.6-b). The observations at (a) occurred in the MSBL under essentially southward magnetic field conditions and exhibit antiparallel accelerated ion flows consistent with MMS now located north of the reconnection line. The observations at (b) occurred in the LLBL under varying magnetic field conditions. Globally, when the magnetic field is southward, antiparallel accelerated ion flows are observed and when magnetic field is northward, parallel accelerated ions are observed. These observations are consistent with MMS now located north of the reconnection line. The MMS satellites have briefly crossed the reconnection location. During the event time period (Figure 3.6-c), there is also a flow switch and the IMF clock angle has increased to 260°. This changes the location of the predicted line, while the actual observed X-line seem to be still located where it was before, at its earlier location. The error is now at about  $3R_E$  [private communication with K. J. Trattner] and the difference at the location can be explained by the results of Trattner et al. (2016) assuming that the X-line location does not respond instantaneously to changes in



IMF clock angle or it can be related to symmetry effect that leads to some anomalies when the clock angle is around  $240^\circ$ . The observations at (c) occurred in the LLBL under northward magnetic field conditions. Ions exhibit parallel accelerated flows with velocities of about  $250 \text{ km/s}$  in the  $Z_{GSE}$  direction, consistent with MMS located north of the reconnection line.

## 3.5. LARGE TIME-SCALE OBSERVATIONS

### 3.5.1. BOUNDARY LAYER STRUCTURE

Two hours of MMS survey data are presented in Figure 3.7. The panels (a) to (g) show, respectively, the GSE components and the strength of the magnetic field, the electron and ion densities, the components and the amplitude of the ion velocity, the spectrograms of the electrons and the ions measured by FPI and the spectrograms of the  $He^{++}$  and  $O^+$  ions measured by HPCA. Initially, the spacecraft were located in the magnetosheath, as shown in the ion and electron spectrograms, high plasma number densities, and the abundance of  $He^{++}$  and the absence of  $O^+$  ion fluxes. After 14:28 UT, the spacecraft were inside the magnetosphere characterized by a positive and dominant  $B_z$ , low number densities and weak flows, as well as significant fluxes of observed high energy electrons, protons, and oxygen ions. Conversely, the  $He^{++}$  fluxes were weak.

Around 13:28 UT, the data show a partial crossing of the magnetopause, as indicated by variable  $B_z$  component and flows. That indicates a brief incursion of the spacecraft from the magnetosheath into the magnetosphere followed by its return into the magnetosheath. The magnetopause is defined by the current sheet that separates the magnetosheath flow from accelerated and diverted flows in the boundary layers (LLBL/inside the MP). We suspect that the sudden magnetopause crossing (i.e. magnetopause expansion) was driven by the decreasing of dynamic pressure, as observed in the OMNI data around that time in Figure 3.5-(d). The spacecraft were in a boundary layer during almost one hour between 13:28:00 and 14:28:00 UT while moving from the magnetosheath into the magnetosphere. Although the boundary layer shows a complex structure as expected from the pronounced variations in solar wind parameters described above, it may be divided into three major

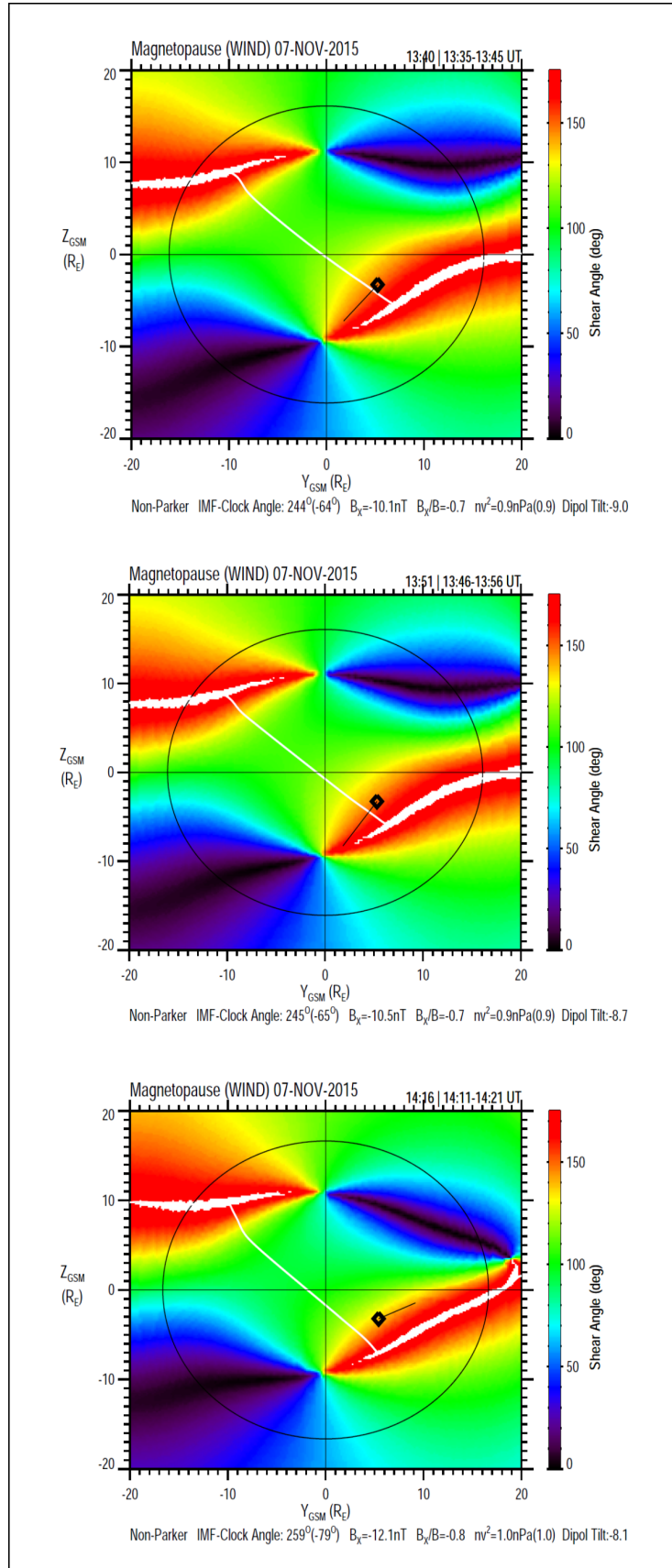


Figure 3.6 – The magnetopause shear angle seen from the Sun with the predicted reconnection and MMS locations at the magnetopause. Courtesy from *K.J. Trattner*.

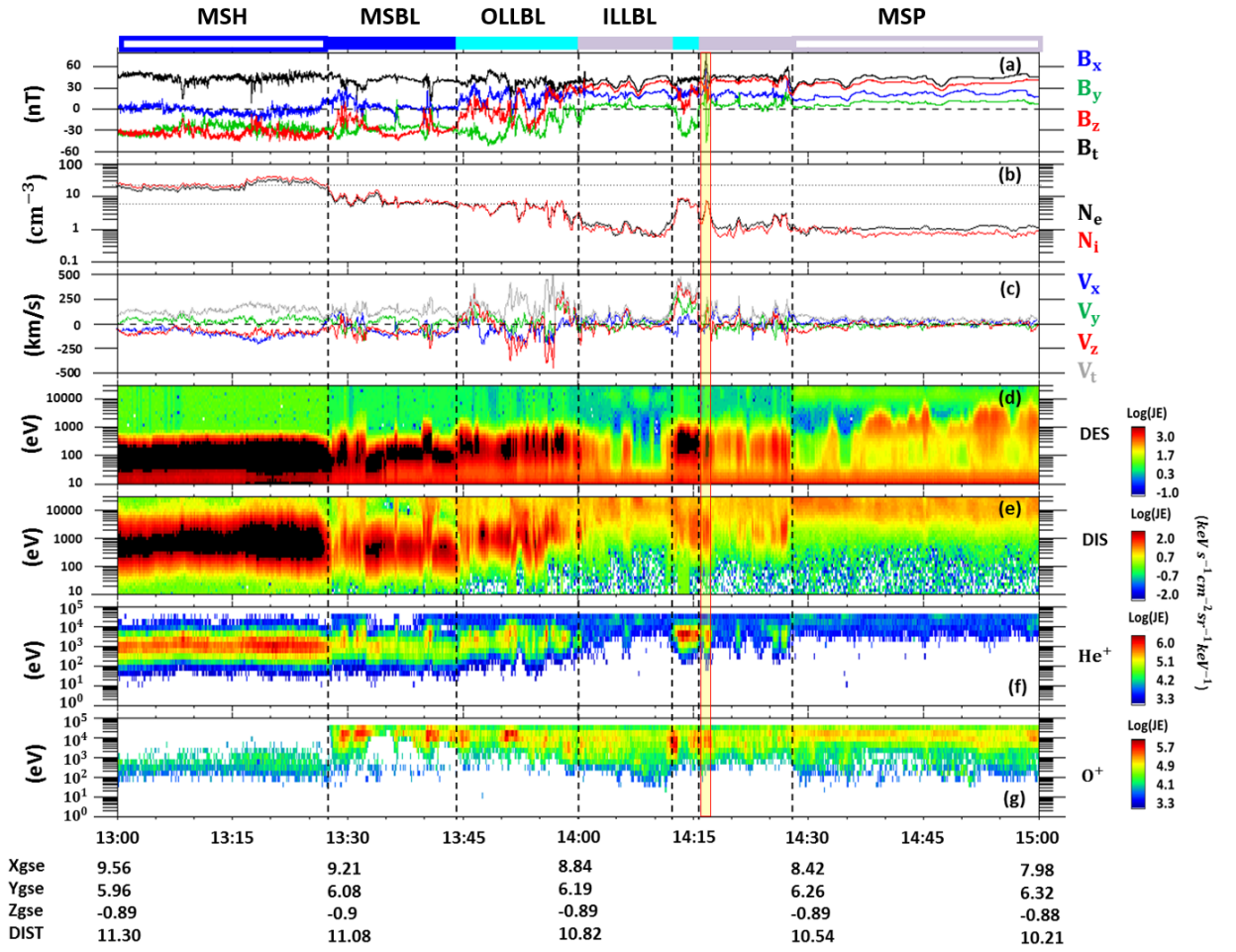


Figure 3.7 – Survey data from MMS1 on 7 November 2015 between 13:00 and 15:00 UT. (a) Magnetic field from FGM, (b) electron and ion densities, (c) ion velocity, (d) electron spectrogram provided by FPI, (e) ion spectrogram provided by FPI, (f)  $He^{2+}$  spectrograms from HPCA and (g)  $O^+$  spectrogram from HPCA.

subregions as illustrated in Figure 3.8. Figure 3.8 shows  $B_z$  as a function of  $B_y$  between 13:00 and 15:00 UT.  $\gamma$  is defined as the ratio of the electron density to the perpendicular electron temperature  $\gamma = \log_{10}(N_e/T_{e_{perp}})$  is color coded on a logarithmic scale. The color of  $(B_y, B_z)$  points refers to the corresponding value of the ratio. As it can be seen, the distribution of the points is well organized into three main regions consistently with the values of  $\gamma$ : The three regions have different characteristics:

- The MSH-MSBL region: Points located in this region have high negative values of  $B_y$  and  $B_z$  with a low  $\gamma$  that indicates a low density. This region is marked by filled and hollow dark blue rectangles in Figure 3.8.

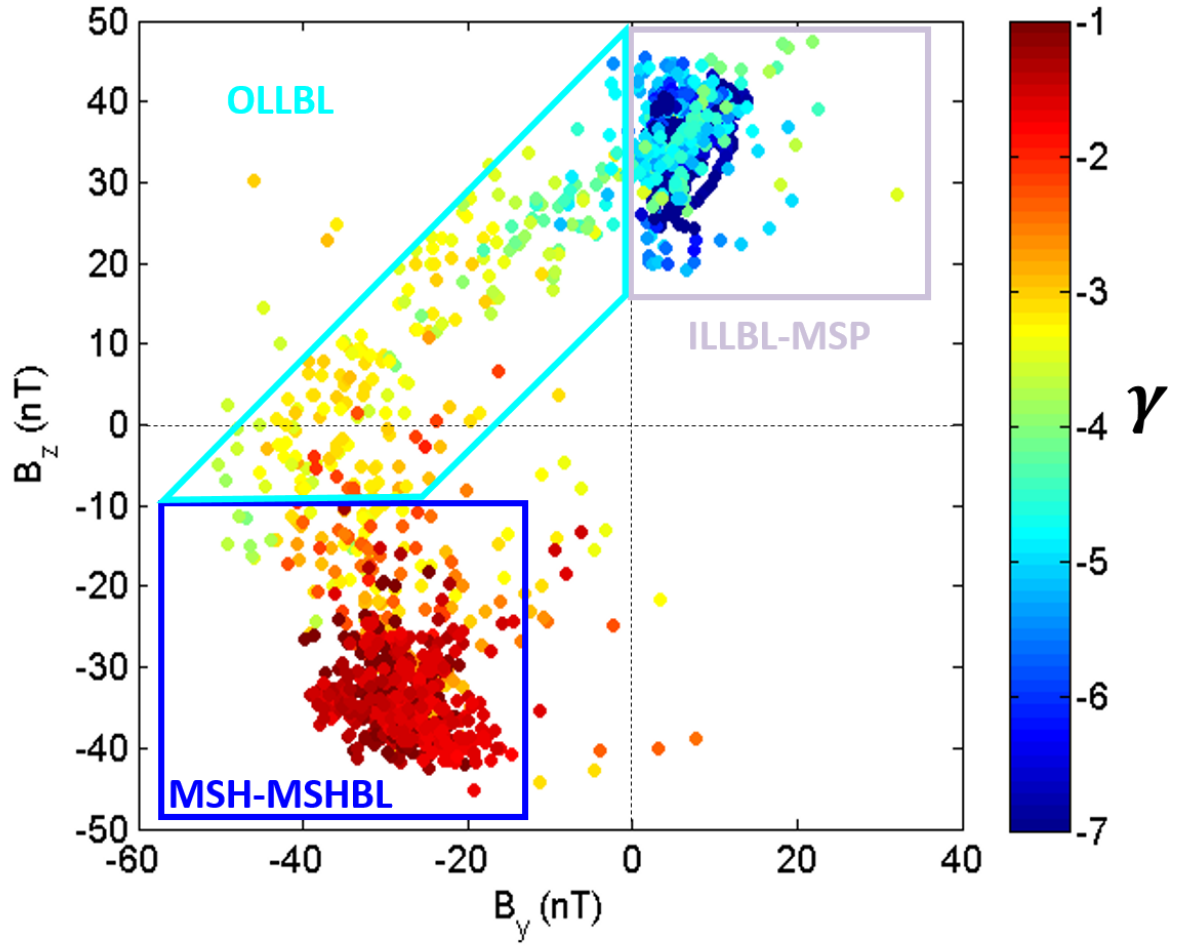


Figure 3.8 – The variations of  $B_z$  as a function of  $B_y$  during the time of the LLBL crossing with the logarithmic of the ratio of electron density over perpendicular electron temperature is represented by the colors of the dots on November 7, 2015 between 13:00 and 15:00 UT.

- The ILLBL-MSP region: This region is characterized by relatively small values of  $B_y$  and positive values of  $B_z$  with a high  $\gamma$  indicating a high density. This region is marked by purple-filled rectangles and hollow rectangle with purple borders in Figure 3.8.
- The OLLBL region: In this region, the variations of  $B_z$  and  $B_y$  reveal a rotation in the magnetic field direction. The values of  $\gamma$  range between  $-2.5$  and  $-4$ . This region is marked by cyan filled rectangles in Figure 3.8.

The thickness of the boundary layer was of the order of  $1R_E$ . As shown in Figure 3.9, the  $X_{GSE}$  component of the spacecraft has varied from  $9.24R_E$  at 13:28 UT to  $8.45R_E$  at 14:28 UT while crossing the boundary layer.

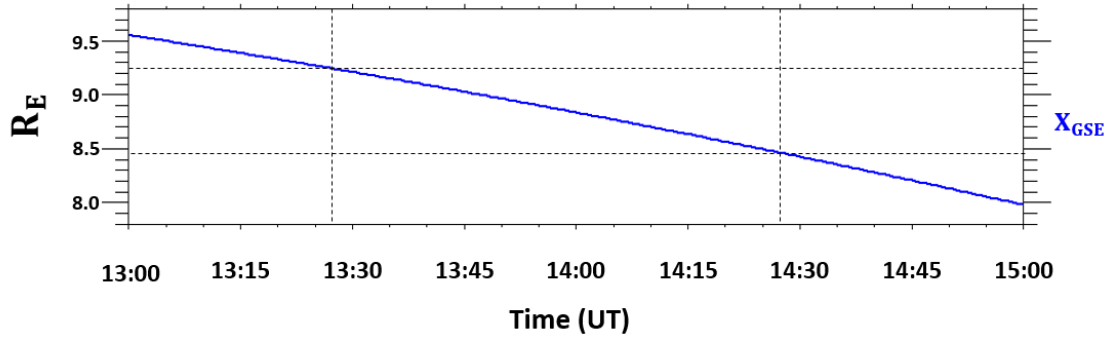


Figure 3.9 – The  $X_{GSE}$  component of the spacecraft position on November 7, 2015 between 13:00 and 15:00 UT Earth Radii. The vertical dashed lines delimit the boundary layer.

At  $\sim 13:35$  UT, the spacecraft exited back into the magnetosheath, as seen from the faster flows, similar to the previous magnetosheath interval. This magnetosheath interval was characterized by a much lower density and included two very short incursions into the magnetosphere. The main magnetopause crossing then occurred at 13:44:30 UT (second dashed line in figure 3.8). The spacecraft crossed the magnetopause current sheet (direct separation with the magnetosheath) and thereafter remained inside the LLBL for a long time. The boundary layer inside the magnetopause, hereafter called low latitude boundary layer (LLBL), was observed from 13:44:30 UT to 14:00 UT. This LLBL interval was also very dynamic. This interval is identified as the outer LLBL (OLLBL) because it contains plasma accelerated through the magnetopause discontinuity as evidenced by the enhanced and diverted flows as compared to the pristine magnetosheath observed before 13:45 UT (cf. panels a and c of Figure 3.7).

The spacecraft entered more clearly into the magnetosphere around 14:00 UT where a second magnetic field rotation occurred, this time mainly in the  $B_y$  component. We note that after this second current sheet the spacecraft did not exit immediately into the pristine magnetosphere given the observation of low energy magnetosheath electrons between 14:00 and 14:05 UT, reminiscent of a kind of, or a more inner part of, the LLBL. The true hot magnetospheric plasma was observed for example around 14:10 UT. The spacecraft exited back into the main (outer) LLBL with enhanced flows and negative  $B_y$  around 14:12 UT just before the event of interest, which was observed between 14:16:00 and 14:17:30 UT. The event time interval is indicated with a yellow shaded area, bracketed by the red vertical

lines in Figure 3.7. A strong peak in magnetic field magnitude consists of the most spectacular feature and is visible in Figure 3.7-a. Just after the event, the spacecraft remain in the LLBL based on the presence of some low energy magnetosheath electrons, but again likely the more inner part of it given the measured low densities and the positive  $B_y$  value. The spacecraft are in the magnetosphere proper after around 14:28 UT. Some middle energy electrons are intermittently observed after that time, but these are believed to be of ionospheric origin.

To summarize, we argue that two kinds of LLBL were present. Observations of two kinds of LLBL have been previously reported by e.g. Fujimoto et al. (1998); Bauer et al. (2001); Hasegawa et al. (2003). The outer LLBL had a high density and showed enhanced  $|V_z|$  flows. The inner LLBL had a lower density and a magnetic field orientation closer to that of the geomagnetic field observed in the pristine magnetosphere. The transition from the main (outer) LLBL to the inner LLBL also corresponded to a current sheet responsible for the main rotation in  $B_y$ .

### 3.5.2. MAGNETOPAUSE TRANSITION PARAMETER

In order to clarify and check the structure of the boundary layer that was proposed in the previous paragraph, we calculated the MP transition parameter  $\tau$  which helps reordering the time series data from magnetosheath to magnetosphere allowing then the identification of boundary layer plasma [Hapgood and Bryant (1990); Lockwood and Hapgood (1997)]. The plasma transition parameter ( $\tau$ ) is used instead of separately using the density and the temperature to provide a more accurate indicator of boundary layer plasma.  $\tau$  is a unitless scalar from 0 to 100. Once  $\tau$  is calculated, the variations in plasma parameters and the magnetic field can be used to assign the corresponding values in the magnetosheath, magnetosphere and the boundary layer for particular events.

Figure 3.10 shows the the variations of  $\tau$ .  $\tau$  was calculated by fitting a curve to a  $\log_{10} - \log_{10}$  scatter plot of perpendicular electron temperature against electron density using all data points between 13:00 and 15:00 UT (see paragraph "Transition Parameter" in Chapter 2). The rectangles in the top of the Figure mark the different plasma regions as they have been identified in the subsection 3.5.1. The transition from the magnetosheath to the magnetosphere had a significant thickness and included a multilayered structure. The structure can

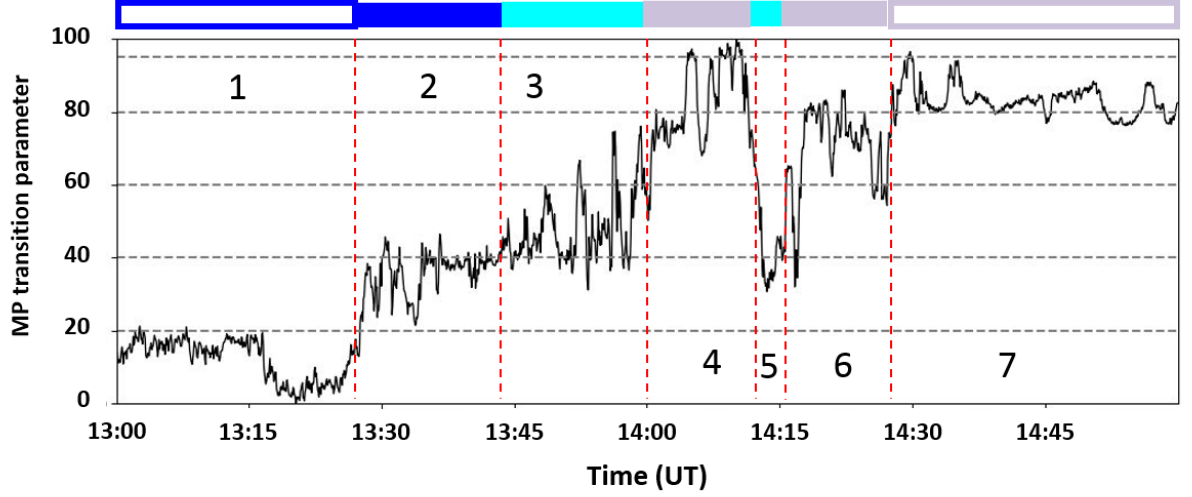


Figure 3.10 – Transition parameter calculated for MMS1 calculated from FPI measurements.

be split into four regions: the MSH, the MSBL, the outer LLBL and the inner LLBL-MSP. The spacecraft were first in the pristine magnetosheath, region 1, where the upper threshold of  $\tau$  was set to be  $\tau = 20$ , consistent with the suggestion by [Lockwood and Hapgood \(1997\)](#). In the MSBL, region 2, the values of  $\tau$  varied between 20 and 40. This region was followed by the OLLBL, region 3, with  $40 < \tau < 60$ . The region 4, which has been identified as the ILLBL, was characterized by values of  $\tau$  that ranged between 60 and 100. Then, in region 5, the values of  $\tau$  dropped to values close to the ones that were observed in the MSBL and the OLLBL. Finally, in regions 6 and 7 which were identified as the ILLBL and the MSP, the values of  $\tau$  were such as  $60 < \tau < 100$ .

## 3.6. ANALYSIS OF THE EVENT

### 3.6.1. OBSERVATIONS

The crossing of the magnetopause and LLBL occurred between 13:44:30 UT and 14:00 UT. The magnetopause normal and associated LMN frame [[Farrugia et al. \(1988\)](#)] were inferred by performing a variance analysis [[Sonnerup and Scheible \(1998\)](#)] of the magnetic field data between 13:42:25 and 14:02:44 UT. The results are given in Table 3.4. The magnetopause normal vector,  $N = [0.84, 0.30, -0.44]$  in GSE, was relatively close to the normal direction calculated from Shue magnetopause model (e.g.  $[0.91, 0.41, -0.06]$  in GSE using the [Shue et al. \(1997\)](#) model). The L and M vectors roughly pointed in the Z and -Y directions.



In Figure 3.11, burst data measured by MMS 1 on 7 November 2015 between 14:15:45

		$L$	$M$	$N$
Magnetopause	$X_{GSE}$	0.24	0.48	0.84
	$Y_{GSE}$	0.53	-0.79	0.3
	$Z_{GSE}$	0.81	0.37	-0.44

Table 3.3 – Local magnetopause coordinate system obtained from the minimum variance analysis of the magnetic field.  $\lambda_L/\lambda_M = 5.75$ ,  $\lambda_L/\lambda_N = 18.64$  and  $\lambda_M/\lambda_N = 3.23$ .

and 14:17:20 UT are presented. Dashed lines labelled  $T_0$  to  $T_5$  delimit the different parts of the event that clearly have different properties and correspond to times 14:16:04; 14:16:25; 14:16:40; 14:16:43; 14:16:58 and 14:17:05 UT, respectively. The vector data are in GSE coordinates. The top panel (a) displays the magnetic field, the (b) panel shows the ion thermal pressure ( $P_p$ ), the magnetic pressure ( $P_m$ ) and the total pressure ( $P_t = P_p + P_m$ ). The (c) panel shows the current density as inferred from the curlometer technique, the (d) panel exhibits the ion velocity and the last panel (e) shows the density of both ions and electrons. Electron data for the same interval are displayed in Figure 3.12. The second panel in Figure 3.12 shows the omni directional energy flux of electrons, and the following three panels (c, d, e) give the electron pitch-angle distributions for three energy ranges: 98-127 eV, 451-575 eV, and 3.3-11.5 keV. These energy bands are considered typical of thermal magnetosheath, accelerated magnetosheath and magnetospheric electron populations, respectively (e.g. Pu et al. (2013); Zhong et al. (2013)). The top panel (a) displays the magnitude and  $B_y$  component of the magnetic field for the sake of completeness.

Figure 3.11 shows that prior to  $T_1$  (14:16:25 UT), the spacecraft were in the inner LLBL, where plasma densities were low and  $B_z$  was the main component of the magnetic field. Then, between  $T_1$  and  $T_5$ , the MMS spacecraft recorded large changes in all parameters. The most remarkable features included peaks in the magnitudes of the magnetic field (by a factor of  $\sim 1.7$ ) and total pressure ( $\sim 2.5$ ), a strong bipolar signature in the  $B_y$  component ( $\Delta B_y \sim 80 nT$ ) and a large ( $\sim 300 km/s$ ) flow directed northward ( $V_z > 0$ ) and eastward ( $V_y > 0$ ). At first glance, these large-scale signatures look consistent with those of an FTE consisting of a flux rope resulting from a reconnection process, that may have occurred southward and dawnward of the spacecraft for the prevailing conditions of IMF negative  $B_z$  and  $B_y$  (see Figure 3.5).



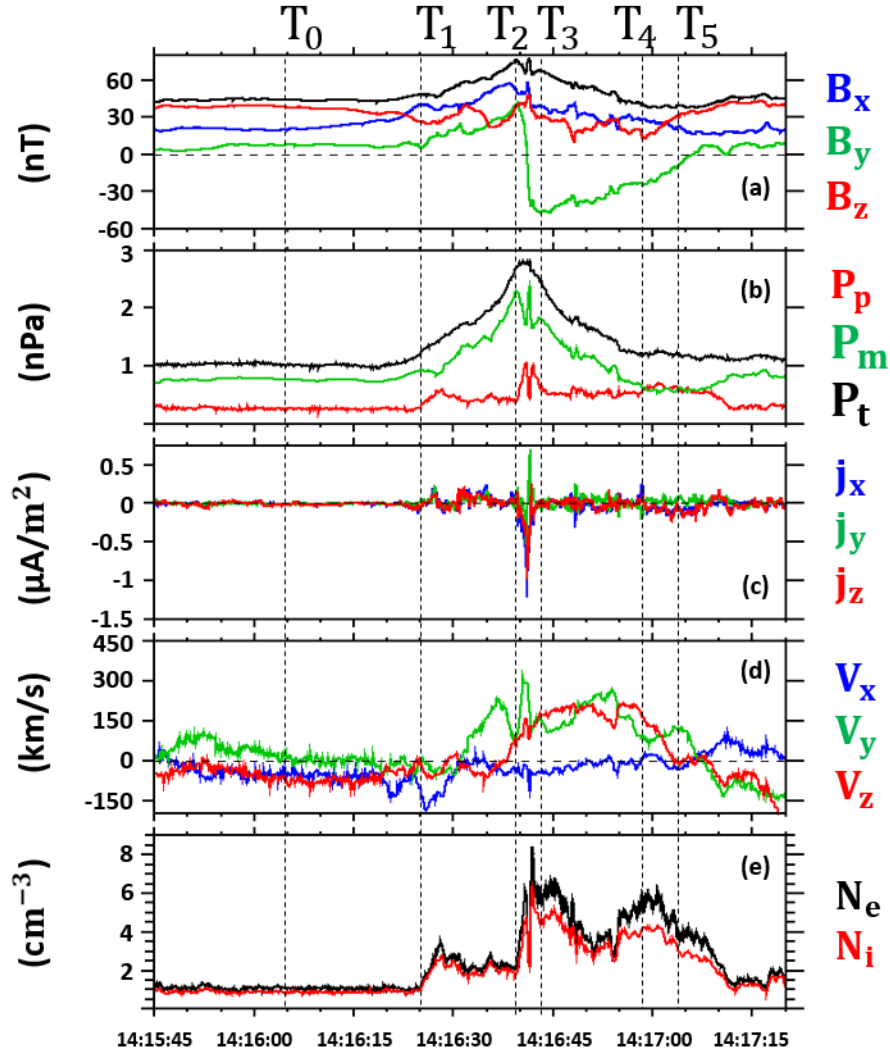


Figure 3.11 – An overview of MMS1 observations between 14:15:45 and 14:17:20 UT in GSE coordinates on 7 November 2015. (a) Magnetic field components and total field strength, (b) pressures (red= plasma (ion), green= magnetic, and black= total), (c) current density from curlometer technique, (d) ion velocity components, (e) electron (black) and ion (red) densities. The black vertical dashed lines labelled T0 to T5, correspond to times 14:16:04; 14:16:25; 14:16:40; 14:16:43; 14:16:58 and 14:17:05 UT.

However, this interpretation appears inconsistent with several observational facts:

- First, the bipolar signature was not observed in the component normal to the magnetopause (mainly along  $X_{GSE}$ ), but rather in a direction almost perpendicular ( $Y_{GSE}$ ) to the magnetopause normal (see Panel a).
- Secondly, there were a small-scale and fast  $V_y = 300 \text{ km/s}$  ion jet (along  $Y_{GSE}$ ) and an intense and thin current structure near the peak of the large scale magnetic field

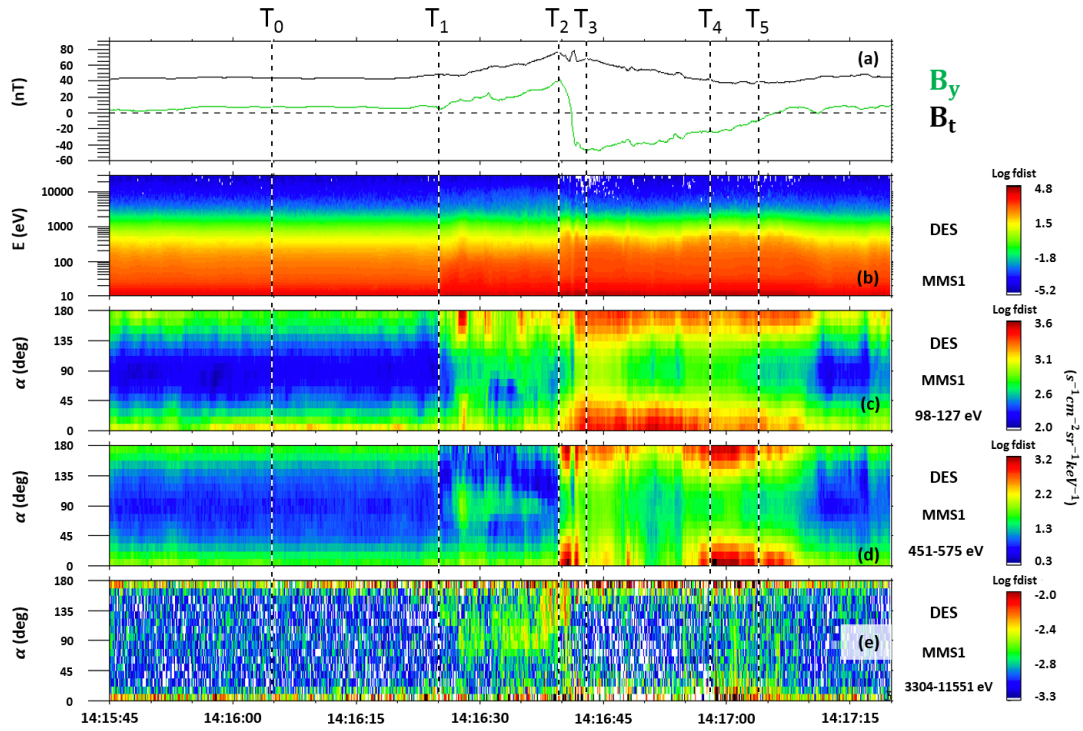


Figure 3.12 – MMS1 data between 14:15:45 and 14:17:20 UT of (a)  $B_y$  and the magnetic field strength in GSE coordinates, (b) electron energy spectrum. Electron pitch angle distribution in the range of (c) 98-127 eV, (d) 451-751 eV, and (e) 3304-11551 eV.

between  $T_2$  and  $T_3$  (Panels d, c and a). Such features do not fit the usual flux rope models of FTEs, although the presence of thin current sheets and reconnection have been reported in the literature [Øieroset et al. (2016)].

- Thirdly, based on the pitch-angle distributions of electrons, there were drastically different regimes before and after the passage of this current structure (last three panels in Figure 3.12). The characteristic features of the first and second part of the event were clearly different. The region between  $T_1$  and  $T_2$  was first characterized by lower fluxes of anti-parallel accelerated magnetosheath electrons, while the parallel fluxes remained unchanged with regards to the fluxes measured before  $T_1$  (Panel d). On the other hand, the thermal magnetosheath electron population tended to have larger fluxes, consistent with an increased density (Panel c). During this interval, MMS also observed a trapped electron population (at 90° pitch angle) which appears in both the accelerated magnetosheath and magnetospheric energy ranges (Panels d and e).

By contrast, during the second part of the event (between  $T_3$  and  $T_4$ ), this trapped population was not present anymore; there were essentially no magnetospheric electrons. The accelerated magnetosheath electrons anti-parallel flux was larger than the parallel one (Panel d). These strongly different features suggest that this sequence is not the signature of a single homogenous structure like a flux rope (expected to be associated with FTEs).

On the basis of these observations, we rather interpret the time sequence between  $T_1$  and  $T_4$  as successive crossings of two distinct flux tubes, henceforth referred to as  $FT_A$  that was observed between  $T_1$  and  $T_2$  and  $FT_B$  that was observed between  $T_3$  and  $T_4$ . Finally, the densities were also drastically different between  $FT_A$  and  $FT_B$  (Figure 3.11, Panel e). In  $FT_B$ , the electron/ion densities and the  $He^{2+}$  fluxes (Figure 3.7) had values typical of the outer LLBL.

A complementary view is provided in Figure 3.13 that introduces our observations in the LMN frame. The components of the magnetic field are shown in panels a to d. The ion velocity components are provided in panels f to i and the angle  $\Psi$ , which corresponds to the angle between the magnetopause normal and the magnetic field, is shown in panel e. The angle  $\Psi$  is given by:

$$\Psi = \arctan\left(\frac{\sqrt{B_L^2 + B_M^2}}{|B_N|}\right) \quad (3.1)$$

Displaying the data in the LMN frame reveals two main features at the scale of the whole event:

- The magnetic changes in the LMN frame did not exhibit an FTE-like bipolar signature, but rather a sharp rotation of the magnetic field through a thin current structure. The maximum magnetic field shear angle, corresponding to that across the central thin current sheet, was about  $73^\circ$ . Before its passage, the magnetic field was progressively deformed throughout  $T_0$ - $T_1$ - $T_2$ , as indicated by the gradual changes in  $\Psi$ . When the spacecraft crossed the current structure, the  $\Psi$  angle recovered quickly its initial value and, thereafter, both the L and N components of the magnetic field remained close to zero for about 15 seconds, while the M-component was strongly enhanced.

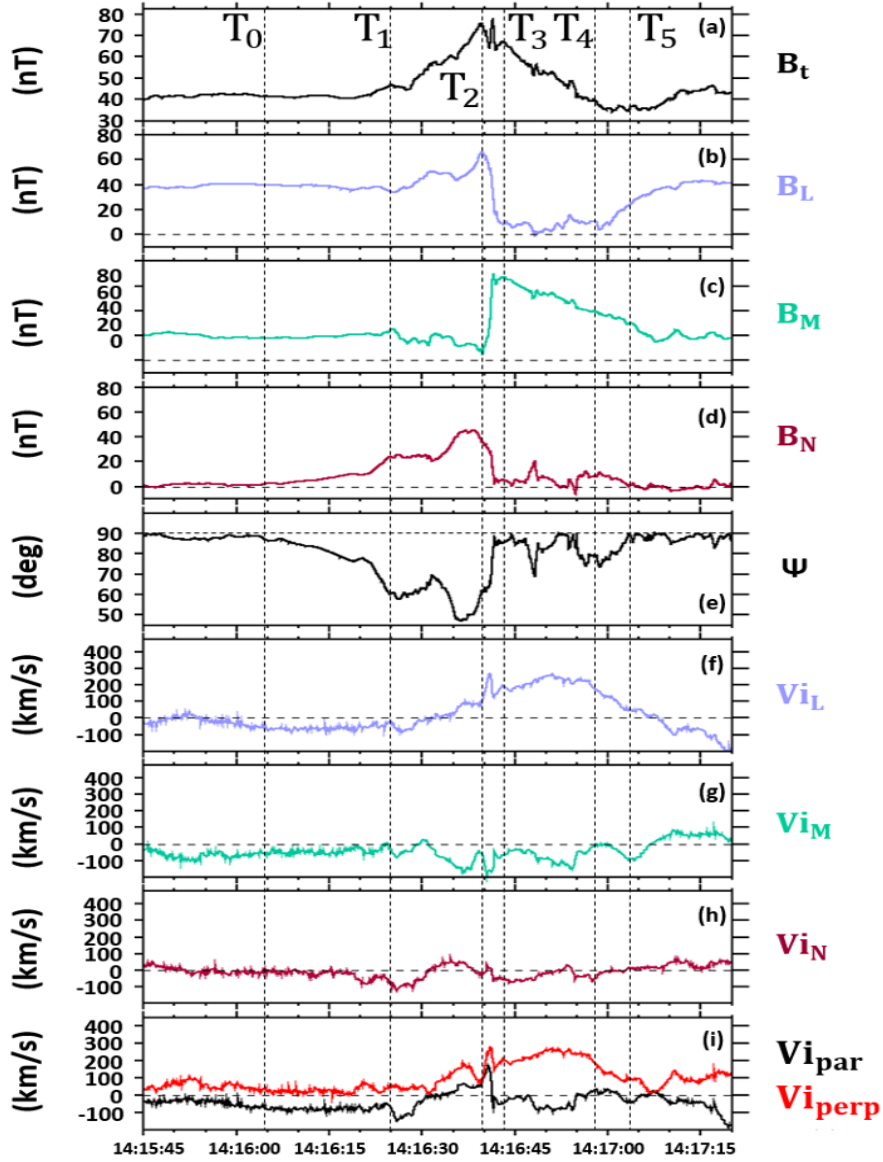


Figure 3.13 – (a) Magnetic field magnitude, (b)-(d) magnetic field components in the magnetopause LMN frame, (e) angle  $\Psi$  between the magnetopause normal and the magnetic field, (f)-(h) ion velocity components in the magnetopause LMN frame, (i) parallel (black) and perpendicular (red) ion velocity in the GSE coordinates system. The black vertical dashed lines labelled  $T_0$  to  $T_5$  are shown at the same times as in Figure 3.11.

- The event was associated with a perpendicular ion flow in the +L direction, suggesting that this flow results from a magnetic reconnection which occurred southward of the spacecraft.

A more detailed examination of the observations indicates that at the beginning of the period, before  $T_0$ , the magnetic field had an orientation tangential to the magnetopause, mainly in the L direction. The  $\Psi$  angle was close to  $90^\circ$ . The ion flows were weak. At time  $T_0$ , while all other parameters remained unchanged, the  $\Psi$  angle ( $B_N$  component) started to decrease (increase). This trend continued until  $T_1$  and indicates that the magnetic field underwent a large-scale deformation. This is interpreted as the remote signature of a propagating process having started before  $T_0$  and approaching closer to the spacecraft. During this period, the ion flow remained constantly weak ( $V_{i_L} \sim -50 \text{ km/s}$ ,  $V_{i_M} \sim -25 \text{ km/s}$ ) except for a small  $V_N$  (also seen on the  $V_{x_{GSE}}$  component) peak  $\sim 5$  seconds prior to  $T_1$ . This  $V_N$  change consisted of a perpendicular flow and was negative indicating an inward motion of plasma. This one could be due to a local retreat of the magnetopause. The time  $T_1$  marks the beginning of the in-situ detection of the event, corresponding to the entry into flux tube  $FT_A$ . Between  $T_1$  and  $T_2$ , the  $B_L$  component and the magnitude of the magnetic field both increased. It was also the general trend for  $B_N$  while  $B_M$  decreased to 15 nT. When the spacecraft penetrated into  $FT_A$  (at  $T_1$ ), it first detected a  $\sim 3$  second duration anti-parallel ion flow that reached a maximum value of  $150 \text{ km/s}$  along the L and N directions. Then, when  $V_L$  and  $V_N$  returned to zero, the flow was mainly perpendicular with a  $-V_M$  component. From that time until  $T_2$  (14:16:40 UT), the main component of the flow was  $-V_M$ , suggesting a westward motion of  $FT_A$ .

Between  $T_2$  and  $T_3$ , the magnetic field rapidly rotated. A localized ion jet was detected at that time, as clearly seen on the  $V_{y_{GSE}}$  component in Figure 3.11. This jet appeared in the L and M components in Figure 3.13. It was thus directed in a direction tangential to the magnetopause and oblique to the magnetic field as it includes both parallel and perpendicular components. Comparison to the electric field data indicates that the ions were decoupled from the magnetic field during the main current structure (section 3.7.2). Being along  $V_M$  during a large rotation of the  $B_M$  component, this ion jet is consistent with expectations from magnetic reconnection between  $FT_A$  and  $FT_B$ , as it is discussed later (section (section 3.7.2)).

Between  $T_3$  and  $T_4$ , the flow was essentially along the L direction and the N and L components of magnetic field were close to zero.

Finally, between  $T_4$  and  $T_5$ , the ion flow vanished gradually and the magnetic field recovered its initial (before  $T_0$ ) orientation. The interface marking the end of the event is not analyzed in further detail in this paper.

### 3.6.2. SMALL-SCALE CURRENT SHEET

In order to infer the motion of the current structure relative to the spacecraft, we performed differential timing analysis using the  $B_{y_{GSE}}$  bipolar transition, which constitutes the clearest change (see Chapter 2-Multi-Spacecraft Timing Analysis: structures orientation and motion). This transition corresponded to the crossing of a strong current structure. We identified times when the 4 MMS spacecraft successively measured a set of identical  $B_y$  values, as illustrated in Figure 3.14 with the horizontal dashed lines. Assuming that the structure is planar, we applied the multi-point triangulation method [Russell C. T. et al. (2012); Dunlop and Woodward (1998); Harvey (1998b)]. For all identified times it provided a set of normal vectors  $N_C$  and propagation speed  $V_P$  along the normal. The results showed that both  $N_C$  and  $V_P$  change only slightly through the transition. From now on we will use a normal vector  $N_C = [-0.54, -0.03, 0.84]_{GSE}$  and a propagation velocity of  $\sim 67 km/s$ , which are obtained from averaging over the full set of values shown in Table 3.5. The propagation velocity slightly increases then decreases. The last column of Table 3.6 shows that the variations of the angle between each normal vector and the  $X$  axis are minimal, which indicates a weak variance of the normal vectors and, therefore, suggests that the structure is planar at the scale of the spacecraft separation.

For inferring the geometry and the orientation of the current structure, we performed

		$L$	$M$	$N$
Magnetopause	$X_{GSE}$	0.24	0.48	0.84
	$Y_{GSE}$	0.53	-0.79	0.3
	$Z_{GSE}$	0.81	0.37	-0.44

Table 3.4 – Local magnetopause coordinate system obtained from the minimum variance analysis of the magnetic field.  $\lambda_L/\lambda_M = 5.75$ ,  $\lambda_L/\lambda_N = 18.64$  and  $\lambda_M/\lambda_N = 3.23$ .

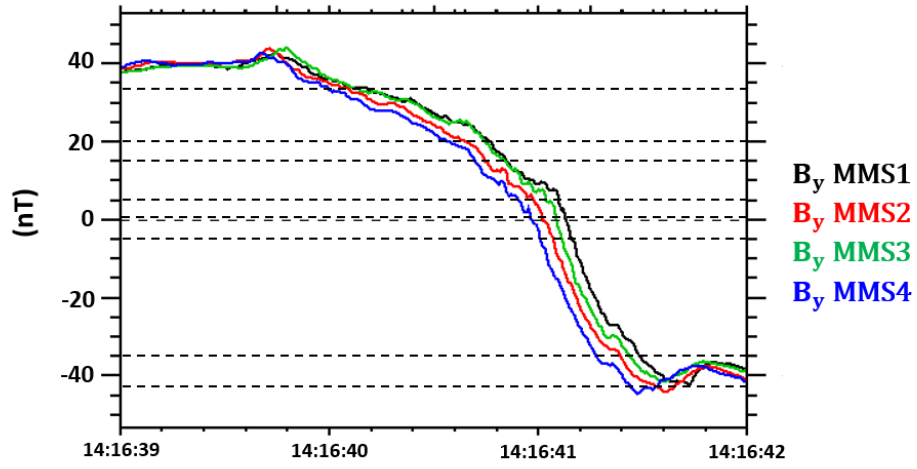


Figure 3.14 –  $B_y$  component of the magnetic field in the GSE coordinates system from the four MMS spacecraft. The horizontal dashed lines represents the several contours of different  $B_y$  values that were used to calculate their normal directions and propagation velocities.

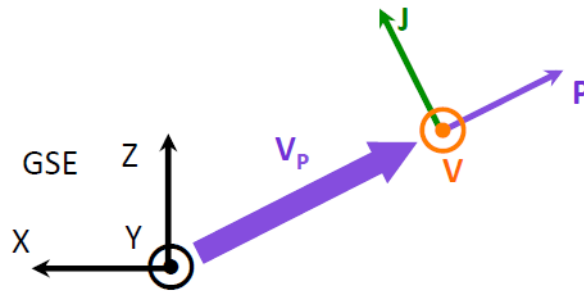


Figure 3.15 – The relative orientation of the PCS frame ( $\mathbf{U}_P$ ,  $\mathbf{U}_J$  and  $\mathbf{U}_V$ ) to the GSE frame. The thick violet arrow shows the direction of the current sheet propagation velocity obtained from multi-spacecraft data analysis. The PCS frame corresponds to a translation of the GSE frame in the direction of the current sheet propagation velocity combined with a rotation about the  $Y_{GSE}$  direction.

$B_y$	$N_x$	$N_y$	$N_z$	$V(km/s)$	Angle
33	-0.50	0.004	0.86	66.08	120°
20	-0.46	-0.15	0.87	60.36	118°
15	-0.50	-0.25	0.83	74.00	120°
5	-0.59	-0.02	0.81	63.63	126°
1	-0.61	-0.08	0.78	73.65	127°
0	-0.59	-0.07	0.79	73.39	126°
-5	-0.58	0.002	0.81	81.04	126°
-35	-0.42	0.012	0.91	58.43	114°
-40	-0.57	0.28	0.77	51.33	125°

Table 3.5 – The normal directions and the velocities of the propagating structure obtained by performing the timing method for multiple values of  $B_y$ . Mean value are:  $V = 66.88 km/s$  and  $N_c = [-0.54, -0.03, 0.84]$ , and the angle of each normal vector relatively to the the  $X$  axis.

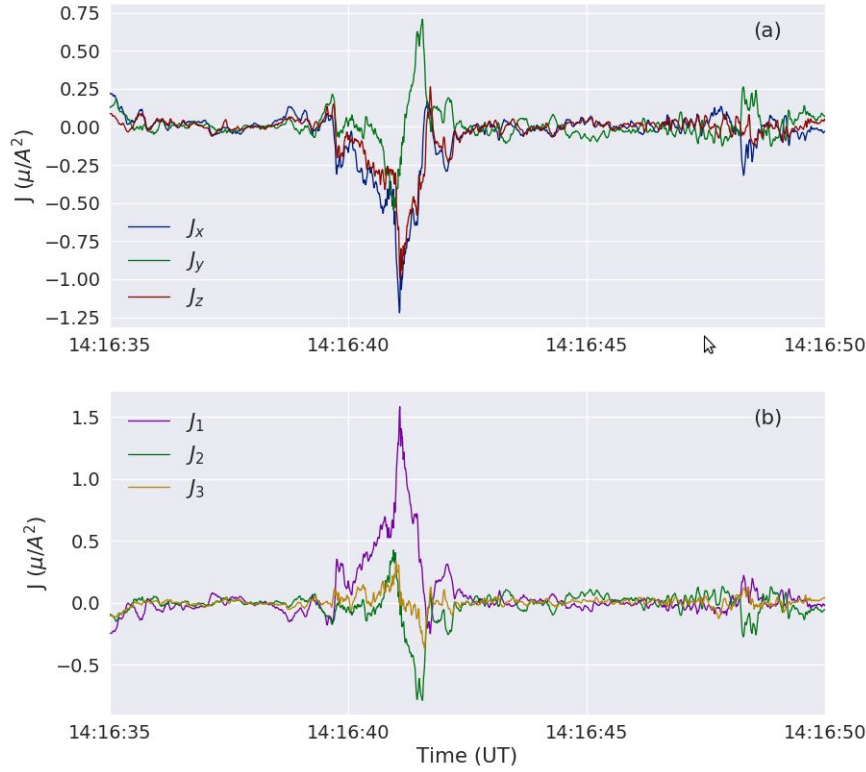


Figure 3.16 – Current density obtained from curlometer technique on 7 November 2015 between 14:16:35 and 14:16:50 UT. (a) in GSE coordinates, (b) in the current principal axis frame.

the variance analysis of the current density measurement obtained with the curlometer technique [Robert et al. (1998)] for the period 14:16:39-14:16:43 UT. The results given in Table 3.6 exhibit a strong contrast between the eigenvalues ( $\lambda_1/\lambda_2 = 2.8$ ,  $\lambda_1/\lambda_3 = 43.2$  and  $\lambda_2/\lambda_3 = 15.43$ ) and thus indicate that the current structure was organized with respect to clearly defined principal axes. Figure 3.16 shows the current density in the GSE and prin-



		$x_1$	$x_2$	$x_3$
Current principal axis	$X_{GSE}$	-0.76	0.03	-0.65
	$Y_{GSE}$	-0.2	-0.96	-0.19
	$Z_{GSE}$	-0.61	0.28	0.74

Table 3.6 – Results of the variance analysis of the current density obtained from the curlometer technique.  $\lambda_1/\lambda_2 = 2.8$ ,  $\lambda_1/\lambda_3 = 43.2$  and  $\lambda_2/\lambda_3 = 15.43$ .

		$U_P$	$U_J$	$U_V$
PCS	$X_{GSE}$	-0.61	0.77	0.19
	$Y_{GSE}$	0.02	-0.22	0.97
	$Z_{GSE}$	0.79	0.60	0.12

Table 3.7 – The unit vectors defining the PCS (Propagating Current Structure) frame.

principal current axis frames. The axis of maximal current (called thereafter "main current") was mainly directed in the  $(-X, -Z)_{GSE}$  direction  $[-0.76, -0.20, -0.61]$ . The main current is therefore perpendicular to the ion jet that is observed in the  $Y_{GSE}$  direction. The second principal axis associated with a significant ( $\lambda_1/\lambda_2 \sim 2.8$ ) current contribution (called thereafter "secondary current") was close to the  $Y_{GSE}$  direction  $[0.03, -0.96, 0.28]$ . It exhibits a bipolar signature that is parallel then anti-parallel to the ion jet. The third principal axis was associated with much lower eigenvalue ( $\lambda_2/\lambda_3 \sim 15.43$ ) with an almost null current component. Its orientation  $[-0.65, 0.19, 0.74]$  was in the  $(-X, +Z)_{GSE}$  direction and was found to be close to the direction of  $N_C$  found from the differential timing analysis.

Both independent approaches (current variance analysis and triangulation method) thus provided a consistent geometry of the current structure. We then considered a new coordinate system referred thereafter as the PCS (Propagation Current Structure) frame, which is illustrated in Figure 3.15. The PCS coordinate system is defined by the vectors  $\mathbf{U}_P$ ,  $\mathbf{U}_J$  and  $\mathbf{U}_V$ . The components of these unit vectors in the GSE frame are shown in Table 3.7. The first unit vector  $\mathbf{U}_P = [-0.61; 0.02; 0.79]_{GSE}$  is close to the propagation direction as well as the normal direction of the current structure. The second axis is oriented in the direction opposite to the main current  $\mathbf{U}_J = [0.77; -0.22; 0.60]_{GSE}$  and the last axis is defined using the unit vector of the ion jet which is also close to the unit vector of the secondary current  $\mathbf{U}_V = [0.19; 0.97; 0.12]_{GSE}$  (almost coinciding with  $Y_{GSE}$ ) and completes the right-handed set. The PCS frame is in translation relatively to the GSE one at a translation velocity equal to the propagation velocity derived from the differential timing analysis.

The Figure 3.17 shows data coming from the FGM and FPI experiments on-board MMS-1

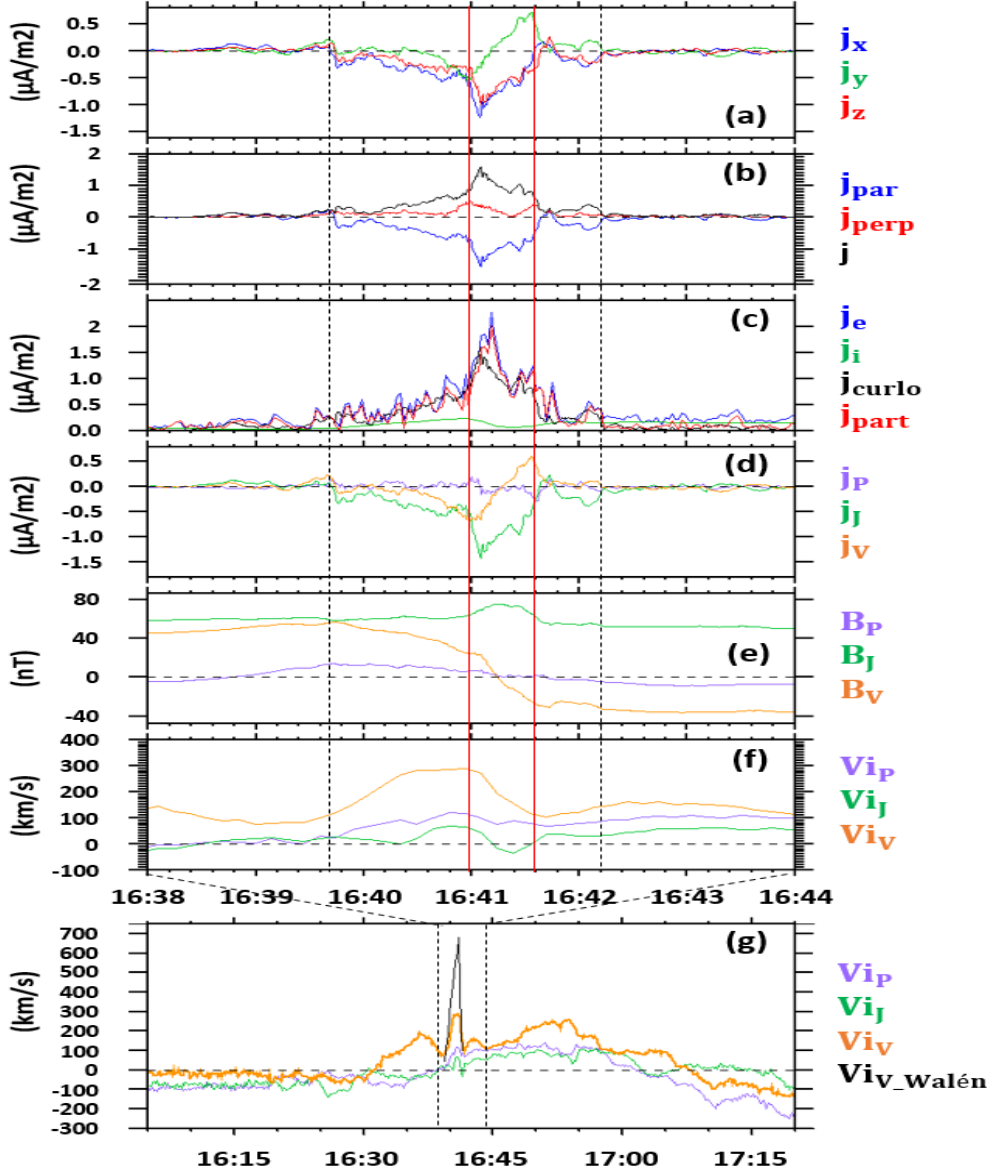


Figure 3.17 – Data from MMS1 between 14:16:38 and 14:16:44 UT (a) current density components in the GSE coordinates system, (b) parallel, perpendicular and the total current densities, (c) electrons and ions current densities as well as the current density obtained from the curlometer technique and the current density obtained from  $ne(V_i - V_e)$ , (d) current density components in the PCS frame (obtained from the curlometer technique), (e) magnetic field components in the PCS frame, (f) ion velocity components in the PCS frame, (g) ion velocity components in the PCS frame between 14:16:05 and 14:17:20 UT.

for a 6-second period including the current structure observation. The GSE coordinates of the current density (from curlometer technique) are represented in panel (a). A correlation between  $J_x$  and  $J_z$  is clearly visible and  $J_y$  exhibits a bipolar signature. As showed in panel (b) the current was mostly parallel to the magnetic field. In panel (c), the magnitude of the

current density obtained from the curlometer technique  $J_{curl}$  (FGM data) and the one directly computed from the particle measurement (FPI data) are compared.  $J_i$  (green) is the ion current,  $J_e$  (blue) the electron current and  $J_{part}$  is obtained from  $ne(V_i - V_e)$ . It appears clearly that the current was carried by the electrons while the ion contribution was almost negligible.

The panel (d) displays the current density (from the curlometer technique) in the PCS frame. The spacecraft reached the structure around 14:16:39.70 UT (time marked by the first black dashed vertical line) as indicated by the little jump seen on  $J_J$ ,  $J_V$  and  $J_{II}$ . Then, the satellites recorded a gradual increase (in absolute value) of the main current component and a sharp peak between 14:16:40.96 UT and 14:16:41.54 UT (times indicated by the red vertical lines). Eventually, MMS-1 exited out of the current structure around 14:16:42.22 UT (time marked by the second black dashed vertical line). Encircling the main current peak, a bipolar secondary current was measured.

Multiplying the 2.52 s duration of the current structure crossing (interval between the pair of black dashed vertical lines in Figure 3.17) with the propagation velocity of  $67 \text{ km/s}$ , we find that the spatial scale of the entire current structure is about  $169 \text{ km}$ . This is about  $\sim 3$  to 4 times the  $\sim 45 \text{ km}$  Larmor radius of thermal protons at the time of the current sheet encounter (see Figure 3.19-(c)). The crossing of the main current peak, as indicated between the two vertical red lines in Figure 3.17, lasted 0.58 seconds, which corresponds to  $\sim 39 \text{ km}$ . That is, the dimension of the main current peak was smaller than the proton Larmor radius. The panel (e) shows the PCS magnetic field components. We note that the  $B_P$  changes remained very small. Similarly,  $B_J$  was also roughly constant except a peak correlated with the main current one. The  $B_J$  peak location is consistent with the magnetic field generated by the bipolar secondary current. The main change of the magnetic field was on the  $B_V$  component suggesting that the main current (along the J-direction) consisted of a current sheet oriented along the V-direction.

The panel (f) displays the ion velocity in the PCS frame. The ion jet is seen as a peak now on the V-component taking place between the first black dashed vertical line and the second red vertical line. The ion jet crossing lasted for  $\sim 1.8$  seconds. Multiplying by the propagation velocity, this gives a thickness of  $120 \text{ km}$ , corresponding to  $\sim 2$  to 3 proton Larmor radii. We note that the ion jet was observed concomitant with the overall current structure,

but that the current peak took place on its downstream side relatively to the structure propagation, i.e., when the main flow component ( $V_{iV}$ ) was decreasing (panel g).

The ion flow velocity is displayed at a larger scale, and in the PCS frame in panel (g) of Figure 3.17). The  $V_{ip}$  component along the propagation direction, which also corresponds to the normal to the current sheet, showed a clear reversal upon crossing the current structure.  $V_{ip}$  was first negative, indicating that the plasma moved slower than the current structure in the propagation direction. After the current sheet and ion jet (observed in  $V_{iV}$ ), it was positive, and the ions moved faster. This means that in the PCS frame (i.e. in the frame moving with the current structure) the flows were converging toward the current structure, suggesting it to be compressed by the surrounding plasma. There was also a flow reversal along the main current direction, as indicated by the reversal in the  $V_{ij}$  component. This suggests that there was also a flow shear along the current structure, in addition to the compression. Around 14:17:05-14:17:10 UT, i.e. just after  $T_5$ , all flow components reversed. This is interpreted as indicating that the spacecraft re-entered into the inner LLBL.

### 3.7. DISCUSSION AND INTERPRETATION

#### 3.7.1. PHENOMENOLOGICAL INTERPRETATION

The event analyzed in this study exhibits some features apparently similar to FTEs at first glance, i.e. bipolar variation of a magnetic field component and a peak in the magnetic field strength. However, a more detailed examination showed that it cannot be interpreted as a single FTE entity consisting of a single helicoidal flux tube. The main reasons are the following:

1. The bipolar change in the magnetic field did not occur in the expected direction normal to the magnetopause.
2. A strong and thin current structure and a localized ion jet, were detected near the center.
3. The electron pitch-angle distributions indicate that the event did not consist of a unique and homogenous structure with a single connectivity as expected for a large-

scale flux rope.

Before proposing an alternative interpretation, let us first summarize the main features of the event. Times  $T_0$  to  $T_5$  mentioned below refer to the vertical dashed lines in Figures 3.11, 3.12 and 3.13.

- The event took place during the passage of an interplanetary magnetic cloud. The solar wind/magnetosphere coupling was intense, with all three GSE components of the IMF being negative. The solar wind pressure and the Alfvén Mach number had very low values.
- The event occurred when the spacecraft were located in the Low Latitude Boundary Layer (LLBL).
- $T_0 \rightarrow T_1$ : The first signature consisted of a change in the magnetic field only, suggestive of remote sensing of the structure propagating toward the spacecraft.
- $T_1 \rightarrow T_2$ : The spacecraft entered a flux tube ( $FT_A$ ) mainly characterized by accelerated magnetosheath electrons exhibiting an anisotropy in the direction parallel to the magnetic field. Moreover, trapped magnetospheric electrons were continuously measured in  $FT_A$ . The density was slightly enhanced and  $B_{Y_{GSE}}$  was positive. Ions first streamed antiparallel to the magnetic field and then perpendicular in the duskward ( $Y_{GSE}$  or  $-M$ ) direction. A trapped population of suprathermal electrons was continuously measured in this flux tube.
- $T_3 \rightarrow T_4$ : In the second part of the event, the spacecraft crossed a very different flux tube ( $FT_B$ ). There was no trapped electron population and the anisotropy of the accelerated magnetosheath was in the opposite sense, in the antiparallel direction.  $B_{Y_{GSE}}$  was the main component of the magnetic field and was negative. The density was higher with values close to the ones measured inside the outer LLBL, between 13:45 and 14:00 UT for example. The plasma flow was in the northward and duskward direction.
- $T_2 \rightarrow T_3$ : Between these two flux tubes, there was a strong and thin current sheet where the magnetic field rotated sharply. A strong and localized duskward ion jet

along the  $Y_{GSE}$  direction was also observed, qualitatively consistent with a reconnection process occurring inside the current sheet owing to the sharp  $B_Y$  reversal. In the frame moving with the structure the surrounding plasma flow was converging towards the current sheet. The current sheet was thus being compressed.

We interpret this sequence of observations as the signature of the successive crossing of the two flux tubes by the spacecraft. These two flux tubes may have been generated by multiple sequential reconnection process, which is expected to occur under strong  $B_Y$  and negative  $B_Z$  IMF conditions, as was observed for a long time around the event [e.g. Raeder (2006); Pu et al. (2013)]. The first flux tube ( $FT_A$ ) contained trapped electrons. This implies that this flux tube has a different history and connectivity compared to the second flux tube which rather contained only magnetosheath electrons with largely different pitch angle properties [Pu et al. (2013)]. A current sheet formed at the interface between the two flux tubes. As shown by the changes in the ion velocity component along the propagation direction (Figure 3.17-g), the second flux tube ( $FT_B$ ) was moving faster than the first one ( $FT_A$ ). This resulted in an interlaced magnetic structure and associated complex 3D geometry, as has been previously studied with Cluster data [Louarn et al. (2004)]. The observed compression is likely at the origin of the current sheet formation and of the possible reconnection occurring inside as described next. Figure 3.18 shows a sliced schematic view of the crossing in the PCS frame. The spacecraft started in the low density flux tube  $FT_A$  at  $T_1$ . The  $V$  component of the magnetic field was positive inside  $FT_A$ . An ion jet, as represented by red arrows with a yellow outline, was observed inside the current sheet (which is about 169 km thick). At the second edge of the jet, the spacecraft crossed a complex current structure (between  $T_2$  and  $T_3$ ). It consisted of a strong and peaked current sheet directed in the  $-\mathbf{U}_J$  direction encircled by a pair of current sheets of opposite polarities along the  $\mathbf{U}_V$  direction. Between  $T_3$  and  $T_4$ , the spacecraft were in  $FT_B$ , where the  $V$  component of the magnetic field is negative. The combined effect of opposite (bipolar) currents as observed in the  $\mathbf{U}_V$  direction was to produce an enhancement of the positive  $B_J$  component in between them (as represented by the green arrows). In doing so, these currents directly supported the rotation of the magnetic field from the  $FT_A$  to the  $FT_B$  orientations. This enhancement in the  $B_J$  component is clearly seen in Figure 3.17-f as a  $15 \sim 20 nT$  peak superimposed on top of the larger-scale constant  $B_J \sim 50 nT$ . The red vectors in the  $\pm \mathbf{U}_V$  directions illustrate

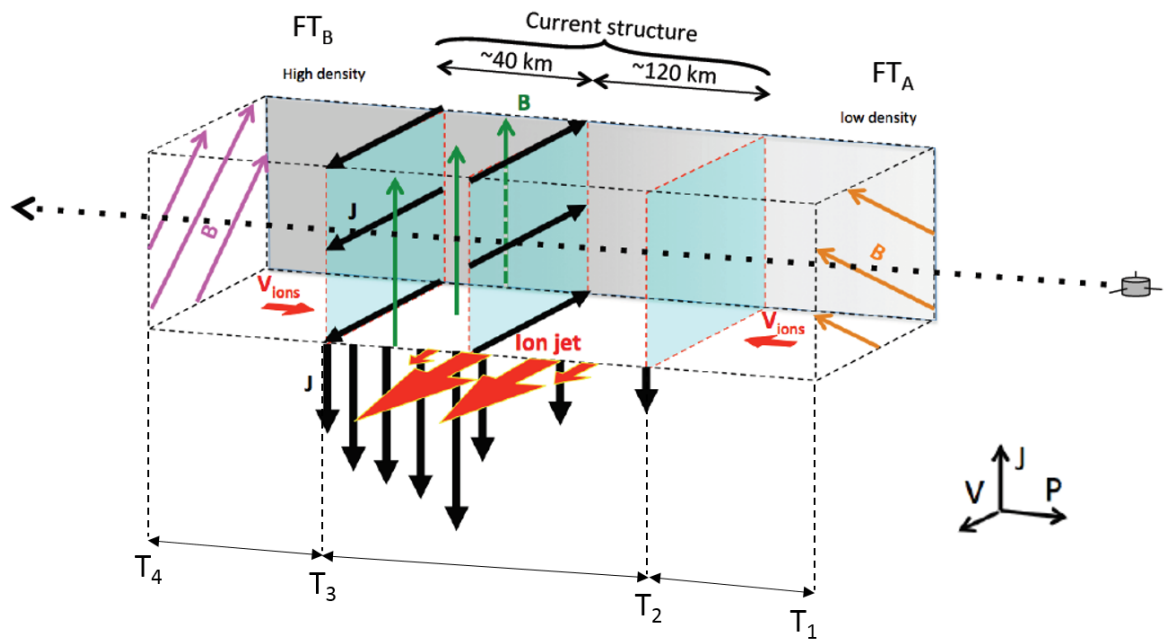


Figure 3.18 – A schematic view of the crossing of the current structure in the PCS frame. The orange, green and magenta arrows show the magnetic field orientation in the  $FT_A$ , current structure and  $FT_B$  respectively. The black arrows in the  $\mathbf{U}_J$  ( $\mathbf{U}_V$ ) direction correspond to the main (bipolar) current density. The two oppositely directed red arrows in the  $\mathbf{U}_P$  direction illustrate the compression of the current structure. The red arrows with yellow edges show the ion jet observed in the current structure. The spacecraft trajectory across the structure is represented by the dashed black arrow.

the compression of the current structure by two oppositely-directed flows (which converge toward it).

### 3.7.2. POSSIBLE RECONNECTION AT THE THIN CURRENT SHEET

Reconnection driven by compression at current sheets formed by the interaction of plasma flows have been suggested for interpreting spacecraft observations from the magnetopause [Øieroset et al. (2016)], in the magnetotail [Alexandrova et al. (2016)] and simulation results as well [Oka et al. (2010); Huang et al. (2014)]. Simulations have been performed in particular to study the coalescence of magnetic islands, and showed features similar to the ones identified in this event. This is true, in particular, for the formation of a thin current sheet with an exhaust in the transverse direction [Zhou et al. (2014)].

Qualitatively, the local conditions satisfied at the interface of coalescing magnetic islands are somewhat similar to those observed in our event. Locally, this corresponds to the interaction between two disconnected magnetic flux tubes pushed against one another by the differential plasma flows in which they are imbedded. MMS measurements permitted a detailed analysis of such a case, but with some conditions specific to the event: the current sheet was characterized by a large density jump and a magnetic shear angle of only  $\sim 73$  degrees as compared with 180 degrees in published simulations with comparable densities.

The process at the origin of the ion jet observed inside the first current sheet was likely magnetic reconnection driven by the compression of the two distinct sets of open field lines. This is partially supported by the Walén test results that are superimposed on the main jet velocity component in Figure 3.17-g. Walén tests [e.g. Phan et al. (2004)] were performed with positive and negative correlations on the Earthward (upstream relative to the structure propagation) and Sunward (downstream) sides of the exhaust, respectively. The exhaust was observed between 14:16:39.7 and 14:16:41.7 UT. This is presented in Figure 3.17-g with  $V_{Ions} - V_{HT} = \pm V_A$ , where  $V_{Ions}$ ,  $V_{HT}$ , and  $V_A$  are the bulk ion, deHoffman-Teller and Alfvén velocity vectors, respectively. The Walén test predicts an ion jet with amplitude  $\sim 688$  km/s. This is larger than the amplitude of the observed jet. The correlation coefficient is of  $-0.92$  and the slope is of  $-0.68$  for the entry to the exhaust between 14:16:39.7 and 14:16:40.95 UT. For the exit from the exhaust, between 14:16:40.95 and 14:16:41.7 UT, the Walén relation provides a correlation coefficient of  $0.92$  with a slope of  $0.18$ , which is



much lower than the ideal value  $\sim 1$ . Although the Walén test shows that the ion bulk flow is not as large as expected, this may be due to the proximity to the X-line [Phan et al. (2016)] because it means that the ion outflow had not yet reached its full speed and is not yet accelerated to the local Alfvén speed.

To support this hypothesis, we note that with densities of 2 and  $6 \text{ cm}^{-3}$ , as measured each

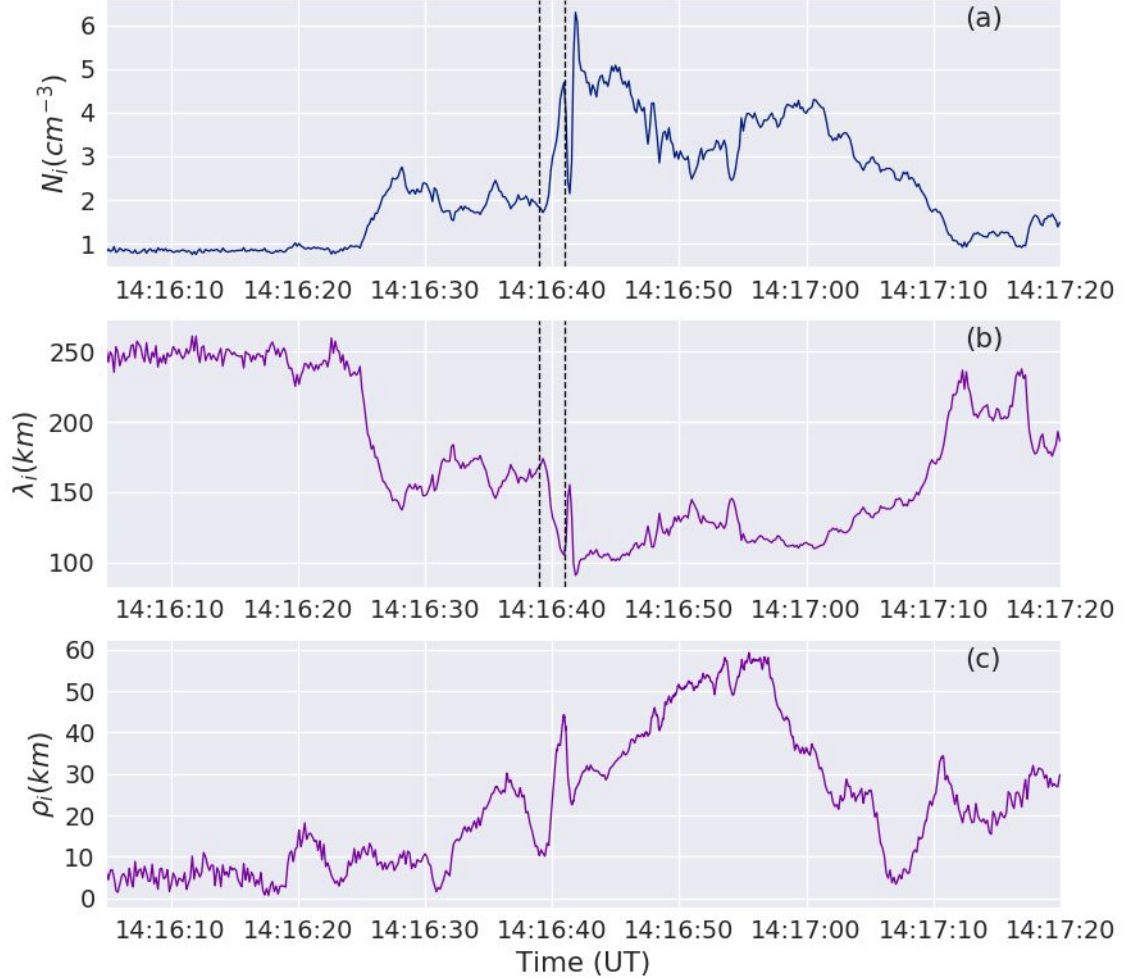


Figure 3.19 – (a) Ion density, (b) Ion skin depth between and (c) the protons Larmor radius 14:16:05 and 14:17:20 UT.

side of the exhaust at 14:16:39.7 UT and 14:16:41.7 UT, the typical ion skin depth  $\lambda_i$  is estimated as 100–155 km and is shown in Figure 3.19. The jet thickness is thus estimated to be approximately 120 km, or about  $0.8 - 1.3\lambda_i$ . Such a thickness implies that the spacecraft are very close to the X-line ( $5 - 8\lambda_i$  or  $\sim 840 \text{ km}$ ), which is consistent with the ion jet not being fully developed yet and thus with the over-estimation of the ion speed from the Walén test. One important signature magnetic reconnection is the decoupling of ions and electrons in

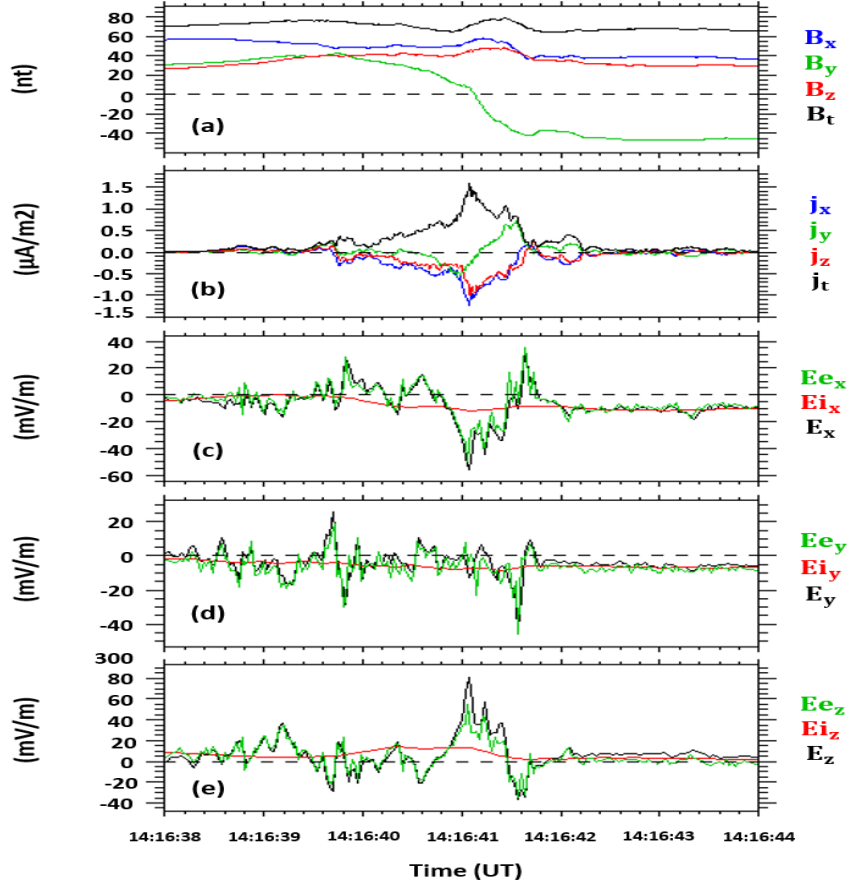


Figure 3.20 – Between 14:16:38 and 14:16:44 UT: (a)  $\mathbf{B}$  data, (b) FPI currents, (c,d,e) comparison between EDP electric field data (black),  $-\mathbf{V}_e \times \mathbf{B}$  (green) and  $-\mathbf{V}_i \times \mathbf{B}$  (red).

their corresponding diffusion regions. Figure 3.20 shows, respectively, the magnetic field components and amplitude, the current density, and a comparison between the electric field components and  $\mathbf{V}_e \times \mathbf{B}$  and  $\mathbf{V}_i \times \mathbf{B}$ . Panels (c) to (e) in Figure 3.20 show that the  $\mathbf{V}_i \times \mathbf{B}$  significantly deviated from  $\mathbf{E}$  while  $\mathbf{V}_e \times \mathbf{B}$  followed  $\mathbf{E}$  as the spacecraft crossed the current structure. This means that the frozen-in condition for ions was violated for this interval. Therefore, ions (red curves) were decoupled from the magnetic field at the center of the structure while the electron (green curves) were still frozen in. As discussed in section 1.2.5, a positive value of  $\mathbf{J} \cdot \mathbf{E}'$  (where  $\mathbf{E}' = \mathbf{E} + \mathbf{V}_e \times \mathbf{B}$ ) is consistent with magnetic reconnection. Figure 3.21-(d) to (g) shows, for MMS1-2-3 and 4, respectively,  $\mathbf{J} \cdot \mathbf{E}'$  which corresponds to the energy conversion rate. This term quantifies the energy transfer between the electromagnetic fields and the plasmas. In the reconnection dissipation region,  $\mathbf{J} \cdot \mathbf{E}'$  is supposed to be positive because magnetic reconnection is known to be a dissipative process that converts magnetic energy into mechanical energy.

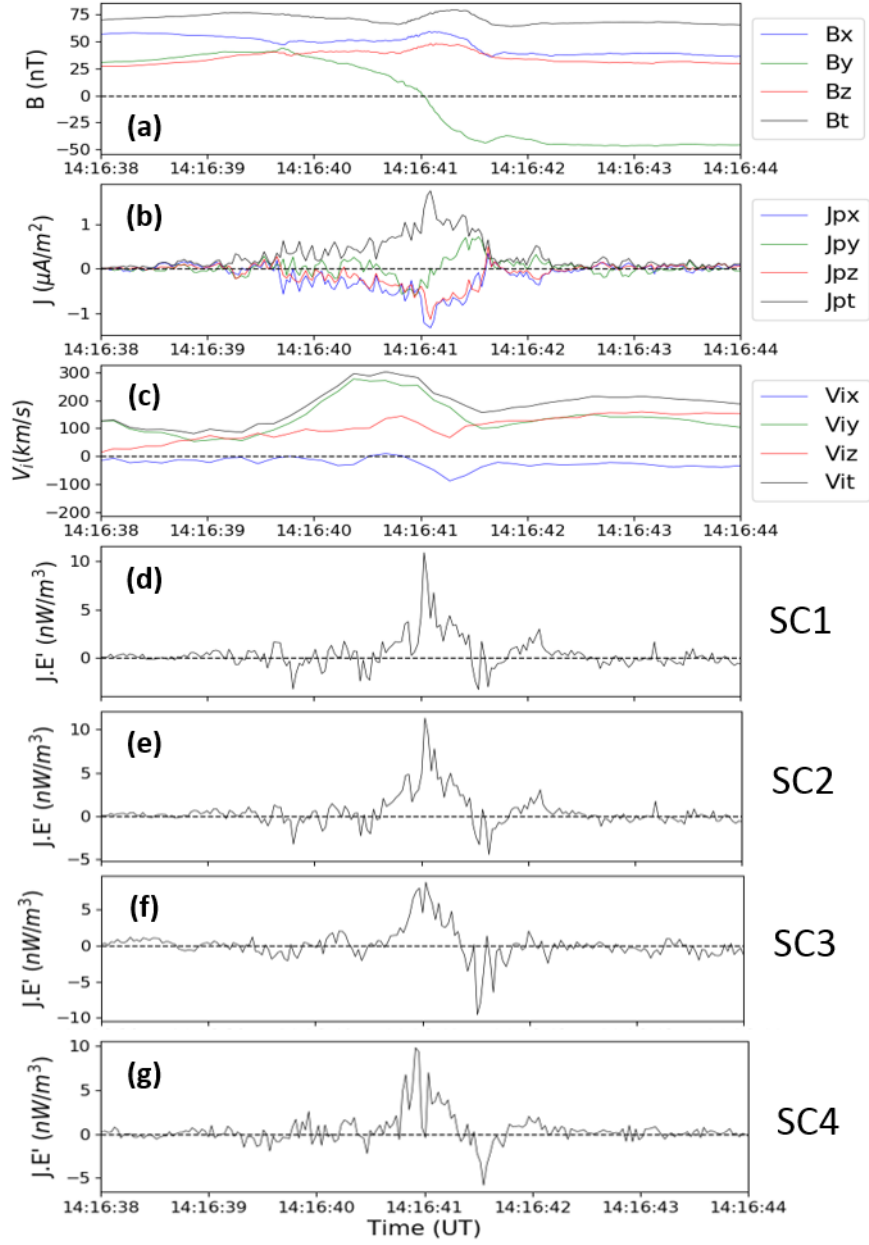


Figure 3.21 – Between 14:16:38 and 14:16:44 UT: (a)  $\mathbf{B}$  data, (b) current density  $qn(V_i - V_e)$  obtained from the computed moments of ion and electron distribution functions, (c) ion velocity, (d) to (g)  $\mathbf{J} \times \mathbf{E}'$  for MMS1, MMS2, MMS3 and MMS4.

When the current sheet is crossed,  $\mathbf{J} \cdot \mathbf{E}'$  is significantly different from zero. It reaches values of  $\sim 11 \text{ nW/m}^3$  for MMS2 and of  $\sim 9 \text{ nW/m}^3$  for MMS3. This strong positive value of  $\mathbf{J} \cdot \mathbf{E}'$  is a strong indicator for magnetic energy dissipation which suggests therefore that magnetic reconnection occurred in this region.

### 3.8. SUMMARY AND CONCLUSION

We have studied in detail what initially looked like a classic FTE at the Earth's dayside magnetopause. Thanks to its high-resolution measurements of MMS, our analysis revealed the following unusual properties:

- The large-scale magnetic field bipolar signature was not found in the component normal to the nominal magnetopause surface  $\mathbf{N}$  that was directed essentially along  $X_{GSE}$ , but rather in the  $B_{Y_{GSE}}$  component, i.e. perpendicular to  $\mathbf{N}$ ;
- The densities and pitch angle distributions of suprathermal electrons show that the current sheet separated two distinct plasmas with different properties and magnetic connectivities;
- An intense and complex current structure was localized at the center of the structure and allowed the transition between the two flux tubes having very different topologies. This current was responsible for the  $\mathbf{B}$ ;
- This current was carried by electrons. Although the scale of the structure is approximately three times the ion Larmor radius, the structure possesses smaller scale substructures, smaller than the ion Larmor radius. The intense current sheet was associated with a strong transverse flow (along  $V_{Y_{GSE}}$ ) consistent with expectations from magnetic reconnection therein.

Our interpretation is that these properties are incompatible with a classic, single FTE structure. Besides, the coalescence process, which involves a reconnection between two magnetic islands, could be a potential interpretation of these observations. But a double bipolar signature belonging to two distinguishable magnetic islands was not observed. Thus, the

coalescence of magnetic islands and the reconnection inside a FTE do not fit all the observations. The observations were suggested to be rather consistent with a complex, three-dimensional interaction of two distinct flux tubes. This compressive interaction led to the formation of a thin and complex current structure between two flux tubes of very different orientations ( $73^\circ$  magnetic shear angle) which mimicked the bipolar magnetic structure and the enhanced core magnetic field, both expected for classic FTEs. The strong magnetic field pile-up and ensuing thin current sheet also appeared to have triggered magnetic reconnection at the interface. In the next Chapter, we will present a study of the waves associated with this reconnecting current sheet.

# 4

## PLASMA WAVES STUDY FOR THE EVENT OF 7 NOVEMBER 2015

### 4.1. INTRODUCTION

In this chapter we will present our study on the plasma waves associated with the event that was discussed in Chapter 3. We will focus on the waves that were observed around the reconnecting current sheet that was detected on 7 November 2015 around 14:16:41 UT as a result of the interaction of two flux tubes (refer to Chapter 3 for more details).

### 4.2. INSTRUMENTATION

The observations in this Chapter were provided by the MMS spacecraft [Burch et al. (2016)]. We used magnetic field measurements from the fluxgate magnetometers [Russell et al. (2016); Torbert et al. (2016)] at a resolution of 128 Hz. We also analyzed ion and electron measurements from the Fast Plasma Instruments with a resolution of 150 milliseconds for ions and 30 milliseconds for electrons [Pollock et al. (2016)]. The Electric Double Probe measurements (EDP) provides three-dimensional quasi-static and high-frequency electric field measurements with 8192 vectors/s in burst mode [Ergun et al. (2016); Lindqvist et al. (2016b)]. Three dimensional measurements of the high-frequency magnetic field fluctu-

ations are provided by the Search Coil Magnetometers (SCM) with same sampling rates (8192 vectors/s) as EDP and with a high pass filtering above 1Hz so covering the frequency range [1Hz-4kHz] [Le Contel et al. (2016)].

### 4.3. MAIN FEATURES OBSERVED AROUND THE CURRENT SHEET

Before we begin studying the waves, it is useful to consider the main relevant features of the event analyzed in Chapter 3 which are summarized in Figure 4.1 presenting data around the current sheet between 14:16:38 and 14:16:44 UT. The  $B_Y$  component of the magnetic field exhibited a bipolar signature. Its value varied from  $\sim 40nT$  to  $\sim -40nT$  as the spacecraft crossed the current sheet. Before the current sheet crossing, the density was about  $\sim 2cm^{-3}$ . Then, it increased to  $\sim 6cm^{-3}$  at 14:16:40.9 UT. Another peak of density of  $\sim 8cm^{-3}$  was observed at 14:16:41.8 UT. A minimum of density, of  $\sim 3cm^{-3}$ , was revealed at 14:16:41.4 UT between these two maxima. After the current sheet crossing, the density reached again the value of  $\sim 6cm^{-3}$ . Hence, the density profile was weakly asymmetric across the current sheet which is consistent with it being generated at the interface of two flux tubes. An ion jet was observed in the low-density part of the event between 14:16:39.7 and 14:16:41.7 UT as seen in panel (f) where the y-component of the ion velocity was close to  $\sim 300km/s$ . The width of the ion jet was found to be of  $120km$  which is about  $0.8 - 1.3\lambda_i$  where  $\lambda_i$  is the ion inertial length each side of the exhaust as shown in Chapter 3. The shear angle between the magnetic fields on the two sides of the current sheet was about  $\sim 73^\circ$ . A total magnetic field enhancement was observed at the center of the current sheet. Figure 4.1-(g) showed that the parallel electron temperature was enhanced on both sides of the current sheet. The electron distribution was anisotropic as the perpendicular temperature of electrons was significantly lower than the parallel temperature.

## 4.4. PLASMA WAVES

### 4.4.1. WHISTLER WAVES

Figure 4.2 shows MMS1 measurements recorded around the current sheet. Power spectra of electric and magnetic fields calculated from MMS1 by using fast Fourier transform (FFT) are displayed in Figure 4.2-(d) and (e), respectively. Panel (d) reveals an intense broadband

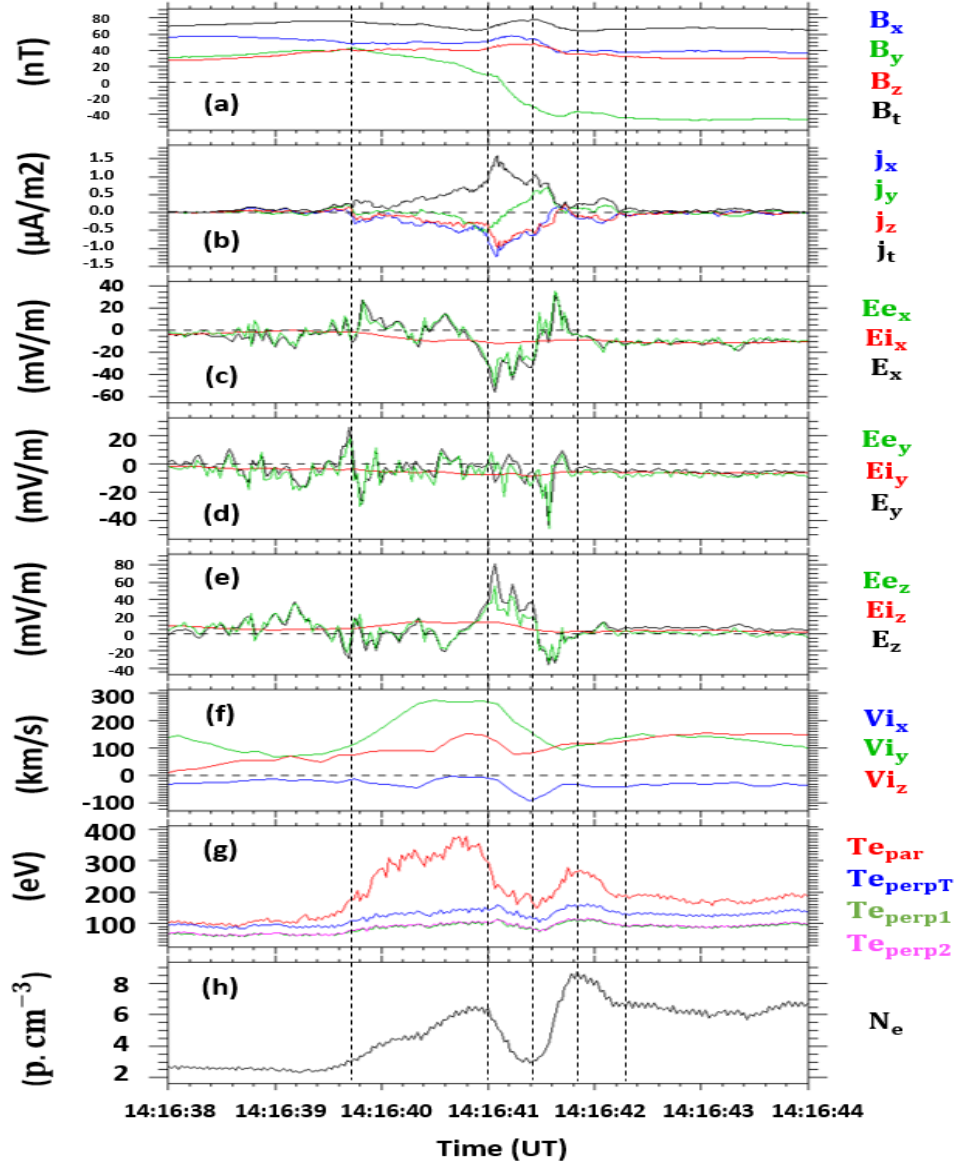


Figure 4.1 – Between 14:16:38 and 14:16:44 UT: (a)  $\mathbf{B}$  data, (b) FPI currents, (c,d,e) comparison between EDP electric field data (black),  $-\mathbf{V}_e \times \mathbf{B}$  (green) and  $-\mathbf{V}_i \times \mathbf{B}$  (red), (f) ion velocity, (g) parallel and perpendicular electron temperatures and (h) electron density.

activity up to 400 Hz between 14:16:38 and 14:16:42 UT. Two wave intensifications, marked by two black ellipses in panel (e), were observed between  $\sim 300$  and  $\sim 500$  Hz. These frequencies are below the electron gyrofrequency ( $f_{ce} \sim 1500 - 2000$  Hz) but higher than the lower hybrid frequency ( $f_{LH} \sim 40 - 50$  Hz) which define the whistler waves frequency domain ( $f_{LH} \ll f \ll f_{ce}$ ). The waveangle values were close to zero as illustrated in the black ellipses in panel (f). The waves were thus propagating along the magnetic field direction. The black ellipses in panel (g) shows that the distribution of wave ellipticity in the plasma



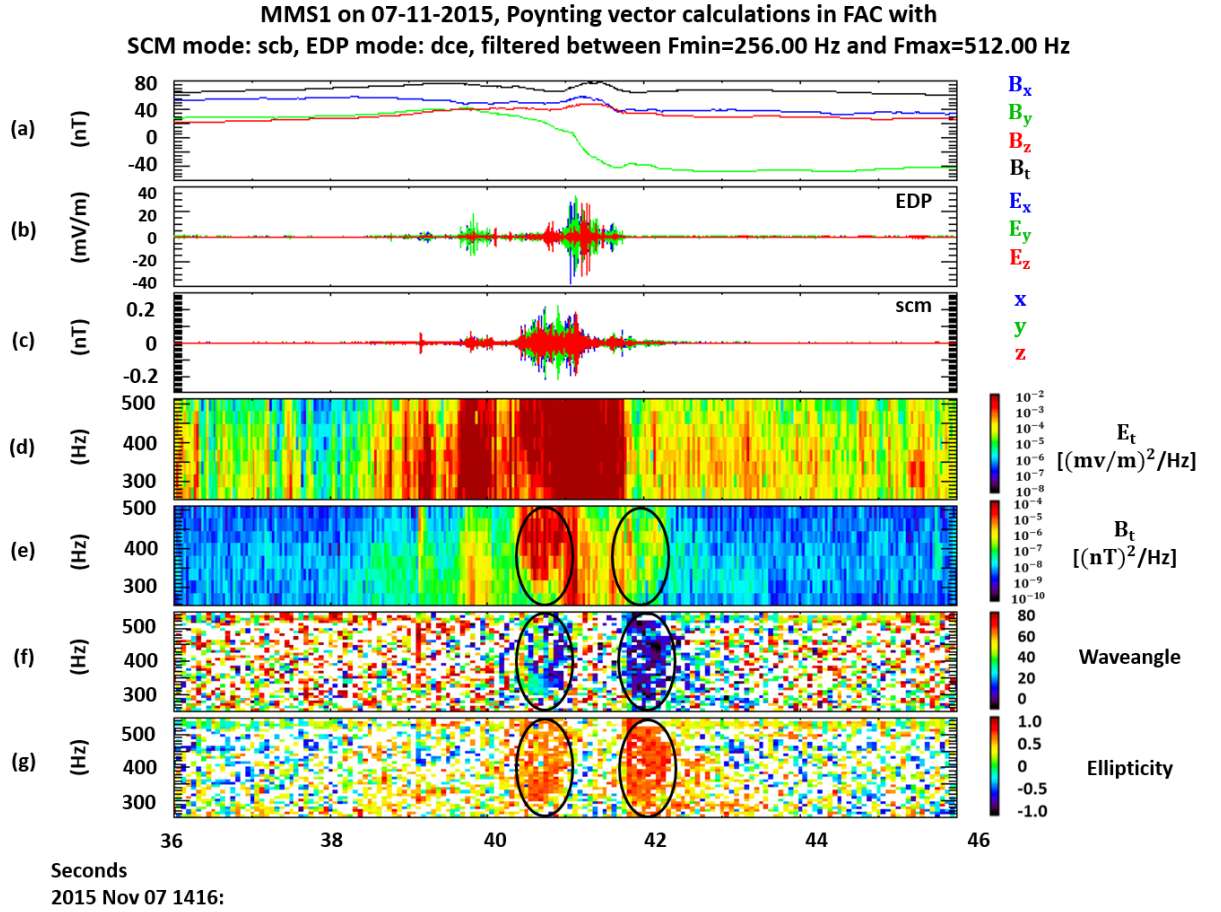


Figure 4.2 – MMS1 observations on 7 November 2015 between 14:16:36 and 14:16:46 UT: (a) magnetic field components and amplitude, (b,c) band-pass filtered between 256 and 512 Hz EDP and SCM waveforms in MFA (d, e) omnidirectional E and B PSD, (f) waveangle and (g) Ellipticity.

frame is strongly peaked at +1, suggesting that the waves were right-handed circularly polarized. This set of observations observations means that these waves are electromagnetic whistler waves.

The spectrograms of the poynting vector components ( $S_X$ ,  $S_Y$  and  $S_Z$ ) are shown in Figure 4.3 in the Magnetic Field Aligned (MFA) coordinates system. This coordinate system is defined such as the  $Z_{MFA}$  axis is directed along the background magnetic field  $\mathbf{B}_0$ . The second axis  $X_{MFA}$  is taken in the direction of  $X_{GSE}$  and the third axis  $Y_{MFA} = Z_{MFA} \times X_{MFA}$  completes the right-handed frame. The positive value of  $S_Z$  for the whistler waves frequencies (white ellipse in Figure 4.3-(d)) reveals that the whistler waves were propagating in the direction of the magnetic field.

Panels (a) to (d) in Figures 4.4, 4.5 and 4.6 show the magnetic field components obtained from FGM, the magnetic field filtered between 40 and 100 Hz from SCM, the electric field

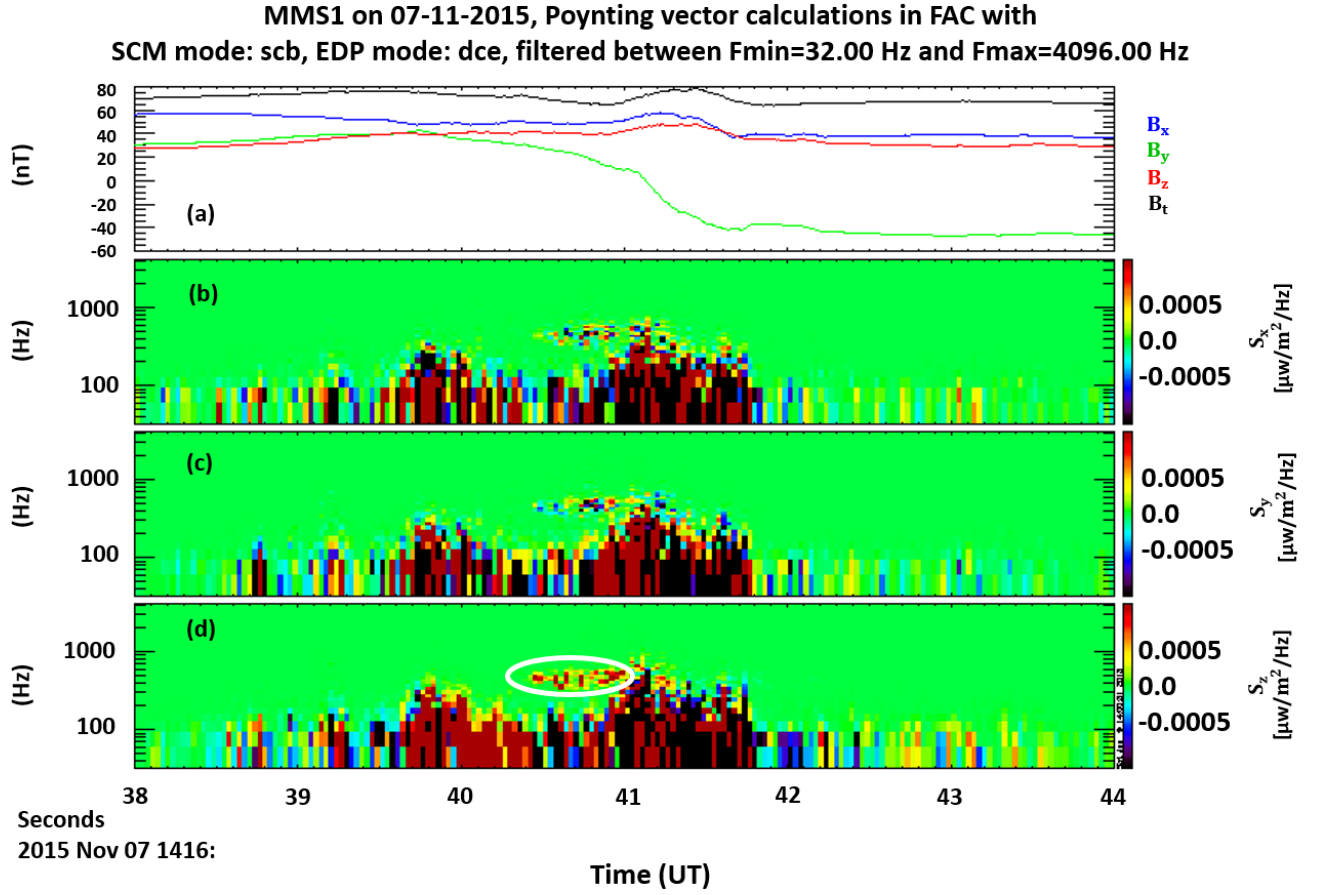


Figure 4.3 – (a) magnetic field components and amplitude in GSE coordinates, (b) to (d) the components of Poynting flux of electromagnetic fields.

components from EDP and the parallel electric field along with its associated error bars (pink shading), respectively. Figures 4.4 and 4.6 show the waveforms of the first and second Whistler wave packets, respectively. A zoomed view of Figure 4.4 between 14:16:40.720 and 14:16:40.760 UT is provided in Figure 4.5. Spiky structure of  $E_{\parallel}$  were observed in Figure 4.4-(d). They reached values of  $\sim 25 mV/m$ . Figures 4.5-(d) and 4.6-(d) show that only the first whistler wave packet was associated with spiky bipolar signatures in the electric field. These bipolar spiky structures are interpreted as electrostatic solitary waves (ESWs).

In order to test the mechanism for the whistler waves, we used WHAMP code (Waves in Homogeneous Anisotropic Multicomponent Magnetized Plasma) [Roennmark (1982)] which calculates general wave dispersion relation in plasmas. Whistler waves may be generated

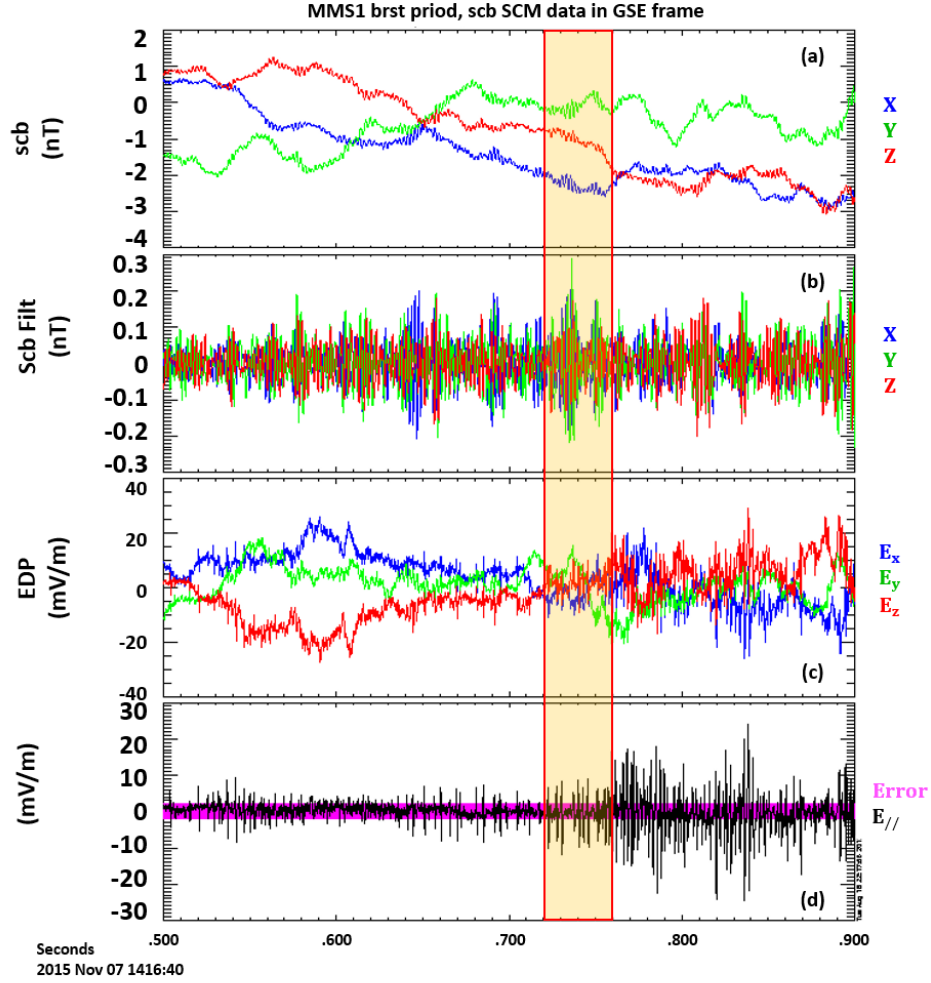


Figure 4.4 – Waveforms of the first Whistler wave packet between 14:16:40.5 and 14:16:40.9 UT in GSE coordinates. (a) the magnetic field components, (b) the magnetic field filtered between 40 and 100 Hz, (c) the electric field components and (d) parallel electric field calculated by using the EDP data and the survey magnetic field and its associated error bars (pink shading).

by electron temperature anisotropy when  $T_{e\perp}/T_{e\parallel} > 1$  where the subscripts denote perpendicular and parallel directions to the magnetic field [kennel and petscheck, 1966]. However, Figure 4.1-(g) shows that this condition is not satisfied. This means that the whistler waves were not locally generated by electron temperature anisotropy.

Electron beams have been also proposed as a possible source for whistler waves [Gary and Wang (1996)]. The observed electron distributions around 14:16:41 UT exhibit a beam-like feature with energies between 100 eV and 400 eV in the parallel direction as evidenced in Figure 4.7. We therefore investigated with WHAMP the plasma instabilities which may develop in the plasma by the observed electron beam.

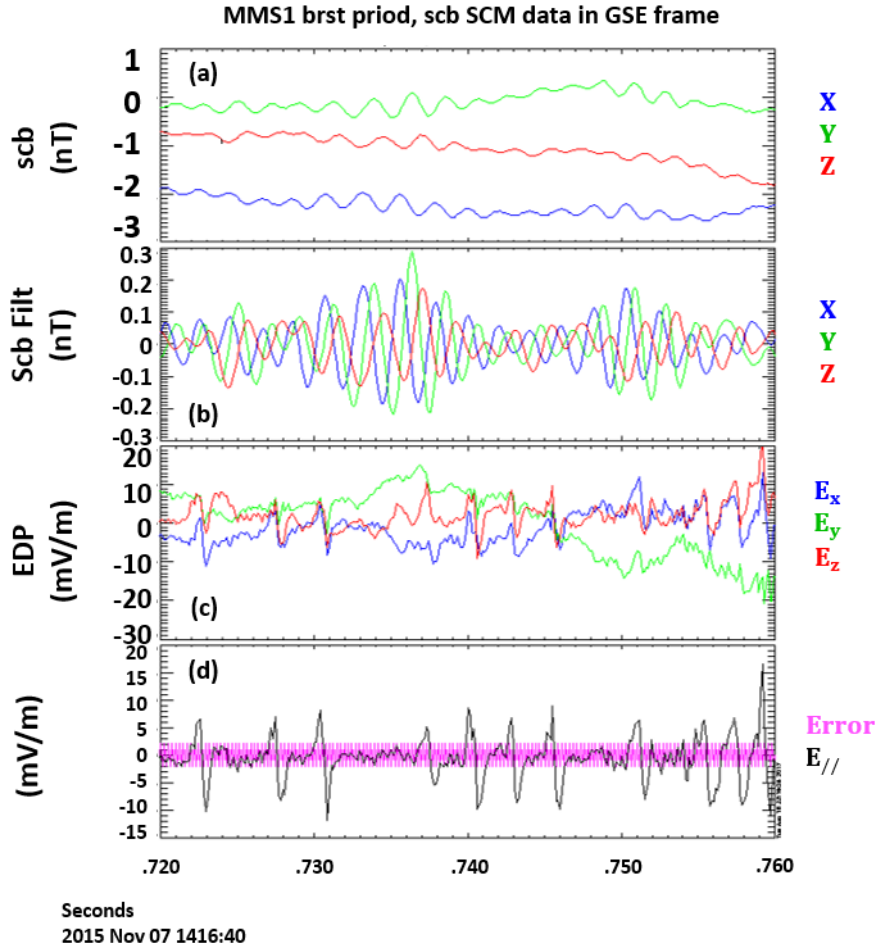


Figure 4.5 – Zoom on the first Whistler wave packet between 14:16:40.72 and 14:16:40.76 UT (yellow shaded area in Figure 4.4). Panels are similar to 4.4.

The modeled distributions included a plasma core and a parallel electron beam. Setting the ambient magnetic field strength  $B_0$  to its observed value, i.e. 65 nT, the stability properties of the plasma were not altered with these distribution functions. However, by reducing the ambient magnetic field strength to 35 nT, the model exhibited emissions in the whistlers frequency range suggesting that the electron beam may generate the observed whistler waves for this value of magnetic field intensity.

The fact that no whistler waves were observed for the local magnetic field intensity ( $B_0 = 65$  nT) but for 35 nT means that the whistler waves were not generated locally but in a region where the magnetic field strength was about 35 nT. This is consistent with the calculated

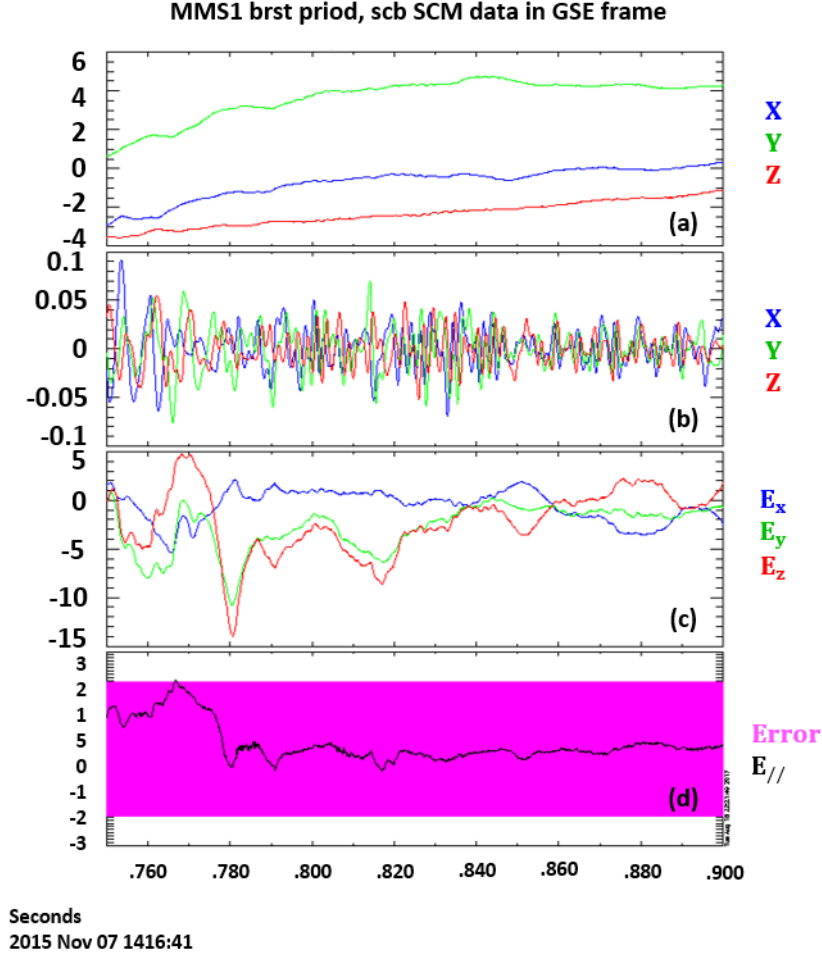


Figure 4.6 – Waveforms of the first Whistler wave packet between 14:16:41.75 and 14:16:41.90 UT. Same legends as Figure 4.4.

wave-particle resonance energy which can be expressed as [Kennel and Engelmann (1966)]:

$$E_{res} = \left( \frac{B_0^2}{2\mu_0 n_e} \right) \left( \frac{\omega_{ce}}{\omega \cos^2 \theta_{kB}} \right) \left( \cos \theta_{kB} - \frac{\omega}{\omega_{ce}} \right) \left[ m + \frac{\omega}{\omega_{ce}} \right]^2 \quad (4.1)$$

where  $B_0$  is the magnetic field field,  $n_e$  is the plasma density,  $\omega_{ce}$  is the electron cyclotron frequency,  $m = 0$  (Landau),  $m = -1$  (normal cyclotron), or  $m = 1$  (anomalous cyclotron) for the different resonances and  $\theta_{kB}$  is the wave propagation angle with respect to the magnetic field. For  $B_0 = 65$  nT, the energy for resonant wave-particle interactions were found to be very far from the observed beam energy (i.e. between 100 and 400 eV). This suggests that the electron beam could not, locally, initiate the waves. However, with  $B_0 = 35$  nT, the predicted resonant energy for observed whistler waves was very close to the observed beam

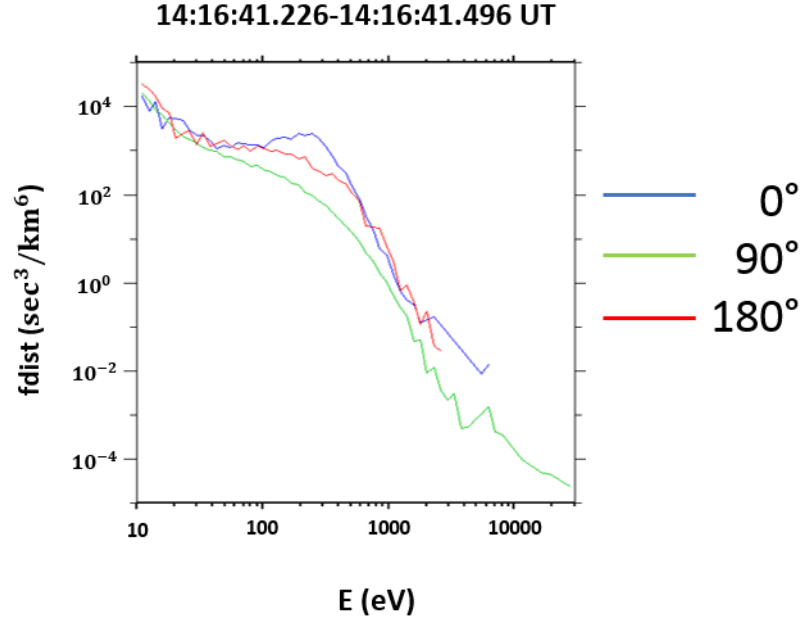


Figure 4.7 – Electron pitch angle distributions averaged between 14:16:41.226-14:16:41.496 UT. Parallel (0°), perpendicular (90°), and anti-parallel (180°) phase space densities are represented by blue, green, and red traces, respectively.

energy and may therefore confirm that the electron beam helped to generate whistlers in a region where the magnetic field intensity was about 35 nT.

This hypothesis is, somehow, consistent with previous studies on possible sources of whistlers on the dayside magnetopause. [Vaivads et al. \(2007\)](#), for example, proposed that, at the Earth's magnetopause, whistler waves can be created along magnetic flux tubes near magnetic field minima. They showed that at the magnetopause, strong whistler emissions can be emitted on newly opened flux tubes through magnetic reconnection. They also showed that the whistler emissions can propagate away from the magnetic field minima. We may therefore think that some local minima of magnetic field exist on each of the flux tubes ( $FT_A$  and  $FT_B$ ), which have been generated by distinct magnetic reconnections, leading to the generation of the whistler waves at these minima (of 35 nT).

#### 4.4.2. LOWER HYBRID DRIFT WAVES (LHDWs)

In the figure 4.8-(a) to (c) are shown the magnetic field data from FGM in GSE coordinates system, the magnetic field from SCM filtered between 40 and 100 Hz (i.e. around the lower hybrid frequency) in MFA, and the electron density from the four spacecraft. The wave-

forms of the lower hybrid drift waves, shown in Figure 4.8-(d) to (g), were obtained by filtering the electric field with a band-pass filter between 40 and 100 Hz which are close to the lower hybrid frequency  $f_{LH}$ . The yellow vertical lines in panels (d) to (g) delimit the LHDW for MMS1, MMS2, MMS3 and MMS4, respectively. The first maximum of density is first detected MMS4, MMS2, MMS3 and MMS 1, respectively. This is the same order of detection of the LHDW. We may then assume that the LHDWs were more probably generated by the density gradient. This density gradient may be created through the interaction between the two flux tubes ( $FT_A$  and  $FT_B$  in Chapter 3). We first analyzed these waves as a single packet. Then, since the amplitude of the fluctuations was much larger between the first and the second yellow vertical lines than between the second and last yellow vertical lines, we also studied the LHDWs as two distinguishable packets. The times corresponding for the LHDW observations for each spacecraft are shown in Table 4.1. We determined the wave

	LHDW		Packet 1		Packet 2	
	$t_i$	$t_f$	$t_i$	$t_f$	$t_i$	$t_f$
MMS1	14:16:40.90	14:16:41.80	14:16:40.90	14:16:41.40	14:16:41.40	14:16:41.80
MMS2	14:16:40.75	14:16:41.75	14:16:40.75	14:16:41.40	14:16:41.40	14:16:41.75
MMS3	14:16:40.75	14:16:41.75	14:16:40.75	14:16:41.40	14:16:41.40	14:16:41.75
MMS4	14:16:40.60	14:16:41.65	14:16:40.60	14:16:41.40	14:16:41.40	14:16:41.65

Table 4.1 – Times corresponding to the observations of the LHDW.

properties, such as phase speed, propagation direction, wavelength, and wave potential using a single-spacecraft method that was proposed by Norgren et al. (2012) (see Chapter 2). The results are shown in tables 4.2 to 4.4 for the four spacecraft. The results shown in Tables 4.2-4.3 are very similar. Conversely, Tables 4.3-4.4 show that the waves properties of the first and second packets of LHDWs are slightly different. One of these differences is the estimated direction of propagation of the waves. The first packet of waves was found to propagate with a positive  $V_y$  component of the phase velocity while the second packet was found to propagate with a negative  $V_y$  component of the phase velocity. The results show that the frequency, phase speed, and perpendicular wavelength estimates are very close for the four spacecraft. Considering the results of Table 4.2, the fluctuations have frequencies of  $\sim 65\text{Hz}$  which are close to  $f_{LH}$ , are propagating perpendicular to the magnetic field toward the dusk side with a phase speed about  $\sim 317\text{ km/s}$ .  $k_{\perp}\rho_e$  was about  $\sim 0.6$  and the perpendicular wavelength  $\lambda_{perp}$  was about  $\sim 5\text{ km}$ . The ratio between the electrostatic po-



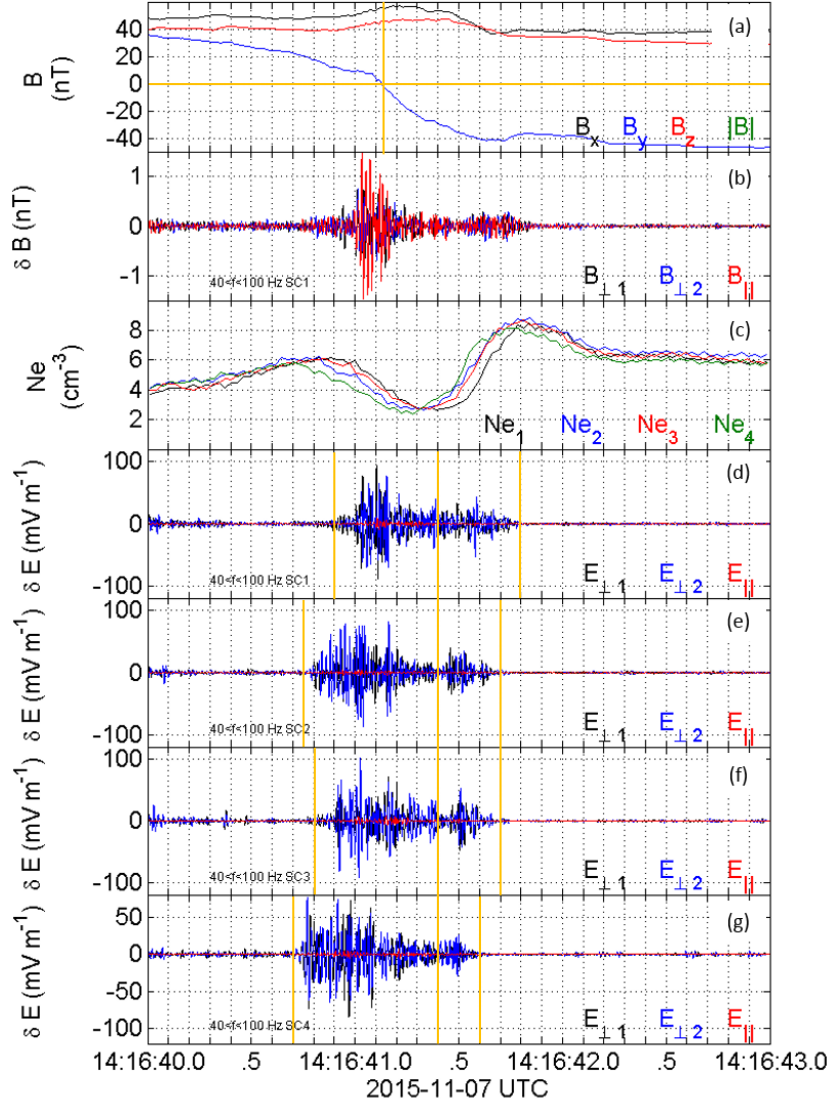


Figure 4.8 – Waveforms of the lower hybrid drift waves in MFA. (a)  $B_X$ ,  $B_Y$  and  $B_Z$ , (b) the magnetic field filtered between 40 and 100 Hz, (c) electron density from the four spacecraft and (d-g) parallel and perpendicular electric field also filtered between 40 and 100 Hz for MMS1, MMS2, MMS3 and MMS4, respectively.

SC	$V_x$	$V_y$	$V_z$	$\ \mathbf{v}\ $	$f(\text{Hz})$	$f_{LH}(\text{Hz})$	$\lambda_{\perp}(\text{km})$	$k_{\perp}\rho_e$	$\delta\phi/T_e$	cc
1	-0.23	0.76	0.46	330.4	65.0	46.8	5.0	0.58	0.63	-0.80
2	-0.09	0.83	0.39	308.1	68.3	47.5	4.5	0.64	0.51	0.820
3	-0.10	0.83	0.37	303.3	64.1	46.5	4.7	0.62	0.52	-0.81
4	-0.19	0.78	0.47	327.6	65.0	47.2	5.1	0.56	0.39	-0.84

Table 4.2 – Properties of the LHDWs in GSE coordinates system for MMS1, MMS2, MMS3 and MMS4, respectively.  $V_x, V_y, V_z$  give the direction of propagation of the waves,  $\|\mathbf{v}\|$  gives its amplitude,  $f$  is the waves frequency,  $f_{LH}$  is the LHDWs frequency,  $\lambda_{\perp}$  is the perpendicular wavelength,  $k_{\perp}\rho_e$  is the position of the maximum growth rate of the waves,  $\delta\phi/T_e$  is the ratio between the electrostatic potential and the electron temperature and  $cc$  is the correlation coefficient between the potential obtained from  $\delta B_{\parallel}$  and from  $\delta E_{\perp}$ .



SC	$V_x$	$V_y$	$V_z$	$\ \mathbf{v}\ $	$f(Hz)$	$f_{LH}(Hz)$	$\lambda_{\perp}(km)$	$k_{\perp}\rho_e$	$\delta\phi/T_e$	cc
1	-0.20	0.90	0.24	376.5	65.0	47.0	5.8	0.50	0.63	-0.89
2	-0.05	0.92	0.19	320.1	68.3	48.1	4.7	0.61	0.51	0.91
3	-0.07	0.93	0.16	320.7	65.1	46.8	4.9	0.59	0.52	0.88
4	-0.18	0.84	0.38	344.2	65.0	47.6	5.4	0.53	0.39	0.89

Table 4.3 – Properties of the first packet of LHDWs in GSE coordinates system for MMS1, MMS2, MMS3 and MMS4, respectively.

SC	$V_x$	$V_y$	$V_z$	$\ \mathbf{v}\ $	$f(Hz)$	$f_{LH}(Hz)$	$\lambda_{\perp}(km)$	$k_{\perp}\rho_e$	$\delta\phi/T_e$	cc
1	-0.75	-0.16	0.64	201.9	93.1	46.6	2.2	1.34	0.11	0.13
2	-0.48	-0.81	-0.32	277.6	56.9	46.3	4.8	0.62	0.16	-0.46
3	-0.78	-0.53	0.32	176.5	54.0	46.0	3.1	0.94	0.18	-0.53
4	-0.70	-0.71	-0.02	262.1	59.4	46.1	4.5	0.66	0.15	0.48

Table 4.4 – Properties of the second packet of LHDWs in GSE coordinates system for MMS1, MMS2, MMS3 and MMS4, respectively.

tential and the electron temperature varies between 0.39 and 0.63.  $\lambda_{perp}$  was significantly lower than the spacecraft separation which was about  $\sim 10km$ .

In the electrons rest frame, the velocity of propagation of the waves  $\mathbf{V}_{\phi}$  is expected to be equal to the ion diamagnetic velocity. We therefore calculated the ion diamagnetic velocity, using two independent relations, in order to check if its value and direction are close to those of the waves. Figures 4.9-(a) and (b) show, respectively, the ion diamagnetic velocity calculated as:

$$\mathbf{V}_{d_{i1}} = \frac{-\nabla \cdot \mathbf{P}_i \times \mathbf{B}}{n_i e B^2} \quad (4.2)$$

and as:

$$\mathbf{V}_{d_{i2}} = \mathbf{V}_{\perp,i} - \frac{\mathbf{E} \times \mathbf{B}}{B^2} \quad (4.3)$$

where all the parameters are averaged over the four MMS spacecraft.  $\mathbf{V}_{d_{i1}}$  and  $\mathbf{V}_{d_{i2}}$  exhibit qualitatively the same behavior, however, the value of the  $y$  component is larger for  $\mathbf{V}_{d_{i1}}$ . It is close to  $\sim -800km/s$  for  $\mathbf{V}_{d_{i1}}$  and  $\sim -600km/s$  for  $\mathbf{V}_{d_{i2}}$ . Figures 4.9 and 4.10 show that the electric drift was nearly equivalent to the ion diamagnetic drift but in the opposite direction ( $+y$ ), which is the same direction of propagation of the LHDWs (Table 4.2).

Since electrons were magnetized, their diamagnetic velocity was very weak and therefore their perpendicular velocity was approximately equal to the electric drift speed (Figures

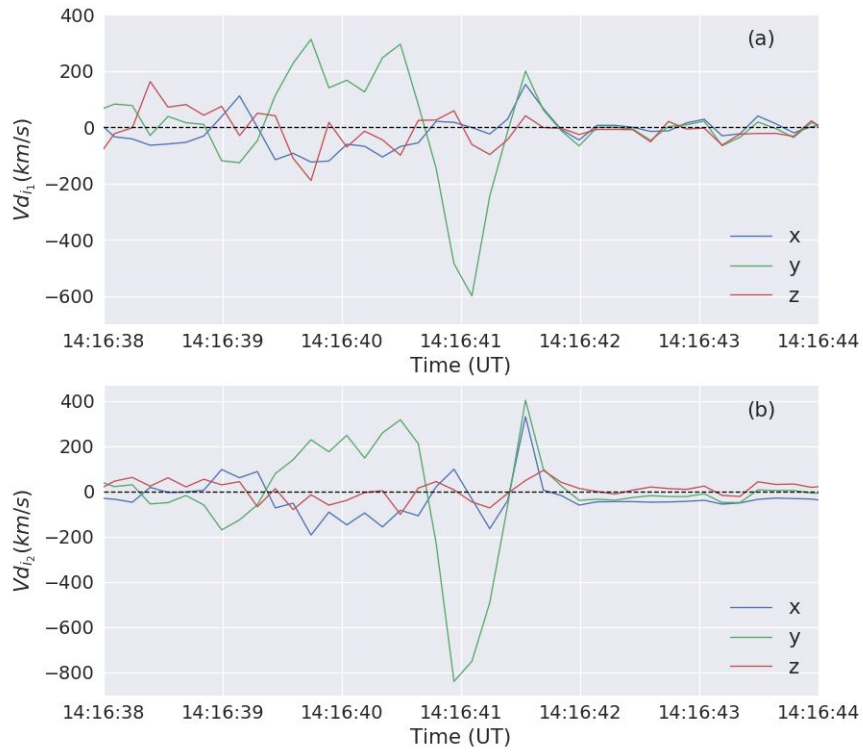


Figure 4.9 – Ion diamagnetic velocity obtained from (a) equation 4.3 and (b) equation 4.2.



Figure 4.10 – Electric drift speed  $(\mathbf{E} \times \mathbf{B})/B^2$ .

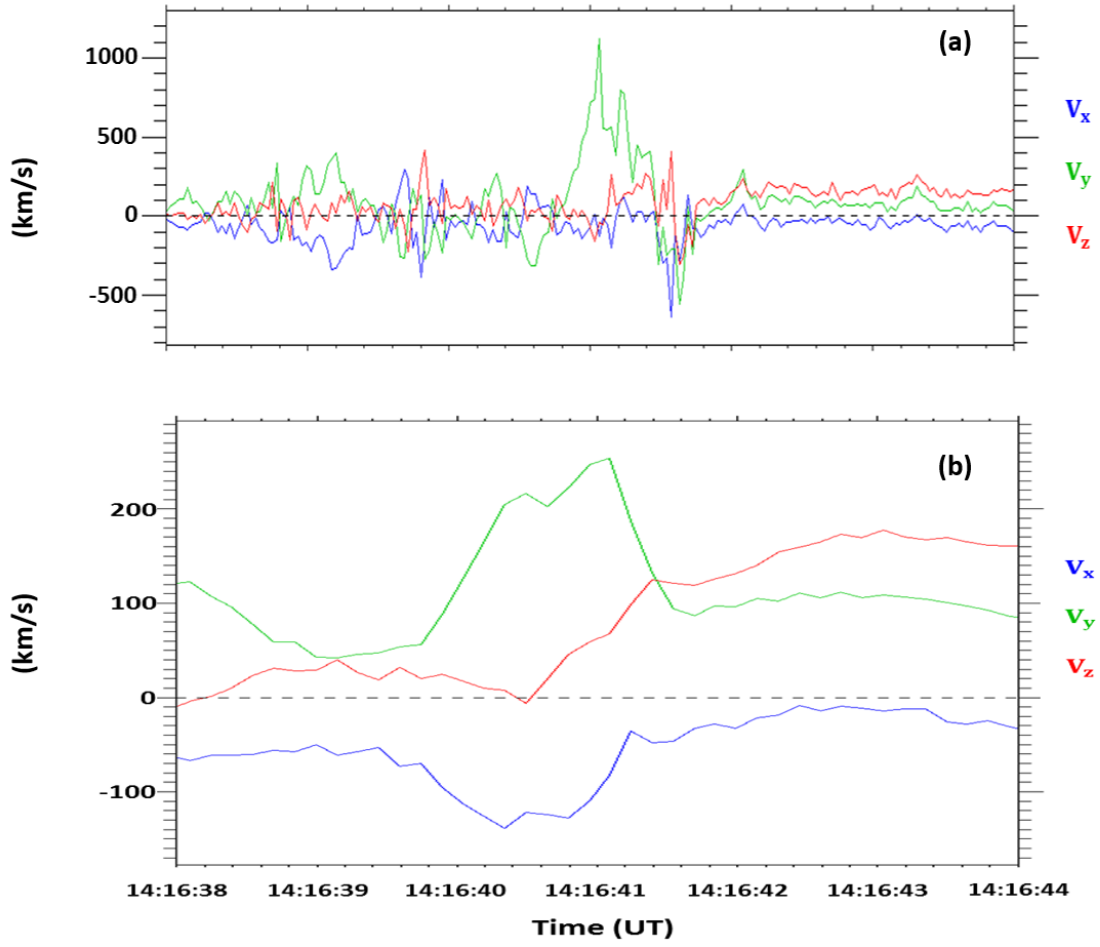


Figure 4.11 – (a) Electron and (b) ion perpendicular velocities in GSE coordinates from FPI.

4.11-(a) and 4.10). If both electrons and ions were magnetized, then they would have the same velocity and propagate at the electric drift speed. The ion perpendicular velocity can be written as:

$$\mathbf{V}_{\perp i} = \mathbf{V}_{d_i} + \frac{\mathbf{E} \times \mathbf{B}}{B^2} \quad (4.4)$$

and is shown in Figure 4.11-(b). The mean of the LHDWs velocity for all the packet of LHDW over the four MMS spacecraft is 317 km/s and is thus close to the  $y$  component of the perpendicular ion velocity. We therefore conclude that the LHDW were moving in the direction of the electric drift speed at the perpendicular ion velocity.

The density gradient led to the generation of a diamagnetic current in the  $y$  direction that

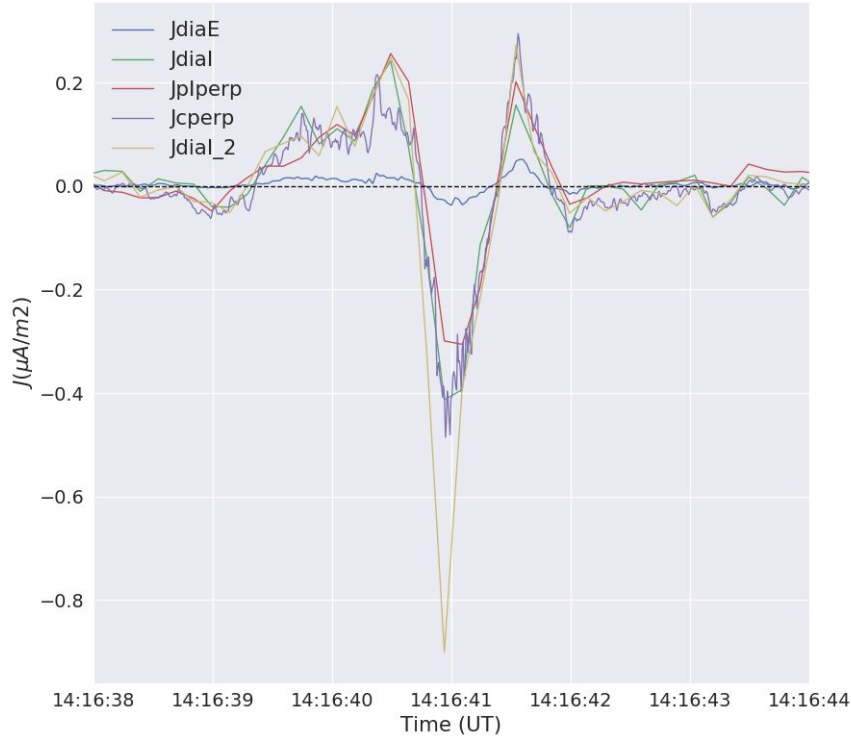


Figure 4.12 – The  $y$  component of: electron diamagnetic current density (blue), ion diamagnetic current density obtained as  $j_{dial} = enV_{d_{i1}}$  (green), perpendicular current densities obtained from FPI (red), perpendicular current densities obtained from the curlometer technique (purple) and ion diamagnetic current density obtained from equation  $j_{dial_2} = enV_{d_{i2}}$  (yellow).

can be calculated as:

$$\mathbf{J}_i = \frac{\mathbf{B} \times \nabla \cdot \mathbf{P}_i}{B^2} \quad (4.5)$$

The electron diamagnetic current was very weak, while the ion diamagnetic current was dominant (Figure 4.12). This is due to the difference in temperature of electrons and ions where  $T_e \ll T_i$ . Figure 4.12 also shows that the  $y$  component of the ion diamagnetic velocity, the  $y$  component of the perpendicular current obtained from the curlometer technique (calculated through  $\nabla \times \mathbf{B}$ ) and perpendicular FPI current densities ( $en(\mathbf{V}_{\perp,i} - \mathbf{V}_{\perp,e})$ ) vary similarly. This indicates that the perpendicular component of the current density was carried by the ion pressure gradient.

The  $y$  component of the ion diamagnetic current density was equal to the  $y$  component of the perpendicular current density but since the total current density was carried by electrons (shown in Chapter 3), this therefore suggests that if the perpendicular current was carried by ions then the parallel current density must be carried by electrons. However, Figure 4.13 shows that both parallel and perpendicular current densities were mainly car-

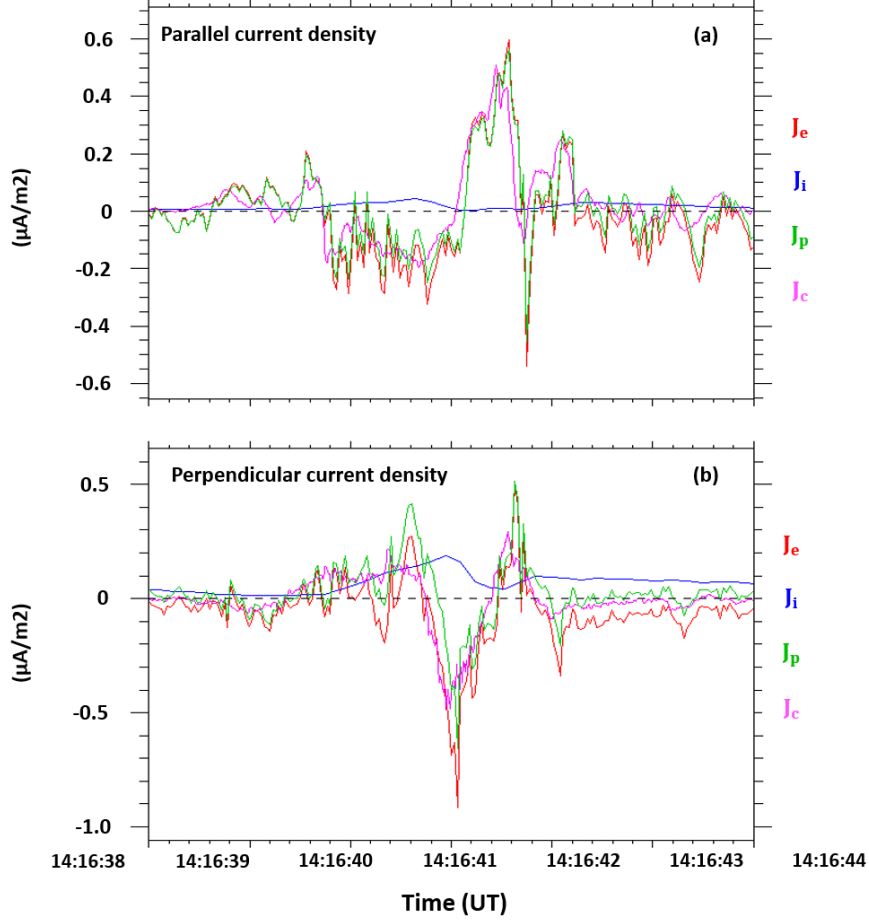


Figure 4.13 – Parallel (a) and perpendicular (b) current densities obtained from the curlometer technique, the particle, the ions ( $enV_{\parallel(\perp,i)}$ ) and the electrons current densities ( $-enV_{\parallel(\perp,e)}$ ).

ried by electrons. A more work is still needed in order to elucidate this point.

## 4.5. DISCUSSION

Plasma waves near the magnetic reconnection region were reported in satellite observations such as whistler waves in the magnetopause [Deng and Matsumoto (2001); Tang et al. (2013); Contel et al. (2016)], electrostatic solitary waves [Cattell et al. (2005); Viberg et al. (2013)] and lower hybrid waves [Zhou et al. (2011)]. Wave-particle interactions can significantly contribute to the energy dissipation and transformation from magnetic energy to kinetic and thermal energies since they provide the anomalous resistivity needed to break the magnetic field lines and accelerate particles [Viberg et al. (2012); Deng et al. (2004a); Retinò et al. (2006)]. Moreover, plasma waves provide information about particle dynamics

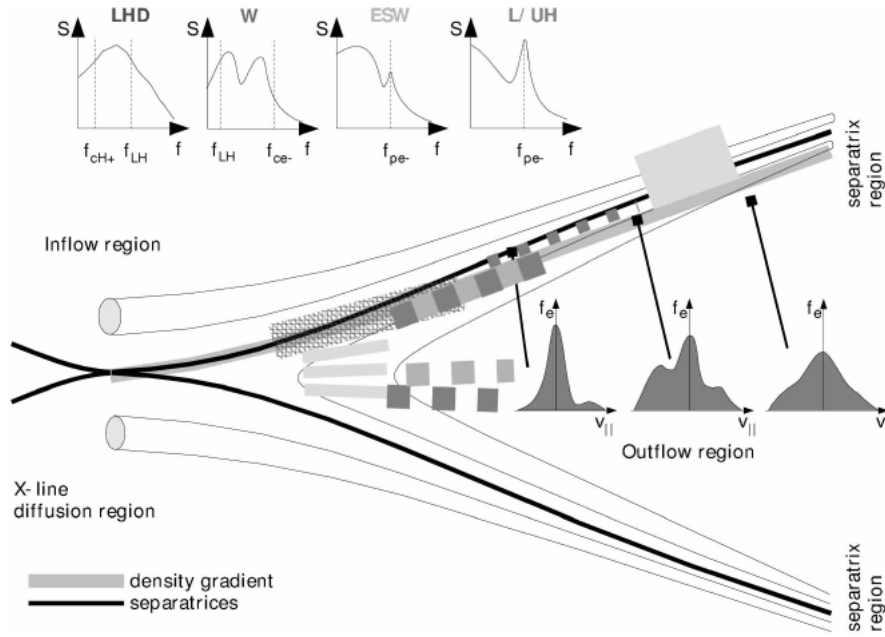


Figure 4.14 – Sketch of a reconnection site. At the top, different kinds of wave spectra commonly observed near reconnection sites are sketched. The common places to observe those waves are marked in different gray shadowing. Typical electron distribution functions in the vicinity of the separatrix are indicated as well. Figure from [Vaivads et al. \(2006\)](#). LHD = Lower Hybrid Drift, W = Whistler, ESW = Electrostatic solitary waves and L/UH = Langmuir/upper-hybrid waves.

since most of waves are driven by unstable particle distributions. Therefore, the knowledge of waves is very helpful to understand the reconnection dynamics.

A simplified structure of the separatrix region was proposed by [Vaivads et al. \(2006\)](#) and is illustrated in Figure 4.14. It shows that whistler waves are usually observed near the X-line. Electrostatic solitary waves and Langmuir/Lower hybrid waves are observed in the separatrix regions.

Reconnection can produce strong and narrow density gradients in space at the separatrixes that separate the inflow region from the outflow region. These density gradients lead to the generation of LHDWs which can have significant effects on magnetic reconnection. First, they can affect reconnection through the anomalous resistivity since they were found to be able to generate anomalous collisions frequencies for electrons of the order of  $\sim 2\pi f_{LH}$  [[Silin et al. \(2005\)](#)]. Secondly, LHDWs can have an impact on magnetic reconnection through electron acceleration. In fact, the phase velocity of the LHDWs along the magnetic field is comparable to the electron thermal velocity. That enables the LHDWs

to resonate with thermal electrons and thus efficiently accelerate them.

One important question about reconnection is to understand the parallel electric fields distributions near the reconnection site. The presence of these parallel electric fields allows the magnetic field-line topology changes associated with magnetic reconnection. One possible source of these parallel electric fields can be the electrostatic solitary waves which have been commonly observed near the reconnection sites [Deng et al. (2004b)]. It has been shown by observations that the strongest emissions of Electrostatic Solitary Waves (ESWs) are observed along the separatrices [Cattell et al. (2005); Farrell et al. (2002); Vaivads et al. (2004)].

Whistler waves are a perfect tool for the remote sensing of reconnection sites since they can propagate over large distances from reconnection sites without appreciable damping. Whistler waves can be also a signature of open magnetic field lines, and thus of ongoing magnetic reconnection as discussed in this Chapter.

## 4.6. SUMMARY AND CONCLUSIONS

In summary, we have studied the properties of waves associated with a reconnecting current sheet resulting from the interaction between two distinguishable flux tubes. We showed observations of two types of whistler waves on both sides of the current sheet. The first whistler wave was associated with electrostatic solitary waves (ESWs) as evidenced by spiky and bipolar signatures of the parallel electric field  $E_{\parallel}$ . The second whistler wave was not associated with any structure in the parallel electric field. They were moving in the direction of the magnetic field. We showed that the whistlers were not generated locally but away from the current sheet by electron beam instability. The density gradient resulting from the interaction between the two flux tubes led to the generation of a diamagnetic current density which was carried by the ion pressure gradient and led also to the generation of lower hybrid drift waves that were observed at the center of the current sheet. We determined the properties of the LHDWs using single spacecraft method that was proposed by Norgren et al. (2012) and found that they were propagating in the direction of the electric drift speed at the perpendicular ion velocity.

# 5

## SUMMARY AND CONCLUSIONS

### 5.1. SUMMARY OF RESULTS

Through the course of my thesis I have aimed to obtain a better understanding of magnetic reconnection signatures at the Earth's magnetopause based on in-situ observations of particles and fields from the MMS spacecraft. In Chapter 3, I investigated an event observed in the vicinity of the Earth's magnetopause on November 7, 2015. The event was characterized by a peak in the magnetic field amplitude and a bipolar signature on one of the magnetic field components, as it is typical for Flux Transfer Events. However, the bipolar signature was not observed in the component normal to the magnetopause, but rather in a direction almost perpendicular to the magnetopause normal. The particularity of this event laid in a very thin and localized current sheet and a small-scale, fast ion jet near the peak of the large scale magnetic field. The pitch-angle distribution of electrons revealed that two different regions were separated by the current sheet, also emphasized by clearly distinct densities. All these features suggested that this event could not be considered as the traversal of a single homogeneous structure. The observations were interpreted as being the result of a complex three-dimensional interaction of two separate sets of magnetic field lines with different connectivities which conspired to produce signatures partially consistent with that of a flux transfer event. Although similar 3D scenarios have



been previously proposed by e.g. [Louarn et al. \(2004\)](#) and [Cardoso et al. \(2013\)](#) using data from the CLUSTER mission, only the tremendous resolution of MMS data could resolve the interfacing thin current sheet, showing that it was possibly reconnecting and that the reconnection was driven by the compression of the two distinct sets of open field lines. This interpretation was partially supported by the Walén test which predicted an ion jet but with an amplitude much larger than the amplitude of the observed jet. We suggested that this appeared to be related to the proximity to the X-line [[Phan et al. \(2016\)](#)] so that the ion outflow had not yet reached its full speed and is not yet accelerated to the local Alfvén speed. Additionally, the jet thickness was also estimated to be about 0.8-1.3 times the ion skin depth ( $\lambda_i$ ). Such a thickness implies that the spacecraft were very close to the X-line ( $5 - 8\lambda_i$ ), which is consistent with an early-stage ion jet and thus with the over-estimation of the ion speed from the Walén test. We also showed that ions were decoupled from the magnetic field at the center of the structure while the electron were still frozen-in, which demonstrates that the spacecraft crossed the ion diffusion region. Finally, the energy dissipation quantified by  $J \cdot E'$  was positive and significantly different from zero during the current sheet crossing which is consistent with reconnection dissipation region. All these observations were therefore consistent with the current sheet undergoing reconnection at the interface between the two flux tubes of very different orientations (73° magnetic shear angle).

Further analysis (Chapter 3, section 3.6.2) highlighted that the current sheet had a particular geometry. The main current was perpendicular to the ion jet direction. The second component of the current density exhibited a bipolar signature and was close to the ion jet direction. The spatial scale of the entire current structure was about 3 to 4 times the Larmor radius of protons at the time of the current sheet encounter. However, the structure possessed smaller scale sub-structures, smaller than the ion Larmor radius. The current sheet allowed the changes in the magnetic field at the center of the event and was mainly carried by electrons.

The event discussed above occurred during the passage of a magnetic cloud at the Earth and under low Alfvén Mach number regime. The  $B_y$  and  $B_z$  components of the interplanetary magnetic field were significantly negative during several hours before the event observation and led to a continuously enhanced solar wind-magnetosphere coupling. Mag-

netic reconnection was expected to occur in the southern hemisphere dawn side according to the IMF orientation. Such conditions corroborate the thick boundary layers encountered by the spacecraft during almost one hour while moving from the magnetosheath into the magnetosphere. Although the boundary layer showed a complex structure as expected from the pronounced variations in solar wind parameters, we showed that it could be divided into three major subregions. One of these subregions was characterized by enhanced and diverted flows as compared to the pristine magnetosheath and was identified as an outer LLBL. The second flux tubes was characterized by electron, ion and  $He^{++}$  fluxes typical of the outer LLBL. Also, the magnetic field orientation was similar to the that found in the first outer LLBL. It may be therefore important to understand the different contexts in which such events may occur.

We complete our study with a plasma waves analysis (see Chapter 4) that focus on the reconnecting current sheet. We evidence the presence of two types of whistler waves on both sides of the current sheet. The first whistler wave was associated with spiky and bipolar signatures of the parallel electric field. The second whistler wave, however, was not associated with any structure in the parallel electric field. The whistler waves were propagating in the direction of the magnetic field. We also showed that the density gradient resulting from the interaction between the two flux tubes led to the generation of a diamagnetic current density carried by the ion pressure gradient and led also to the generation of electrostatic lower hybrid drift waves (LHDWs) that were observed at the center of the current sheet. The LHDWs were propagating at the perpendicular ion velocity, in the direction of the  $\mathbf{E} \times \mathbf{B}$  drift.

Given the particularity of the whole event described here, we looked for similar events in MMS data between September 1, 2015 and November 30, 2016. This study was initiated at the Space and Astronautical Science (ISAS) with Hiroshi Hasegawa and showed that although such events are not common they are also not too unusual (a dozen of events for the time interval considered were identified).

## 5.2. OUTLOOK ON POSSIBLE DEVELOPMENTS

The research presented in my thesis, although started from a case study, illustrated the need of introducing new categories in the classification of magnetosheath events. I will conclude this dissertation with a brief summary of some perspectives for future work.

The suggestions presented here are based on a statistical analysis of events observed by the MMS spacecraft between September 1, 2015 and November 30, 2016, all presenting similar features to the one discussed in detail. Namely, those characterizing features are:

- a magnetic field intensity peak,
- a total pressure peak.

An overall division into two categories was performed then by analysing the magnetic field component  $B_N$ , that is the one normal to the magnetopause frame as calculated using the Shue model [Shue et al. (1997)]. All those possessing a bipolar  $B_N$  signature were recognized as "proper" flux transfer events. Among the remaining events, a new category was defined based on the similarities with the event analyzed in this manuscript, namely:

- The presence of a localized and isolated current sheet near the center of the event,
- The difference of magnetic connectivity on each side of the current sheet.

The events in the latter category were considered as being possibly the result of the three-dimensional interaction between two distinguishable structures such as flux tubes, flux ropes or magnetic islands.

Since the event discussed in Chapter 3 occurred under unusual and extreme solar wind conditions and a continuously enhanced solar wind-magnetosphere coupling, it may therefore be important to put forward this statistical analysis and to study possible correlations with solar wind parameters in order to identify the conditions that may lead to similar events. This may help verifying if this kind of interactions can be generated only in extremely and continuously perturbed solar wind-magnetosphere coupling where magnetic reconnection is expected to occur at different locations, leading to significant flows at the magnetopause and generating complex magnetic structures. Another important point is to compare the properties of such events with those of classical FTEs such as their scale,

duration, propagation and location at the magnetopause. Another area which could be developed is the study of current sheet geometry with respect to the local flows and magnetopause and to the IMF orientation as well. The study of plasma waves associated to these events would be also helpful to understand the role they play during the interaction of the flux tubes and during magnetic reconnection at the current sheet.

### 5.3. A WIDER PERSPECTIVE ON THIS WORK

After having taken into account the immediate possible developments of my work, I would like to put forward some more general considerations, taking a wider perspective on flux tubes dynamics within magnetized plasmas.

First and foremost, I recall that magnetic flux tubes like the ones studied in this thesis are widely diffused structures. For this reason, all sufficiently detailed understandings of the dynamical evolution of both this environment cannot neglect to take into account the evolution of flux tubes, especially through reconnection. While efforts in this direction have already been made, notably by [Borovsky \(2008\)](#), the state of the art cannot be deemed complete.

Yet, we recall that solar wind magnetopause modelling is of fundamental importance to space weather forecasting which may help to predict conditions of the Earth's magnetosphere based on solar wind measurements. Such predictions find multiple practical applications, mostly regarding the protection of people and machinery possibly operating under showers of energetic magnetospheric particles (aircraft personnel, astronauts, artificial satellites).

Solar wind and magnetopause are not only characterized at large scale by the presence of evolving flux tubes, on the contrary, these environment seem to develop such structures through extremely different scales and under a variety of local conditions. In particular, small scale flux tubes characterize all processes of plasma turbulence, a phenomenon active on many lengths through space environments. The event discussed in [Chapter 3](#) showed evidences of three-dimensional reconnection under enhanced solar wind-magnetosphere coupling, occurring between two flux tubes resulting from independent magnetic reconnections at large-scale. However, similar merging phenomena seem to be a rather general feature of magnetized plasma dynamics, for example following the formation of large num-

bers of thin current sheets between the small-scale flux tubes present in turbulent conditions. Evidence of such dynamics, occurring in a fashion that is in many ways analogue to that of the event discussed throughout all this work has been presented for instance by [Retinò et al. \(2007\)](#) and [Phan et al. \(2018\)](#). In particular, [Retinò et al. \(2007\)](#) showed for the first time in situ evidence of magnetic reconnection at a thin current sheet with a width of a few ion inertial lengths using Cluster data. More recently, [Phan et al. \(2018\)](#) reported observations of plasma jetting associated with magnetic reconnection at even smaller structures, an electron-scale current sheet in the turbulent magnetosheath region of the Earth using MMS data. Even though it seems that magnetic reconnection at ion-scale and electron-scale current sheets differs from that of large-scale ones (in particular, failing to develop the structured pattern observed at MHD scales), the overall magnetic field dynamics is comparable under many aspects to the one clarified through the previous sections of this thesis. Concluding, the Earth's magnetosphere is the only place where direct, small scale in-situ measurements of magnetic reconnection between flux tubes can be conducted at the moment, due to technical constraints. And only the understanding of such phenomenon as clarified by studies at the Earth's magnetosphere can allow us to shed full light on magnetic reconnection processes in astrophysical systems where such high-resolution observations are not possible.



## RÉSUMÉ ET CONCLUSIONS

### A.1. RÉSUMÉ DES RÉSULTATS

Au cours de ma thèse, j'ai cherché à obtenir une meilleure compréhension de la reconnexion magnétique observée à la magnétopause de la Terre à partir des mesures in-situ de particules et de champs électromagnétiques provenant de la mission MMS comme cela est rapporté dans le Chapitre 3. Je me suis focalisée sur un événement atypique observé au voisinage de la magnétopause terrestre le 7 novembre 2015. L'événement caractérisé par un pic d'amplitude du champ magnétique et par une signature bipolaire sur l'une des composantes du champ magnétique ressemble à première vue à un événement à transfert de flux. Cependant, la signature bipolaire n'a pas été observée sur la composante normale à la magnétopause, mais plutôt dans une direction presque perpendiculaire à celle-ci. Une autre particularité de cet événement réside dans l'existence d'une couche de courant très fine et localisée et un jet d'ions rapides observés autour du pic dans l'intensité du champ magnétique. La distribution en angle d'attaque des électrons montre l'existence de deux régimes de plasma distincts séparés par une couche de courant. Toutes ces caractéristiques ont suggéré que cet événement ne pouvait pas être considéré comme la traversée d'une seule structure homogène. Les observations ont été interprétées comme étant le résultat d'une interaction complexe de deux ensembles distincts de lignes de champ magnétique

avec des connectivités magnétiques différentes qui ont produit des signatures partiellement cohérentes avec celles d'un événement à transfert de flux. Bien que des scénarios 3D similaires aient été précédemment proposés par ex. [Louarn et al. \(2004\)](#) et [Cardoso et al. \(2013\)](#) en utilisant les données de la mission CLUSTER, seule la très grande résolution des données MMS a permis de résoudre la fine couche de courant qui assure l'interface. L'étude a aussi montré que la couche de courant était compressée et était aussi le siège d'un processus de reconnexion active. Cette interprétation a été partiellement corroborée par le test de Walén qui a prédit un jet d'ions avec une amplitude beaucoup plus grande que l'amplitude du jet observé. Nous avons suggéré que cela semblait être lié à la proximité de la X-line [[Phan et al. \(2016\)](#)], de sorte que le flux d'ions n'avait pas encore atteint sa vitesse maximale et n'était pas encore accéléré à la vitesse d'Alfvén locale. De plus, l'épaisseur du jet a également été estimée à environ 0.8-1.3 fois la longueur d'inertie des ions ( $\lambda_i$ ). Une telle épaisseur suggère que le satellite était très proche de la X-line ( $5 - 8\lambda_i$ ), ce qui est cohérent avec le début d'un jet d'ions et donc avec la surestimation de la vitesse ionique du test de Walén. Nous avons également montré que les ions étaient découplés du champ magnétique au centre de la structure alors que les électrons étaient toujours gelés, ce qui démontre que les satellites ont probablement traversé la région de diffusion des ions. J'ai montré que de l'énergie magnétique était efficacement dissipée dans cette couche de courant. L'ensemble de ces observations est donc cohérent avec l'interprétation d'une couche de courant en cours de reconnexion et constituant l'interface entre les deux tubes de flux d'orientations très différentes (angle de cisaillement magnétique de  $73^\circ$ ).

L'analyse plus approfondie (chapitre 3, section 3.6.2) a aussi mis en évidence que la couche de courant avait une géométrie particulière. Le courant principal était perpendiculaire à la direction du jet d'ions. La deuxième composante de la densité de courant présentait une signature bipolaire et était proche de la direction du jet d'ions. La taille de l'ensemble de la structure actuelle était d'environ 3 à 4 fois le rayon de Larmor des protons au moment de l'observation la couche de courant. En outre, la structure possédait des sous-structures, plus petites que le rayon de Larmor ionique. La couche de courant assurant la rotation du champ magnétique entre les deux tubes de flux s'est révélée être principalement portée par des électrons.

L'événement discuté ci-dessus s'est produit pendant le passage d'un nuage magnétique à

la Terre et sous un faible Mach Alfvénique. Les composantes  $B_y$  et  $B_z$  du champ magnétique interplanétaire étaient significativement négatives pendant plusieurs heures avant l'observation de l'événement. Ce dernier a donc pris place pendant une longue période de couplage fort et continu entre le vent solaire et la magnétosphère. De telles conditions permettent d'expliquer l'épaisseur importante des couches de transition traversées par les satellites pendant près d'une heure en se déplaçant de la magnétogaine vers la magnétosphère. Bien que la couche intermédiaire ait montré une structure complexe, j'ai montré qu'elle pouvait être divisée en trois sous-régions principales.

Cette étude a été étendue à l'analyse des ondes dans le plasma (voir Chapitre 4) au voisinage et dans la couche de courant. J'ai démontré la présence de deux types d'ondes de mode sifflement des deux cotés de la couche de courant. La première onde était associée à des signatures en pic et bipolaires du champ électrique parallèle. Le second paquet d'ondes, cependant, n'était associé à aucune structure dans le champ électrique parallèle. Les ondes de mode sifflement se propageaient dans le sens du champ magnétique. Nous avons également montré que le gradient de densité résultant de l'interaction entre les deux tubes de flux a conduit à la création d'une densité de courant diamagnétique portée par le gradient de pression ionique et à la génération d'ondes de dérive hybrides électrostatiques (LHDWs) observées au centre de la couche de courant. Les LHDWs se propageaient à la vitesse ionique perpendiculaire, dans le sens de la dérive  $\mathbf{E} \times \mathbf{B}$ .

Compte tenu de la particularité de l'ensemble de l'événement décrit ci-dessus, nous avons recherché des événements similaires dans les données MMS entre le 1er septembre 2015 et le 30 novembre 2016. Cette étude a été initiée à la Science spatiale et astronautique (ISAS) avec Hiroshi Hasegawa et a montré que les événements ne sont pas communs, sans être inhabituels non plus (une douzaine d'événements pour l'intervalle de temps considéré ont été identifiés).

## A.2. PERSPECTIVES SUR LES DÉVELOPPEMENTS POSSIBLES

La recherche présentée dans ma thèse, bien que commencée à partir d'une étude de cas, a illustré la nécessité d'introduire de nouvelles catégories dans la classification des événements au niveau de la magnétopause. Je conclurai cette thèse par un bref énoncé de quelques perspectives pour les travaux futurs.



Les suggestions présentées ici sont basées sur une analyse statistique des événements observés par MMS entre le 1er septembre 2015 et le 30 novembre 2016, présentant les caractéristiques suivantes:

- un pic dans l'intensité du champ magnétique,
- un pic dans la pression totale.

Une division globale en deux catégories a été réalisée puis en analysant la composante de champ magnétique  $B_N$ , c'est-à-dire la normale à la magnétopause calculée en utilisant le modèle de Shue [Shue et al. (1997)]. Tous les cas qui possédaient une signature bipolaire  $B_N$  ont été reconnus comme des événements de transfert de flux classiques. Parmi les événements restants, une nouvelle catégorie a été définie sur la base des similitudes avec l'événement analysé dans ce manuscrit, à savoir:

- La présence d'une couche de courant localisée et isolée près du centre de l'événement,
- Une différence de connectivité magnétique de chaque côté de la couche de courant.

Les événements de cette dernière catégorie ont été considérés comme étant probablement le résultat de l'interaction entre deux structures distinctes telles que des tubes de flux, des cordes de flux ou des îlots magnétiques.

Puisque l'événement discuté dans le chapitre 3 s'est produit sous des conditions prolongées de couplage renforcé entre le vent solaire et la magnétosphère, il peut être important de continuer cette analyse statistique et d'étudier les corrélations possibles avec les paramètres du vent solaire afin d'identifier les conditions pouvant conduire à des événements similaires. Un autre point important est de comparer les propriétés de tels événements avec celles des FTEs classiques tels que leur taille, leur durée, leur propagation et leur localisation à la magnétopause. Un autre domaine qui pourrait être développé est l'étude de la géométrie de la couche de courant en ce qui concerne les flux locaux et la magnétopause ainsi que l'orientation du champ magnétique interplanétaire. L'étude des ondes de plasma associées à ces événements est à approfondir pour comprendre le rôle qu'elles jouent dans la reconnexion magnétique au sein de la couche de courant.

### A.3. PERSPECTIVES PLUS LARGES

Après avoir pris en compte les développements immédiats possibles de mon travail, je voudrais avancer quelques considérations plus générales, en prenant une perspective plus large sur la dynamique des tubes de flux dans les plasmas magnétisés.

Tout d'abord, rappelons que les tubes de flux magnétiques comme ceux étudiés dans cette thèse sont des structures largement répandues. Pour cette raison, toutes les interprétations suffisamment détaillées de l'évolution dynamique de l'environnement ne peuvent négliger de prendre en compte l'évolution des tubes de flux, notamment à travers la reconnexion.

Le vent solaire et la magnétopause ne sont pas caractérisés par la présence de tubes de flux évolutifs seulement à grande échelle, mais au contraire, ces environnements semblent développer de telles structures à des échelles extrêmement différentes et dans des conditions locales variées. En particulier, les tubes de flux à petite échelle caractérisent le processus de turbulence du plasma, un phénomène actif sur de nombreuses échelles dans les environnements spatiaux. L'événement discuté dans le chapitre 3 a montré des preuves de reconnexion tridimensionnelle sous un couplage vent-magnétosphère solaire intense, se produisant entre deux tubes de flux résultant de reconnexions magnétiques indépendantes de grande taille. Cependant, des phénomènes de reconnexion similaires semblent être une caractéristique universelle de la dynamique des plasmas magnétisés, comme par exemple suite à la formation d'un grand nombre de fines couches de courant entre les tubes de flux de petite taille présents dans des conditions turbulentes. L'évidence de telles dynamiques, se produisant d'une manière qui est analogue à celle de l'événement discuté dans ce manuscrit, a été présentée par exemple par [Retinò et al. \(2007\)](#) et [Phan et al. \(2018\)](#). En particulier, [Retinò et al. \(2007\)](#) a montré pour la première fois une preuve de reconnexion magnétique au niveau d'une fine couche de courant avec une largeur de quelques longueurs d'inertie ionique en utilisant les données mesurées in-situ par Cluster. Plus récemment, [Phan et al. \(2018\)](#) a rapporté des observations de jets de plasma associés à une reconnexion magnétique dans des structures encore plus petites, une couche de courant de taille électronique dans la région de la magnétogaine turbulente de la Terre en utilisant des données MMS. Même s'il semble que la reconnexion magnétique à l'échelle ionique et à l'échelle électronique diffère de celle à grande échelle (en particulier, en ne développant pas le schéma structuré observé aux échelles MHD), la dynamique globale du

champ magnétique a des aspects comparables à celui clarifié à travers les parties précédentes de cette thèse.

En conclusion, la magnétosphère terrestre est le seul endroit où des mesures directes in-situ à petite échelle de la reconnexion magnétique entre les tubes de flux peuvent être réalisées pour le moment, en raison de contraintes techniques. Et seule la compréhension d'un phénomène basé sur des études des observations dans la magnétosphère terrestre peut nous permettre d'éclaircir le processus de reconnexion magnétique dans les systèmes astrophysiques où de telles observations à haute résolution ne sont pas possibles.

## LIST OF ABBREVIATIONS

ACE	Advanced Composition Explorer
ADP	Axial Double Probe
AFG	Analog Fluxgate Magnetometer
ASIC	Application Specific Integrated Circuit
CIDP	Central Instrument Data Processor
DFG	Digital Fluxgate Magnetometer
DIS	Dual Ion Sensors
DST	Disturbance Storm Time
EDI	Electron Drift Instrument
EDR	Electron Diffusion Region
EPD	Energetic particles
ESW	Electrostatic Solitary Wave
FFT	Fast Fourier Transform
FPI	Fast Plasma Investigation
HEO	Highly Elliptical Orbit
HPCA	Hot Plasma Composition
IDR	Ion Diffusion Region
ILLBL	Inner Low Latitude Boundary Layer

IMF Interplanetary Magnetic Field

IMF Interplanetray Magnetic Field

LHDW Lower Hybrid Drift Waves

LLBL Low Latitude Boudnary Layer

LLBL The Low Latitude Boundary Layer

MCPs Micro Channel Plates

MFA Magnetic Field-Aligned

MSBL Magnetosheath Boudnary Layer

MSBL Magnetosheath Boundary Layer

MSBL The Magnetosheath Boundary Layer

MSH Magnetosheath

MSP Magnetosphere

MVA Minimum Variance Analysis

MXR Multiple X-line reconnection

OLLBL Outer Low Latitude Boundary Layer

PCS Propagating Structure Frame

RF Radiofrequency

RH Right-Handed

ROI Region Of Interest

SCM Search Coil Magnetometer

SDP Spin-plane Double Probe

SITL Scientists-In-The-Loop

SOC Science Operation System

SXR Single X-line reconnection

TOF Time-of-fligth

WHAMP Waves in Homogeneous Anisotropic Multicomponent Magnetized Plasma



## BIBLIOGRAPHY

- Alexandrova, A., R. Nakamura, E. V. Panov, Y. L. Sasunov, T. Nakamura, Z. Vörös, A. Retinò, and V. S. Semenov (2016, August). Two interacting X lines in magnetotail: Evolution of collision between the counterstreaming jets. *Geophysical Research Letters* 43(15), 2016GL069823.
- Bauer, T. M., R. A. Treumann, and W. Baumjohann (2001, September). Investigation of the outer and inner low-latitude boundary layers. *Annales Geophysicae* 19, 1065–1088.
- Baumjohann, W. and R. Treumann (1996, January). *Basic Space Plasma Physics*, Volume 15-22.
- Blake, J. B., B. H. Mauk, D. N. Baker, P. Carranza, J. H. Clemmons, J. Craft, W. R. Crain, A. Crew, Y. Dotan, J. F. Fennell, R. H. Friedel, L. M. Friesen, F. Fuentes, R. Galvan, C. Ibscher, A. Jaynes, N. Katz, M. Lalic, A. Y. Lin, D. M. Mabry, T. Nguyen, C. Pancratz, M. Redding, G. D. Reeves, S. Smith, H. E. Spence, and J. Westlake (2016, March). The Fly’s Eye Energetic Particle Spectrometer (FEEPS) Sensors for the Magnetospheric Multiscale (MMS) Mission. *Space Science Reviews* 199(1-4), 309–329.
- Bogdanova, Y. V., C. J. Owen, M. W. Dunlop, J. A. Wild, J. A. Davies, A. D. Lahiff, M. G. G. T. Taylor, A. N. Fazakerley, I. Dandouras, C. M. Carr, E. A. Lucek, and H. Rème (2008, July). Formation of the low-latitude boundary layer and cusp under the northward IMF: Simultaneous observations by Cluster and Double Star. *Journal of Geophysical Research (Space Physics)* 113, A07S07.
- Borovsky, J. E. (2008, August). Flux tube texture of the solar wind: Strands of the magnetic carpet at 1 AU? *Journal of Geophysical Research (Space Physics)* 113, A08110.
- Bryant, D. A. and S. Riggs (1989, June). At the Edge of the Earth’s Magnetosphere: A Survey by AMPTE-UKS. *Philosophical Transactions of the Royal Society of London Series A* 328, 43–55.



- Burch, J. L., T. E. Moore, R. B. Torbert, and B. L. Giles (2016, March). Magnetospheric Multiscale Overview and Science Objectives. *Space Science Reviews* 199, 5–21.
- Burlaga, L., E. Sittler, F. Mariani, and R. Schwenn (1981, August). Magnetic loop behind an interplanetary shock: Voyager, Helios, and IMP 8 observations. *Journal of Geophysical Research: Space Physics* 86(A8), 6673–6684.
- Cairns, I. H. and B. F. McMillan (2005, October). Electron acceleration by lower hybrid waves in magnetic reconnection regions. *Physics of Plasmas* 12, 102110.
- Cardoso, F. R., W. D. Gonzalez, D. G. Sibeck, M. Kuznetsova, and D. Koga (2013, October). Magnetopause reconnection and interlinked flux tubes. *Annales Geophysicae* 31, 1853–1866.
- Cassak, P. A., Y.-H. Liu, and M. A. Shay (2017, October). A Review of the 0.1 Reconnection Rate Problem. *Journal of Plasma Physics* 83(05). arXiv: 1708.03449.
- Cattell, C., J. Dombek, J. Wygant, J. F. Drake, M. Swisdak, M. L. Goldstein, W. Keith, A. Fazakerley, M. André, E. Lucek, and A. Balogh (2005, January). Cluster observations of electron holes in association with magnetotail reconnection and comparison to simulations. *Journal of Geophysical Research (Space Physics)* 110, A01211.
- Chapman, S. and V. C. A. Ferraro (1930, July). A New Theory of Magnetic Storms. *Nature* 126, 129–130.
- Chen, F. F. (1974). *Introduction to Plasma Physics*. Springer US.
- Chen, L.-J., M. Hesse, S. Wang, D. Gershman, R. E. Ergun, J. Burch, N. Bessho, R. B. Torbert, B. Giles, J. Webster, C. Pollock, J. Dorelli, T. Moore, W. Paterson, B. Lavraud, R. Strangeway, C. Russell, Y. Khotyaintsev, P.-A. Lindqvist, and L. Avanov (2017, May). Electron diffusion region during magnetopause reconnection with an intermediate guide field: Magnetospheric multiscale observations. *Journal of Geophysical Research (Space Physics)* 122, 5235–5246.
- Contel, O. L., A. Retinò, H. Breuillard, L. Mirioni, P. Robert, A. Chasapis, B. Lavraud, T. Chust, L. Rezeau, F. D. Wilder, D. B. Graham, M. R. Argall, D. J. Gershman, P.-A. Lindqvist,

- Y. V. Khotyaintsev, G. Marklund, R. E. Ergun, K. A. Goodrich, J. L. Burch, R. B. Torbert, J. Needell, M. Chutter, D. Rau, I. Dors, C. T. Russell, W. Magnes, R. J. Strangeway, K. R. Bromund, H. K. Leinweber, F. Plaschke, D. Fischer, B. J. Anderson, G. Le, T. E. Moore, C. J. Pollock, B. L. Giles, J. C. Dorelli, L. Avanov, and Y. Saito (2016, June). Whistler mode waves and Hall fields detected by MMS during a dayside magnetopause crossing. *Geophysical Research Letters* 43(12), 2016GL068968.
- Daum, P., J. A. Wild, T. Penz, E. E. Woodfield, H. Rème, A. N. Fazakerley, P. W. Daly, and M. Lester (2008, July). Global MHD simulation of flux transfer events at the high-latitude magnetopause observed by the Cluster spacecraft and the SuperDARN radar system. *Journal of Geophysical Research (Space Physics)* 113, A07S22.
- Davidson, R. C. and N. T. Gladd (1975, October). Anomalous transport properties associated with the lower-hybrid-drift instability. *Physics of Fluids* 18, 1327–1335.
- Deng, X. H. and H. Matsumoto (2001, March). Rapid magnetic reconnection in the Earth's magnetosphere mediated by whistler waves. *Nature* 410, 557–560.
- Deng, X. H., H. Matsumoto, H. Kojima, T. Mukai, R. R. Anderson, W. Baumjohann, and R. Nakamura (2004a, May). Geotail encounter with reconnection diffusion region in the Earth's magnetotail: Evidence of multiple X lines collisionless reconnection? *Journal of Geophysical Research (Space Physics)* 109, A05206.
- Deng, X. H., H. Matsumoto, H. Kojima, T. Mukai, R. R. Anderson, W. Baumjohann, and R. Nakamura (2004b, May). Geotail encounter with reconnection diffusion region in the Earth's magnetotail: Evidence of multiple X lines collisionless reconnection? *Journal of Geophysical Research (Space Physics)* 109, A05206.
- Divin, A., Y. V. Khotyaintsev, A. Vaivads, and M. André (2015, February). Lower hybrid drift instability at a dipolarization front. *Journal of Geophysical Research (Space Physics)* 120, 1124–1132.
- Dunlop, M. W., A. Balogh, K.-H. Glassmeier, and P. Robert (2002, November). Four-point Cluster application of magnetic field analysis tools: The Curlometer. *Journal of Geophysical Research (Space Physics)* 107, 1384.

- Dunlop, M. W., D. J. Southwood, K.-H. Glassmeier, and F. M. Neubauer (1988). Analysis of multipoint magnetometer data. *Advances in Space Research* 8, 273–277.
- Dunlop, M. W. and T. I. Woodward (1998). Multi-Spacecraft Discontinuity Analysis: Orientation and Motion. *ISSI Scientific Reports Series 1*, 271–306.
- Dunlop, M. W., T. I. Woodward, and C. J. Farrugia (1995, September). Minimum Variance Analysis: Cluster Themes. Volume 371, pp. 33.
- Eastman, T. E. and E. W. Hones, Jr. (1979, May). Characteristics of the magnetospheric boundary layer and magnetopause layer as observed by Imp 6. *Journal of Geophysical Research* 84, 2019–2028.
- Egedal, J., W. Fox, N. Katz, M. Porkolab, K. Reim, and E. Zhang (2007, January). Laboratory Observations of Spontaneous Magnetic Reconnection. *Physical Review Letters* 98(1), 015003.
- Ergun, R., K. Goodrich, F. Wilder, J. Holmes, J. Stawarz, S. Eriksson, A. Sturmer, D. Malaspina, M. Usanova, R. Torbert, P.-A. Lindqvist, Y. Khotyaintsev, J. Burch, R. Strangeway, C. Russell, C. Pollock, B. Giles, M. Hesse, L. Chen, G. Lapenta, M. Goldman, D. Newman, S. Schwartz, J. Eastwood, T. Phan, F. Mozer, J. Drake, M. Shay, P. Cassak, R. Nakamura, and G. Marklund (2016, June). Magnetospheric Multiscale Satellites Observations of Parallel Electric Fields Associated with Magnetic Reconnection. *Physical Review Letters* 116(23), 235102.
- Ergun, R. E., S. Tucker, J. Westfall, K. A. Goodrich, D. M. Malaspina, D. Summers, J. Wallace, M. Karlsson, J. Mack, N. Brennan, B. Pyke, P. Withnell, R. Torbert, J. Macri, D. Rau, I. Dors, J. Needell, P.-A. Lindqvist, G. Olsson, and C. M. Cully (2016, March). The Axial Double Probe and Fields Signal Processing for the MMS Mission. *Space Science Reviews* 199(1-4), 167–188.
- Escoubet, C. P., M. Fehringer, and M. Goldstein (2001, September). Introduction The Cluster mission. *Ann. Geophys.* 19(10/12), 1197–1200.
- Farrell, W. M., M. D. Desch, M. L. Kaiser, and K. Goetz (2002, October). The dominance

- of electron plasma waves near a reconnection X-line region. *Geophysical Research Letters* 29, 1902–1.
- Farrugia, C. J., B. Lavraud, R. B. Torbert, M. Argall, I. Kacem, W. Yu, L. Alm, J. Burch, C. T. Russell, J. Shuster, J. Dorelli, J. P. Eastwood, R. E. Ergun, S. Fuselier, D. Gershman, B. L. Giles, Y. V. Khotyaintsev, P. A. Lindqvist, H. Matsui, G. T. Marklund, T. D. Phan, K. Paulson, C. Pollock, and R. J. Strangeway (2016, June). Magnetospheric Multiscale Mission observations and non-force free modeling of a flux transfer event immersed in a super-Alfvénic flow. *Geophysical Research Letters* 43, 6070–6077.
- Farrugia, C. J., D. J. Southwood, and S. W. H. Cowley (1988, January). Observations of flux transfer events. *Advances in Space Research* 8(9), 249–258.
- Fear, R. C., A. N. Fazakerley, C. J. Owen, A. D. Lahiff, E. A. Lucek, A. Balogh, L. M. Kistler, C. Mouikis, and H. Rème (2005, October). Cluster observations of boundary layer structure and a flux transfer event near the cusp. *Ann. Geophys.* 23(7), 2605–2620.
- Fear, R. C., S. E. Milan, A. N. Fazakerley, K.-H. Fornaçon, C. M. Carr, and I. Dandouras (2009, October). Simultaneous observations of flux transfer events by THEMIS, Cluster, Double Star, and SuperDARN: Acceleration of FTEs. *Journal of Geophysical Research (Space Physics)* 114, A10213.
- Fedder, J. A., S. P. Slinker, J. G. Lyon, and C. T. Russell (2002, May). Flux transfer events in global numerical simulations of the magnetosphere. *Journal of Geophysical Research: Space Physics* 107(A5), SMP 1–1.
- Formisano, V. (1979, September). Orientation and shape of the earth's bow shock in three dimensions. *Planetary and Space Science* 27, 1151–1161.
- Fox, W., F. Sciortino, A. v. Stechow, J. Jara-Almonte, J. Yoo, H. Ji, and M. Yamada (2017, March). Experimental Verification of the Role of Electron Pressure in Fast Magnetic Reconnection with a Guide Field. *Physical Review Letters* 118(12), 125002.
- Fujimoto, M., T. Mukai, H. Kawano, M. Nakamura, A. Nishida, Y. Saito, T. Yamamoto, and S. Kokubun (1998, February). Structure of the low-latitude boundary layer: A case study with Geotail data. *Journal of Geophysical Research* 103, 2297–2308.

- Fuselier, S. A., W. S. Lewis, C. Schiff, R. Ergun, J. L. Burch, S. M. Petrinec, and K. J. Trattner (2016, March). Magnetospheric Multiscale Science Mission Profile and Operations. *Space Science Reviews* 199, 77–103.
- Fuselier, S. A., E. G. Shelley, and O. W. Lennartsson (1997, January). Solar wind composition changes across the Earth’s magnetopause. *Journal of Geophysical Research* 102, 275–284.
- Gary, S. P. and J. Wang (1996, May). Whistler instability: Electron anisotropy upper bound. *Journal of Geophysical Research* 101, 10749–10754.
- Génot, V., L. Beigbeder, D. Popescu, N. Dufourg, M. Gangloff, M. Bouchemit, S. Caussarieu, J. P. Toniutti, J. Durand, R. Modolo, N. André, B. Cecconi, C. Jacquey, F. Pitout, A. Rouillard, R. Pinto, S. Erard, N. Jourdane, L. Leclercq, S. Hess, M. Khodachenko, T. Al-Ubaidi, M. Scherf, and E. Budnik (2018, January). Science data visualization in planetary and heliospheric contexts with 3dview. *Planetary and Space Science* 150, 111–130.
- Haaland, S., B. U. . Sonnerup, M. W. Dunlop, E. Georgescu, G. Paschmann, B. Klecker, and A. Vaivads (2004, May). Orientation and motion of a discontinuity from Cluster curlometer capability: Minimum variance of current density. *Geophysical Research Letters* 31, L10804.
- Hall, D. S., C. P. Chaloner, D. A. Bryant, D. R. Lepine, and V. P. Tritakis (1991, May). Electrons in the boundary layers near the dayside magnetopause. *Journal of Geophysical Research* 96, 7869–7891.
- Hapgood, M. A. and D. A. Bryant (1990, October). Re-ordered electron data in the low-latitude boundary layer. *Geophysical Research Letters* 17, 2043–2046.
- Harvey, C. C. (1998a). Spatial Gradients and the Volumetric Tensor. *ISSI Scientific Reports Series 1*, 307–322.
- Harvey, C. C. (1998b). Spatial Gradients and the Volumetric Tensor. *ISSI Scientific Reports Series 1*, 307–322.
- Hasegawa, H., M. Fujimoto, K. Maezawa, Y. Saito, and T. Mukai (2003, April). Geotail observations of the dayside outer boundary region: Interplanetary magnetic field control and dawn-dusk asymmetry. *Journal of Geophysical Research (Space Physics)* 108, 1163.

- Hasegawa, H., B. U. . Sonnerup, C. J. Owen, B. Klecker, G. Paschmann, A. Balogh, and H. Rème (2006, March). The structure of flux transfer events recovered from Cluster data. *Annales Geophysicae* 24, 603–618.
- Horbury, T. S. and K. T. Osman (2008). Multi-Spacecraft Turbulence Analysis Methods. *ISSI Scientific Reports Series* 8, 55–64.
- Huang, S. Y., M. Zhou, Z. G. Yuan, X. H. Deng, F. Sahraoui, Y. Pang, and S. Fu (2014, September). Kinetic simulations of electric field structure within magnetic island during magnetic reconnection and their applications to the satellite observations. *Journal of Geophysical Research (Space Physics)* 119, 7402–7412.
- Huba, J. D., N. T. Gladd, and K. Papadopoulos (1977). The lower-hybrid-drift instability as a source of anomalous resistivity for magnetic field line reconnection. *Geophysical Research Letters* 4, 125–128.
- Hudson, P. D. (1970, November). Discontinuities in an anisotropic plasma and their identification in the solar wind. *Planetary and Space Science* 18, 1611–1622.
- Hudson, P. D. (1971, December). Rotational discontinuities in an anisotropic plasma. *Planetary and Space Science* 19, 1693–1699.
- Hwang, K.-J., D. G. Sibeck, B. L. Giles, C. J. Pollock, D. Gershman, L. Avanov, W. R. Paterson, J. C. Dorelli, R. E. Ergun, C. T. Russell, R. J. Strangeway, B. Mauk, I. J. Cohen, R. B. Torbert, and J. L. Burch (2016, September). The substructure of a flux transfer event observed by the MMS spacecraft. *Geophysical Research Letters* 43, 9434–9443.
- Øieroset, M., T. D. Phan, C. Haggerty, M. A. Shay, J. P. Eastwood, D. J. Gershman, J. F. Drake, M. Fujimoto, R. E. Ergun, F. S. Mozer, M. Oka, R. B. Torbert, J. L. Burch, S. Wang, L. J. Chen, M. Swisdak, C. Pollock, J. C. Dorelli, S. A. Fuselier, B. Lavraud, B. L. Giles, T. E. Moore, Y. Saito, L. A. Avanov, W. Paterson, R. J. Strangeway, C. T. Russell, Y. Khotyaintsev, P. A. Lindqvist, and K. Malakit (2016, June). MMS observations of large guide field symmetric reconnection between colliding reconnection jets at the center of a magnetic flux rope at the magnetopause. *Geophysical Research Letters* 43, 5536–5544.

- Kacem I., Jacquy C., Génot V., Lavraud B., Vernisse Y., Marchaudon A., Le Contel O., Breuillard H., Phan T. D., Hasegawa H., Oka M., Trattner K. J., Farrugia C. J., Paulson K., Eastwood J. P., Fuselier S. A., Turner D., Eriksson S., Wilder F., Russell C. T., Øieroset M., Burch J., Graham D. B., Sauvaud J.-A., Avanov L., Chandler M., Coffey V., Dorelli J., Gershman D. J., Giles B. L., Moore T. E., Saito Y., Chen L.-J., and Penou E. (2018, March). Magnetic Reconnection at a Thin Current Sheet Separating Two Interlaced Flux Tubes at the Earth's Magnetopause. *Journal of Geophysical Research: Space Physics* 0(0).
- Karlson, K. A., M. Øieroset, J. Moen, and P. E. Sandholt (1996, January). A statistical study of flux transfer event signatures in the dayside aurora: The IMF By-related prenoon-postnoon asymmetry. *Journal of Geophysical Research* 101, 59–68.
- Kawano, H. and T. Higuchi (1996, October). A generalization of the minimum variance analysis method. *Annales Geophysicae* 14, 1019–1024.
- Kennel, C. F. and F. Engelmann (1966, December). Velocity Space Diffusion from Weak Plasma Turbulence in a Magnetic Field. *Physics of Fluids* 9, 2377–2388.
- Khotyaintsev, Y. V., A. Vaivads, A. Retinò, M. André, C. J. Owen, and H. Nilsson (2006, November). Formation of Inner Structure of a Reconnection Separatrix Region. *Physical Review Letters* 97(20), 205003.
- Khrabrov, A. V. and B. U. . Sonnerup (1998). DeHoffmann-Teller Analysis. *ISSI Scientific Reports Series 1*, 221–248.
- King, J. H. and N. E. Papitashvili (2005, February). Solar wind spatial scales in and comparisons of hourly Wind and ACE plasma and magnetic field data. *Journal of Geophysical Research (Space Physics)* 110, A02104.
- Kivelson, M. G., M. G. Kivelson, and C. T. Russell (1995, April). *Introduction to Space Physics*. Cambridge University Press. Google-Books-ID: qWHSqXGfsfQC.
- Kobel, E. and E. O. Flückiger (1994, December). A model of the steady state magnetic field in the magnetosheath. *Journal of Geophysical Research* 99, 23.
- Krall, N. A. and P. C. Liewer (1971, November). Low-Frequency Instabilities in Magnetic Pulses. *Physical Review A* 4(5), 2094–2103.

- Labelle, J. and R. A. Treumann (1988, July). Plasma waves at the dayside magnetopause. Technical report.
- Lavraud, B. and J. E. Borovsky (2008, September). Altered solar wind-magnetosphere interaction at low Mach numbers: Coronal mass ejections. *Journal of Geophysical Research (Space Physics)* 113, A00B08.
- Le, G., C. T. Russell, J. T. Gosling, and M. F. Thomsen (1996, December). ISEE observations of low-latitude boundary layer for northward interplanetary magnetic field: Implications for cusp reconnection. *Journal of Geophysical Research* 101, 27239–27250.
- Le Contel, O., P. Leroy, A. Roux, C. Coillot, D. Alison, A. Bouabdellah, L. Mirioni, L. Meslier, A. Galic, M. C. Vassal, R. B. Torbert, J. Needell, D. Rau, I. Dors, R. E. Ergun, J. Westfall, D. Summers, J. Wallace, W. Magnes, A. Valavanoglou, G. Olsson, M. Chutter, J. Macri, S. Myers, S. Turco, J. Nolin, D. Bodet, K. Rowe, M. Tanguy, and B. de la Porte (2016, March). The Search-Coil Magnetometer for MMS. *Space Science Reviews* 199, 257–282.
- Lee, L. C., Y. Lin, and G. S. Choe (1996, February). Generation of Rotational Discontinuities by Magnetic Reconnection Associated with Microflares. *Solar Physics* 163, 335–359.
- Lepping, R. P., J. A. Jones, and L. F. Burlaga (1990, August). Magnetic field structure of interplanetary magnetic clouds at 1 AU. *Journal of Geophysical Research: Space Physics* 95(A8), 11957–11965.
- Lindqvist, P.-A., G. Olsson, R. B. Torbert, B. King, M. Granoff, D. Rau, G. Needell, S. Turco, I. Dors, P. Beckman, J. Macri, C. Frost, J. Salwen, A. Eriksson, L. Åhlén, Y. V. Khotyaintsev, J. Porter, K. Lappalainen, R. E. Ergun, W. Wermeer, and S. Tucker (2016a, March). The Spin-Plane Double Probe Electric Field Instrument for MMS. *Space Science Reviews* 199(1-4), 137–165.
- Lindqvist, P.-A., G. Olsson, R. B. Torbert, B. King, M. Granoff, D. Rau, G. Needell, S. Turco, I. Dors, P. Beckman, J. Macri, C. Frost, J. Salwen, A. Eriksson, L. Åhlén, Y. V. Khotyaintsev, J. Porter, K. Lappalainen, R. E. Ergun, W. Wermeer, and S. Tucker (2016b, March). The Spin-Plane Double Probe Electric Field Instrument for MMS. *Space Science Reviews* 199, 137–165.



- Liu, Y.-H., M. Hesse, P. A. Cassak, M. A. Shay, S. Wang, and L.-J. Chen (2018, April). On the collisionless asymmetric magnetic reconnection rate. *Geophysical Research Letters* 45(8), 3311–3318. arXiv: 1711.06708.
- Lockwood, M., A. Fazakerley, H. Opgenoorth, J. Moen, A. P. van Eyken, M. Dunlop, J.-M. Bosqued, G. Lu, C. Cully, P. Eglitis, I. W. McCrea, M. A. Hapgood, M. N. Wild, R. Stamper, W. Denig, M. Taylor, J. A. Wild, G. Provan, O. Amm, K. Kauristie, T. Pulkkinen, A. Strømme, P. Prikryl, F. Pitout, A. Balogh, H. Rème, R. Behlke, T. Hansen, R. Greenwald, H. Frey, S. K. Morley, D. Alcaydé, P.-L. Blelly, E. Donovan, M. Engebretson, M. Lester, J. Watermann, and M. F. Marcucci (2001, October). Coordinated Cluster and ground-based instrument observations of transient changes in the magnetopause boundary layer during an interval of predominantly northward IMF: relation to reconnection pulses and FTE signatures. *Annales Geophysicae* 19, 1613–1640.
- Lockwood, M. and M. A. Hapgood (1997). How the magnetopause transition parameter works. *Geophysical Research Letters* 24, 373–376.
- Louarn, P., A. Fedorov, E. Budnik, G. Fruit, J. A. Sauvaud, C. C. Harvey, I. Dandouras, H. Rème, M. C. Dunlop, and A. Balogh (2004, October). Cluster observations of complex 3d magnetic structures at the magnetopause. *Geophysical Research Letters* 31(19), L19805.
- Matsumoto, H., H. Kojima, T. Miyatake, Y. Omura, M. Okada, I. Nagano, and M. Tsutsui (1994, December). Electrotastic Solitary Waves (ESW) in the magnetotail: BEN wave forms observed by GEOTAIL. *Geophysical Research Letters* 21, 2915–2918.
- Mauk, B. H., J. B. Blake, D. N. Baker, J. H. Clemmons, G. D. Reeves, H. E. Spence, S. E. Jaskulek, C. E. Schlemm, L. E. Brown, S. A. Cooper, J. V. Craft, J. F. Fennell, R. S. Gurnee, C. M. Hammock, J. R. Hayes, P. A. Hill, G. C. Ho, J. C. Hutcheson, A. D. Jacques, S. Kerem, D. G. Mitchell, K. S. Nelson, N. P. Paschalidis, E. Rossano, M. R. Stokes, and J. H. Westlake (2016, March). The Energetic Particle Detector (EPD) Investigation and the Energetic Ion Spectrometer (EIS) for the Magnetospheric Multiscale (MMS) Mission. *Space Science Reviews* 199(1-4), 471–514.

- Norgren, C., A. Vaivads, Y. V. Khotyaintsev, and M. André (2012, August). Lower Hybrid Drift Waves: Space Observations. *Physical Review Letters* 109, 055001.
- Oka, M., T.-D. Phan, S. Krucker, M. Fujimoto, and I. Shinohara (2010, May). Electron Acceleration by Multi-Island Coalescence. *The Astrophysical Journal* 714, 915–926.
- Onsager, T. G., J. D. Scudder, M. Lockwood, and C. T. Russell (2001, November). Reconnection at the high-latitude magnetopause during northward interplanetary magnetic field conditions. *Journal of Geophysical Research* 106, 25467–25488.
- Owen, C. J., A. N. Fazakerley, P. J. Carter, A. J. Coates, I. C. Krauklis, S. Szita, M. G. G. T. Taylor, P. Travnicek, G. Watson, R. J. Wilson, A. Balogh, and M. W. Dunlop (2001, October). Cluster PEACE observations of electrons during magnetospheric flux transfer events. *Annales Geophysicae* 19, 1509–1522.
- Parker, E. N. (1958, November). Dynamics of the Interplanetary Gas and Magnetic Fields. *The Astrophysical Journal* 128, 664.
- Paschmann, G., G. Haerendel, I. Papamastorakis, N. Sckopke, S. J. Bame, J. T. Gosling, and C. T. Russell (1982, April). Plasma and magnetic field characteristics of magnetic flux transfer events. *Journal of Geophysical Research* 87, 2159–2168.
- Peratt, A. L. (1996, March). Advances in Numerical Modeling of Astrophysical and Space Plasmas. *Astrophysics and Space Science* 242, 93–163.
- Phan, T., M. Dunlop, G. Paschmann, B. Klecker, J. Bosqued, H. Rème, A. Balogh, C. Twitty, F. Mozer, C. Carlson, C. Mouikis, and L. Kistler (2004, July). Cluster observations of continuous reconnection at the magnetopause under steady interplanetary magnetic field conditions. *Annales Geophysicae* 22, 2355–2367.
- Phan, T. D., J. P. Eastwood, M. A. Shay, J. F. Drake, B. U. . Sonnerup, M. Fujimoto, P. A. Cassak, M. Øieroset, J. L. Burch, R. B. Torbert, A. C. Rager, J. C. Dorelli, D. J. Gershman, C. Pollock, P. S. Pyakurel, C. C. Haggerty, Y. Khotyaintsev, B. Lavraud, Y. Saito, M. Oka, R. E. Ergun, A. Retino, O. L. Contel, M. R. Argall, B. L. Giles, T. E. Moore, F. D. Wilder, R. J. Strangeway, C. T. Russell, P. A. Lindqvist, and W. Magnes (2018, May). Electron magnetic reconnection without ion coupling in Earth’s turbulent magnetosheath. *Nature* 557(7704), 202–206.

- Phan, T.-D., G. Paschmann, W. Baumjohann, N. Sckopke, and H. Luehr (1994, January). The magnetosheath region adjacent to the dayside magnetopause: AMPTE/IRM observations. *Journal of Geophysical Research* 99, 121–141.
- Phan, T. D., G. Paschmann, J. T. Gosling, M. Oieroset, M. Fujimoto, J. F. Drake, and V. Angelopoulos (2013, January). The dependence of magnetic reconnection on plasma beta and magnetic shear: Evidence from magnetopause observations. *Geophysical Research Letters* 40, 11–16.
- Phan, T. D., M. A. Shay, C. C. Haggerty, J. T. Gosling, J. P. Eastwood, M. Fujimoto, K. Malakit, F. S. Mozer, P. A. Cassak, M. Oieroset, and V. Angelopoulos (2016, September). Ion Larmor radius effects near a reconnection X line at the magnetopause: THEMIS observations and simulation comparison. *Geophysical Research Letters* 43, 8844–8852.
- Pollock, C., P. Cson-Brandt, J. Burch, M. Henderson, J.-M. Jahn, D. McComas, S. Mende, D. Mitchell, G. Reeves, E. Scime, R. Skoug, M. Thomsen, and P. Valek (2003, October). The Role and Contributions of Energetic Neutral Atom (ENA) Imaging in Magnetospheric Substorm Research. *Space Science Reviews* 109, 155–182.
- Pollock, C., T. Moore, A. Jacques, J. Burch, U. Gliese, Y. Saito, T. Omoto, L. Avanov, A. Barrie, V. Coffey, J. Dorelli, D. Gershman, B. Giles, T. Rosnack, C. Salo, S. Yokota, M. Adrian, C. Aoustin, C. Auletta, S. Aung, V. Bigio, N. Cao, M. Chandler, D. Chornay, K. Christian, G. Clark, G. Collinson, T. Corris, A. De Los Santos, R. Devlin, T. Diaz, T. Dickerson, C. Dickson, A. Diekmann, F. Diggs, C. Duncan, A. Figueroa-Vinas, C. Firman, M. Freeman, N. Galassi, K. Garcia, G. Goodhart, D. Guererro, J. Hageman, J. Hanley, E. Hemminger, M. Holland, M. Hutchins, T. James, W. Jones, S. Kreisler, J. Kujawski, V. Lavu, J. Lobell, E. LeCompte, A. Lukemire, E. MacDonald, A. Mariano, T. Mukai, K. Narayanan, Q. Nguyen, M. Onizuka, W. Paterson, S. Persyn, B. Piepgrass, F. Cheney, A. Rager, T. Raghuram, A. Ramil, L. Reichenthal, H. Rodriguez, J. Rouzaud, A. Rucker, Y. Saito, M. Samara, J.-A. Sauvaud, D. Schuster, M. Shappirio, K. Shelton, D. Sher, D. Smith, K. Smith, S. Smith, D. Steinfeld, R. Szymkiewicz, K. Tanimoto, J. Taylor, C. Tucker, K. Tull, A. Uhl, J. Vloet, P. Walpole, S. Weidner, D. White, G. Winkert, P.-S. Yeh, and M. Zeuch (2016, March). Fast Plasma Investigation for Magnetospheric Multiscale. *Space Science Reviews* 199, 331–406.

- Pu, Z. Y., J. Raeder, J. Zhong, Y. V. Bogdanova, M. Dunlop, C. J. Xiao, X. G. Wang, and A. Fazakerley (2013, July). Magnetic topologies of an in vivo FTE observed by Double Star/TC-1 at Earth's magnetopause. *Geophysical Research Letters* 40, 3502–3506.
- Raeder, J. (2006, March). Flux Transfer Events: 1. generation mechanism for strong southward IMF. *Ann. Geophys.* 24(1), 381–392.
- Retinò, A., D. Sundkvist, A. Vaivads, F. Mozer, M. André, and C. J. Owen (2007, April). *In situ* evidence of magnetic reconnection in turbulent plasma. *Nature Physics* 3(4), 235–238.
- Retinò, A., A. Vaivads, F. Saharoui, Y. Khotyaintsev, J. S. Pickett, B. Cattaneo, M. B. M. F. Maruccci, M. Morooka, C. J. Owen, S. C. Buchert, and N. Cornilleau-Wehrin (2006). Structure of the separatrix region close to a magnetic reconnection X-line: Cluster observations. *Geophysical Research Letters* 33.
- Robert, P., M. W. Dunlop, A. Roux, and G. Chanteur (1998). Accuracy of Current Density Determination. *ISSI Scientific Reports Series 1*, 395–418.
- Roennmark, K. (1982, June). Waves in homogeneous, anisotropic multicomponent plasmas (WHAMP). Technical report.
- Roux, A., P. Robert, D. Fontaine, O. L. Contel, P. Canu, and P. Louarn (2015, June). What is the nature of magnetosheath FTEs? *Journal of Geophysical Research: Space Physics* 120(6), 2015JA020983.
- Russell, C. T., B. J. Anderson, W. Baumjohann, K. R. Bromund, D. Dearborn, D. Fischer, G. Le, H. K. Leinweber, D. Leneman, W. Magnes, J. D. Means, M. B. Moldwin, R. Nakamura, D. Pierce, F. Plaschke, K. M. Rowe, J. A. Slavin, R. J. Strangeway, R. Torbert, C. Hagen, I. Jernej, A. Valavanoglou, and I. Richter (2016, March). The Magnetospheric Multiscale Magnetometers. *Space Science Reviews* 199, 189–256.
- Russell, C. T. and R. C. Elphic (1978, December). Initial ISEE magnetometer results: magnetopause observations. *Space Science Reviews* 22(6), 681–715.
- Russell, C. T. and R. C. Elphic (1979, January). ISEE observations of flux transfer events at the dayside magnetopause. *Geophysical Research Letters* 6(1), 33–36.

- Russell, C. T., M. M. Mellott, E. J. Smith, and J. H. King (1983, June). Multiple spacecraft observations of interplanetary shocks Four spacecraft determination of shock normals. *Journal of Geophysical Research* 88, 4739–4748.
- Russell C. T., Mellott M. M., Smith E. J., and King J. H. (2012, September). Multiple spacecraft observations of interplanetary shocks: Four spacecraft determination of shock normals. *Journal of Geophysical Research: Space Physics* 88(A6), 4739–4748.
- Saunders, M. A., C. T. Russell, and N. Sckopke (1984, February). Flux transfer events: Scale size and interior structure. *Geophysical Research Letters* 11(2), 131–134.
- Shue, J.-H., J. K. Chao, H. C. Fu, C. T. Russell, P. Song, K. K. Khurana, and H. J. Singer (1997, May). A new functional form to study the solar wind control of the magnetopause size and shape. *Journal of Geophysical Research: Space Physics* 102(A5), 9497–9511.
- Shue, J.-H., P. Song, C. T. Russell, J. T. Steinberg, J. K. Chao, G. Zastenker, O. L. Vaisberg, S. Kokubun, H. J. Singer, T. R. Detman, and H. Kawano (1998, August). Magnetopause location under extreme solar wind conditions. *Journal of Geophysical Research* 103, 17691–17700.
- Silin, I., J. Büchner, and A. Vaivads (2005, June). Anomalous resistivity due to nonlinear lower-hybrid drift waves. *Physics of Plasmas* 12, 062902.
- Silveira, M. V., W. D. Gonzalez, D. G. Sibeck, and D. Koga (2012, December). Study on Flux Transfer Events at the Earth's Magnetopause Observed by THEMIS Satellites. *AGU Fall Meeting Abstracts* 13.
- Song, P. and C. T. Russell (1999, January). Time Series Data Analyses in Space Physics. *Space Science Reviews* 87, 387–463.
- Sonnerup, B. U. . and M. Scheible (1998). Minimum and Maximum Variance Analysis. *ISSI Scientific Reports Series 1*, 185–220.
- Sonnerup, B. U. O., G. Paschmann, I. Papamastorakis, N. Sckopke, G. Haerendel, S. J. Bame, J. R. Asbridge, J. T. Gosling, and C. T. Russell (1981, November). Evidence for magnetic field reconnection at the earth's magnetopause. *Journal of Geophysical Research* 86, 10049–10067.

- Stenzel, R. L. and W. Gekelman (1979, April). Experiments on Magnetic-Field-Line Reconnection. *Physical Review Letters* 42(16), 1055–1057.
- Tang, X., C. Cattell, J. Dombeck, L. Dai, L. B. Wilson, A. Breneman, and A. Hupach (2013, June). THEMIS observations of the magnetopause electron diffusion region: Large amplitude waves and heated electrons. *Geophysical Research Letters* 40, 2884–2890.
- Tooley, C. R., R. K. Black, B. P. Robertson, J. M. Stone, S. E. Pope, and G. T. Davis (2016, March). The Magnetospheric Multiscale Constellation. *Space Science Reviews* 199, 23–76.
- Torbert, R. B., C. T. Russell, W. Magnes, R. E. Ergun, P.-A. Lindqvist, O. Le Contel, H. Vaith, J. Macri, S. Myers, D. Rau, J. Needell, B. King, M. Granoff, M. Chutter, I. Dors, G. Olsson, Y. V. Khotyaintsev, A. Eriksson, C. A. Kletzing, S. Bounds, B. Anderson, W. Baumjohann, M. Steller, K. Bromund, G. Le, R. Nakamura, R. J. Strangeway, H. K. Leinweber, S. Tucker, J. Westfall, D. Fischer, F. Plaschke, J. Porter, and K. Lappalainen (2016, March). The FIELDS Instrument Suite on MMS: Scientific Objectives, Measurements, and Data Products. *Space Science Reviews* 199, 105–135.
- Torbert, R. B., H. Vaith, M. Granoff, M. Widholm, J. A. Gaidos, B. H. Briggs, I. G. Dors, M. W. Chutter, J. Macri, M. Argall, D. Bodet, J. Needell, M. B. Steller, W. Baumjohann, R. Nakamura, F. Plaschke, H. Ottacher, J. Hasiba, K. Hofmann, C. A. Kletzing, S. R. Bounds, R. T. Dvorsky, K. Sigsbee, and V. Kooi (2016, March). The Electron Drift Instrument for MMS. *Space Science Reviews* 199(1-4), 283–305.
- Torkar, K., R. Nakamura, M. Tajmar, C. Scharlemann, H. Jeszenszky, G. Laky, G. Fremuth, C. P. Escoubet, and K. Svenes (2016, March). Active Spacecraft Potential Control Investigation. *Space Science Reviews* 199, 515–544.
- Trattner, K. J., J. L. Burch, R. Ergun, S. A. Fuselier, R. G. Gomez, E. W. Grimes, W. S. Lewis, B. Mauk, S. M. Petrinec, C. J. Pollock, T. D. Phan, S. K. Vines, F. D. Wilder, and D. T. Young (2016, May). The response time of the magnetopause reconnection location to changes in the solar wind: MMS case study. *GRL* 43, 4673–4682.
- Trattner, K. J., J. S. Mulcock, S. M. Petrinec, and S. A. Fuselier (2007, February). Location of

- the reconnection line at the magnetopause during southward IMF conditions. *Geophysical Research Letters* 34, L03108.
- Trenchi, L., R. C. Fear, K. J. Trattner, B. Mihaljcic, and A. N. Fazakerley (2016, September). A sequence of flux transfer events potentially generated by different generation mechanisms. *Journal of Geophysical Research (Space Physics)* 121, 8624–8639.
- Tsyganenko, N. A. and D. P. Stern (1996, December). Modeling the global magnetic field of the large-scale Birkeland current systems. *Journal of Geophysical Research* 101, 27187–27198.
- Vaivads, A., M. André, S. C. Buchert, J.-E. Wahlund, A. N. Fazakerley, and N. Cornilleau-Wehrlin (2004, February). Cluster observations of lower hybrid turbulence within thin layers at the magnetopause. *Geophysical Research Letters* 31, L03804.
- Vaivads, A., Y. Khotyaintsev, M. André, and R. A. Treumann (2006). Plasma Waves Near Reconnection Sites. In *Geospace Electromagnetic Waves and Radiation*, Lecture Notes in Physics, pp. 251–269. Springer, Berlin, Heidelberg.
- Vaivads, A., O. Santolik, G. Stenberg, M. André, C. Owen, P. Canu, and M. Dunlop (2007). Source of whistler emissions at the dayside magnetopause. *Geophysical Research Letters* 34(9), L09106.
- Viberg, H., Y. V. Khotyaintsev, A. Vaivads, M. André, and J. S. Pickett (2013, March). Mapping HF waves in the reconnection diffusion region. *Geophysical Research Letters* 40, 1032–1037.
- Viberg, H., Y. V. Khotyaintsev, A. Vaivads, and M. Andre (2012, December). Mapping High-Frequency Waves in the Reconnection Diffusion Region. *AGU Fall Meeting Abstracts* 21.
- Wang Y. L., Elphic R. C., Lavraud B., Taylor M. G. G. T., Birn J., Russell C. T., Raeder J., Kawano H., and Zhang X. X. (2006, April). Dependence of flux transfer events on solar wind conditions from 3 years of Cluster observations. *Journal of Geophysical Research: Space Physics* 111(A4).
- Wild, J. A., S. W. H. Cowley, J. A. Davies, H. Khan, M. Lester, S. E. Milan, G. Provan, T. K. Yeoman, A. Balogh, M. W. Dunlop, K.-H. Fornaçon, and E. Georgescu (2001, October). First

simultaneous observations of flux transfer events at the high-latitude magnetopause by the Cluster spacecraft and pulsed radar signatures in the conjugate ionosphere by the CUTLASS and EISCAT radars. *Annales Geophysicae* 19, 1491–1508.

Xiao, C. J., Z. Y. Pu, Z. W. Ma, S. Y. Fu, Z. Y. Huang, and Q. G. Zong (2004, November). Inferring of flux rope orientation with the minimum variance analysis technique. *Journal of Geophysical Research (Space Physics)* 109, A11218.

Young, D. T., J. L. Burch, R. G. Gomez, A. De Los Santos, G. P. Miller, P. Wilson, N. Paschalidis, S. A. Fuselier, K. Pickens, E. Hertzberg, C. J. Pollock, J. Scherrer, P. B. Wood, E. T. Donald, D. Aaron, J. Furman, D. George, R. S. Gurnee, R. S. Hourani, A. Jacques, T. Johnson, T. Orr, K. S. Pan, S. Persyn, S. Pope, J. Roberts, M. R. Stokes, K. J. Trattner, and J. M. Webster (2016, March). Hot Plasma Composition Analyzer for the Magnetospheric Multiscale Mission. *Space Science Reviews* 199, 407–470.

Zhong, J., Z. Y. Pu, M. W. Dunlop, Y. V. Bogdanova, X. G. Wang, C. J. Xiao, R. L. Guo, H. Hasegawa, J. Raeder, X. Z. Zhou, V. Angelopoulos, Q. G. Zong, S. Y. Fu, L. Xie, M. G. G. T. Taylor, C. Shen, J. Berchem, Q. H. Zhang, M. Volwerk, and J. P. Eastwood (2013, May). Three-dimensional magnetic flux rope structure formed by multiple sequential X-line reconnection at the magnetopause. *Journal of Geophysical Research (Space Physics)* 118, 1904–1911.

Zhou, M., Y. Pang, X. Deng, S. Huang, and X. Lai (2014, August). Plasma physics of magnetic island coalescence during magnetic reconnection. *Journal of Geophysical Research (Space Physics)* 119, 6177–6189.

Zhou, M., Y. Pang, X. H. Deng, Z. G. Yuan, and S. Y. Huang (2011, June). Density cavity in magnetic reconnection diffusion region in the presence of guide field. *Journal of Geophysical Research (Space Physics)* 116, A06222.

Zhou, X.-Z., Q.-G. Zong, Z. Y. Pu, T. A. Fritz, M. W. Dunlop, Q. Q. Shi, J. Wang, and Y. Wei (2006, July). Multiple Triangulation Analysis: another approach to determine the orientation of magnetic flux ropes. *Annales Geophysicae* 24, 1759–1765.



## RESEARCH ARTICLE

10.1002/2017JA024537

## Special Section:

Magnetospheric Multiscale (MMS) mission results throughout the first primary mission phase

## Key Points:

- We characterized the scale, geometry, and propagation of an ion scale current structure resulting from the interaction between interlaced flux tubes
- Some signatures of magnetic reconnection are found at the interaction interface
- The intrinsic properties of this event are inconsistent with a single, homogenous helicoidal magnetic structure as expected from a typical flux transfer event (FTE)

## Correspondence to:

I. Kacem,  
issaad.kacem@irap.omp.eu

## Citation:

Kacem, I., Jacquey, C., Génot, V., Lavraud, B., Vernisse, Y., Marchaudon, A., et al. (2018). Magnetic reconnection at a thin current sheet separating two interlaced flux tubes at the Earth's magnetopause. *Journal of Geophysical Research: Space Physics*, 123, 1779–1793. <https://doi.org/10.1002/2017JA024537>




Received 30 JUN 2017

Accepted 27 JAN 2018

Accepted article online 20 FEB 2018

Published online 6 MAR 2018

## Magnetic Reconnection at a Thin Current Sheet Separating Two Interlaced Flux Tubes at the Earth's Magnetopause

I. Kacem<sup>1</sup> , C. Jacquey<sup>1</sup>, V. Génot<sup>1</sup>, B. Lavraud<sup>1</sup> , Y. Vernisse<sup>1</sup> , A. Marchaudon<sup>1</sup> , O. Le Contel<sup>2</sup> , H. Breuillard<sup>2</sup>, T. D. Phan<sup>3</sup> , H. Hasegawa<sup>4</sup> , M. Oka<sup>3</sup> , K. J. Trattner<sup>5</sup> , C. J. Farrugia<sup>6</sup> , K. Paulson<sup>6</sup> , J. P. Eastwood<sup>7</sup> , S. A. Fuselier<sup>8,9</sup> , D. Turner<sup>10</sup> , S. Eriksson<sup>5</sup> , F. Wilder<sup>5</sup> , C. T. Russell<sup>11</sup> , M. Øieroset<sup>3</sup>, J. Burch<sup>8</sup> , D. B. Graham<sup>12</sup> , J.-A. Sauvaud<sup>1</sup> , L. Avanov<sup>13</sup> , M. Chandler<sup>14</sup> , V. Coffey<sup>14</sup> , J. Dorelli<sup>13</sup>, D. J. Gershman<sup>13</sup> , B. L. Giles<sup>13</sup> , T. E. Moore<sup>13</sup> , Y. Saito<sup>4</sup>, L.-J. Chen<sup>13</sup> , and E. Penou<sup>1</sup>
<sup>1</sup>Institut de Recherche en Astrophysique et Planétologie, CNRS, UPS, CNES, Université de Toulouse, Toulouse, France,

<sup>2</sup>Laboratoire de Physique des Plasmas, Palaiseau, France, <sup>3</sup>Space Sciences Laboratory, University of California, Berkeley, CA, USA, <sup>4</sup>Institute of Space and Astronautical Science, JAXA, Sagami-hara, Japan, <sup>5</sup>Laboratory for Atmospheric and Space Physics, University of Colorado Boulder, Boulder, CO, USA, <sup>6</sup>Physics Department and Space Science Center, University of New Hampshire Durham, NH, USA, <sup>7</sup>The Blackett Laboratory, Department of physics, Imperial College London, London, UK, <sup>8</sup>Southwest Research Institute, San Antonio, TX, USA, <sup>9</sup>Department of Physics, University of Texas at San Antonio, San Antonio, TX, USA, <sup>10</sup>Space Sciences Department, The Aerospace Corporation, El Segundo, CA, USA, <sup>11</sup>Institute of Geophysics, Earth, Planetary, and Space Sciences, University of California, Los Angeles, CA, USA, <sup>12</sup>Swedish Institute of Space Physics, Uppsala, Sweden, <sup>13</sup>NASA Goddard Space Flight Center, Greenbelt, MD, USA, <sup>14</sup>NASA Marshall Space Flight Center, Huntsville, AL, USA

**Abstract** The occurrence of spatially and temporally variable reconnection at the Earth's magnetopause leads to the complex interaction of magnetic fields from the magnetosphere and magnetosheath. Flux transfer events (FTEs) constitute one such type of interaction. Their main characteristics are (1) an enhanced core magnetic field magnitude and (2) a bipolar magnetic field signature in the component normal to the magnetopause, reminiscent of a large-scale helicoidal flux tube magnetic configuration. However, other geometrical configurations which do not fit this classical picture have also been observed. Using high-resolution measurements from the Magnetospheric Multiscale mission, we investigate an event in the vicinity of the Earth's magnetopause on 7 November 2015. Despite signatures that, at first glance, appear consistent with a classic FTE, based on detailed geometrical and dynamical analyses as well as on topological signatures revealed by suprathermal electron properties, we demonstrate that this event is not consistent with a single, homogenous helicoidal structure. Our analysis rather suggests that it consists of the interaction of two separate sets of magnetic field lines with different connectivities. This complex three-dimensional interaction constructively conspires to produce signatures partially consistent with that of an FTE. We also show that, at the interface between the two sets of field lines, where the observed magnetic pileup occurs, a thin and strong current sheet forms with a large ion jet, which may be consistent with magnetic flux dissipation through magnetic reconnection in the interaction region.

## 1. Introduction

Magnetic reconnection is a ubiquitous and fundamental process in space plasma physics. When the interplanetary magnetic field (IMF) is directed southward, magnetic reconnection occurs at the Earth's dayside magnetopause current sheet and in the magnetotail current sheet as a result of the interaction between the solar wind and the Earth's magnetic field lines. Magnetic reconnection plays a major role in magnetospheric dynamics (Dungey, 1961). It governs the transport of energy, momentum, and plasma from the solar wind into the Earth's magnetosphere (Biernat, 1991; Dungey, 1961; Eastwood et al., 2013; Lemaire & Roth, 1978). Indeed, magnetic reconnection is associated with the conversion of magnetic energy into kinetic and thermal energies after a rearrangement of magnetic field lines. Despite numerous studies on this subject, many aspects about magnetic reconnection remain unclear, in particular, due to the limited temporal resolution of instruments aboard past missions such as Time History of Events and Macroscale Interactions during Substorms (Angelopoulos, 2008) and Cluster (Escoubert et al., 2001). The Magnetospheric Multiscale

mission (MMS) (Burch et al., 2016) was launched on 12 March 2015. Its prime goal is the understanding of the microphysics of magnetic reconnection (Burch & Phan, 2016). For that purpose, MMS is designed to provide unprecedented time resolution and measurement accuracy, which make the study of microscopic structures possible. The mission has allowed detailed studies of the electron diffusion region of magnetic reconnection, that is, the smallest-scale region where even the electron motion decouples from the magnetic field (Burch et al., 2016).

Complex magnetic structures can form at the magnetopause as a result of magnetic reconnection. Bursty and/or patchy magnetic reconnection may lead to the formation of flux transfer events (FTEs) on the dayside magnetopause (Hasegawa et al., 2006; Russell & Elphic, 1978, 1979). The two prime signatures of FTEs observed in situ are (1) an enhancement in the magnetic field magnitude and (2) a bipolar signature in the component of the magnetic field normal to the magnetopause. A mixture of magnetosheath and magnetospheric ion and electron populations is often detected within FTEs (Le et al., 1999). FTEs have been studied using simulations (Daum et al., 2008; Fedder et al., 2002; Raeder, 2006), laboratory experiments (e.g., Egedal et al., 2007; Fox et al., 2017; Stenzel & Gekelman, 1979; Yamada, 1999), ground measurements (Lockwood, Fazakerley, et al., 2001; Lockwood, Opgenoorth, et al., 2001; Wild et al., 2001), and multispacecraft missions as Cluster (e.g., Fear et al., 2005; Hasegawa et al., 2006; Roux et al., 2015; Sönnnerup et al., 2004), Time History of Events and Macroscale Interactions during Substorms (Fear et al., 2009; Silveira et al., 2012), and now MMS (Farrugia et al., 2016; Hwang et al., 2016). FTE models can essentially be classified into three types of models: elbow-shaped flux rope model (Russell & Elphic, 1978), multiple X-line model (Lee & Fu, 1985), and single X-line model (Fear et al., 2008; Scholer, 1988; Southwood et al., 1988). The properties and structure of FTEs have been the subject of many studies (e.g., Fear et al., 2008, 2017; Scholer, 1988; Southwood et al., 1988).

Multispacecraft missions have advanced the understanding of FTEs shape, motion, and extent (e.g., Fear et al., 2009; Trenchi et al., 2016). However, despite the abundance of FTE observations, their formation mechanism is not fully understood yet. More studies are still needed to better understand the detailed structure of FTEs and to link the observed properties to those at the formation site. The magnetic field topology within FTEs and their 3-D magnetic structure have also not been completely elucidated. Aside from large-scale FTEs often observed at the magnetopause, small-scale perturbations with magnetic signatures akin to those of FTEs might indicate the existence of very localized magnetic island structures (Hesse et al., 1990). Such magnetic islands may also be generated by multiple X-line reconnection (Pu et al., 2013; Zhong et al., 2013) (i.e., between two X-lines created sequentially on the magnetopause) or at a single X-line owing to rapid variations of the reconnection rate (Huang et al., 2014). Their typical signatures are an enhancement of the total magnetic field strength and a magnetic bipolar signature (Teh et al., 2010). In addition, plasma density dips have been reported at their center (Zhou et al., 2014). The core region is bounded by an electric current loop mainly carried by electrons (Zhou et al., 2014). The coalescence of magnetic islands, which corresponds to the merging of two islands into a larger one, has been observed in simulations (Drake et al., 2006; Huang et al., 2014; Oka et al., 2010; Zhou et al., 2014). Series of magnetic islands at the magnetopause have been reported (Eastwood et al., 2007; Song et al., 2012; Teh et al., 2010). During the coalescence of magnetic islands, a secondary magnetic reconnection process occurs at the interface of the two islands (Pritchett, 2008). The compression associated with the coalescence leads to the formation of localized current sheets. Øieroset et al. (2016) reported MMS observations of magnetic reconnection in a compressed current sheet between colliding jets at the center of a flux rope. Those observations were quite similar to the one that will be further discussed in the present paper. In their paper, they concluded that the reconnection observed at the thin current sheet inside the flux rope was not consistent with coalescence of two flux ropes. Instead, they suggested that reconnection was 3-D such that field lines did not form closed loops. Observations of magnetic flux ropes flanked by two X-lines between two converging jets were first reported by Hasegawa et al. (2010) and Øieroset et al. (2011).

The direct observation of complex 3-D magnetic structures resulting from multiple X-line reconnection at the magnetopause have been also reported (e.g., Øieroset et al., 2011; Pu et al., 2013; Zhong et al., 2013). Multiple X line magnetic reconnection occurs when magnetic reconnection takes place along several X-lines at the magnetopause. The model by Lee and Fu (1985) explains the complex geometrical properties of FTEs. The occurrence of reconnection at multiple sites may imply reconfigurations of the magnetic field into a complex 3-D magnetic topology. This may thus create complex 3-D structures such as FTEs or other structures, some of

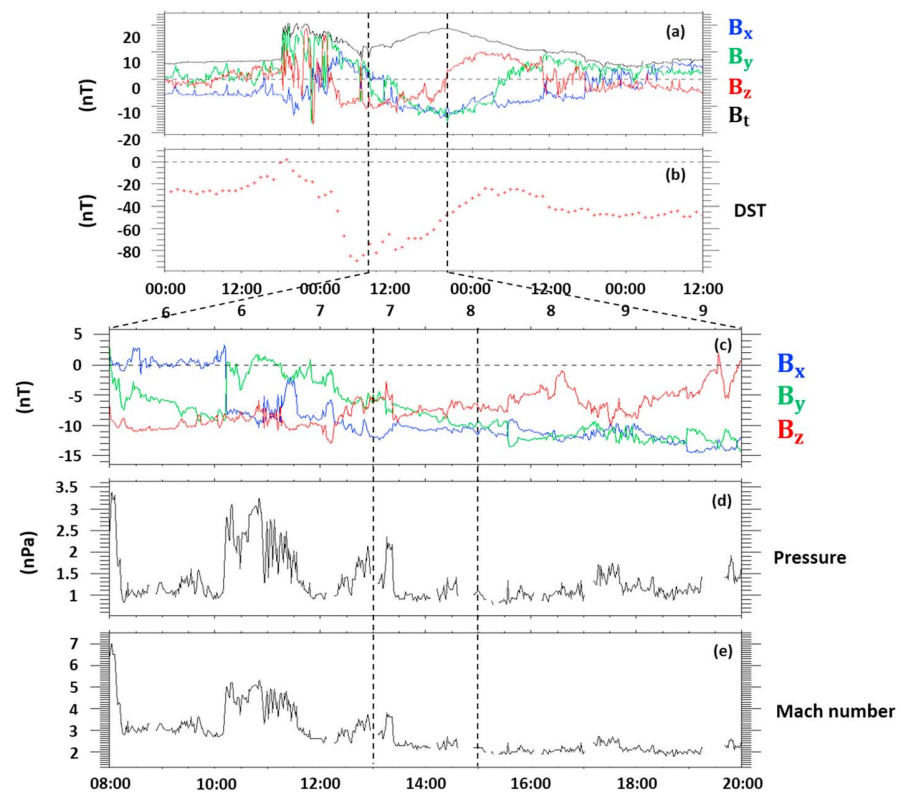


**Figure 1.** Solar wind conditions from the OMNI 1 min resolution database from 6 November 2015 00:00 UT through 9 November 2015 12:00 UT. (a) Interplanetary magnetic field components in GSE coordinates. (b) Disturbance storm time index. Solar wind conditions during 08:00–20:00 UT on 7 November 2015. (c) Interplanetary magnetic field components in GSE coordinates, (d) solar wind dynamic ram pressure, and (e) Alfvén Mach number.

which have been interpreted as interlaced magnetic flux tubes (Cardoso et al., 2013; Louarn et al., 2004). For example, Zhong et al. (2013) showed that both open and closed field lines can coexist inside the central region of the FTE flux ropes. They considered this observation as a characteristic feature of 3-D reconnected magnetic flux ropes resulting from multiple, sequential X-line reconnection. In this model, FTEs are generated by multiple X-line reconnection where new X-lines form sequentially. Furthermore, in Pu et al. (2013), electron energy-pitch angle distributions were used to infer the magnetic topology of field lines within an FTE. They found that the FTE was composed of flux ropes of four different magnetic topologies which indicates that the field lines must have reconnected multiple times. The coexistence of four different magnetic topologies was interpreted as the distinguishing feature of intrinsically 3-D multiple X-line reconnection.

In this paper, we analyze an event which looks like a typical FTE at first sight. After detailed analysis, we interpret the event as a current sheet resulting from the interaction of two converging and interlaced flux tubes. A similar interpretation has been suggested by Louarn et al. (2004) based on Cluster observations for an event that was observed on 30 June 2001, around 05:30 UT. They suggested a complex 3-D topology resulting from the interlinking of two magnetic flux tubes produced by two separate magnetic reconnection sites. They showed that the core fields of the two interacting and converging flux tubes had distinct orientations. The detailed interaction between the two flux tubes was not completely understood, however, owing to the limited time resolution of Cluster instrumentation. For the event considered in this paper, we show evidence for magnetic reconnection at the thin current sheet separating the two flux tubes, which was not observed for the event of Louarn et al. (2004).

We use the measurements from MMS spacecraft to study an event that was observed on 7 November 2015. We use ion and electron data from the Fast Plasma Investigation (FPI) instrument (Pollock et al., 2016), ion composition data from Hot Plasma Composition Analyzer (Young et al., 2016), and magnetic field from the

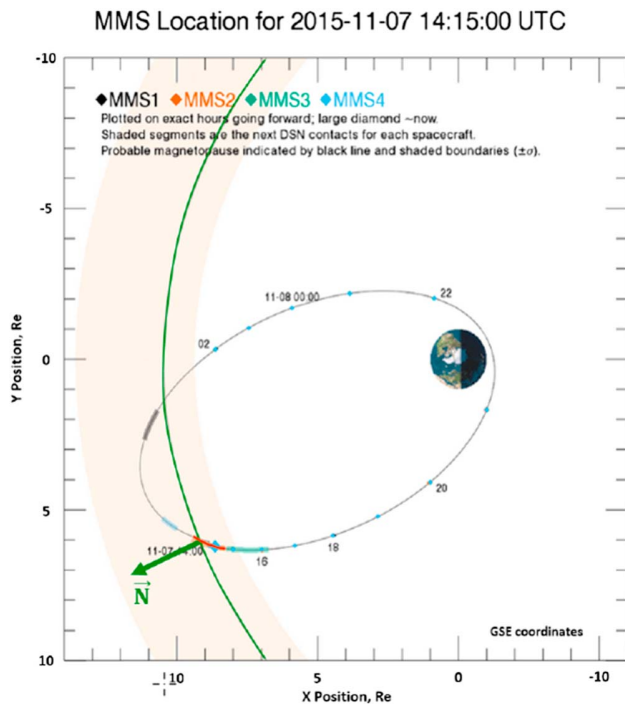


**Figure 2.** Magnetospheric Multiscale mission (MMS) orbit on 7 November 2015 and the normal to the magnetopause (green arrow) corresponding to the spacecraft location in the ecliptic plane. The red line corresponds to the crossing of a boundary layer.

fluxgate magnetometer (FGM) (Russell et al., 2016; Torbert et al., 2016). We first discuss whether the event can be considered as an FTE or not. The structure of a thin current sheet encountered by MMS in the center of the event is analyzed in details. We interpret the presence of this current sheet inside the event as a result of the collision of two converging flux tubes.

## 2. Context

Figure 1a shows the IMF from OMNI (King & Papitashvili, 2005) data over a few days surrounding the event. The period of interest, centered around 14:00 UT on 7 November 2015, occurred during the passage of a magnetic cloud at Earth. The magnetic cloud speed led to the formation of a shock in the solar wind, observed at 18:13 UT on 6 November, followed by a corresponding sheath, which lasted until ~8:00 UT on 7 November. Figures 1c–1e show the magnetic field, dynamic pressure, and Alfvén Mach number zoomed in around the time of interest, during the first part of the magnetic cloud when its magnetic field had strong southward and dawnward components. The MMS event that was observed around 14:00 UT on 7 November, occurred during a period of both strong driving of the magnetosphere ( $Dst = -69$  nT,  $k_p = 4$ ) and low Alfvén Mach number ( $<3$ ). Under these conditions, solar wind-magnetosphere interaction is expected to be altered affecting in particular the flows in the magnetosheath uncommonly enhanced and distributed, the magnetopause shape, and magnetic reconnection factors (see Lavraud & Borovsky, 2008).

Around 14:00 UT on 7 November (third dashed line in Figure 3), the MMS spacecraft were located in the dusk sector near the magnetopause. As illustrated in Figure 2, their barycenter was located at  $(8.6, 6.2, -0.9)$   $R_E$  in GSE coordinates. Separated by about 10 km, they were in a good tetrahedron configuration with a quality factor of 0.84 (Fuselier et al., 2016), which is suited for applying multipoint spacecraft methods (Dunlop & Woodward, 1998) as used in this study.

Two hours of MMS survey data are presented in Figure 3. Panels (a) to (g) show, respectively, in GSE coordinates, the magnetic field components and total field strength, the electron and ion density, the ion velocity components and amplitude, the electron, ion,  $He^{2+}$ , and  $O^+$  energy spectrograms. Initially, the spacecraft were located in the magnetosheath, as shown in the ion and electron spectrograms typical of the magnetosheath, high plasma number densities, and the abundance of  $He^{2+}$  and the absence of  $O^+$  ion fluxes. After 14:28 UT, the spacecraft were inside the magnetosphere characterized by a positive and dominant  $B_z$ , low number densities, and weak flows, as well as high fluxes of observed energetic electrons, protons, and oxygen ions. Conversely, the  $He^{2+}$  fluxes were weak.

Around 13:28 UT, the data show a partial crossing of the magnetopause, as indicated by variable  $B_z$  component and flows. We suspect that the sudden magnetopause crossing (i.e., magnetopause expansion) was produced by the arrival of the solar wind discontinuity that separates a high Mach number solar wind from low Mach number solar wind, as observed in the OMNI data around that time in Figure 1e. From then on, the prevailing solar wind has a low Mach number. Soon thereafter (~13:35 UT) the spacecraft exited back into the magnetosheath, as seen from the faster flows, similar to the previous magnetosheath interval. This magnetosheath interval was characterized by a much lower density and included two very short incursions into the magnetosphere. The main magnetopause crossing then occurred at 13:44:30 UT (second dashed line in Figure 3). The boundary layer inside the magnetopause, hereafter called LLBL (for low-latitude boundary layer), was observed from 13:44:30 UT to 14:00 UT. This LLBL interval was also very dynamic. This interval is identified as the outer LLBL because it contains plasma accelerated through the magnetopause discontinuity (marked by the magnetic field rotation), as evidenced by the enhanced and diverted flows as compared to the pristine magnetosheath observed before 13:45 (cf. panels (a) and (c)). The spacecraft entered more clearly into the magnetosphere around ~14:00 UT where a second magnetic field rotation occurred,



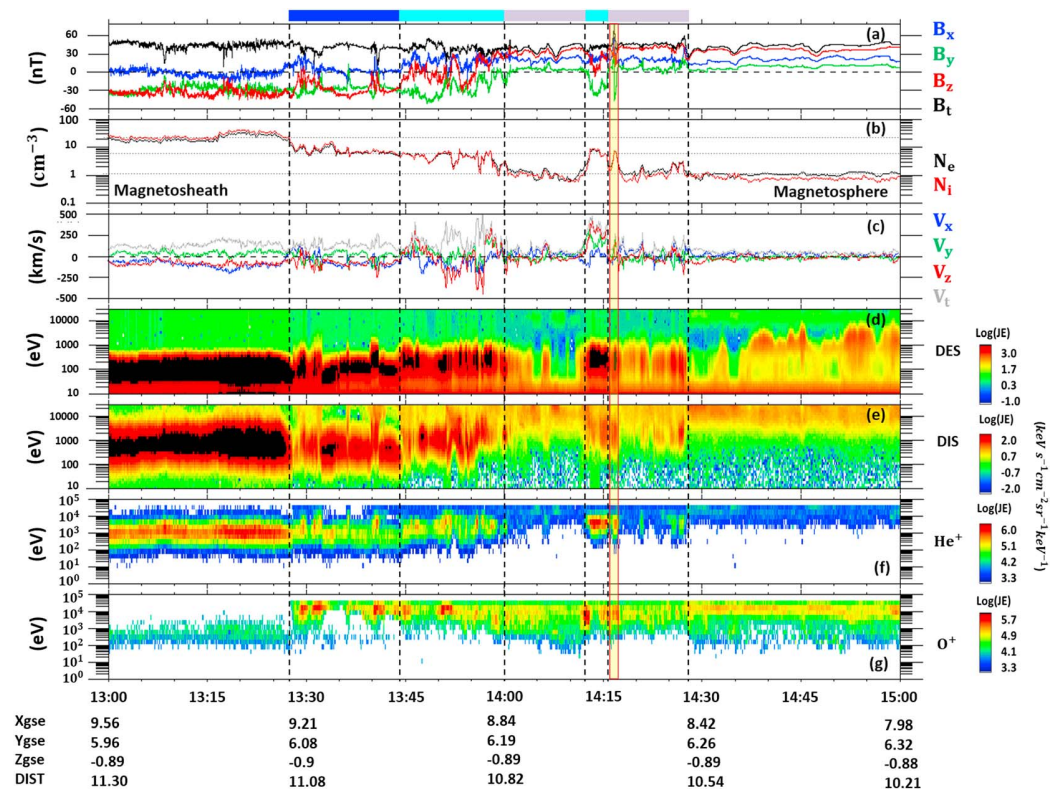


**Figure 3.** Magnetic field (panel (a)) from fluxgate magnetometer, electron and ion densities (b), ion velocity (c), and electron and ion spectrograms (d, e) provided by FPI, as well as  $\text{He}^{2+}$  (f) and  $\text{O}^+$  (g) spectrograms from Hot Plasma Composition Analyzer from Magnetospheric Multiscale mission 1.

this time mainly in the  $B_y$  component. We note that after this second current sheet the spacecraft did not exit immediately into the pristine magnetosphere given the observation of low-energy magnetosheath electrons between 14:00 and 14:05 UT, reminiscent of a kind of, or a more inner part of, the LLBL. The true hot magnetospheric plasma was observed, for example, around 14:10 UT. The spacecraft exited back into the main (outer) LLBL with enhanced flows and negative  $B_y$  around  $\sim 14:12$  UT just before the event of interest, which was observed between 14:16:00 and 14:17:30 UT. The event time interval is indicated with a yellow shaded area, bracketed by the red vertical lines. A strong peak in magnetic field magnitude consists of the most spectacular feature and is visible in Figure 3a. Just after the event, the spacecraft remain in the LLBL based on the presence of some low-energy magnetosheath electrons, but again likely the more inner part of it given the measured low densities and the positive  $B_y$  value. The spacecraft are in the magnetosphere proper after around 14:28 UT (some middle-energy electrons are intermittently observed after that time, but these are believed to be of ionospheric origin).

To summarize, we believe that two kinds of LLBL were present, as has been reported previously (e.g., Hasegawa et al., 2003). The outer LLBL had a high density and showed enhanced  $|V_z|$  flows consistent with the passage through the magnetopause current sheet, which is characterized by a rotation of the magnetic field ( $B_z$  increase) as well. The inner LLBL had, on the other hand, a lower density and a magnetic field orientation more consistent with the geomagnetic field observed in the pristine magnetosphere. The transition from the main (outer) LLBL to the inner LLBL also corresponded to a current sheet responsible for the main rotation in  $B_y$ .

### 3. Data Analysis

#### 3.1. Large-Scale Structure

The crossing of the magnetopause and LLBL occurred between 13:44:30 UT and 14:00 UT. The magnetopause normal and associated LMN frame (Farrugia et al., 1988) were inferred by performing a variance analysis

**Table 1**  
Local Magnetopause Coordinate System Obtained From the Minimum Variance Analysis of the Magnetic Field

Component	L	M	N
$X_{GSE}$	0.24	0.48	0.84
$Y_{GSE}$	0.53	-0.79	0.3
$Z_{GSE}$	0.81	0.37	-0.44

Note.  $\lambda_L/\lambda_M = 5.75$ ;  $\lambda_L/\lambda_N = 18.64$ ;  $\lambda_M/\lambda_N = 3.23$ .

The vector data are in GSE coordinates. The top panel (a) displays the magnetic field, the (b) panel the ion thermal pressure ( $P_p$ ), the magnetic pressure ( $P_m$ ), and the total pressure ( $P_t = P_p + P_m$ ). The (c) panel shows the current density as inferred from the curlometer technique, and the (d) and (e) panels exhibit the ion velocity and the density of both ions and electrons. Electron data for the same interval are displayed in Figure 5. The second panel in Figure 5 shows the omnidirectional energy flux of electrons, and the following three panels ((c)–(e)) give the electron pitch angle distributions for three energy ranges: 98–127 eV, 451–575 eV, and 3.3–11.5 keV. These energy bands are considered typical of thermal magnetosheath, accelerated magnetosheath, and magnetospheric electron populations, respectively (e.g., Pu et al., 2013; Zhong et al., 2013). The top panel (a) displays the magnitude and  $B_y$  component of the magnetic field for the sake of completeness.

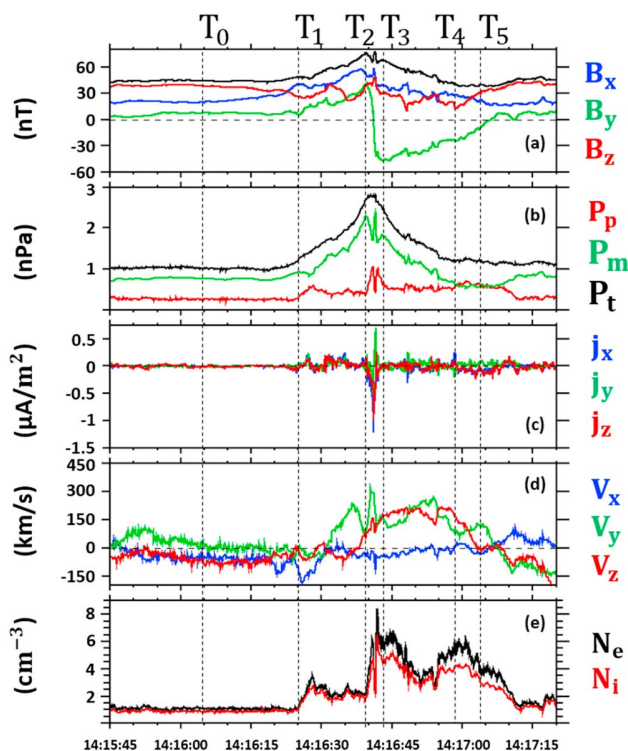


**Figure 4.** An overview of Magnetospheric Multiscale mission 1 observations between 14:15:45 and 14:17:20 UT in GSE coordinates on 7 November 2015. (a) Magnetic field components and total field strength, (b) pressures (red = plasma (ion), green = magnetic, and black = total), (c) current density from curlometer technique, (d) ion velocity components, (e) electron (black), and ion (red) densities. The black vertical dashed lines labeled  $T_0$  to  $T_5$ , correspond to times 14:16:04; 14:16:25; 14:16:40; 14:16:43; 14:16:58; and 14:17:04.5 UT.

(Sönnnerup & Scheible, 1998) of the magnetic field data between 13:42:25 and 14:02:44 UT. The results are given in Table 1. The magnetopause normal vector ( $N = [0.84, 0.30, -0.44]$  in GSE) was relatively close to the normal direction calculated from magnetopause models (e.g.,  $[0.91, 0.41, -0.06]$  in GSE using the Shue et al., 1997 model). The  $L$  and  $M$  vectors roughly pointed in the  $Z$  and  $-Y$  directions.

In Figures 4, 100 s of burst data measured by MMS 1 are presented. Dashed lines labeled  $T_0$  to  $T_5$  delimit the different parts of the event that clearly have different properties and correspond to times 14:16:04; 14:16:25; 14:16:40; 14:16:43; 14:16:58; and 14:17:04.5 UT, respectively.

Figure 4 shows that prior to  $T_1$  (14:16:25 UT), the spacecraft were in the inner LLBL, where plasma densities were low and  $B_z$  was the main component of the magnetic field. Then, between  $T_1$  and  $T_5$ , the MMS spacecraft recorded large changes in all parameters. The most remarkable features included peaks in the magnitudes of the magnetic field (by a factor of  $\sim 1.7$ ) and total pressure ( $\sim 2.5$ ), a strong bipolar signature in the  $B_y$  component ( $\Delta B_y \sim 80$  nT) and a large ( $\sim 300$  km/s) flow directed northward ( $V_z > 0$ ) and eastward ( $V_y > 0$ ). At first glance, these large-scale signatures are consistent with those of an FTE consisting of a flux rope resulting from a reconnection process, which may have occurred southward and downward of the spacecraft for the prevailing conditions of IMF negative  $B_z$  and  $B_y$  (see Figure 1).

This interpretation appears, however, inconsistent with several observational facts. (i) First, the bipolar signature was not observed in the component normal to the magnetopause (mainly along  $X_{GSE}$ ), but rather in a direction almost perpendicular ( $B_{YGSE}$ ) to the magnetopause normal (see panel (a)). (ii) Second, there were a small-scale and fast  $V_y = 300$  km/s ion jet (along  $Y_{GSE}$ ) and an intense and thin current structure near the peak of the large scale magnetic field between  $T_2$  and  $T_3$  (panels (d), (c), and (a)). Such features do not fit the usual flux rope models of FTEs, although the presences of thin current sheets and reconnection have been reported in the literature (Øieroset et al., 2016). (iii) Third, based on the pitch angle distribution of electrons, there were drastically different regimes before and after the passage of this current structure (last three panels in Figure 5). The characteristic features of the first and second parts of the event were clearly different. The region between  $T_1$  and  $T_2$  was first characterized by lower fluxes of antiparallel accelerated magnetosheath electrons, while the parallel fluxes remained unchanged with regard to the fluxes measured before  $T_1$  (panel (d)). On the other hand, the thermal magnetosheath electron population tended to have larger fluxes, consistent with an increased density (panel (c)). During this interval, MMS also observed a trapped electron population (at  $90^\circ$  pitch angle) which appears in both the

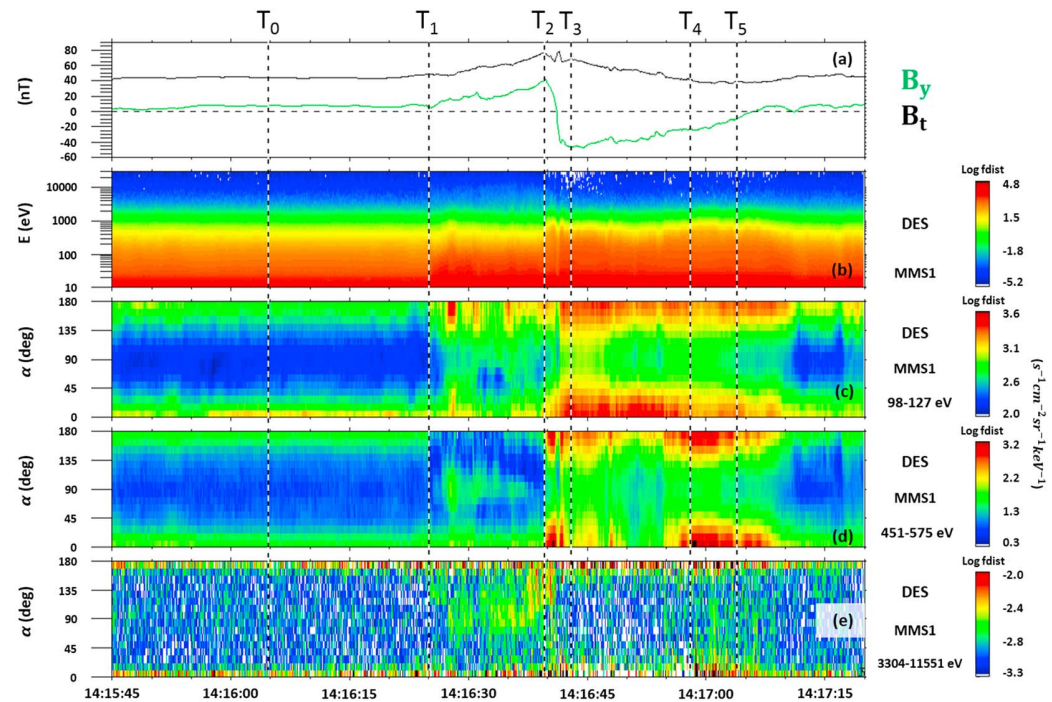


**Figure 5.** Magnetospheric Multiscale mission 1 data between 14:15:45 and 14:17:20 UT of (a)  $B_y$  and the magnetic field strength in GSE coordinates; (b) electron energy spectrum. Electron pitch angle distribution in the range of (c) 98–127 eV, (d) 451–751 eV, and (e) 3,304–11,551 eV.

accelerated magnetosheath and magnetospheric energy ranges (panels (d) and (e)). By contrast, during the second part of the event (between  $T_3$  and  $T_4$ ), this trapped population was not present anymore; there were essentially no magnetospheric electrons. The accelerated magnetosheath electrons antiparallel flux was larger than the parallel one (panel (d)). These strongly different features suggest that this sequence is not the signature of a single homogenous structure like a flux rope (expected to be associated with FTEs). We rather interpret the time sequence between  $T_1$  and  $T_4$  as successive crossings of two distinct flux tubes, henceforth referred to as  $FT_A$  ( $T_1$ – $T_2$ ) and  $FT_B$  ( $T_3$ – $T_4$ ). Finally, the densities were also drastically different between  $FT_A$  and  $FT_B$  (Figure 4e). In  $FT_B$ , the electron/ion densities and the  $He^{2+}$  fluxes (Figure 2) had values typical of the outer LLBL.

A complementary view is provided in Figure 6 that introduces our observations in the LMN frame. The components of the magnetic field are shown in panels (a) to (d). The ion velocity components are provided in panels (f) to (i), and the angle  $\Psi$  is shown in panel (e).  $\Psi$  is the angle between the magnetopause normal and the magnetic field ( $\Psi = \arctan\{(B_L^2 + B_M^2)^{1/2}/|B_N|\}$ ). Displaying the data in the LMN frame reveals two main features at the scale of the whole event: (i) the magnetic changes in the LMN frame did not exhibit an FTE-like bipolar signature, but rather a sharp rotation of the magnetic field through a thin current structure. The maximum magnetic field shear angle, corresponding to that across the central thin current sheet, was about  $73^\circ$ . Before its passage, the magnetic field was progressively deformed throughout  $T_0$ – $T_1$ – $T_2$ , as indicated by the gradual changes in  $\Psi$ . When the spacecraft crossed the current structure, the  $\Psi$  angle recovered quickly its initial value and, thereafter, both the L and N components of the magnetic field remained close to zero for about 15 s, while the M component was strongly enhanced. (ii) The event was associated with a perpendicular ion flow in the +L direction, suggesting that reconnection occurred southward of the spacecraft.

A more detailed examination of the observations indicates that at the beginning of the period, before  $T_0$ , the magnetic field had an orientation tangential to the magnetopause, mainly in the L direction. The  $\Psi$  angle was close to  $90^\circ$ . The ion flows were weak. At time  $T_0$ , while all other parameters remained unchanged, the  $\Psi$  angle ( $B_N$  component) started to decrease (increase). This trend continued until  $T_1$  and indicates that the



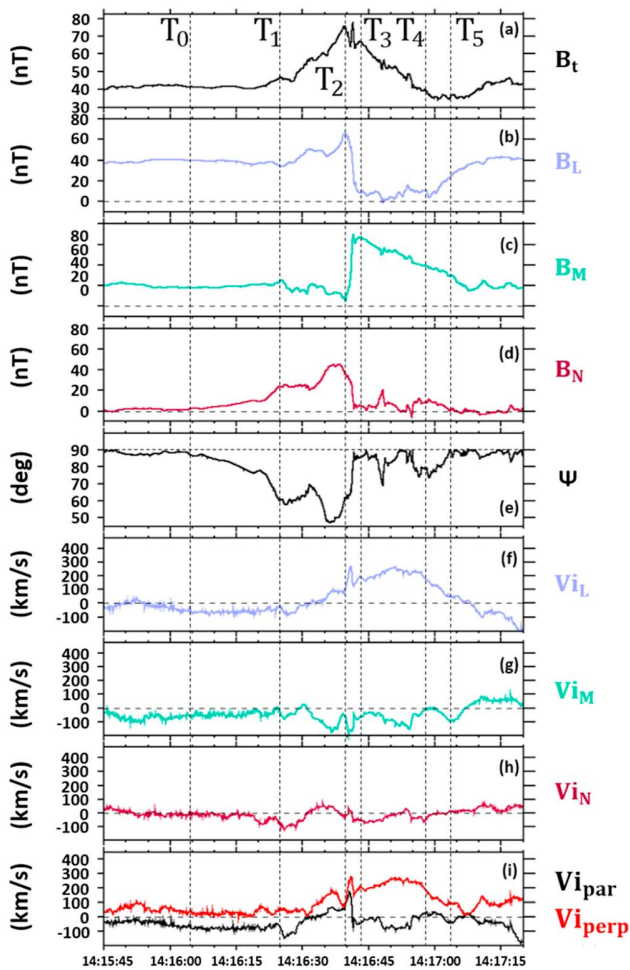


**Figure 6.** (a) Magnetic field magnitude, (b)–(d) magnetic field components in the magnetopause LMN frame, (e) angle  $\Psi$  between the magnetopause normal and the magnetic field, (f)–(h) ion velocity components in the magnetopause LMN frame, and (i) parallel (black) and perpendicular (red) ion velocity in the GSE coordinates system. The black vertical dashed lines labeled  $T_0$  to  $T_5$  are shown at the same times as in Figure 4.

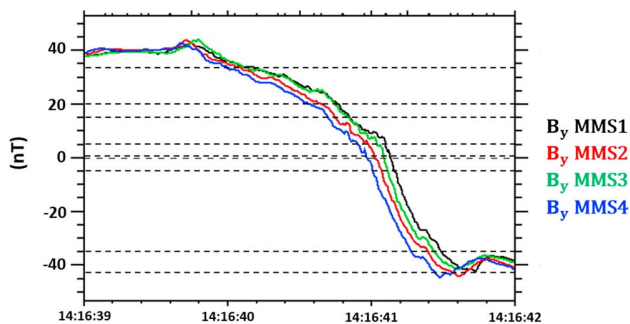


**Figure 7.**  $B_y$  component of the magnetic field in the GSE coordinates system from the four Magnetospheric Multiscale mission spacecraft. The horizontal dashed lines represent the several contours of different  $B_y$  values that were used to calculate their normal directions and propagation velocities.

magnetic field underwent a large-scale deformation. This is interpreted as the remote signature of a propagating process having started before  $T_0$  and approaching closer to the spacecraft. During this period, the ion flow remained constantly weak ( $V_{iL} \sim -50$  km/s,  $V_{iM} \sim -25$  km/s) except for a small  $V_N$  (also seen on the  $V_{YGSE}$  component) peak  $\sim 5$  s prior to  $T_1$ . This  $V_N$  change consisted of a perpendicular flow and was negative indicating an inward motion of plasma. This one could be due to a local retreat of the magnetopause. The time  $T_1$  marks the beginning of the in situ detection of the event, corresponding to the entry into flux tube  $FT_A$ . Between  $T_1$  and  $T_2$ , the  $B_L$  component and the magnitude of the magnetic field both increased. It was also the general trend for  $B_N$  while  $B_M$  decreased to  $\sim 15$  nT. When the spacecraft penetrated into  $FT_A$  (at  $T_1$ ), it first detected a  $\sim 3$  s duration antiparallel ion flow that reached a maximum value of 150 km/s along the L and N directions. Then, when  $V_L$  and  $V_N$  returned to zero, the flow was mainly perpendicular with a  $-V_M$  component. From that time until  $T_2$  (14:16:40 UT), the main component of the flow was  $-V_M$ , suggesting a westward motion of  $FT_A$ .

Between  $T_2$  and  $T_3$ , the magnetic field rapidly rotated. A localized ion jet was detected at that time, as clearly seen on the  $V_{YGSE}$  component in Figure 4. This jet appeared in the L and M components in Figure 6. It was thus directed in a direction tangential to the magnetopause and oblique to the magnetic field as it includes both parallel and perpendicular components. Comparison to the electric field data (not shown) indicates that the ions were decoupled from the magnetic field during the main current structure. Being along  $V_M$  during a large rotation of the  $B_M$  component, this ion jet is consistent with expectations from magnetic reconnection between  $FT_A$  and  $FT_B$ , as is discussed later.

Between  $T_3$  and  $T_4$ , the flow was essentially along the L direction and the N and L components of magnetic field were close to zero.

Finally, between  $T_4$  and  $T_5$ , the ion flow vanished gradually and the magnetic field recovered its initial (before  $T_0$ ) orientation. The interface marking the end of the event is not analyzed in further detail in this paper.

### 3.2. Small-Scale Current Sheet

In order to infer the motion of the current structure relative to the spacecraft, we performed differential timing analysis using the  $B_{YGSE}$  bipolar transition, which constitutes the clearest change. This transition corresponded to the crossing of a strong current structure. We identified times when the four MMS spacecraft successively measured a set of identical  $B_y$  values, as illustrated in Figure 7 with the horizontal dashed lines. Assuming that the structure is planar, we applied the multi-point triangulation method (Harvey, 1998; Russell et al., 1983). For all identified times it provided a set of normal vectors  $\mathbf{N}_C$  and propagation speed  $V_P$  along the normal. The results showed that both  $\mathbf{N}_C$  and  $V_P$  change only slightly through the transition. From now on we thus use a normal vector  $\mathbf{N}_C = [-0.5456; -0.0308; 0.8375]_{GSE}$  and a propagation velocity of  $\sim 67$  km/s, which are obtained from averaging over the full set of values shown in Table 2.

For inferring the geometry and the orientation of the current structure, we performed the variance analysis of the current density measurement



**Table 2**

The Normal Directions and the Velocities of the Propagating Structure Obtained by Performing the Timing Method for Multiple Values of  $B_Y$

$B_Y$ (nT)	$N_x$	$N_y$	$N_z$	$V$ (km/s)
33	-0.5026	0.0040	0.8645	66.08
20	-0.4621	-0.1507	0.8739	60.36
15	-0.5038	-0.2519	0.8263	74.00
5	-0.5915	-0.0201	0.8061	63.63
1	-0.6140	-0.0805	0.7852	73.65
0	-0.5969	-0.0708	0.7992	73.39
-5	-0.5822	0.0018	0.8131	81.04
-35	-0.4206	0.0120	0.9072	58.43
-40	-0.5755	0.2827	0.7674	51.33

Note. Mean values are  $V = 66.88$  km/s and  $\mathbf{N}_C = [-0.5456, -0.0308, 0.8375]$ .

obtained with the curlometer technique (Robert et al., 1998) for the period 14:16:39–14:16:43 UT. The results given in Table 3 exhibit a strong contrast between the eigenvalues and thus indicate that the current structure was organized with respect to clearly defined principal axes. The axis of maximal current (called thereafter “main current”) was directed in the  $(-X, -Z)_{GSE}$  direction  $[-0.76, -0.20, -0.61]$ . The second principal axis associated with a significant ( $\lambda_1/\lambda_2 \sim 2.8$ ) current contribution (called thereafter “secondary current”) was close to the  $Y_{GSE}$  direction  $[0.03, -0.96, 0.28]$ . The third principal axis was associated with much lower eigenvalue ( $\lambda_2/\lambda_3 \sim 15.43$ ) with an almost null current component. Its orientation  $[-0.65, 0.19, 0.74]$  was in the  $(-X, +Z)_{GSE}$  direction and was found to be close to the direction of  $\mathbf{N}_C$  found from the differential timing analysis.

Both independent approaches (current variance analysis and triangulation method) thus provided a consistent geometry of the current

structure. We then considered a new coordinate system referred thereafter as the PCS (Propagation Current Structure) frame, which is illustrated in Figure 8. The PCS coordinate system is defined by the vectors  $\vec{U}_P$ ,  $\vec{U}_J$ , and  $\vec{U}_V$ . The components of these unit vectors in the GSE frame are shown in Table 4. The first unit vector  $[-0.6124; 0.0239; 0.7902]_{GSE}$  is close to the propagation direction as well as the normal direction of the current structure. The second axis is chosen to be a direction opposite to the main current  $[0.7676; -0.2209; 0.6016]_{GSE}$  and the last axis is defined using the unit vector of the ion jet which is also close to the unit vector of the secondary current  $[0.1889; 0.9750; 0.1169]_{GSE}$  (almost coinciding with  $Y_{GSE}$ ). In order to follow the current structure, the PCS frame is in translation relatively to the GSE one at a translation velocity equal to the propagation velocity derived from the differential timing analysis.

The Figure 9 shows data coming from the FGM and FPI experiments on board MMS-1 for a 6 s period including the current structure observation. The GSE coordinates of the current density (from curlometer technique) are represented in panel (a). A correlation between  $J_X$  and  $J_Z$  is clearly visible and  $J_Y$  exhibits a bipolar signature. As showed in panel (b) the current was mostly parallel to the magnetic field. In panel (c), the magnitudes of the current density obtained from the curlometer technique  $J_{curl}$  (FGM data) and the ones directly computed from the particle measurement (FPI data) are compared.  $J_i$  (green) is the ion current,  $J_e$  (blue) the electron current, and  $J_{part}$  is obtained from  $ne(V_i - V_e)$ . It appears clearly that the current was carried by the electrons while the ion contribution was almost negligible.

The panel (d) displays the current density (from the curlometer technique) in the PCS frame. The spacecraft reached the structure around 14:16:39.70 UT (time marked by the first black dashed vertical line) as indicated by the little jump seen on  $J_x$ ,  $J_y$ , and  $J_z$ . Then, the satellites recorded a gradual increase (in absolute value) of the main current component and a sharp peak between 14:16:40.96 UT and 14:16:41.54 UT (times indicated by the red vertical lines). Eventually, MMS-1 exited out of the current structure around 14:16:42.22 UT (time marked the second black dashed vertical line). Encircling the main current peak, a bipolar secondary current was measured.

Multiplying the 2.52 s duration of the current structure crossing (interval between the pair of black dashed vertical lines in Figure 9) with the propagation velocity, we find that the spatial scale of the entire current structure is about 169 km. This is about 3 times the  $\sim 60$  km Larmor radius of thermal protons at the time of the current sheet encounter. The crossing of the main current peak, as indicated between the two vertical redlines in Figure 9, lasted 0.58 s, which corresponds to  $\sim 39$  km. That is, the dimension of the main current peak was smaller than the proton Larmor radius.

The panel (e) shows the PCS magnetic field components. We note that the  $B_P$  changes remained very small. Similarly,  $B_J$  was also roughly constant except a peak correlated with the main current one. The  $B_V$  peak is consistent with the bipolar secondary current. The main change of the

**Table 3**

Results of the Variance Analysis of the Current Density Obtained From the Curlometer Technique

Component	$x_1$	$x_2$	$x_3$
$x_{GSE}$	-0.76	0.03	-0.65
$y_{GSE}$	-0.2	-0.96	-0.19
$z_{GSE}$	-0.61	0.28	0.74

Note.  $\lambda_1/\lambda_2 = 2.8$ ;  $\lambda_1/\lambda_3 = 43.2$ ;  $\lambda_2/\lambda_3 = 15.43$ .

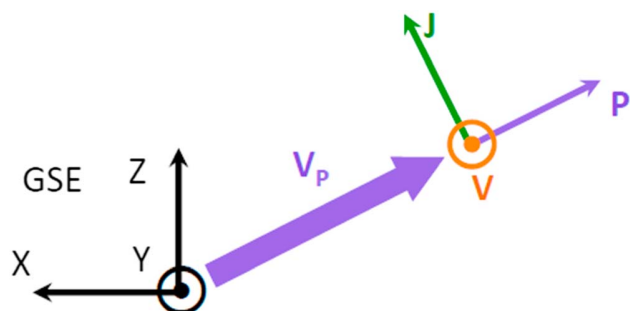


**Figure 8.** The relative orientations of the Propagation Current Structure frame vectors  $\vec{U}_P$ ,  $\vec{U}_J$ , and  $\vec{U}_V$  and the GSE axes. The thick violet arrow shows the direction of the current sheet propagation velocity obtained from multispacecraft data analysis. The Propagation Current Structure frame corresponds to a translation of the GSE frame in the direction of the current sheet propagation velocity combined with a rotation about the y-GSE direction.

magnetic field was on the  $B_V$  component suggesting that the main current (along the  $J$  direction) consisted of a current sheet oriented along the  $V$  direction.

The panel (f) displays the ion velocity in the PCS frame. The ion jet is seen as a peak now on the  $V$  component taking place between the first black dashed vertical line and the second red vertical line. The ion jet crossing lasted for  $\sim 1.8$  s. Multiplying by the propagation velocity, this gives a thickness of 120 km, corresponding to  $\sim 2$  proton Larmor radii. We note that the ion jet was observed concomitant with the overall current structure but that the current peak took place on its downstream side relatively to the structure propagation, that is, when the main flow component ( $V_{IV}$ ) was decreasing (panel (g)).

The ion flow velocity is displayed at a larger scale, and in the PCS frame in panel (g) of Figure 9. The  $V_{IP}$  component along the propagation direction, which also corresponds to the normal to the current sheet, showed a clear reversal upon crossing the current structure.  $V_{IP}$  was first negative, indicating that the plasma moved slower than the current structure

in the propagation direction. After the current sheet and ion jet (observed in  $V_{IV}$ ), it was positive, and the ions moved faster. This means that in the PCS frame (i.e., in the frame moving with the current structure) the flows were converging toward the current structure, which thus was being compressed by the surrounding plasma. There was also a flow reversal along the main current direction, as indicated by the reversal in the  $V_{IJ}$  component. This suggests that there was also a flow shear along the current structure, in addition to the compression. Around 14:17:05–14:17:10 UT, that is, just after  $T_5$ , all flow components reversed. This is interpreted as indicating that the spacecraft reentered into the inner LLBL.

## 4. Discussion and Interpretation

### 4.1. Phenomenological Interpretation

The event analyzed in this study exhibits some features apparently similar to FTEs at first glance, that is, bipolar variation of a magnetic field component and a peak in the magnetic field strength. However, a more detailed examination showed that it cannot be interpreted as a single FTE entity consisting of a single helical flux tube. The main reasons are the following: (i) The bipolar change in the magnetic field did not occur in the expected direction normal to the magnetopause, (ii) a strong and thin current structure and a localized ion jet were detected near the center, and (iii) the electron pitch angle distributions indicate that the event did not consist of a unique and homogenous structure with a single connectivity as expected for a large-scale flux rope. Before proposing an alternative interpretation, let us first summarize the main features of the event. Times  $T_0$  to  $T_5$  mentioned below refer to the vertical dashed lines in Figures 4–6.

1. The event took place during the passage of an interplanetary magnetic cloud. The IMF was intense and stable, with all three GSE components being negative. The solar wind pressure and the Alfvén Mach number were very low.
2. The event occurred when the spacecraft were in the LLBL.
3.  $T_0 \rightarrow T_1$ : The first signature consisted of a change in the magnetic field only, suggestive of remote sensing of the structure propagating toward the spacecraft.
4.  $T_1 \rightarrow T_2$ : The spacecraft entered a flux tube ( $FT_A$ ) mainly characterized by accelerated magnetosheath

electrons exhibiting an anisotropy in the direction parallel to the magnetic field. Moreover, trapped magnetospheric electrons were continuously measured in  $FT_A$ . The density was slightly enhanced and  $B_{YGSE}$  was positive. Ions first streamed antiparallel to the magnetic field and then perpendicular in the duskward ( $Y_{GSE}$  or  $-M$ ) direction. A trapped population of suprathermal electrons was continuously measured in this flux tube.

5.  $T_3 \rightarrow T_4$ : In the second part of the event, the spacecraft crossed a very different flux tube ( $FT_B$ ). There was no trapped electron population

**Table 4**  
The Unit Vectors Defining the PCS (Propagating Current Structure) Frame

Component	$U_P$	$U_J$	$U_V$
$x_{GSE}$	−0.6124	0.7676	0.1889
$y_{GSE}$	0.0239	−0.2209	0.9750
$z_{GSE}$	0.7902	0.6016	0.1169

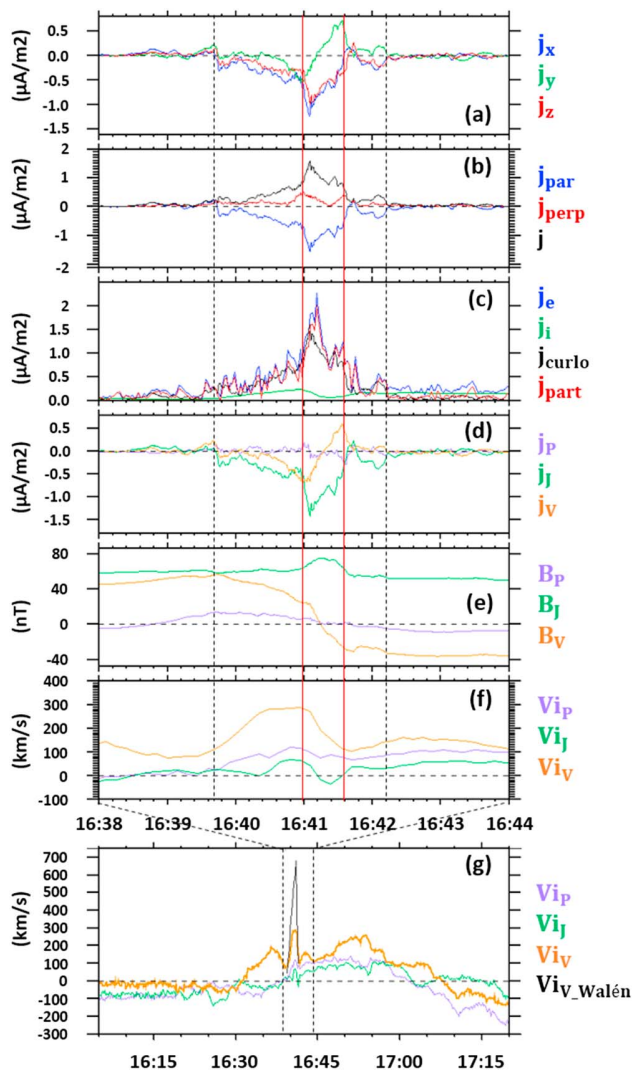


**Figure 9.** Data from Magnetospheric Multiscale mission 1 between 14:16:38 and 14:16:44 UT (a) current density components in the GSE coordinates system; (b) parallel, perpendicular, and the total current densities; (c) electrons and ions current densities as well as the current density obtained from the curlometers technique and the current density obtained from  $ne(V_i - V_e)$ ; (d) current density components in the PCS frame; (e) magnetic field components in the PCS frame; (f) ion velocity components in the PCS frame; and (g) ion velocity components in the PCS frame between 14:16:05 and 14:17:20 UT.

and the anisotropy of the accelerated magnetosheath was in the opposite sense, in the antiparallel direction.  $B_{Y_{GSE}}$  was the main component of the magnetic field and was negative. The density was higher with values close to the ones measured inside the outer LLBL, between 13:45 and 14:00, for example. The plasma flow was in the northward and duskward direction.

6.  $T_2 \rightarrow T_3$ : Between these two flux tubes, there was a strong and thin current sheet where the magnetic field rotated sharply. A strong and localized duskward ion jet along the  $Y_{GSE}$  direction was also observed, qualitatively consistent with a reconnection process occurring inside the current sheet owing to the sharp  $B_Y$  reversal. In the frame moving with the structure the surrounding plasma flow was converging toward the current sheet. The current sheet was thus being compressed.

We interpret this sequence of observations as the signature of the successive crossing of the two flux tubes by the spacecraft. These two flux tubes may have been generated by multiple sequential reconnection process, which is expected to occur under strong  $B_Y$  and negative  $B_Z$  IMF conditions, as was observed for a long time around the event (e.g., Pu et al., 2013; Raeder, 2006). The first flux tube ( $FT_A$ ) contained trapped electrons. This implies that this flux tube has a different history and connectivity compared to the second flux tube which rather contained only magnetosheath electrons with largely different pitch angle properties (Pu et al., 2013). A current sheet formed at the interface between the two flux tubes. As shown by the changes in the ion velocity component along the propagation direction (Figure 8g), the second flux tube ( $FT_B$ ) was moving faster than the first one ( $FT_A$ ). This resulted in an interlaced magnetic structure and associated complex 3-D topology, as has been previously studied with Cluster data (Louarn et al., 2004). The observed compression is likely at the origin of the current sheet formation and of the reconnection occurring inside as described next.

#### 4.2. Reconnection at the Thin Current Sheet

Reconnection driven by compression at current sheets formed by the interaction of plasma flows have been suggested for interpreting spacecraft observations from the magnetopause (Øieroset et al., 2016), in the magnetotail (Alexandrova et al., 2016), and simulation results as well (Huang et al., 2014; Oka et al., 2010). Simulations have been performed in particular to study the coalescence of magnetic islands and showed features similar to the ones identified in this event. This is true, in particular, for the formation of a thin current sheet with an exhaust in the transverse direction (Zhou et al., 2014).

Qualitatively, the local conditions satisfied at the interface of coalescing magnetic islands are somewhat similar to those observed in our event.

Locally, this corresponds to the interaction between two disconnected magnetic flux tubes pushed against one another by the differential plasma flows in which they are imbedded. MMS measurements thus permit a detailed analysis of such a case, but with some conditions specific to the event: the current sheet was characterized by a large density jump and a magnetic shear angle of only  $\sim 73^\circ$  as compared with  $180^\circ$  in published simulations with comparable densities (Galsgaard et al., 2000).

Figure 10 shows a sliced schematic view of the crossing in the PCS frame. The spacecraft started in the low-density flux tube  $FT_A$  at  $T_1$ . The  $V$  component of the magnetic field was positive inside  $FT_A$ . An ion jet, as represented by red arrows with a yellow outline, was observed inside the current sheet (which is about 169 km thick). At the second edge of the jet, the spacecraft crossed a complex current structure (between  $T_2$

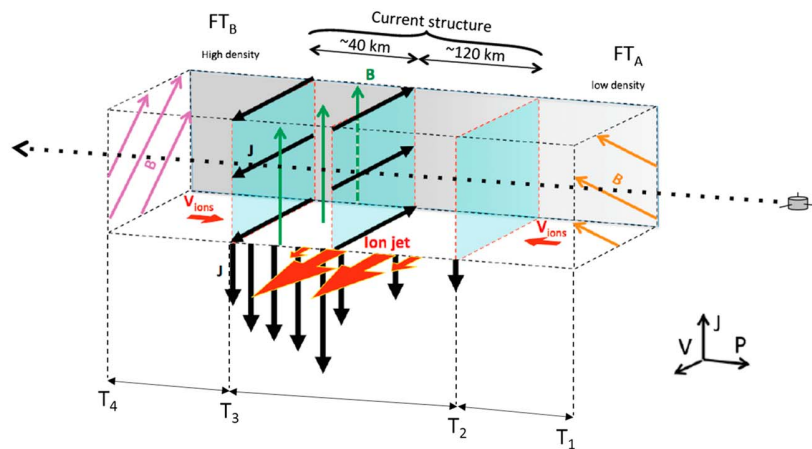


**Figure 10.** A schematic view of the crossing of the current structure in the Propagation Current Structure frame. The orange, green, and magenta arrows show the magnetic field orientation in the  $FT_A$ , current structure and  $FT_B$ , respectively. The black arrows in the  $\vec{U}_J$  ( $\vec{U}_V$ ) direction correspond to the main (bipolar) current density. The two oppositely directed red arrows in the  $\vec{U}_P$  direction illustrate the compression of the current structure. The red arrows with yellow edges show the ion jet observed in the current structure. The spacecraft trajectory across the structure is represented by the dashed black arrow.

and  $T_3$ ). It consisted of a strong and peaked current sheet directed in the  $-\vec{U}_J$  direction encircled by a pair of current sheets of opposite polarities along the  $\vec{U}_V$  direction. Between  $T_3$  and  $T_4$ , the spacecraft were in  $FT_B$ , where the  $V$  component of the magnetic field is negative. The combined effect of opposite (bipolar) currents as observed in the  $\vec{U}_V$  direction was to produce an enhancement of the positive  $B_J$  component in between them (as represented by the green arrows). In doing so, these currents directly supported the rotation of the magnetic field from the  $FT_A$  to the  $FT_B$  orientations. This enhancement in the  $B_J$  component is clearly seen in Figure 9f as a 15–20 nT peak superimposed on top of the larger-scale constant  $B_J \sim 50$  nT. The red vectors in the  $\pm\vec{U}_P$  directions illustrate the compression of the current structure by two oppositely directed flows (which converge toward it).

The process at the origin of the ion jet observed inside the first current sheet was likely magnetic reconnection driven by the compression of the two distinct sets of open field lines. This is partially supported by the Walén test results that are superimposed on the main jet velocity component in Figure 9g. Walén tests (e.g., Phan et al., 2004) were performed with positive and negative correlations on the earthward (upstream relative to the structure propagation) and sunward (downstream) sides of the exhaust, respectively. The exhaust was observed between 14:16:39.7 and 14:16:41.7 UT. This is presented in Figure 9g with  $V_{IONS} - V_{HT} = \pm V_A$ , where  $V_{IONS}$ ,  $V_{HT}$ , and  $V_A$  are the bulk ion, deHoffman-Teller, and Alfvén velocity vectors, respectively. The Walén test would predict an ion jet with amplitude  $\sim 688$  km/s. This is much larger than the amplitude of the observed jet. The correlation coefficient is of  $-0.92$  and the slope is of  $-0.68$  for the entry to the exhaust between 14:16:39.7 and 14:16:40.95 UT. For the exit from the exhaust, between 14:16:40.95 and 14:16:41.7 UT, the Walén relation provides a correlation coefficient of  $0.92$  with a slope of  $0.18$ , which is much lower than the ideal value  $\pm 1$ . Although the Walén test shows that the ion bulk flow is not as large as expected, this may be due to the proximity to the X-line (Phan et al., 2016). To support this hypothesis, we note that with densities of 2 and  $6 \text{ cm}^{-3}$ , as measured each side of the exhaust at 14:16:39.7 UT and 14:16:41.7 UT, the typical ion skin depth  $\lambda_i$  is estimated as 100–155 km. The jet thickness is thus estimated to be approximately 120 km, or about  $0.8\text{--}1.3 \lambda_i$ . Such a thickness implies that we are very close to the X-line ( $5\text{--}8 \lambda_i$  or  $\sim 840$  km), which is consistent with the ion jet not being fully developed yet and thus with the overestimation of the ion speed from the Walén test.

## 5. Summary and Conclusions

We have studied in detail what initially looked on face value like a classic FTE at the Earth's dayside magnetopause, as observed by the MMS mission. Due to its high-resolution measurements, our analysis revealed the following unusual properties:



1. The large-scale magnetic field bipolar signature was not found in the component normal to the nominal magnetopause surface, but rather in the  $B_{Y_{GSE}}$  component.
2. The densities and pitch angle distributions of suprathermal electrons shows that the current sheet separated two distinct plasmas with different properties and magnetic connectivities.
3. An intense and complex current structure, supporting the large reversal in the  $B_{Y_{GSE}}$  component, was observed near the peak in the magnetic field strength.
4. This current was carried by electrons. Although the scale of the structure is approximately three times the ion Larmor radius, the structure possesses smaller scale substructures, smaller than the ion Larmor radius. The intense current sheet was associated with a strong transverse flow (along  $V_{Y_{GSE}}$ ) consistent with expectations from magnetic reconnection therein.

Our interpretation is that these properties are incompatible with a classic, single FTE structure. The data are rather consistent with a complex, three-dimensional interaction of two distinct flux tubes. This compressive interaction led to the formation of a thin and complex current structure between two flux tubes of very different orientations ( $73^\circ$  magnetic shear angle) which mimicked the bipolar magnetic structure and the enhanced core magnetic field, both expected for classic FTEs. The strong magnetic field pileup and ensuing thin current sheet also appeared to have triggered magnetic reconnection at the interface.

#### Acknowledgments

We thank all the MMS teams and instrument PIs for data access and process. Work at IRAP was supported by CNRS and CNES. The work of Jonathan Eastwood was funded by STFC (UK) grant ST/N000692/1. C. J. F. work was partially supported by NASA grants 499878Q and NNX16AO04G. MMS data visualization and analysis was performed with the CL software (<http://clweb.irap.omp.eu/>). We used also AMDA science analysis system and 3DView visualization tool provided by the Centre de Données de la Physique des Plasmas (CDPP) supported by CNRS, CNES, Observatoire de Paris and Université Paul Sabatier, Toulouse (<http://amda.irap.omp.eu/> and <http://3dview.irap.omp.eu/>). MMS data are available at <https://lasp.colorado.edu/mms/sdc/public/>. The work of Jonathan Eastwood was funded by STFC (UK) grant ST/N000692/1.

#### References

- Alexandrova, A., Nakamura, R., Panov, E. V., Sasunov, Y. L., Nakamura, T., Vörös, Z., et al. (2016). Twointeracting X lines in magne-totail: Evolution of collisionbetween the counterstreaming jets. *Geophysical Research Letters*, 43, 7795–7803. <https://doi.org/10.1002/2016GL069823>
- Angelopoulos, V. (2008). The THEMIS mission. *Space Science Reviews*, 141(1–4), 5–34. <https://doi.org/10.1007/s11214-008-9336-1>
- Biernat, H. K. (1991). Coupling processes at the magnetopause. In H. K. Biernat, S. J. Bauer, & M. Heinder (Eds.), *Theoretical problems in space and fusion plasmas* (pp. 105–118). Wien: Oesterreichischen Akademie der Wissenschaften.
- Burch, J. L., Moore, T. E., Torbert, R. B., & Giles, B. L. (2016). Magnetospheric multiscale overview and science objectives. *Space Science Reviews*, 199(1–4), 5–21. <https://doi.org/10.1007/s11214-015-0164-9>
- Burch, J. L., & Phan, T. D. (2016). Magnetic reconnection at the dayside magnetopause: Advances with MMS. *Geophysical Research Letters*, 43, 8327–8338. <https://doi.org/10.1002/2016GL069787>
- Cardoso, F. R., Gonzalez, W. D., Sibeck, D. G., Kuznetsova, M., & Koga, D. (2013). Magnetopause reconnection and interlinked flux tubes. *Annales Geophysicae*, 31(10), 1853–1866. <https://doi.org/10.5194/angeo-31-1853-2013>
- Daum, P., Wild, J. A., Penz, T., Woodfield, E. E., Rème, H., Fazakerley, A. N., et al. (2008). Global MHD simulation of flux transfer events at the high-latitude magnetopause observed by the Cluster spacecraft and the SuperDARN radar system. *Journal of Geophysical Research*, 113, A07522. <https://doi.org/10.1029/2007JA012749>
- Drake, J. F., Swisdak, M., Che, H., & Shay, M. A. (2006). Electron acceleration from contracting magnetic islands during reconnection. *Nature*, 443(7111), 553–556. <https://doi.org/10.1038/nature05116>
- Dungey, J. W. (1961). Interplanetary magnetic field and the auroral zones. *Physical Review Letters*, 6(2), 47–48. <https://doi.org/10.1103/PhysRevLett.6.47>
- Dunlop, M. W., & Woodward, T. I. (1998). Discontinuity analysis: Orientation and motion. In *Analysis methods for multispacecraft data, ISSI Sci. Rep. SR-001* (pp. 271–302). Norwell, MA: Kluwer Academic.
- Eastwood, J. P., Phan, T.-D., Mozer, F. S., Shay, M. A., Fujimoto, M., Retinò, A., et al. (2007). Multi-point observations of the Hall electromagnetic field and secondary island formation during magnetic reconnection. *Journal of Geophysical Research*, 112, A06235. <https://doi.org/10.1029/2006JA012158>
- Eastwood, J. P., Phan, T. D., Øieroset, M., Shay, M. A., Malakit, K., Swisdak, M., et al. (2013). Influence of asymmetries and guide fields on the magnetic reconnection diffusion region in collisionless space plasmas. *Plasma Physics and Controlled Fusion*, 55(12), 124001. <https://doi.org/10.1088/0741-3335/55/12/124001>
- Egedal, J., Fox, W., Katz, N., Porkolab, M., Reim, K., & Zhang, E. (2007). Laboratory observations of spontaneous magnetic reconnection. *Physical Review Letters*, 98(1), 015003. <https://doi.org/10.1103/PhysRevLett.98.015003>
- Escoubet, C. P., Fehringer, M., & Goldstein, M. (2001). Introduction the Cluster mission. *Annales Geophysique*, 19(10/12), 1197–1200. <https://doi.org/10.5194/angeo-19-1197-2001>
- Farrugia, C. J., Lavraud, B., Torbert, R. B., Argall, M., Kacem, I., Yu, W., et al. (2016). Magnetospheric Multiscale mission observations and non-force free modeling of a flux transfer event immersed in a super-Alfvénic flow. *Geophysical Research Letters*, 43, 6070–6077. <https://doi.org/10.1002/2016GL068758>
- Farrugia, C. J., Southwood, D. J., & Cowley, S. W. H. (1988). Observations of flux transfer events. *Advances in Space Research*, 8(9–10), 249–258. [https://doi.org/10.1016/0273-1177\(88\)90138-X](https://doi.org/10.1016/0273-1177(88)90138-X)
- Fear, R. C., Fazakerley, A. N., Owen, C. J., Lahiff, A. D., Lucek, E. A., Balogh, A., et al. (2005). Cluster observations of boundary layer structure and a flux transfer event near the cusp. *Annales Geophysique*, 23(7), 2605–2620. <https://doi.org/10.5194/angeo-23-2605-2005>
- Fear, R. C., Milan, S. E., Fazakerley, A. N., Fornaçon, K.-H., Carr, C. M., & Dandouras, I. (2009). Simultaneous observations of flux transfer events by THEMIS, cluster, double star, and SuperDARN: Acceleration of FTEs. *Journal of Geophysical Research*, 114, A10213. <https://doi.org/10.1029/2009JA014310>
- Fear, R. C., Milan, S. E., Fazakerley, A. N., Lucek, E. A., Cowley, S. W. H., & Dandouras, I. (2008). The azimuthal extent of three flux transfer events. *Annales Geophysique*, 26(8), 2353–2369. <https://doi.org/10.5194/angeo-26-2353-2008>
- Fear, R. C., Trenchi, L., Coxon, J. C., & Milan, S. E. (2017). How much flux does a flux transfer event transfer? *Journal of Geophysical Research: Space Physics*, 122, 12,310–12,327. <https://doi.org/10.1002/2017JA024730>
- Fedder, J. A., Slinker, S. P., Lyon, J. G., & Russell, C. T. (2002). Flux transfer events in global numerical simulations of the magnetosphere. *Journal of Geophysical Research*, 107(A5), 1048. <https://doi.org/10.1029/2001JA000025>

- Fox, W., Sciortino, F., Stechow, A. V., Jara-Almonte, J., Yoo, J., Ji, H., & Yamada, M. (2017). Experimental verification of the role of electron pressure in fast magnetic reconnection with a guide field. *Physical Review Letters*, 118(12), 125002. <https://doi.org/10.1103/PhysRevLett.118.125002>
- Fuselier, S. A., Lewis, W. S., Schiff, C., Ergun, R., Burch, J. L., Petriner, S. M., & Trattner, K. J. (2016). Magnetospheric multiscale science mission profile and operations. *Space Science Reviews*, 199(1-4), 77–103. <https://doi.org/10.1007/s11214-014-0087-x>.
- Galsgaard, K., Parnell, C. E., & Blaizot, J. (2000). Elementary heating events—Magnetic interactions between two flux sources. *Astronomy and Astrophysics*, 362, 395–405.
- Harvey, C. C. (1998). Spatial gradients and the volumetric tensor. In G. Paschmann & P. W. Daly (Eds.), *Analysis methods for multi-spacecraft data* (pp. 307–348). Bern, Switzerland: International Space Science Institute.
- Hasegawa, H., Fujimoto, M., Maezawa, K., Saito, Y., & Mukai, T. (2003). Geotail observations of the dayside outer boundary region: Interplanetary magnetic field control and dawn-dusk asymmetry. *Journal of Geophysical Research*, 108(A4), 1163. <https://doi.org/10.1029/2002JA009667>
- Hasegawa, H., Sönnnerup, B. U. Ö., Owen, C. J., Klecker, B., Paschmann, G., Balogh, A., & Rème, H. (2006). The structure of flux transfer events recovered from cluster data. *Annales Geophysicae*, 24(2), 603–618. <https://doi.org/10.5194/angeo-24-603-2006>
- Hasegawa, H., Wang, J., Dunlop, M. W., Pu, Z. Y., Zhang, Q.-H., Lavraud, B., et al. (2010). Evidence for a flux transfer event generated by multiple X-Line reconnection at the magnetopause. *Geophysical Research Letters*, 37, L16101. <https://doi.org/10.1029/2010GL044219>
- Hesse, M., Birn, J., & Schindler, K. (1990). On the topology of flux transfer events. *Journal of Geophysical Research*, 95(A5), 6549–6560. <https://doi.org/10.1029/JA095iA05p06549>
- Huang, S. Y., Zhou, M., Yuan, Z. G., Deng, X. H., Sahraoui, F., Pang, Y., & Fu, S. (2014). Kinetic simulations of electric field structure within magnetic island during magnetic reconnection and their applications to the satellite observations. *Journal of Geophysical Research: Space Physics*, 119, 7402–7412. <https://doi.org/10.1002/2014JA020054>
- Hwang, K.-J., Sibeck, D. G., Giles, B. L., Pollock, C. J., Gershman, D., Avakov, L., et al. (2016). The substructure of a flux transfer event observed by the MMS spacecraft. *Geophysical Research Letters*, 43, 9434–9443. <https://doi.org/10.1002/2016GL070934>
- King, J. H., & Papitashvili, N. E. (2005). Solar wind spatial scales in and comparisons of hourly wind and ACE plasma and magnetic field data. *Journal of Geophysical Research*, 110, A02104. <https://doi.org/10.1029/2004JA010649>
- Lavraud, B., & Borovsky, J. E. (2008). Altered solar wind-magnetosphere interaction at low Mach numbers: Coronal mass ejections. *Journal of Geophysical Research*, 113, A00808. <https://doi.org/10.1029/2008JA013192>
- Le, G., Gosling, J. T., Russell, C. T., Elphic, R. C., Thomsen, M. F., & Newbury, J. A. (1999). The magnetic and plasma structure of flux transfer events. *Journal of Geophysical Research*, 104(A1), 233–245. <https://doi.org/10.1029/1998JA000023>
- Lee, L. C., & Fu, Z. F. (1985). A theory of magnetic flux transfer at the Earth's magnetopause. *Geophysical Research Letters*, 12(2), 105–108. <https://doi.org/10.1029/GL012i002p00105>
- Lemaire, J., & Roth, M. (1978). Penetration of solar wind plasma elements into magnetosphere. *Journal of Atmospheric and Terrestrial Physics*, 40(3), 331–335. [https://doi.org/10.1016/0021-9169\(78\)90049-1](https://doi.org/10.1016/0021-9169(78)90049-1)
- Lockwood, M., Fazakerley, A., Opgenoorth, H., Moen, J., van Eyken, A. P., Dunlop, M., et al. (2001). Coordinated Cluster and ground-based instrument observations of transient changes in the magnetopause boundary layer during an interval of predominantly northward IMF: Relation to reconnection pulses and FTE signatures. *Annales Geophysique*, 19(10/12), 1613–1640. <https://doi.org/10.5194/angeo-19-1613-2001>
- Lockwood, M., Opgenoorth, H., van Eyken, A. P., Fazakerley, A., Bosqued, J.-M., Denig, W., et al. (2001). Coordinated Cluster, ground-based instrumentation and low-altitude satellite observations of transient poleward-moving events in the ionosphere and in the tail lobe. *Annales Geophysique*, 19(10/12), 1589–1612. <https://doi.org/10.5194/angeo-19-1589-2001>
- Louarn, P., Fedorov, A., Budnik, E., Fruit, G., Sauvaud, J. A., Harvey, C. C., et al. (2004). Cluster observations of complex 3D magnetic structures at the magnetopause. *Geophysical Research Letters*, 31, L19805. <https://doi.org/10.1029/2004GL020625>
- Øieroset, M., Phan, T. D., Eastwood, J. P., Fujimoto, M., Daughton, W., Shay, M. A., et al. (2011). Direct evidence for a three-dimensional magnetic flux rope flanked by two active magnetic reconnection X lines at Earth's magnetopause. *Physical Review Letters*, 107(16), 165007. <https://doi.org/10.1103/PhysRevLett.107.165007>
- Øieroset, M., Phan, T. D., Haggerty, C., Shay, M. A., Eastwood, J. P., Gershman, D. J., et al. (2016). MMS observations of large guide field symmetric reconnection between colliding reconnection jets at the center of a magnetic flux rope at the magnetopause. *Geophysical Research Letters*, 43, 5536–5544. <https://doi.org/10.1002/2016GL069166>
- Oka, M., Phan, T. D., Krucker, S., Fujimoto, M., & Shinohara, I. (2010). Electron acceleration by multi-island coalescence. *The Astrophysical Journal*, 714(1), 915–926. <https://doi.org/10.1088/0004-637X/714/1/915>
- Phan, T. D., Dunlop, M. W., Paschmann, G., Klecker, B., Bosqued, J. M., Rème, H., et al. (2004). Cluster observations of continuous reconnection at the magnetopause under steady interplanetary magnetic field conditions. *Annales Geophysique*, 22(7), 2355–2367. <https://doi.org/10.5194/angeo-22-2355-2004>
- Phan, T. D., Shay, M. A., Haggerty, C. C., Gosling, J. T., Eastwood, J. P., Fujimoto, M., et al. (2016). Ion Larmor radius effects near a reconnection X line at the magnetopause: THEMIS observations and simulation comparison. *Geophysical Research Letters*, 43, 8844–8852. <https://doi.org/10.1002/2016GL070224>
- Pollock, C., Moore, T., Jacques, A., Burch, J., Gliese, U., Saito, Y., et al. (2016). Fast plasma investigation for magnetospheric multiscale. *Space Science Reviews*, 199(1-4), 331–406. <https://doi.org/10.1007/s11214-016-0245-4>
- Pritchett, P. L. (2008). Energetic electron acceleration during multi-island coalescence. *Physics of Plasmas*, 15, 102105. <https://doi.org/10.1063/1.2996321>
- Pu, Z. Y., Raeder, J., Zhong, J., Bogdanova, Y. V., Dunlop, M., Xiao, C. J., et al. (2013). Magnetic topologies of an in vivo FTE observed by Double Star/TC-1 at Earth's magnetopause. *Geophysical Research Letters*, 40, 3502–3506. <https://doi.org/10.1002/grl.50714>
- Raeder, J. (2006). Flux transfer events: 1. Generation mechanism for strong southward IMF. *Annales Geophysique*, 24(1), 381–392. <https://doi.org/10.5194/angeo-24-381-2006>
- Robert, P., Dunlop, M. W., Roux, A., & Chanteur, G. (1998). Accuracy of current density determination. In G. Paschmann & P. W. Daly (Eds.), *Analysis methods for multi-spacecraft data* (pp. 395–412). Noordwijk, Netherlands: ESA Publications. <https://doi.org/10.1517/13543784.7.6.929>
- Roux, A., Robert, P., Fontaine, D., Le Contel, O., Canu, P., & Louarn, P. (2015). What is the nature of magnetosheath FTEs? *Journal of Geophysical Research: Space Physics*, 120, 4576–4595. <https://doi.org/10.1002/2015JA020983>
- Russell, C. T., Anderson, B. J., Baumjohann, W., Bromund, K. R., Dearborn, D., Fischer, D., et al. (2016). The magnetospheric multiscale magnetometers. *Space Science Reviews*, 199(1-4), 189–256. <https://doi.org/10.1007/s11214-014-0057-3>
- Russell, C. T., & Elphic, R. C. (1978). Initial ISEE magnetometer results: Magnetopause observations. *Space Science Reviews*, 22(6), 681–715. <https://doi.org/10.1007/BF00212619>

- Russell, C. T., & Elphic, R. C. (1979). ISEE observations of flux transfer events at the dayside magnetopause. *Geophysical Research Letters*, 6(1), 33–36. <https://doi.org/10.1029/GL006i001p00033>
- Russell, C. T., Mellott, M. M., Smith, E. J., & King, J. H. (1983). Multiple spacecraft observations of interplanetary shocks: Four spacecraft determination of shock normals. *Journal of Geophysical Research*, 88(A6), 4739–4748. <https://doi.org/10.1029/JA088iA06p04739>
- Scholer, M. (1988). Magnetic flux transfer at the magnetopause based on single X line bursty reconnection. *Geophysical Research Letters*, 15(4), 291–294. <https://doi.org/10.1029/GL015i004p00291>
- Shue, J.-H., Chao, J. K., Fu, H. C., Russell, C. T., Song, P., Khurana, K. K., & Singer, H. J. (1997). A new functional form to study the solar wind control of the magnetopause size and shape. *Journal of Geophysical Research*, 102(A5), 9497–9511. <https://doi.org/10.1029/97JA00196>
- Silveira, M. V., Gonzalez, W. D., Sibeck, D. G., & Koga, D. (2012). Study on flux transfer events at the Earth's magnetopause observed by THEMIS satellites. AGU Fall Meeting Abstracts 13. Retrieved from <http://adsabs.harvard.edu/abs/2012AGUFMSM13A2335S>
- Song, H. Q., Chen, Y., Li, G., & Kong, X. L. (2012). Coalescence of macroscopic magnetic islands and electron acceleration from STEREO observation. *Physical Review X*, 2, 021015. <https://doi.org/10.1103/PhysRevX.2.021015>
- Sonnerup, B. U. Ö., Hasegawa, H., & Paschmann, G. (2004). Anatomy of a flux transfer event seen by Cluster. *Geophysical Research Letters*, 31, L11803. <https://doi.org/10.1029/2004GL020134>
- Sonnerup, B. U. Ö., & Scheible, M. (1998). Minimum and maximum variance analysis. In G. Paschmann & P. W. Daly (Eds.), *Analysis methods for multi-spacecraft data* (pp. 185–220). Bern, Switzerland: International Space Science Institute.
- Southwood, D. J., Farrugia, C. J., & Saunders, M. A. (1988). What are flux transfer events? *Planetary and Space Science*, 36(5), 503–508. [https://doi.org/10.1016/0032-0633\(88\)90109-2](https://doi.org/10.1016/0032-0633(88)90109-2)
- Stenzel, R. L., & Gekelman, W. (1979). Experiments on magnetic-field-line reconnection. *Physical Review Letters*, 42(16), 1055–1057. <https://doi.org/10.1103/PhysRevLett.42.1055>
- Teh, W.-L., Eriksson, S., Sonnerup, B. U. Ö., Ergun, R., Angelopoulos, V., Glassmeier, K. H., et al. (2010). THEMIS observations of a secondary magnetic island within the Hall electromagnetic field region at the magnetopause. *Geophysical Research Letters*, 37, L21102. <https://doi.org/10.1029/2010GL045056>
- Torbert, R. B., Russell, C. T., Magnes, W., Ergun, R. E., Lindqvist, P.-A., LeContel, O., et al. (2016). The FIELDs instrument suite on MMS: Scientific objectives, measurements, and data products. *Space Science Reviews*, 199(1–4), 105–135. <https://doi.org/10.1007/s11214-014-0109-8>
- Trenchi, L., Fear, R. C., Trattner, K. J., Mihaljcic, B., & Fazakerley, A. N. (2016). A sequence of flux transfer events potentially generated by different generation mechanisms. *Journal of Geophysical Research: Space Physics*, 121, 8624–8639. <https://doi.org/10.1002/2016JA022847>
- Wild, J. A., Cowley, S. W. H., Davies, J. A., Khan, H., Lester, M., Milan, S. E., et al. (2001). First simultaneous observations of flux transfer events at the high-latitude magnetopause by the Cluster spacecraft and pulsed radar signatures in the conjugate ionosphere by the CUTLASS and EISCAT radars. *Annales Geophysique*, 19(10/12), 1491–1508. <https://doi.org/10.5194/angeo-19-1491-2001>
- Yamada, M. (1999). Review of controlled laboratory experiments on physics of magnetic reconnection. *Journal of Geophysical Research*, 104(A7), 14,529–14,541. <https://doi.org/10.1029/1998JA900169>
- Young, D. T., Burch, J. L., Gomez, R. G., De Los Santos, A., Miller, G. P., Wilson, P., et al. (2016). Hot plasma composition analyzer for the Magnetospheric Multiscale mission. *Space Science Reviews*, 199(1–4), 407–470. <https://doi.org/10.1007/s11214-014-0119-6>
- Zhong, J., Pu, Z. Y., Dunlop, M. W., Bogdanova, Y. V., Wang, X. G., Xiao, C. J., et al. (2013). Three-dimensional magnetic flux rope structure formed by multiple sequential X-line reconnection at the magnetopause. *Journal of Geophysical Research: Space Physics*, 118, 1904–1911. <https://doi.org/10.1002/jgra.50281>
- Zhou, M., Pang, Y., Deng, X., Huang, S., & Lai, X. (2014). Plasma physics of magnetic island coalescence during magnetic reconnection. *Journal of Geophysical Research: Space Physics*, 119, 6177–6189. <https://doi.org/10.1002/2013JA019483>





## Abstract

Magnetic reconnection is a ubiquitous and fundamental process in space plasma physics. The NASA's Magnetospheric Multiscale mission (MMS) launched on 12 March 2015 was designed to provide in-situ measurements for analyzing the reconnection process at the Earth's magnetosphere. In this aim, four identically instrumented spacecraft measure fields and particles in the reconnection regions with a time resolution which is one hundred times faster than previous missions. MMS allows for the first time to study the microscopic structures associated with magnetic reconnection and, in particular, the thin electron diffusion region. At the Earth's magnetopause, magnetic reconnection governs the transport of energy and momentum from the solar wind plasma into the Earth's magnetosphere through conversion of magnetic energy into kinetic and thermal energies after a rearrangement of magnetic field lines. Flux Transfer Events (FTEs) are considered to be one of the main and most typical products of magnetic reconnection at the Earth's magnetopause. However, more complex 3D magnetic structures with signatures akin to those of FTEs might also occur at the magnetopause like interlaced flux tubes resulting from magnetic reconnection at multiple sites. The first part of the work presented in this thesis consisted of the investigation of one of these events that was observed, under unusual and extreme solar wind conditions, in the vicinity of the Earth's magnetopause by MMS. Despite signatures that, at first glance, appeared consistent with a classic FTE, this event was interpreted to be the result of the interaction of two separate sets of magnetic field lines with different connectivities. The high time resolution of MMS data allowed to resolve a thin current sheet that was observed at the interface between the two sets of field lines. The current sheet was associated with a large ion jet suggesting that the current sheet was submitted to a compression which drove magnetic reconnection and led to the formation of the ion jet. The direction, velocity and scale of different structures were inferred using multi-spacecraft data analysis techniques. This study was completed with a plasma wave analysis that focused on the reconnecting current sheet.

**Keywords:** Space plasmas, magnetic reconnection, MMS mission, in-situ observations, multi-spacecraft analysis methods, wave-particle interactions.

## Résumé

La reconnexion magnétique est un processus omniprésent et fondamental dans la physique des plasmas spatiaux. La "Magnetospheric multiscale mission" (MMS) de la NASA, lancée le 12 mars 2015, a été conçue pour fournir des mesures in-situ permettant d'analyser le processus de reconnexion dans la magnétosphère terrestre. Dans ce but, quatre satellites identiquement instrumentés mesurent les champs électromagnétiques et les particules chargées dans les régions de reconnexion, avec une résolution temporelle cent fois meilleure que celle des missions précédentes. MMS permet, pour la première fois, d'étudier les structures microscopiques associées à la reconnexion magnétique et, en particulier, la région de diffusion électronique. Au niveau de la magnétopause terrestre, la reconnexion magnétique a un rôle chef dans le transport de l'énergie du vent solaire vers la magnétosphère terrestre, en convertissant l'énergie magnétique en énergie cinétique et thermique. Les événements à transfert de flux (FTEs) sont considérés comme l'un des produits principaux et les plus typiques de la reconnexion magnétique à la magnétopause terrestre. Cependant, des structures magnétiques 3D plus complexes, avec des signatures similaires à celles des FTEs, peuvent également exister à la magnétopause. On retrouve, par exemple, des tubes de flux entrelacés qui résultent de reconnexions magnétiques ayant eues lieu à des sites différents. La première partie de cette thèse étudie l'un de ces événements, qui a été observé dans des conditions de vent solaire inhabituelles, au voisinage de la magnétopause terrestre par MMS. Malgré des signatures qui, à première vue, semblaient cohérentes avec un FTE classique, cet événement a été interprété comme étant le résultat de l'interaction de deux tubes de flux avec des connectivités magnétiques différentes. La haute résolution temporelle des données MMS a permis d'étudier en détail une fine couche de courant observée à l'interface entre les deux tubes de flux. La couche de courant était associée à un jet d'ions, suggérant ainsi que la couche de courant était soumise à une compression qui a entraîné une reconnexion magnétique à l'origine du jet d'ions. La direction, la vitesse de propagation et la taille de différentes structures ont été déduites en utilisant des techniques d'analyse de données de plusieurs satellites. La deuxième partie de la thèse fournit une étude complémentaire à la précédente et s'intéresse aux ondes observées autour de la couche de courant.

**Most clés :** Plasmas spatiaux, reconnexion magnétique, mission MMS, observations in-situ, méthodes d'analyse multi-satellite, interactions onde-plasma.